ORGANO-OSMIUM ANTICANCER COMPLEXES WITH NOVEL AZO-LIGANDS

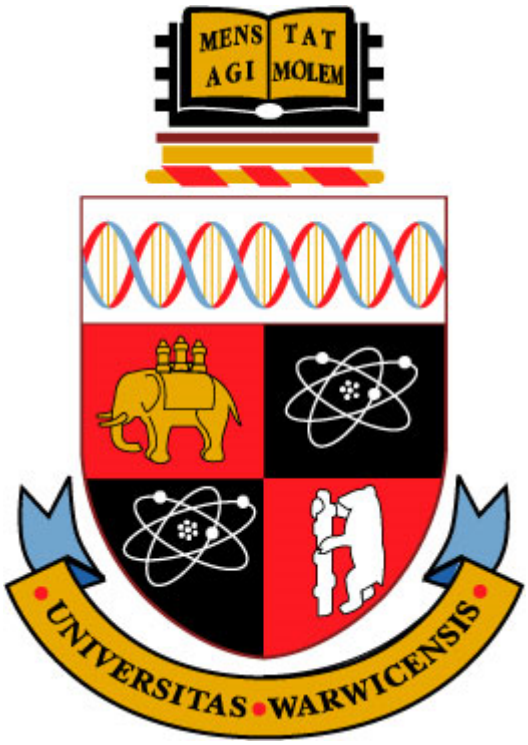

A Thesis Submitted for the Degree of Doctor of Philosophy

Russell James Needham, MSci

Supervisor: Prof. Peter J. Sadler

July 2016

Contents

Acknowledgements

I would like to thank my supervisor Prof. Peter J. Sadler for the opportunity to work within one of the most prestigious groups in its field. It has been an honour. I am very grateful for all the encouragement and support he's given me throughout my course and the opportunity to work in a very diverse area of research and develop new skills. I have very much enjoyed working in the Sadler group and the annual BBQs hosted by him and his wife. Also providing me with part time work synthesising complexes for the group towards the end of my course has been of great financial help indeed.

A very big thanks goes to Abraha for all his professional assistance with the synthesis aspects of my project. Thanks for helping me develop the ideas necessary to complete my project and also for offering words of reassurance during my most stressful times. Also, a very big thanks to Isolda. There is no way I could have possibly obtained all the biological data that I have without your tireless work in Life Sciences and dedication to the group.

I'd also like to thank Carlos for his collaboration. Hopefully soon I will have my very first publication thanks to his input. Thank you to Nicolas for help with electrochemistry and computational calculations. Thanks to Ruth for technical HPLC support and for training me to use the instrument, and many thanks to Maria and Ying for useful discussions along the way. I have also very much enjoyed working alongside Nichola, Adam and Jess who all started their PhDs at the same time as me, and thank you to everyone in the Sadler group past

and present. It's been an enjoyable experience working in our labs and in our lively offices with everyone.

Also a big thank you to those who've provided technical support from outside my group. Dr. Ivan Prokes for his assistance and training with NMR. Dr. Lijiang Song and Mr. Phillip Aston for giving up time to train me in mass spectrometry, LC-MS and ICP. I wouldn't have got very far without your help. And of course thanks to Dr. Guy Clarkson for helping me obtain a rather large number of crystal structures throughout my years at Warwick (still not quite as many as Ying who I think holds the group record!).

Thank you to Prof. Phil Blower for welcoming me to his group during my 3 month collaboration project at King's College London in 2013. I had a very enjoyable time living and working in London and the people in your group made me feel at home. Thanks to Mr. David Thakor, Dr. Levente Meszaros, Dr. Maggie Cooper, Dr. Putthiporn Charoenphun and Dr. Florian Kampmeier who provided me with all the training, advice and supervision to handle radio-active isotopes and cell cultures. Both were very new to me at the time.

I would also like to say thank you to my sponsors, ERC and WCPRS. Without their funding this great opportunity would not have been possible.

Finally, I would like to thank all my family and friends (and pets). Particularly my parents, who have stood by me and helped me financially as well as offer support and encouragement throughout. I could not have done it without you.

Declaration

I hereby declare that except where specific reference is made to other sources, the work contained in this thesis is the original work of the author. It has been composed by myself and has not been submitted, in whole or in part, for any other degree, diploma or other qualification.

Russell J. Needham
November 2016

Conferences and Meetings Attended

1) RSC Dalton Division Joint Interest Groups Meeting. Coventry, UK (April 2012).

2) COST Action CM1105 Working Group #4 Meeting. Metallodrugs II: design and mechanism of action. Olomouc, Czech Republic (March 2013). Oral presentation.

3) Warwick University Postgraduate Symposium. Coventry, UK (May 2013). Poster presentation.

4) RSC Dalton Division Joint Interest Groups Meeting. Coventry, UK (April 2014). Poster presentation.

5) Warwick University Postgraduate Symposium. Coventry, UK (May 2014). Oral presentation.

6) RSC Dalton Discussion 15: Metal ions in medical imaging: optical, radiopharmaceutical and MRI contrast. York, UK (September 2014). Poster presentation.

7) 8th International Symposium on Bioorganometallic Chemistry. Moscow, Russia (September 2016). Poster presentation.

Abstract

Piano-stool iodido Os(II) arene complexes containing AZPY (phenylazopyridine) π-acceptor bidentate ligands have been previously shown to exhibit potent anti-cancer activity and mechanisms of action that involve ROS generation, and differ greatly from early Os(II) arene complexes baring σ-donor bidentate ligands. The aim of this thesis was to explore Os(II) complexes containing other types of azo-ligands as well as continue our studies into AZPY complexes. Develop methods for improving the solubility of complexes, explore their intracellular activation, and further understand the mechanisms in which ROS levels are elevated inside cells.

Firstly I explored Os(II) arene complexes with AZBTZ (phenylazobenzothiazole) bidentate liagnds. It was found that AZBTZ ligands can undergo unaided cyclo-metallation with Os(II) to form *N,C*-coordinated osmacycles as well as *N,N*-coordination. The amount of cyclo-metallation taking place seemed to be dependent on steric factors and occurred more for iodido complexes than chlorido and bromido analogues. The osmacycles were more stable than *N,N*-coordinated species and exhibited unique properties such as regio-specific deuteration of the aniline ring, but were too hydrophobic for biological evaluation.

A total of 31 new Os(II) arene AZPY complexes were synthesised using the previously determined structure-activity relationships as a basis. The majority contained alkoxy and glycolic side chain substituents on the AZPY ligand, which was achieved *via* a novel synthesis protocol. Their trends in anti-cancer activity, solubility, lipophilicity and cell uptake were explored. It was found that varying the anion was the best method for improving aqueous solubility without affecting activity, lipophilicity or uptake. Key complexes were found to be very active against OE19 oesophageal cancer cells, were capable of inducing apoptosis and elevating ROS levels in A2780 cells, as well as causing cell cycle arrest in different phases of the cell cycle.

Complexes $[Os(\eta^6\text{-}p\text{-cym})(5\text{-EtO-AZPY})I]^+$ and $[Os(\eta^6\text{-}p\text{-cym})(AZPY\text{-}NMe_2)I]^+$ were labelled with radioisotope ^{131}I (β^-/γ emitter, $t_{½}$ 8.02 d) in Kings College London. They were relatively stable in human blood serum and cell culture medium over 24 h. However, in the presence of MCF-7 cells, rapid dissociation of the iodide monodentate ligand was observed in the supernatants. Cell uptake studies revealed a spike in ^{131}I uptake after 5-10 min, which proceeds to steadily decline. The complexes seemed to undergo intracellular activation involving dissociation of the iodide ligand, and uptake of the complex is in competition with a rapid rate of iodide efflux, probably involving chloride transport channels.

The aqua species, $[Os(\eta^6\text{-}p\text{-cym})(5\text{-EtO-AZPY})H_2O]^{2+}$, was synthesised and its pK_a was determined as 4.55, meaning it exists predominantly as a +1 charged hydroxido species under physiological conditions. Using UV-Vis spectroscopy and EPR (DEPMPO spin trap), $[Os(\eta^6\text{-p-cym})(5\text{-EtO-AZPY})OH]^+$, and its chlorido and iodido analogues were found to catabolise H_2O_2, generating HO· radicals in the process that were capable of cleaving lysozyme protein with effectiveness in the order OH>Cl>I. Interestingly it was discovered that iodido complexes are activated by iodide ligand dissociation in the presence of low concentrations of GSH (75 μM) to form the more active hydroxido species. However, in higher concentrations (7.5 mM), they formed Os-SG and Os-SOG adducts. Likewise, $[Os(\eta^6\text{-p-cym})(5\text{-EtO-AZPY})OH]^+$ and its iodido analogue were both capable of oxidising NADH to NAD^+ with effectiveness in the order OH>I. NADH was also capable of activating iodido species in a similar manner and generating the hydroxido species was required for NADH oxidation to proceed.

Abbreviations

2-PhPy	2-Phenylpyridine
9-EtG	9-Ethyl guanine
ABPY	Azo*bis*pyridine ligand
acac	Acetylacetone
ATP	Adenosine triphosphate
atRA	All-*trans* retinoic acid
AZBTZ	Phenylazobenzothiazole ligand
AZPY	Phenylazopyridine ligand
AZPYZ	Phenylazopyrazole ligand
BCL-2	B-cell lymphoma 2 protein
BCL-X_L	B-cell lymphoma-extra large protein
bip	Biphenyl
CFTR	Cystic fibrosis transmembrane regulator
COSY	Correlation spectroscopy (2D NMR)
Cp	Cyclopentadienyl
Cp*	Pentamethylcyclopentadienyl
Cp^{xbip}	Biphenyltetramethylcyclopentadienyl
cpm	Counts per minute
CPP	Cell penetrating peptide
cps	Counts per second
CV	Cyclic voltammogram
DCM	Dichloromethane

DEPMPO	5-Diethoxyphosphoryl-5-methyl-1-pyrroline *N*-oxide
Dex	Dexamethasone
DFT	Density functional theory
DMEM	Dulbecco's modified eagle medium
DMF	Dimethylformamide
DMSO	Dimethylsulfoxide
DNA	Deoxyribonucleic acid
EDTA	Ethylenediaminetetraacetic acid
EGFR	Epidermal growth factor receptor
en	ethylenediamine
EPR	Electron paramagnetic resonance
ESI-MS	Electrospray ionisation mass spectrometry
Et_2O	Diethyl ether
EtOH	Ethanol
GC	Gas chromatography
GMP	Guanosine monophosphate
GPx	Glutathione peroxidases
GR	Glutathione reductase
GSH	Glutathione
GSK-3β	Glycogen synthase kinase 3
GSSG	Glutathione disulphide
H-bond	Hydrogen bond
hmb	Hexamethylbenzene
HPLC	High pressure liquid chromatography

IC_{50}	50% growth inhibitory concentration
ICP-MS	Inductively-coupled plasma mass spectrometry
ICP-OES	Inductively-coupled plasma optical emission spectroscopy
IMPY	Phenyliminopyridine ligand
IRR99	Ionising Radiation Regulations 1999
K	Capacity factor
KCL	Kings College London
L-BSO	*L*-buthionine sulfoximine
LC-MS	Liquid chromatography-mass spectrometry
MeCN	Acetonitrile
MeOH	Methanol
m/z	Mass to charge ratio
NAC	N-acetyl-*L*-cysteine
NAD^+	Nicotinamide adenine dinucleotide
NADH	Nicotinamide adenine dinucleotide reduced
$NADP^+$	Nicotinamide adenine dinucleotide phosphate
NADPH	Nicotinamide adenine dinucleotide phosphate reduced
NHC	N-Heterocyclic carbene
NIS	Na^+/I^- Symporter
NMR	Nuclear magnetic resonance
Nox	NADPH oxidases
OsAPTA	Osmium arene PTA complex
ORTEP	Oak Ridge Thermal Ellipsoid Plot Program
PBS	Phosphate buffer saline

p-cym	*Para*-cymene ligand
PI	Propidium iodide
$P_{o/w}$	Octanol-water partition coefficient
ppb	Parts per billion
ppm	Parts per million
PTA	1,3,5-triaza-7-phosphatricyclo-[3.3.1.1]decane
RAPTA	Ruthenium arene PTA complex
Ro5	Lipinski's 'rule of five'
ROS	Reactive oxygen species
rpm	rotations per minute
RPMI-1640	Rosswell Park memorial institute medium 1640
sel-NOE	Selective nuclear Overhauser effect
SARs	Structure-activity relationships
SF	Selectivity factor
SOD	Superoxide dismutase
SPECT	Single photon emission computed tomography
TEA	Triethylamine
TFA	Trifluoroacetic acid
THF	Tetrahydrofuran
TLC	Thin-layer chromatography
TMS	Tetramethylsilane
UV-Vis	Ultraviolet-visible light
v/v	volume to volume ratio
XANES	X-ray absorption near-edge spectroscopy

Chapter 1

Introduction

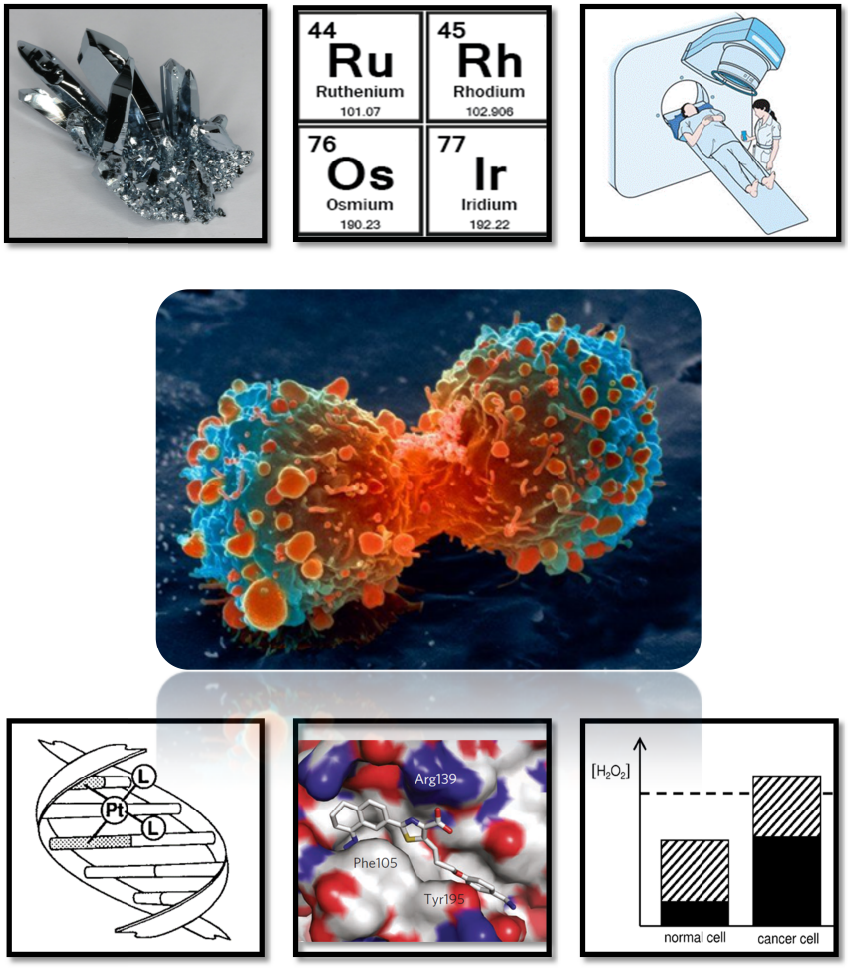

1.1. Cancer and cancer treatments

1.1.1. What is cancer?

Cancer is the collective term for a group of diseases characterised by unregulated cell growth and the spread of unhealthy cells from their site of origin. There are over 200 different types of cancer as there are over 200 cell types in the human body. Cancer occurs when the genes of normal cells become damaged or mutated, causing them to escape the many biological regulations that make them behave normally.[1] Typical abnormal behaviours of cancerous cells include the following characteristics: 1) cell proliferation in an uncontrolled manner, 2) an 'anchorage independence' of cells, enhancing their ability to spread to other parts of the body, and 3) immortality, whereby cancerous cells bypass apoptosis (the programmed cell death mechanism) which is otherwise normally triggered in unhealthy cells.[2] The progression of a cancer typically results in the formation of a malignant tumour (Figure 1.1).[3] These are physical obstructions in the human body that compromise the function of vital organs and compete fiercely with healthy tissues for nutrients and oxygen. If left untreated, the growth of a malignant tumour will spiral out of control, spreading to other parts of the body and eventually resulting in the death of the host. However, unlike many other diseases such as the human immunodeficiency virus (HIV), cancer does not behave with malicious intent; it is not a foreign invader infecting and destroying its host for self benefit. Cancer is a disease that arises from the tissue of its host. It gains no benefit from the host's demise and is not passed onto a new host for future survival.[1]

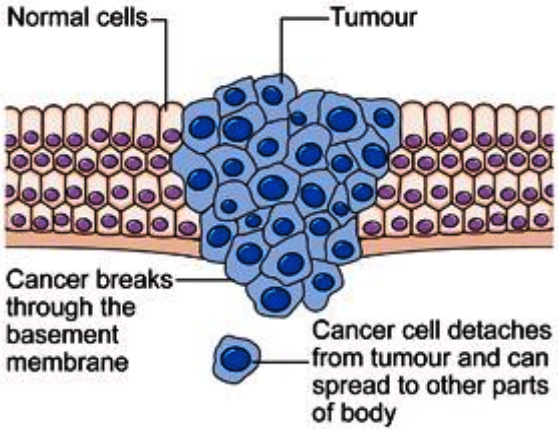

Figure 1.1. The anatomy of a tumour in normal tissue. Diagram taken from reference.[3]

Cancer is one of the most life threatening diseases of the modern era, second only to heart disease. According to Cancer Research UK in 2012 in the UK, 338,623 people were diagnosed with cancer and 161,823 people lost their lives to cancer.[3] A startling new projection according to Macmillan Cancer Support reveals that by 2020, almost half of Britons will be diagnosed with cancer at some stage in their life time.[4] Despite the increasing rates of incidence, the survival rates of cancer patients for 10 years or more is 50%, which has seen an increase over the past 40 years from 24%. This increased survival rate can be attributed to the introduction of improved treatments for cancer patients and early diagnosis.

1.1.2. Conventional treatments for cancer

1.1.2.1. Surgery

For several millennia surgery has long been a stable form of treatment for many cancers. Even as far back as 3000 – 1500 BC, an ancient Egyptian medical manuscript known as the Edwin Smith Papyrus recalls the use of early surgical techniques to remove 'growths' that today would likely be classified as breast cancers.[1] Surgery is still used today to remove malignant tumours, relieving the patient from the bulk of a cancer with immediate effect. There is no guarantee that surgery can remove every cancerous cell from the body, especially considering the nature of cancer is to spread. This is why in the modern era surgery is normally accompanied with radio therapy and/or chemotherapy.

1.1.2.2. Radiotherapy

Radiotherapy is a very powerful technique in cancer treatment. It utilises the energy of high powered ionising radiation to shrink or destroy tumours.[3] Paradoxically, sources of ionising radiation are known to cause cancer. However, the levels of radiation required to cause mutations that may lead to cancers are low in comparison to levels used in radiotherapy, where high levels of radiation are directed at a tumour in a uniform beam.[4] The idea being that the damage sustained by cancerous tissue is so extensive that it cannot survive, and any mutations caused are not passed into the next generation of cells. The downside of radiotherapy is that ionising radiation cannot distinguish between cancerous cells and normal cells. It will damage or destroy normal cells within its path.[1] Strategies must be employed to minimise the exposure of normal cells to such powerful radiation. One such method is to irradiate a tumour using a

rotating beam that consistently intersects the tumour from different angles, hence providing a much greater absorbed dose to the tumour than the surrounding normal tissues.

1.1.2.3. Chemotherapy

Of all the therapies used to treat cancer, chemotherapy has the greatest likelihood of reaching every cancerous cell inside the patient. A patient is injected with a chemical substance which accesses all areas of the body as it is absorbed and distributed.[1] DNA, proteins and cellular redox systems are the three main targets of anti-cancer therapeutics. Many cytotoxic agents work by attacking or inhibiting essential cell functions. This is usually achieved by damaging/binding to DNA, or by causing oxidative stress in cells.[5] Targeted therapies work by inhibiting specific proteins that are essential for the growth and proliferation of cancer cells. Unfortunately, as with radiotherapy, many anti-cancer drugs are non-selective and target normal cells as well as cancerous cells, leading to detrimental side effects. It is a great challenge for today's researchers to design novel and potent chemotherapies that favour the destruction of cancerous cells over normal cells.

1.2. Cellular targets in chemotherapy

1.2.1. DNA

Drugs that target DNA are considered to be the conventional approach for targeting cancer in chemotherapy. Such drugs work by forming strong interactions with DNA nucleobases, either by binding to the nitrogen donor groups (Figure 1.2), or *via* π-π stacking interactions which distort the DNA's geometry and structure.[6,7] Both examples will typically lead to S-phase cell cycle arrest and subsequent cellular processes that result in apoptosis. Metal-based DNA binders usually rely on the replacement of labile ligands (such as chloride) with water, which is crucial for their activity and toxicity. The obvious disadvantage of targeting DNA is that it is a non-selective approach, affecting the DNA of both normal and cancerous cells.[8] This type of treatment relies on the drug being absorbed more rapidly into cancer cells than normal cells based on their faster proliferation rates. G. Sava and P. J. Dyson have published a call to arms, to abandon the targeting of DNA with metallo-drugs in favour of more novel and selective approaches in what is now described as the 'genomic era', where present understanding of the various biochemical pathways responsible for the maintenance of tumours has vastly expanded.[9]

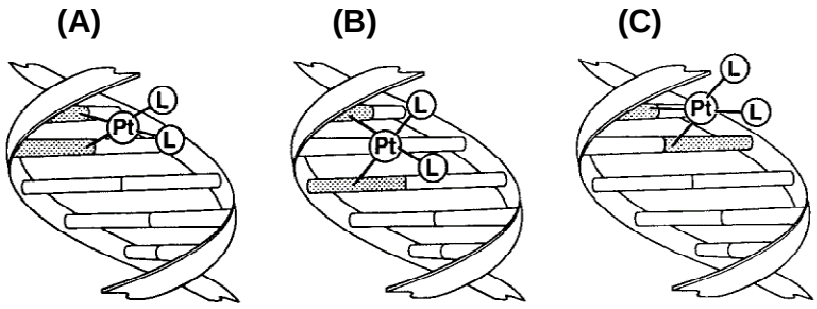

Figure 1.2. Schematic depiction of the bi-functional DNA binding modes of well known anti-cancer drug, *cis*-platin. (A) 1,2-Intrastrand cross-link. (B) 1,3-Intrastrand cross-link. (C) Interstrand cross-link. Picture taken from reference.[6]

1.2.2. Proteins involved in proliferation

Targeted therapy involves the targeting and inhibition of particular proteins that are associated with cancer cell proliferation. This is a much more selective approach for destroying cancer cells over normal cells. In particular, kinase inhibitors have become an important branch of therapeutics in recent years. Kinases are enzymes that are responsible for mediating the transfer of phosphate moieties from higher energy phosphate donating molecules (such as adenosine triphosphate, ATP) to specific substrate molecules. They are involved in the regulation of most cellular processes such as metabolism, proliferation, damage repair, and apoptosis.[10] Disturbances in the signalling pathways of these processes are common in cancer cells, and so efforts are made to intervene therapeutically with kinases. Erlotinib is an example of a tyrosine kinase inhibitor that acts on the epidermal growth factor receptor (EGFR), which is highly expressed and sometimes mutated in some forms of cancer (Figure 1.3, A). It is commercially available and commonly used in the treatment of pancreatic cancer and non-small cell lung cancer, working by reversibly binding to the ATP binding site of EGFR.[11]

Likewise, targeting pro-survival proteins is a novel and more recent approach towards targeting cancer cells. The ability to evade apoptosis is a key characteristic of cancerous cells and overcoming this barrier is a compelling therapeutic goal. The major gateway to apoptosis is guarded by the BCL-2 protein family, which regulate cell death and are often over-expressed in tumours, rendering cancerous cells resistant to some chemotherapies. Intervening therapeutically to inhibit BCL-2 proteins can allow the apoptotic

pathways in cancer cells to be restored. To date, only a few compounds that target BCL-2 proteins have reached clinical trials.[12] G. Lessene *et al* are currently developing a selective inhibitor of the BCL-X_L protein, WEHI-539, which contains a lipophilic benzothiazole moiety that is capable of docking into a key hydrophobic pocket of the protein, rendering it inactive (Figure 1.3, B).[13]

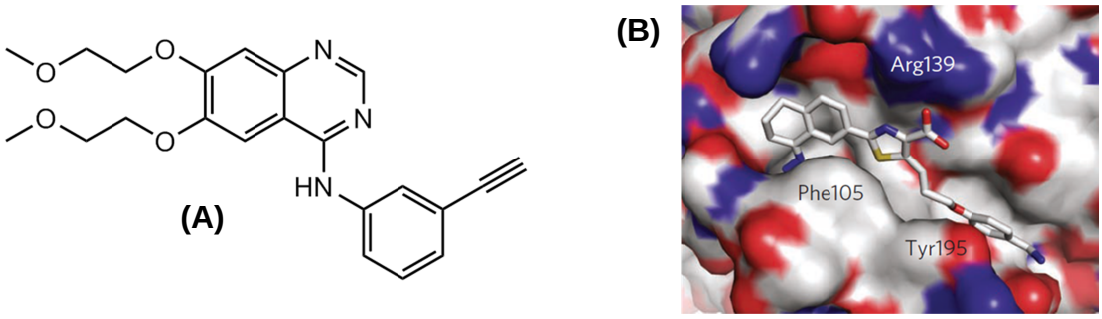

Figure 1.3. (A) Molecular structure of the EGFR inhibitor, Erlotinib. (B) X-ray crystal structure of WEHI-539 in complex with BCL-X_L (picture taken from reference[13]).

1.2.3. Cellular redox systems

All cells require strict regulation of their redox processes in order to maintain proper redox signalling.[14] The generation of reactive oxygen species (ROS) occurs mainly in the mitochondria, the most redox active intracellular component. ROS play an important role in the normal functioning of metabolism, signal transduction and other cellular functions, but the high reactivity of ROS makes their tight regulation necessary for cell survival.[15] In cancer cells, the redox balance is disturbed resulting in enhanced levels of ROS. The most common physiologically relevant ROS include; $O_2\cdot^-$, H_2O_2 and

$HO\cdot$.[15] In particular, it has been well established that production and secretion of H_2O_2 in an uncontrolled manner is a very characteristic biological feature of cancerous tumours. H_2O_2 acts as a 'fertiliser', driving processes such as DNA alterations, cell proliferation, apoptosis resistance and metastasis, hence advancing tumour development and providing the ideal micro-environment for tumours to thrive.[16] Interestingly, cancer cells adapt to increased levels of oxidative stress by up-regulating antioxidant systems. This counteracts the damaging effects caused by excessive ROS levels that lead to cell death.[17] It is therefore postulated that cancer cells are closer to a ROS threshold whereby cell death can occur.

A novel approach for anti-cancer therapeutics is to perturb redox processes in such a manner that leads to a significant elevation of ROS. This is known as ‘oxidative therapy’.[17] Since cancer cells operate in abnormally high levels of ROS, such an increase can push cancerous cells beyond the threshold where ROS-induced damages lead to cell cycle arrest and apoptosis (Figure 1.4).[18] The most important ROS-induced damages include: 1) DNA single strand breaks, 2) mitochondrial dysfunction caused by disruption of the mitochondrial inner membrane, 3) disturbed cell membranes caused by lipid peroxidation, and 4) oxidation of cysteine protein residues that result in changes to protein structures.[14,15] One way in which ROS increases are achieved is by targeting ROS detoxification systems such as glutathione (GSH), which is responsible for scavenging $O_2\cdot^-$ and $HO\cdot$.[19] The role of GSH is explained in greater depth in Chapter 6, Section **6.1**.[20] Another approach involves exploiting the over

production of H_2O_2 in cancer cells and utilising it as a pro-drug for conversion to HO·, a considerably more reactive ROS.[21]

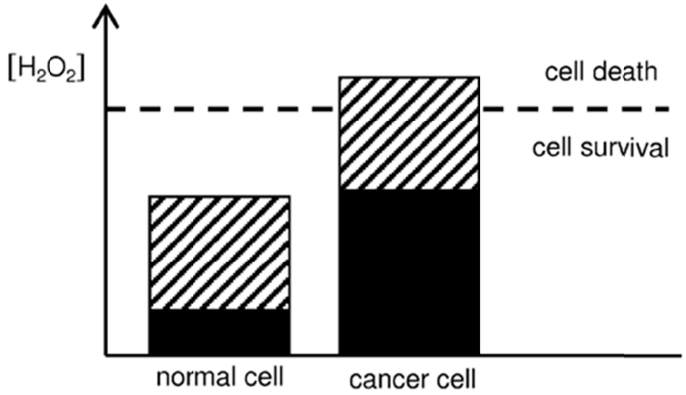

Figure 1.4. Selective killing of cancer cells by ROS. There is evidence that cancer cells have higher levels of ROS than normal cells (represented in black) and there is a threshold of ROS in which cells cannot survive. Increasing the levels of ROS (represented in striped area) can selectively produce cell death for cancer cells. Picture taken from reference.[18]

1.3. Metal-based anti-cancer therapeutics

In comparison to traditional organic-based pharmaceuticals, organometallic complexes can offer greater versatility in terms of electronic and structural features. This is owing to their capacity to achieve a variety of oxidation states, incorporate multiple types and numbers of ligands, and adopt different coordination geometries around their metal centres.[22] Organometallic complexes can offer a variety of novel chemistry, such as redox and catalytic reactions that are not widely accessible using purely organic molecules. These can be exploited for medicinal purposes. Furthermore, drug activity can be fine-tuned by making subtle changes to the electronic[23] and steric properties of the

bound ligands,[24] or varying the metal and its oxidation state. There now exists vast libraries of transition metal complexes exhibiting promising anti-cancer activity, incorporating metal centres of; titanium,[24,25] vanadium,[26] iron,[21,24,27] ruthenium,[24,27] rhodium,[28,29] silver,[30] tin,[24] osmium,[23,24,27] iridium,[27,31,32] platinum[27,33] and gold.[24,27,33,34] However, it was not until the discovery of *cis*-platin as an anti-tumour agent that this field of drug discovery was so widely explored.

1.3.1. The discovery of *cis*-platin

One of the greatest milestones in chemotherapy history was the discovery of the classical non-selective DNA binder, *cis*-platin. Its structure and synthesis has been known since 1893,[35] however, the discovery of its anti-tumour properties occurred much later when interest was sparked over an unusual observation. In 1965, during a panel of experiments to determine the effects of electric fields on *E. coli*, Rosenberg *et al* discovered that normal cell growth was inhibited and cells grew up to 300 times their normal length.[36] Further studies revealed the presence of Pt(II) and Pt(IV) ammine chloride complexes in the electrolyte, generated *in situ* by electrolysis. The generated Pt(II) complex, *cis*-platin, was found to be one of the species responsible for the filamentation of *E. coli* cells. Animal testing revealed *cis*-platin to be a very effective anti-tumour agent, and once the transition was made to human trials it proved effective against testicular, ovarian, lung, bladder, head, neck and cervical cancers.[3,6]

The mechanism of action of *cis*-platin involves hydrolysis of the Pt-Cl bonds followed by binding to nitrogen donors of DNA nucleobases. Such binding causes structural distortions in DNA that lead to S-phase cell cycle arrest.[6,37] This non-selective targeting of DNA in both normal and cancerous cells has been associated with many toxic side effects. In particular, irreversible kidney damage is a major concern and limits the dosage that can be administered.[3] Second generation platinum drugs, carboplatin and oxaliplatin, have since been produced and exhibit lesser side effects (Figure 1.5).[37] Interestingly, it has been discovered more recently that only a tiny fraction of *cis*-platin reaches nuclear DNA because of the ability of platinum(II) to bind more favourably to sulphur donors such as cysteines, than to the nitrogen donors in DNA. Glutathione (GSH, a tripeptide containing *L*-cysteine) binds irreversibly to *cis*-platin and is now known to be a cellular detoxifier of *cis*-platin and other platinum drugs.[38,39] The efficacy of *cis*-platin is limited by the occurrence of platinum drug resistance, caused by cells expressing elevated levels of GSH and up-regulation mechanisms of DNA repair. There is now greater demand to discover new anti-cancer therapeutics with alternative mechanisms of activity to overcome *cis*-platin resistance.

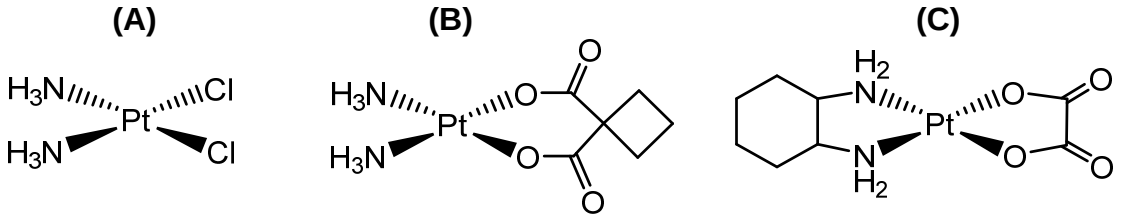

Figure 1.5. The structures of (A) *cis*-platin, and second generation platinum drugs; (B) carboplatin, and (C) oxaliplatin.

1.3.2. Titanocene dichloride and its derivatives

Along with *cis*-platin, titanocene dichloride (Figure 1.6) will be remembered in history as a major milestone in the discovery of metal-based anti-cancer complexes. In the 1970s, Köpf-Maier *et al* explored the anti-cancer activity of a series of metallocenes and reported on the anti-cancer activity of titanocene dichloride on various cancer cell lines in 1979.[24] It successfully progressed into phase II clinical trials for the treatment of renal and breast cancers. Similarly to *cis*-platin, titanocene dichloride undergoes hydrolysis in intracellular conditions, but DNA does not appear to be the target. Moreover, Ti(IV) binds strongly to human serum transferrin, which could be involved in the delivery of Ti(IV) into cancer cells.[24] This involves hydrolysis of the Ti-Cl bonds alongside cleavage of the Ti-Cp bonds, followed by binding of Ti(IV) to the specific iron sites of transferrin.

Unfortunately, attempts to formulate titanocene dichloride for clinical use were halted due to issues with instability, resulting from fast hydrolysis rates and low efficacy rates in Phase II trials.[6] However, a new generation of titanocene derivatives were later explored, which exhibit improved aqueous stability and anti-cancer activity comparable to that of *cis*-platin. Improvements to structures include: bridging of the Cp rings to prevent Ti-Cp bond cleavage (Tacke *et al*),[25] exchanging the chloride ligands with a more suitable oxalate ligand (Tacke *et al*),[24] and ionic titanocene complexes synthesised by McGowan *et al*, which improved aqueous solubility and activity[40] (Figure 1.6).

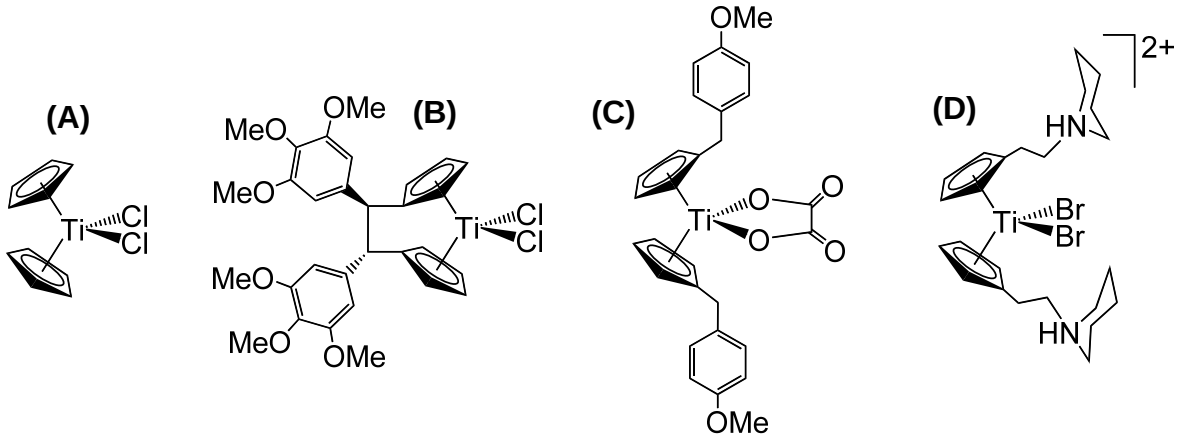

Figure 1.6. Molecular structures of (A) titanocene dichloride, (B) an *ansa*-titanocene bridged derivative, (C) an oxalate derivative, and (D) an ionic titanocene derivative.

1.3.3. Ruthenium anti-cancer complexes

1.3.3.1. Ru(III) complexes

Anti-cancer ruthenium complexes have been explored for many years, as far back as 1977 when Clarke *et al* reported pentaamino-ruthenium(III) purine complexes that were capable of inhibiting DNA and protein synthesis in human nasopharyngeal carcinoma cells *in vitro*.[41] This discovery initiated a strong interest and ruthenium anti-cancer complexes have been studied extensively by various research groups ever since. The success of ruthenium has led to two octahedral Ru(III) based anti-cancer drugs reaching clinical trials; NAMI-A (Sava *et al*),[42] and KP1019 (Keppler *et al*),[43] see Figure 1.7.

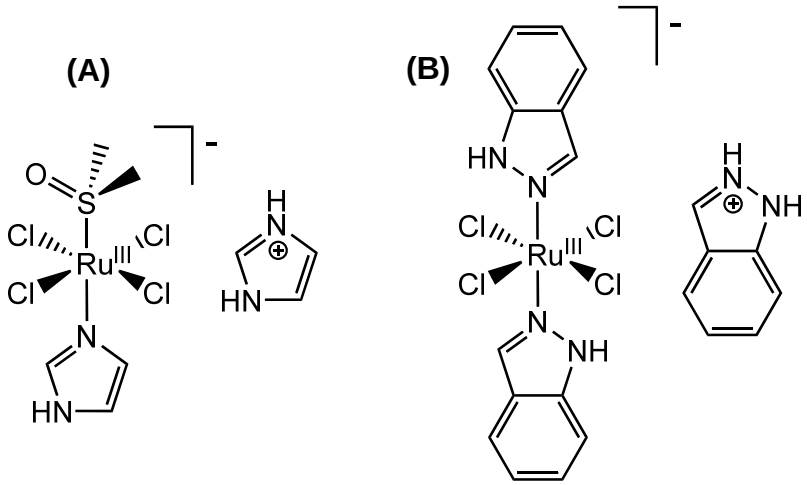

Figure 1.7. The molecular structures of (A) NAMI-A, and (B) KP1019.

1.3.3.2. Ru(II) η^6-arene complexes

As Ru(II) is believed to be the oxidation state responsible for anti-cancer activity in ruthenium complexes, there has been much interest in exploring Ru(II) complexes (and Os(II) complexes shown in Section **1.3.4**).[24] Consequently, piano-stool arene complexes of Ru(II) have attracted much interest for their promising activity, which is comparible to that of *cis*-platin and carboplatin. Figure 1.8 shows the general structure of ruthenium(II) piano-stool complexes with η^6-arene ligands, where X is a monodentate ligand and Y-Z is a bidentate ligand. These have been explored in much depth by the Sadler group.[24] Owing to the high crystal field splitting energy prevalent in heavier transition metals, these *pseudo*-octahedral d^6 complexes are low-spin and diamagnetic.

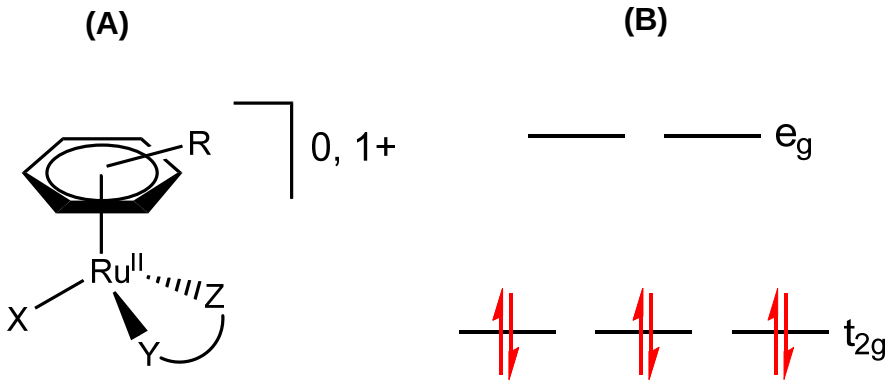

Figure 1.8. (A) The general structure of *pseudo*-octahedral 3-legged piano-stool complexes synthesised by the Sadler group, where R refers to alkyl/aryl substituents on the arene, X is a monodentate ligand (typically a halide), and Y-Z is a bidentate ligand. (B) The diamagnetic d^6 electron configuration of the ruthenium *pseudo*-octahedral low-spin state.

The η^6-arene plays an important role in stabilisation of the Ru(II) state by preventing oxidation to Ru(III) from readily occurring, and their lies a delicate balance between electron donation from the arene into the empty e_g orbitals, and back donation from the filled t_{2g} into the arene π* anti-bonding orbitals.[24] Arene ligands such as *p*-cymene (*p*-cym) and hexamethylbenzene (hmb) are known to be stronger electron donors, owing to the presence of electron donating alkyl substituents. In contrast, biphenyl (bip) may act as an electron acceptor. Numerous *N,N*-, and *O,O*-coordinating bidentate ligands have been explored for these systems, which play a role in stabilising the Ru(II) metal centre with the added advantage of being able to tailor the electronic properties of the metal centre through the choice of substituents.[44] The choice of chelating ligand dictates how labile the monodentate ligand will be and ultimately the mechanism of anti-cancer activity of the complex.[24] The monodentate ligand (X)

is important in defining the reactivity of the complex. Complexes with monodentate ligands that are too labile tend to show little or low no anti-cancer activity, likely because the complex becomes inactivated before reaching target sites.

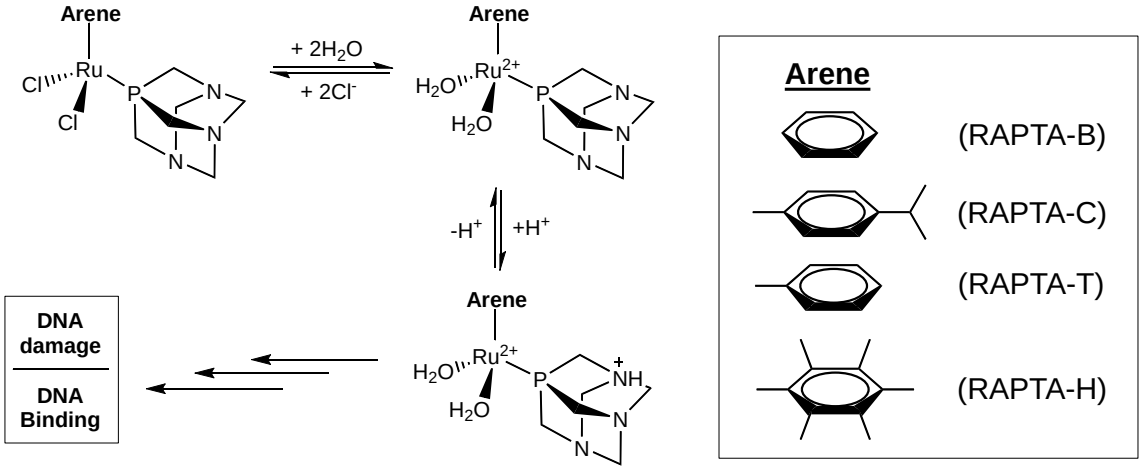

Scheme 1.1. RAPTA complexes of the Dyson group and their proposed activation method involving hydrolysis then protonation of the PTA ligand.

Ruthenium(II) piano-stool complexes have also attracted interest in other groups such as Dyson's. Dyson *et al* have synthesised Ru(II) η^6-arene complexes with 3 monodentate ligands making up the three legs of the piano-stool, known as RAPTA complexes.[45] The three legs consist of two labile chloride ligands and a novel 1,3,5-triaza-7-phosphatricyclo-[3.3.1.1]decane (PTA) ligand, which has been attributed to providing good aqueous solubility. RAPTA complexes have indicated high selectivity towards cancerous cells over normal cells, however, their cytotoxicity towards cancer cells *in vitro* is relatively

low. Such complexes are known to undergo pH dependent binding to DNA nucleobases in their hydrolysed (active) form (Scheme 1.1).[46]

1.3.3.2.1. Sadler group complexes with σ-donor bidentate ligands

Early ruthenium piano-stool complexes of the Sadler group contain chloride monodentate ligands and simple chelating σ-donor ligands, such as *N,N*-chelating ethylenediamine (en),[47,48] and *O,O*-chelating acetylacetone (acac),[49] see Figure 1.9. These complexes have labile chloride ligands and are believed to bind to DNA inside cells, involving a mechanism of action similar to *cis*-platin. Outside the cell where chloride concentrations are high (c.a. ~103 mM), hydrolysis of the Ru-Cl bond is suppressed. However, once inside the cell where chloride concentrations are much lower (c.a. ~23 mM and ~4 mM for intracellular and intranuclear conditions, respectively) the Ru-Cl bond hydrolyses readily to form an aqua species (see Scheme 1.2).[24] Owing to the strong σ-donor nature of these bidentate ligands, electron density is pushed onto the Ru(II) centre rendering it more electronegative in character. As a consequence, their corresponding aqua species are basic and high pK_a* values were observed for their monodentate H_2O ligands (pK_a* 7.7-9.4, pK_a* refers to the pK_a measurement of a complex in D_2O solution using a pH-meter calibrated with H_2O standard solutions).[24] Under physiological conditions, the aqua species exist predominantly with the labile Ru-OH_2 bond as opposed to the more stable Ru-OH bond, thus enabling easier binding to DNA nucleobases.[24] The complex $[Ru(\eta^6\text{-}p\text{-cym})(en)Cl]^+$ was shown experimentally to bind

selectively to guanine bases on DNA oligonucleotides in aqueous solution (see Scheme 1.2).[50] It is proposed that when the aqua species enters the cellular nuclei it can bind to DNA and inhibit DNA synthesis.

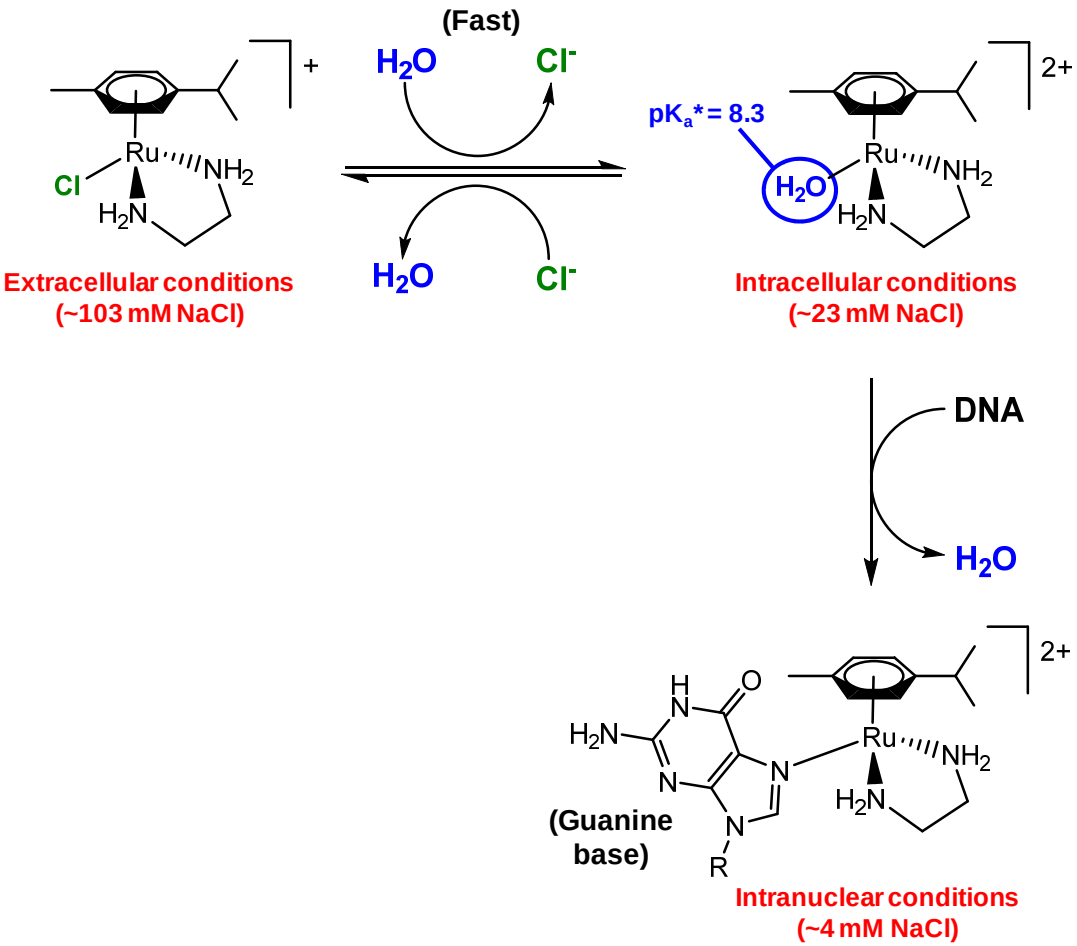

Scheme 1.2. Proposed mechanism of DNA binding for [Ru(η^6-*p*-cym)(en)Cl]$^+$. The complex is stable in extracellular conditions where chloride concentrations are high. Fast hydrolysis occurs in intracellular conditions where chloride concentrations are considerably lower. In intranuclear conditions, binding to the guanine bases in DNA occurs.

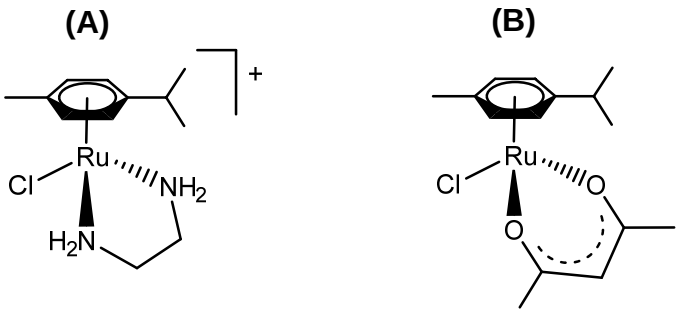

Figure 1.9. Ru(II) arene complexes with monodentate chloride ligands and bidentate σ-donor ligands. (A) with an ethylenediamine (en) ligand, and (B) with an acetylacetonate (acac) ligand.

Ru(II) arene complexes with σ-donor (acac and en) are also capable of targeting the NADH/NAD^+ redox system in the presence of formate[51] (the NADH/NAD^+ system is explained in greater depth in Chapter 6, Section **6.1**). After hydrolysis, the complexes can transfer hydride from formate to NAD^+. Such synergistic effects can induce reductive stress on cancer cells. Later Ru(II) arene complexes capable of NAD^+ reduction contain bidentate sulfonamido-ethylenediamine ligands,[52] and were found to be considerably more active (Figure 1.10). The anti-cancer activity of such complexes is enhanced by up to 50x in the presence of low non-toxic doses of formate, and the extent of NAD^+ oxidation is dependent on formate concentration. This novel reductive stress mechanism of cell death does not involve apoptosis and may prove to be effective in overcoming *cis*-platin resistance.[53]

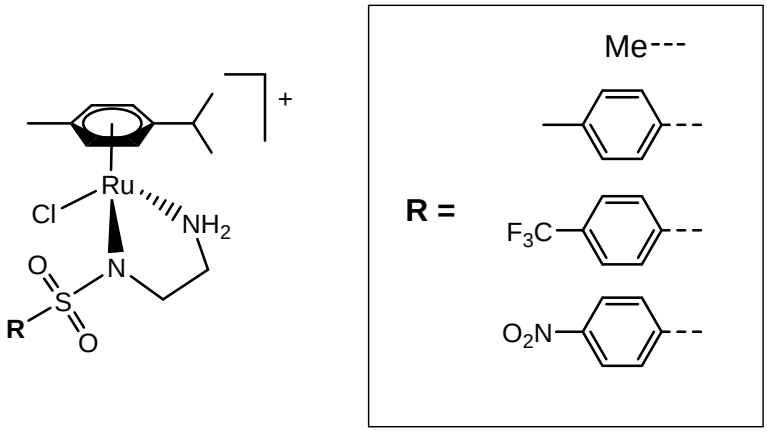

Figure 1.10. Ru(II) arene complexes containing sulfonamido-ethylenediamine bidentate ligands that are capable of reducing NAD^+ to NADH in the presence of low doses of formate.

1.3.3.2.2. Sadler group complexes with π-acceptor AZPY ligands

Phenylazopyridine (AZPY) ligands consist of a pyridyl moiety and a phenyl moiety linked together by an azo-bond (see Figure 1.11). The pyridine ring is an intermediate π-acceptor and its nitrogen is a weak σ-donor. The nitrogens of the azo-bond are also weak σ-donors but are capable of strong π-acceptor ability due to the presence of the azo π* orbital.[54]

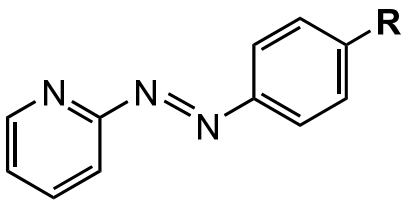

R = H, OH or NMe_2

Figure 1.11. Phenylazopyridine (AZPY) ligands with a pyridyl and phenyl moiety linked together by an azo-bond. Electron-donating groups can be incorporated onto the phenyl ring *para* to the azo-bond.

In contrast to the ruthenium complexes described previously with strong σ-donor ligands, Ru(II) arene complexes with halide monodentate ligands and bidentate AZPY ligands exhibit entirely different properties. Owing to the strong π-acceptor capability of AZPY ligands, they withdraw electron density away from the Ru(II) metal centre which in turn renders their corresponding aqua species more acidic. The aqua species, $[Ru(\eta^6\text{-p-cym})(AZPY\text{-}NMe_2)H_2O]^{2+}$, has a pK_a* of 4.6 and predominantly exists in water with the more stable Ru-OH bond.[54] As a consequence, such species do not bind as readily and as extensively to DNA nucleobases as their σ-donor bidentate ligand bearing counterparts. Interestingly, the anti-cancer activity of these species is not dependent on the lability of the monodentate ligand and their readiness to hydrolyse in intracellular conditions. In fact, complexes containing iodido monodentate ligands are more active than their chlorido analogues despite being more stable towards hydrolysis, suggesting that entirely different mechanisms of activity are involved.

Ru(II) complexes of the type $[Ru(\eta^6\text{-arene})(AZPY\text{-}R)I]PF_6$ (where arene = *p*-cym or bip, and R = OH or NMe_2) were found to increase ROS levels in cancer cells and hence cause cell death *via* oxidative stress. On the basis that GSH is the primary cellular antioxidant defence, they raise ROS by catalytically oxidising GSH to glutathione disulfide (GSSG).[19] The mechanism of GSH oxidation is speculated to be mediated through the azo-bond of the AZPY ligand in a catalytic cycle, whereby the azo-bond is reduced by GSH (forming a hydrazo intermediate), followed by the formation of GSSG and regeneration of the azo-bond (see Scheme 1.3). Ru(II) arene AZPY complexes and free AZPY ligands

have two reduction potentials corresponding to the addition of two electrons into the azo-bond's π*-orbital, when analysed by cyclic voltammetry. Interestingly, coordination of an AZPY ligand to an electropositive Ru(II) arene centre shifts the first reduction potential within the biologically relevant range (-0.50 to +0.40 V),[55] which may account for ligand based reductions caused by GSH under physiological conditions.[19]

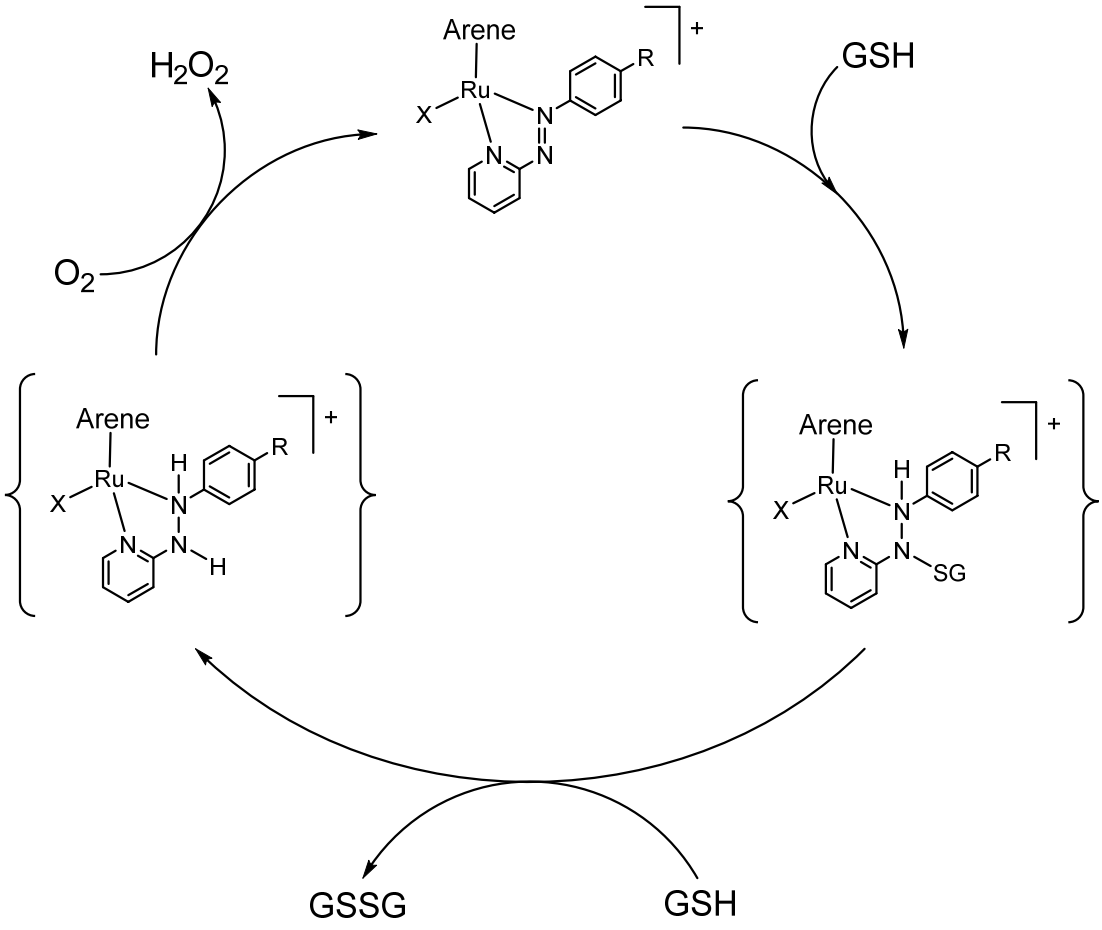

Scheme 1.3. Proposed catalytic cycle for the oxidation of GSH to GSSG by Ru(II) arene AZPY complexes, where arene = *p*-cym or bip and R = OH or NMe_2. Initially X is iodide, which is displaced by GS^- in the early stages of reaction. Released iodide can catalyse the decomposition of H_2O_2.[19]

1.3.4. Osmium anti-cancer complexes

1.3.4.1. Introduction to osmium

Osmium has an atomic number of 76 and belongs to a group of six elements on the periodic table that make up the 'platinum group' elements (ruthenium, rhodium, palladium, osmium, iridium and platinum), defined by having similar physical and chemical properties and tending to occur together in the same mineral deposits (Figure 1.12). Osmium is the rarest stable element in the periodic table with an average abundance in the Earth's crust of around 1 g per 200 tonnes,[56] and is commonly found in nature as an alloy with iridium, known as 'osmiridium'. Neighbouring metals, osmium and iridium, have long been known as the densest of all metals, both being over twice as dense as lead. It was not until 1995 that a more accurate study confirmed osmium's density is just slightly greater with a value of 22.587 g/cm^3 at 20°C.[57] Despite its rarity the blue-grey hard and brittle metal is less valuable than gold and platinum, lacking the desired visual and physical properties for commercial applications. Furthermore, osmium has a total of seven stable naturally occurring isotopes: ^{184}Os, ^{186}Os, ^{187}Os, ^{188}Os, ^{189}Os, ^{190}Os, ^{192}Os, one of which (^{186}Os) is a radioisotope with an extremely long half-life of 2.011 x 10^{15} years and α-decay mode, which for practical purposes is considered as stable.[58] Figure 1.13 shows each naturally occurring isotope and its % abundance.

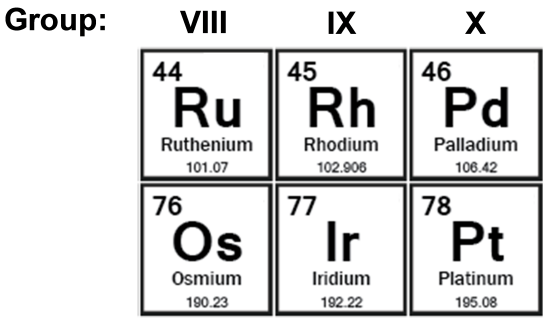

Figure 1.12. The platinum group elements, consisting of groups 8-10 of the 2nd and 3rd row transition metals in the periodic table.

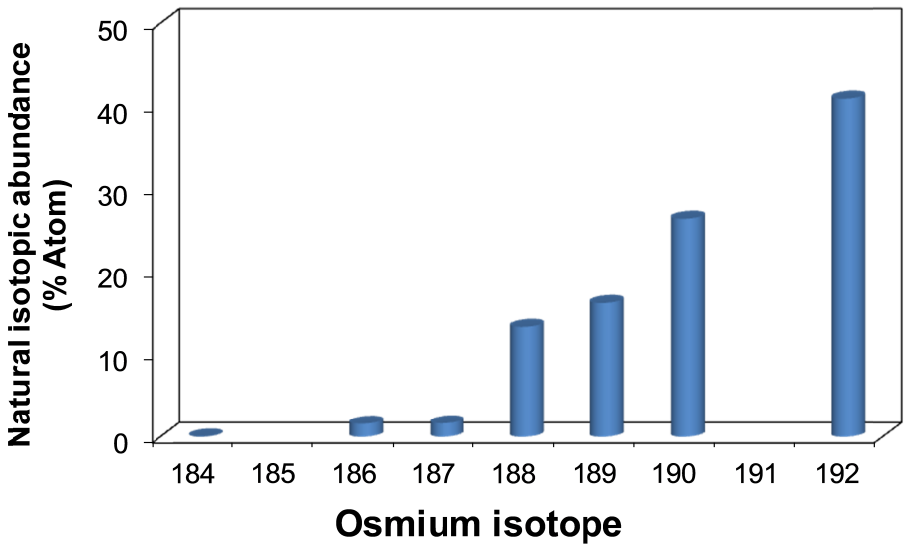

Figure 1.13. Seven naturally occurring isotopes of osmium and their isotopic abundances.

Although lacking the desired properties for commercial uses in metallic form, its chemical behaviour is rather interesting. The element was first discovered in 1802 by Smithson Tennant when preparing the volatile osmium tetroxide by acid distillation of the black residues remaining from digestion of native platinum

in aqua regia.[59] Osmium is highly versatile and capable of adopting up to 11 different oxidation states (ranging from -2 to +8) in its various compound forms. An oxidation state of +8 is the highest possible state reached by any element under normal circumstances, a feat shared only with iron, ruthenium and xenon.[56]

Osmium tetroxide (oxidation state +8) has been the most useful of all osmium compounds. It is used as a stain in microscopy and in fingerprint detection, as well as a catalyst for a few industrial processes such as the production of some anti-obesity and anti-diabetic drugs.[60] The clinical applications of osmium compounds are currently limited, however osmium tetroxide has been used clinically for the treatment of arthritis. For 56 years it has been injected into arthritic knee joints on a limited basis to chemically destroy diseased tissue in a process known as 'chemical synovectomy'.[61] Due to the highly toxic nature of osmium tetroxide this procedure has been considered very controversial. A class of osmium carbohydrate polymers known as 'osmarins' have been proposed to replace osmium tetroxide as an anti-arthritic drug due to their significantly lower toxicity. Osmarins are prepared from osmium tetroxide with the final product containing between 30-40% of osmium(IV) in a water soluble gel consisting of glucose and gluconate.[61]

1.3.4.2. The extension from ruthenium to osmium

As they belong to the same periodic group, it was not long before various research groups began making the extension from ruthenium to osmium in anti-

cancer complexes. Having an electronic configuration of [Xe]$4f^{14}5d^{6}6s^{2}$, osmium is subject to the 'lanthanoid contraction' (affecting 3rd row transition metals), where the outer most electrons are inadequately shielded from the nuclear charge by f-orbitals, giving rise to a smaller atomic radius than expected.[62] Its atomic radius is comparable to that of ruthenium (Figure 1.14).[63] The consequence being that complexes of osmium are almost structurally identical to their ruthenium analogues, giving them similar biological activities. Various research groups began synthesising osmium analogues of their previously active ruthenium complexes and osmium has since become increasingly successful with rapidly growing interest.

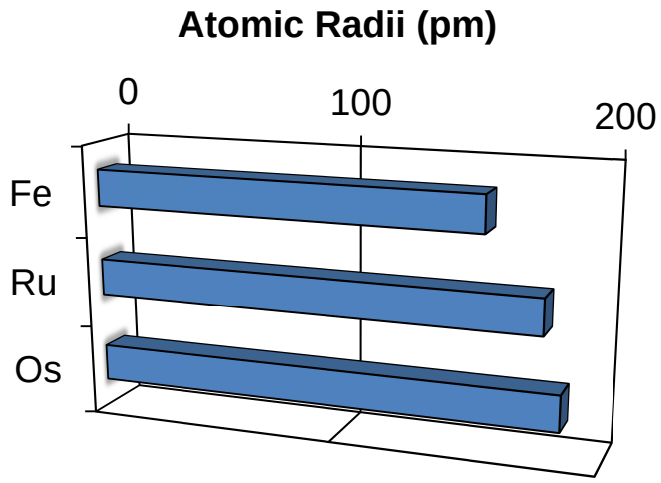

Figure 1.14. Comparison of the atomic radii of group 8 metals.

1.3.4.3. Sadler group osmium anti-cancer complexes

Osmium analogues of Ru(II) arene complexes containing simple σ-donor ligands have been explored and notable differences in their chemical properties

and reactivities were observed.[24] Os(II) is inherently more electropositive than Ru(II) and their complexes tend to exhibit lower pK_a values for coordinated H_2O molecules in their aqua-adducts. The rate of hydrolysis for $[Os(\eta^6\text{-bip})(en)Cl]^+$ is 100x slower than its Ru(II) counterpart and unlike Ru(II), its aqua-species exists predominantly in the more stable Os-OH form under physiological conditions.[64] Initially, $[Os(\eta^6\text{-bip})(en)Cl]^+$ was found to be inactive against A2780 cells which was attributed to its kinetic inertness and lower reactivity towards guanine nucleobases in solution. However, a later study confirmed that its activity was comparable to that of the Ru(II) analogue and the previous erroneous finding was due to partial decomposition of the complex in stock solutions containing DMSO.[65]

In contrast, chlorido Os(II) arene complexes of acac hydrolyse very rapidly. They lack cytotoxicity towards cancer cells due to a lack of stability and a tendency to form an un-reactive hydroxide-bridged dimer in solution.[64,66] *N,O*-coordinating picolinate ligands provide a good compromise for Os(II), between the inert complexes of *N,N*-coordinating en ligands and the over-reactive complexes of *O,O*-coordinating acac ligands.[67,68] Chlorido Os(II) arene picolinate complexes hydrolyse readily, but do not form unreactive hydroxido dimers and are active towards A2780 cancer cells (Figure 1.15).

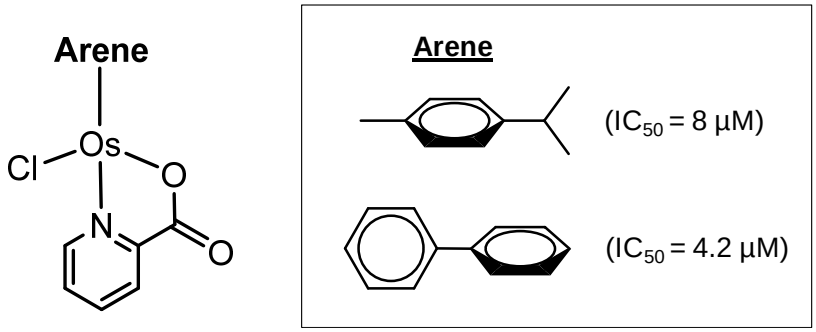

Figure 1.15. Chlorido osmium(II) arene complexes with picolinate ligands and their IC_{50} values for the A2780 cancer cell line.

1.3.4.3.1. Os(II) complexes with peptide side chains

One of the many problems to overcome in anti-cancer complex design is the efficient passage of drugs into cells. Many complexes fail due to insufficient cellular uptake. One interesting and novel method to improve the biological properties of a metallo-drug and help alleviate this problem is the attachment of cell penetrating peptides (CPPs) to complexes. A CPP is a short peptide chain which, when chemically linked, facilitates the cellular uptake of molecular 'cargo' into the cell. This idea was explored by Van Rijt *et al* in the Sadler group for Os(II) bip picolinate complexes.[69] Peptide conjugates of the osmium complex were synthesised with different arginine chain lengths. The picolinate ligand has a carboxylic acid group at the 4-position on the ring that provides a binding site for which peptides can be attached (Figure 1.16). It was found that the conjugation of five arginine monomers doubled cellular uptake of the complex into A2780 human ovarian cancer cells, and a 10-fold increase in cellular uptake was observed when complexes were conjugated to eight arginine

monomers. The 10-fold increase was also accompanied with a 15-fold increase in the binding of osmium to DNA.

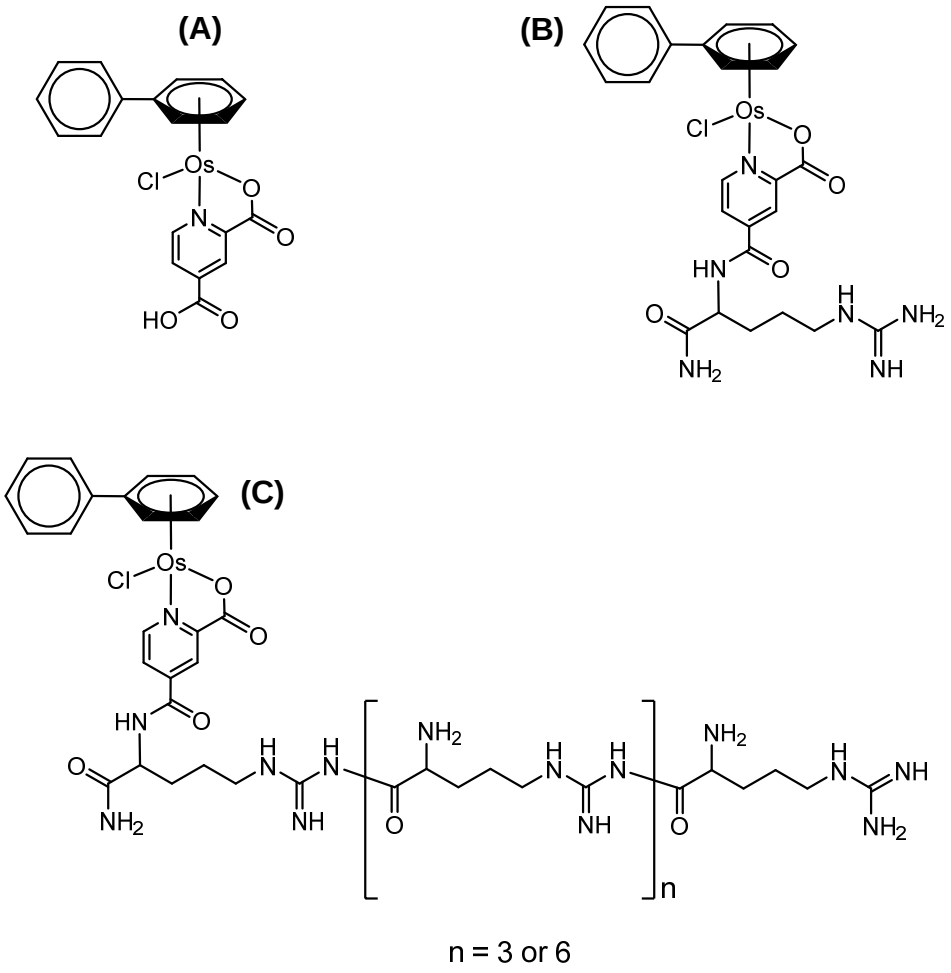

Figure 1.16. Structures of chlorido Os(II) bip picolinate complexes; (A) with a carboxylic acid side chain which provides a platform for the attachment of peptides, (B) with an attached arginine molecule, and (C) with an attached arginine peptide conjugate of varying chain length.

1.3.4.3.2. Os(II) complexes with AZPY ligands

A large and diverse range of 40 Os(II) arene AZPY complexes was synthesised by Ying *et al* in the Sadler group with a variety of different electron

withdrawing/donating substituents on the AZPY ligand (see Figure 1.17), providing further opportunity to tailor the electronic properties of the complex.[5,23,70] All of the complexes were tested against A2780 cancer cells for anti-cancer activity and only three were found to be inactive (>100 μM IC_{50} values), and eight had IC_{50} values in the nano-molar range. Some of the most active complexes were also active in other human cancer cell lines: A549 lung cancer cells, HCT-116 colon cancer cells, PC-3 prostate cancer cells, MCF-7 breast cancer cells, and *cis*-platin resistant A2780cis ovarian cancer cells. In general, a considerable increase in activity was observed on switching from ruthenium to osmium for these species.

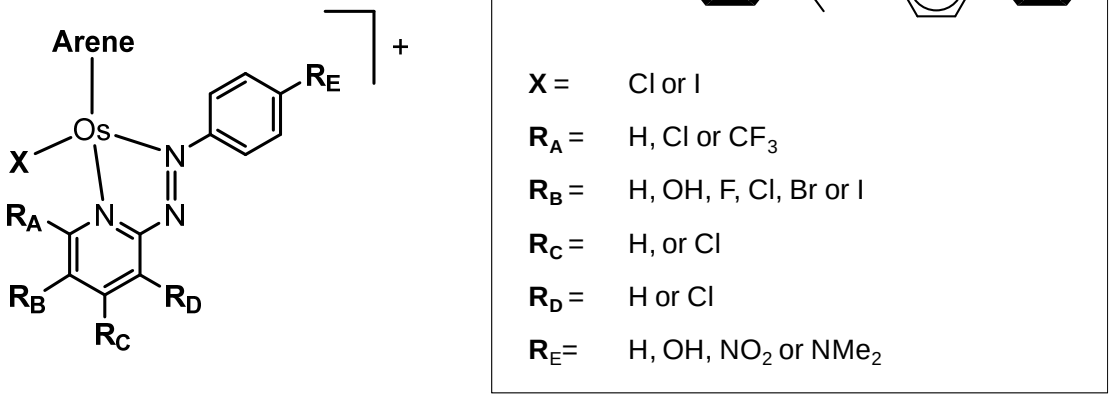

Figure 1.17. General structure of Os(II) arene AZPY complexes, where arene = *p*-cym or bip, X is a monodentate halide ligand (Cl or I), and R_A-R_B are either electron donating/withdrawing groups or H on the AZPY ligand.

Structure-activity relationships (SARs) were determined for these complexes and the following trends were found (Figure 1.18). (1) Iodido complexes have much higher activity than chlorido complexes. This is owing to the strong covalent nature of the Os-I bond, which in turn allows for strong back-donation of electron density from the metal centre to the phenylazopyridine ligand. (2) In general bip complexes are 10-times more active than *p*-cym complexes. Bip is more lipophilic than *p*-cym and the observed increase in activity is due to better cellular accumulation of bip complexes.[71] (3) When an electron donating group is introduced to the phenyl ring *para* to the azo-bond, a substantial increase in activity is observed compared to when no substituent is introduced. This is likely due to improved stability of the complex.[70] (4) When a chloro-substituent is introduced to the pyridyl ring, the activity depends on its position (R_B>R_A>R_C). Addition at the position *para* to the azo-bond gives the greatest activity. (5) Changing the halo-substituent at the *para*-position (R_B) on the pyridyl ring increases the activity of the complex in the following order; Cl<Br≤F<I. Furthermore, complexes which have an electron donating OH group at R_B and an electron withdrawing NO_2 group at R_E (both *para* to the azo-bond) have very potent activity.[23]

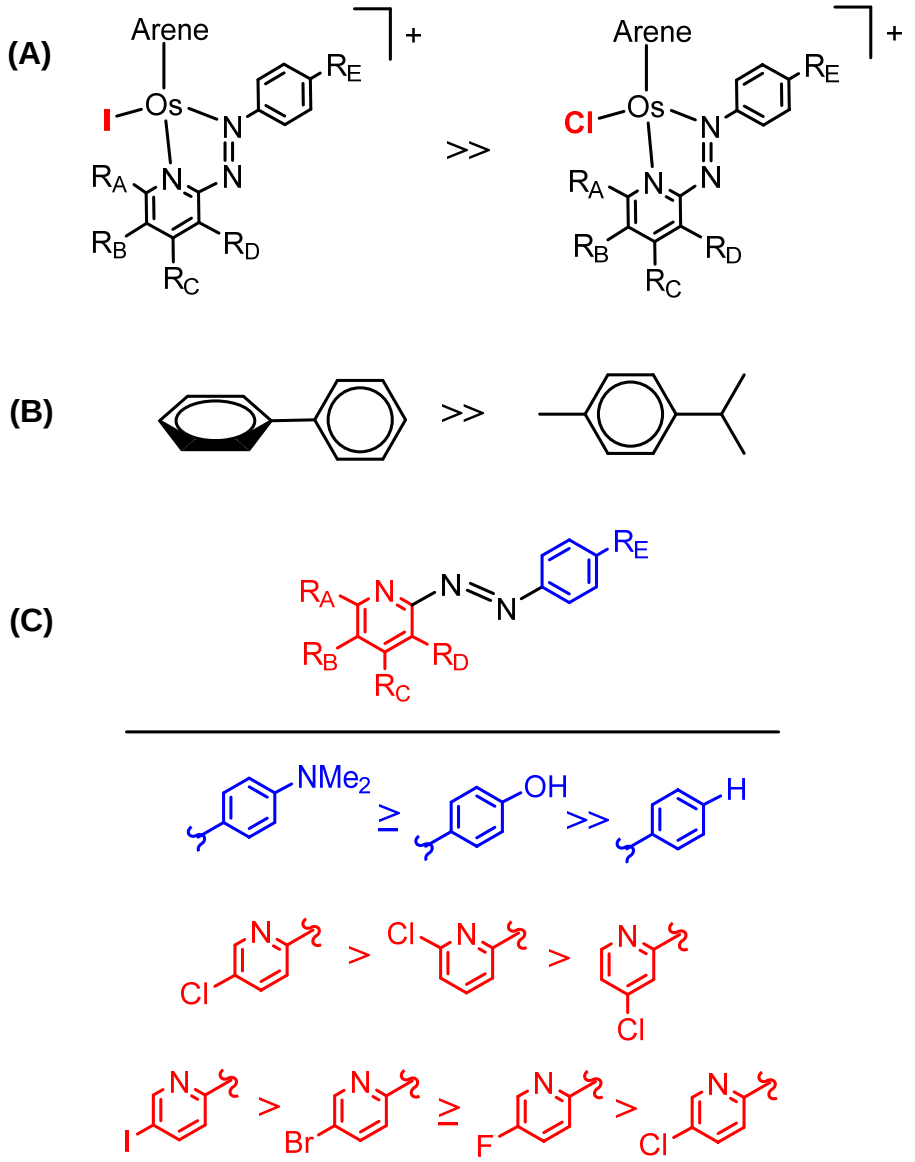

Figure 1.18. Structure-activity relationships of Os(II) arene AZPY complexes against A2780 cancer cells. (A) Effect of the monodentate ligand. (B) Effect of the arene ligand. (C) Effects of electron withdrawing/donating substituents on the AZPY ligands.

In comparison to their ruthenium analogues, Os(II) arene AZPY complexes are very stable towards hydrolysis and hence not capable of binding to DNA nucleobases such as guanine. Even the chlorido species, $[Os(\eta^6\text{-}p\text{-cym})(AZPY\text{-}NMe_2)Cl]^+$, is stable and attempts to remove the chloride ligand using $AgNO_3$

proved unsuccessful.[70] These findings led to the conclusion that, like their Ru(II) analogues, hydrolysis is not critical for activation and the AZPY ligand may play a role in anti-cancer activity. However it still remains unknown as to whether the monodentate ligand stays bound to Os(II) inside cells. Similarly to their ruthenium analogues, Os(II) arene AZPY complexes are also capable of raising ROS levels in cancer cells which is believed to be the primary mechanism of activity.[23] In stark contrast to its ruthenium analogue, $[Os(\eta^6\text{-p-cym})(AZPY\text{-}NMe_2)I]^+$ (**FY026**) does not raise ROS levels by catalytically oxidising GSH to GSSG and therefore must operate by other means.[70] The mechanism by which Os(II) arene AZPY complexes raise ROS levels is still an area that requires further investigation.

Interestingly, the active complex $[Os(\eta^6\text{-bip})(5\text{-F-AZPY})I]^+$ which contains an electron withdrawing fluoro-substituent on the pyridyl ring (*para* to the azo-bond), was found to cause S-phase and G2/M-phase cell cycle arrest. Further studies showed that it is capable of inhibiting tubulin polymerisation process by up to 21%.[5] The polymerisation of microtubules is vital for the cells' ability to form mitotic spindles appropriately in order for normal cell division to occur.[72] This is a novel mechanism of activity for which there are currently no reports for organometallic complexes, and highlights the ability of Os(II) arene AZPY complexes to exert multiple mechanisms of anti-cancer activity inside cancer cells.

1.3.4.3.3. FY026

Complex **FY026** (see Figure 1.19) is one of the most promising osmium anti-cancer drugs in the Sadler group and a potential candidate for clinical trials. It contains a *p*-cym arene ligand, a monodentate iodide ligand, and an AZPY ligand with an electron donating NMe_2 group on its phenyl ring.[70] The +1 charge on the cation is balanced with a PF_6^- anion, which plays no role in the anti-cancer activity of the overall complex.

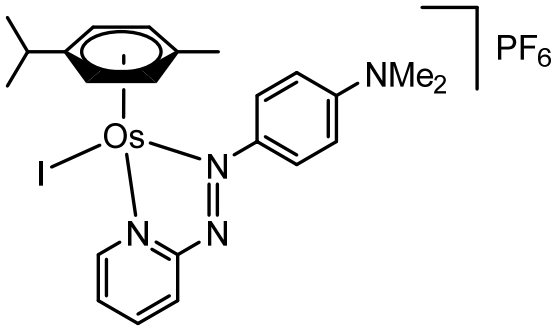

Figure 1.19. The molecular structure of potent osmium anti-cancer complex **FY026**, [Os(η^6-*p*-cym)(AZPY-NMe_2)I]PF_6.

FY026 has potent nano-molar activity against a variety of human cancer cell lines; A2780 (IC_{50} = 0.18 ±0.01 μM), A2780cis (IC_{50} = 0.23 ±0.05 μM), A549 (IC_{50} = 0.38 ±0.07 μM), HCT-116 (IC_{50} = 0.22 ±0.02 μM), MCF-7 (IC_{50} = 0.20 ±0.01 μM), PC-3 (IC_{50} = 0.62 ±0.12 μM) and RT-112 (IC_{50} = 0.25 ±0.02 μM).[70] Furthermore, it is 49x more potent than *cis*-platin in the 809-cell line screen of the Sanger Institute (Mean GI_{50} of **FY026** is 0.75 μM vs. 36.7 μM for that of *cis*-platin).[73] Preclinical development has shown that FY026 is capable of delaying the growth of HCT-116 human colon cancer xenographs in mice.[74] Furthermore, in the same xenograph model and at concentrations 6x higher than that of the

maximum tolerable dose of *cis*-platin (40 mg/Kg), **FY026** caused negligible deleterious effects to mice, suggesting a comparative lack of toxicity to the host.[70]

The selectivity of **FY026** also makes it a desirable drug candidate as studies have shown it to be 28.4x more selective towards A2780 cells than MCR-5 normal lung fibroblast cells. Interestingly, its selectivity factor was further improved to 63.5 when cells were treated synergistically with non-toxic levels of *L*-buthionine-sulfoximine (*L*-BSO, 5 μM).[75] *L*-BSO reduces GSH levels, hence undermining cellular detoxification pathways and compromising their ability to respond to the oxidative stress brought about by **FY026**. As stated earlier, **FY026** does not catalytically oxidise GSH. Its first reduction potential (involving the addition of 1 electron into the π*-orbital of the azo-bond) is at -0.64 V,[74] lower than that of its ruthenium analogue (-0.40 V)[19] and is therefore less biologically accessible. This may account for the low reactivity of **FY026** towards GSH. The mechanism by which **FY026** increases ROS levels within cancer cells remained uncertain until studies involving mitochondria were explored. **FY026** alters the mitochondrial transmembrane potential in both A2780 and A549 cells (explained in greater detail in Chapter 7, Section **7.4**).[71,75] Furthermore, **FY026** causes S-phase cell cycle arrest in A549 cells, which may be advantageous in slowing the proliferation of cancer cells.

1.3.4.3.4. Os(II) complexes with IMPY ligands

Phenyliminopyridine (IMPY) ligands are structurally similar to their AZPY counterparts but possess an imino-bond in place of an azo-bond. Their use was inspired by previous work in the Sadler group involving Ru(II) complexes[55] and the general structure of Os(II) arene IMPY complexes is shown in Figure 1.20.[5]

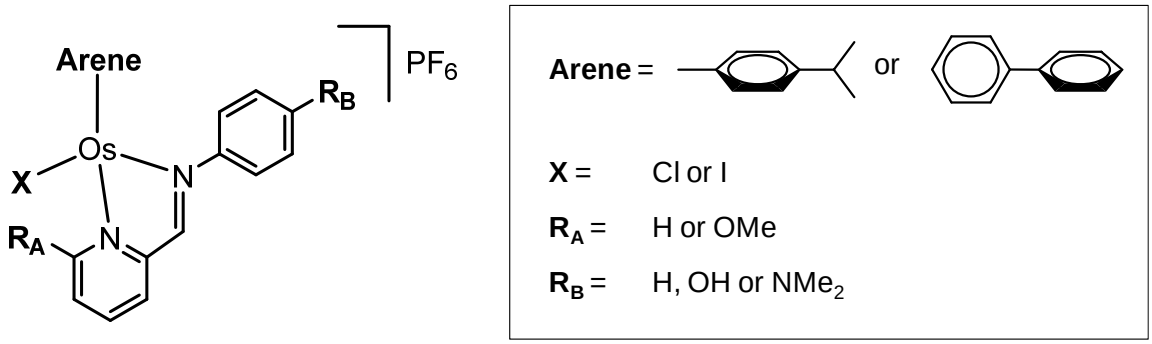

Figure 1.20. General structure of Os(II) arene IMPY complexes, where arene = *p*-cym or bip, X is a monodentate halide ligand (Cl or I), and R_A and R_B are either electron-donating groups or H on the IMPY ligand.

In contrast to AZPY complexes, Os(II) arene IMPY complexes hydrolyse in aqueous media. After 24 h incubation at 37°C in D_2O, the extent of hydrolysis for $[Os(\eta^6\text{-}p\text{-cym})(IMPY\text{-}NMe_2)I]^+$ reached 50%, and 99% for its chlorido analogue. Furthermore, the pK_a* of the water molecule in the corresponding aqua-adduct is 5.2, characteristic of a complex containing a π-acceptor bidentate ligand and therefore existing predominantly as the more stable hydroxido-species, $[Os(\eta^6\text{-}p\text{-cym})(IMPY\text{-}NMe_2)OH]^+$, under physiological conditions.[76] Similarly to Ru(II) arene AZPY complexes they are capable of binding to guanine derivatives. They were also found to raise ROS levels in

cancer cells, but in contrast to Ru(II) arene AZPY complexes, are not capable of catalytically oxidising GSH which may be explained by greater negative values observed for their reduction potentials. Moreover they were found to target the NADH/NAD^+ redox system, causing catalytic oxidation of NADH to NAD^+.[76] A mechanism of action was proposed, whereby hydride is transferred from NADH to the complex to form NAD^+. The hydride is then transferred to O_2 leading to regeneration of the catalyst and formation of H_2O_2 (Scheme 1.4). Table 1.1 shows a comparison chart of the currently known capabilities of osmium IMPY and AZPY complexes, and ruthenium AZPY complexes.

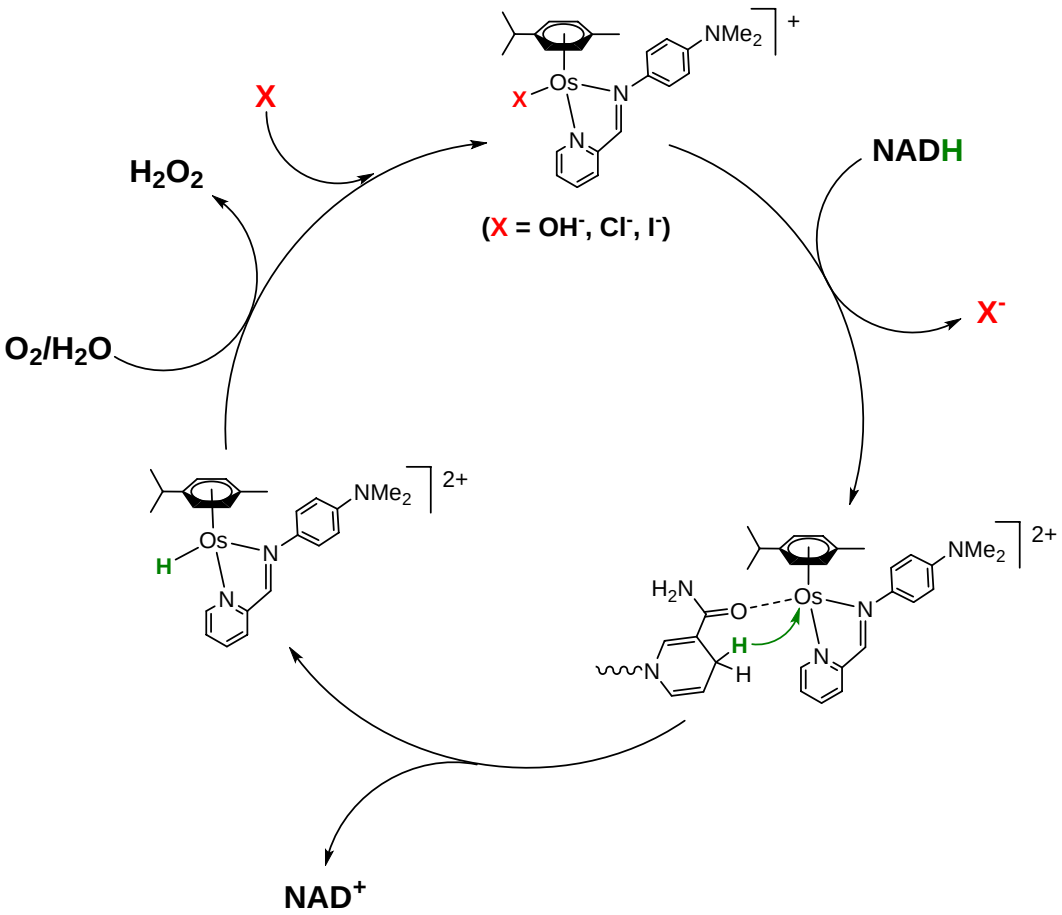

Scheme 1.4. Proposed catalytic cycle for the oxidation of NADH with $[Os(\eta^6\text{-}p\text{-cym})(IMPY\text{-}NMe_2)X]^+$, where X = I^-, Cl^- or OH^-.[5]

Table 1.1. List of chemical and biological capabilities that are currently known for Ru(II) arene complexes of AZPY and Os(II) arene complexes of AZPY and IMPY.

	Ru(II) arene AZPYs	Os(II) arene AZPYs	Os(II) arene IMPYs
Hydrolysis	Yes	No	Yes
Binding with Guanine	Yes	No	Yes
Increase in ROS	Yes	Yes	Yes
Oxidation of GSH	Yes	No	No
Oxidation of NADH	n.d.	No	Yes
Inhibit polymerisation of tubulin	n.d.	Yes	No

1.3.4.4. Osmium complexes of other research groups

Various other prominent research groups such as those of Keppler, Meggers, Sava and Dyson, have also made the extension from ruthenium to osmium with varied results. Osmium analogues of NAMI-A,[77] KP1019[78] and RAPTA (OsAPTA) complexes[29] have been synthesised and were found to exhibit slightly lower or comparable biological activities to their ruthenium counterparts. The search for further osmium anti-cancer complexes continues and has led to a variety of novel and promising structures.

1.3.4.4.1. Osmium complexes with pharmacophoric fragments

The combination of metal complexes with ligands containing protein targeting groups is becoming an increasingly popular field in anti-cancer research. It typically allows for better cancer cell selectivity as well as incorporating further

mechanisms of anti-cancer activity.[8] Kinases are involved in the regulation of most cellular processes and so their therapeutic inhibition has particularly attracted a lot of attention. The Keppler group have produced novel chlorido Ru(II) and Os(II) complexes with bidentate ligands containing quinoxalinone groups.[10] The ligand exhibits a pharmacophoric feature of several ATP competitive protein kinase inhibitors, and the chloride is a labile leaving group which could provide a site for coordinative interaction with targets (see Figure 1.21). The solubility of the free ligands is generally very poor, but their coordination to a metal centre scaffold facilitates their solubility in aqueous media and improves their anti-cancer activities. The complexes are capable of hydrolysis to form an aqua-adduct, which was reversed on the addition of sodium chloride. Interestingly, osmium complexes were more active than their ruthenium counterparts, which could be a result of their higher chemical inertness preventing deactivating side reactions.

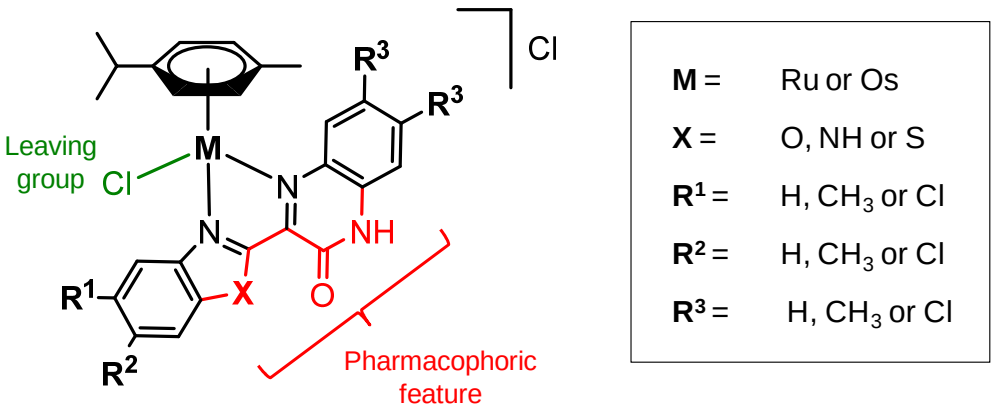

Figure 1.21. General structure of chlorido Os(II) and Ru(II) arene complexes containing quinoxalinone bidentate ligands.

In contrast, Meggers group have produced Ru(II) complexes that are based on the structure of a naturally occurring kinase inhibitor, staurosporine.[22] The metal acts as a scaffold for a bidentate ligand, forming a structurally rigid and stable complex mimicking staurosporine's shape and size (see Figure 1.22). The complexes are unreactive with an inert metal centre and possess a purely structural function. They are potent inhibitors of GSK-3β (glycogen synthase kinase), capable of blocking its ATP-active site.[79,80] Moreover, an osmium analogue was synthesised and compared to its ruthenium counterpart.[81] It was found to have very similar or slightly better biological activity in terms of anti-proliferative activity against 1205Lu melanoma cells and ability to inhibit GSK-3β.

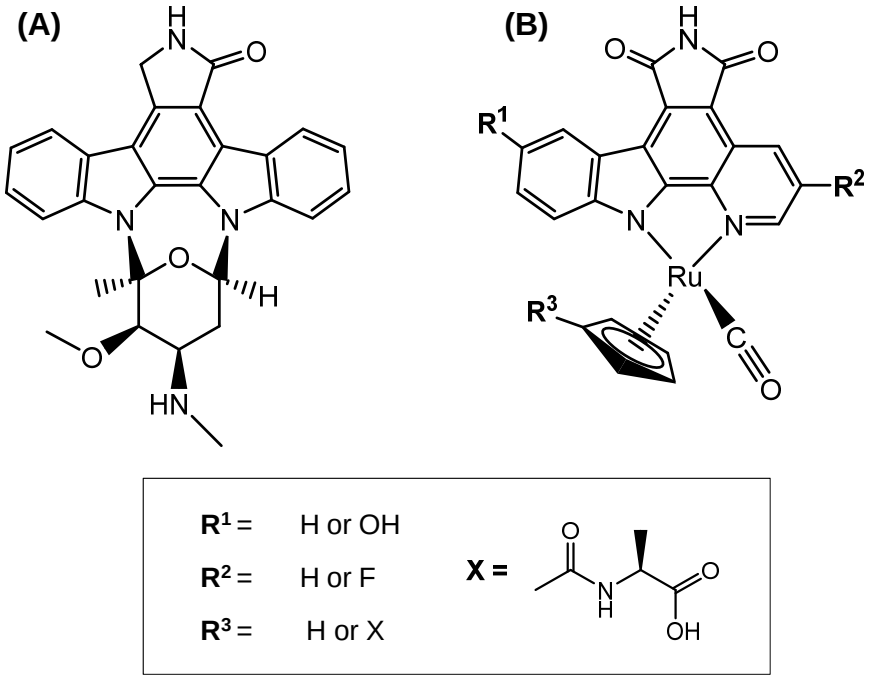

Figure 1.22. The molecular structure of (A) staurosporine, and (B) the general structure of Ru(II) GSK-3β inhibitors synthesised by the Meggers' group.

1.3.4.4.2. 'Click' carbene complexes

One class of complexes that has been relatively neglected in the field of anti-cancer research is that of N-heterocyclic carbenes (NHCs), which interestingly have been very successful in catalytic applications.[82] The Dyson group has successfully produced biologically active 'click' 1,2,3-triazolylidene NHC complexes. Analogous to their RAPTA/OsAPTA complexes, the PTA ligand is replaced with an NHC ligand that can incorporate various substituents to tailor lipophilicity (see Figure 1.23).[83]

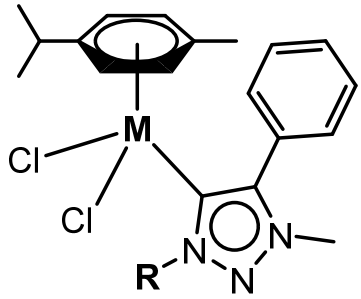

M =	Ru or Os
R =	ethyl, n-hexyl, n-dodecyl, benzyl, 2,3,4,6-tetra-*O*-β-D-glucopyranosyl, or 2,6-diisopropylphenyl

Figure 1.23. General structure of Ru(II) and Os(II) arene dichlorido complexes incorporating monodentate 'click' 1,2,3-triazolylidene NHCs.

Hydrolysis of these complexes (involving the displacement of one or both of the chloride ligands with water) occurs very rapidly compared to RAPTA-C and is suppressed in the presence of NaCl. The complexes showed selectivity towards A2780 and A2780cis cells over normal human embryonic kidney cells (HEK),

with some showing IC_{50} values in the nano-molar range. Improved activity over RAPTA/OsAPTA type complexes may be in part explained by the fast hydrolysis process, as a relationship between fast hydrolysis (activation) and cytotoxicity has been demonstrated before.[24] No obvious trends were observed when switching the metal centre from Ru(II) to Os(II), however increasing the lipophilicity by varying the substituent (R) did produce an improvement in activity.

1.3.4.4.3. Complexes with glucose-derived ligands

Similarly to 'click' carbene complexes, the Dyson group has reported complexes analogous to RAPTA/OsAPTA complexes where the PTA ligand is replaced with a glucose-derived ligand (see Figure 1.24).[84] The motivation was to exploit the altered metabolism of cancer cells, their increased glucose uptake in comparison with normal cells. The rate of hydrolysis of osmium complexes was very slow in comparison to their ruthenium analogues. In this instance, the ruthenium analogues were generally 2x more cytotoxic towards selected cancer cell lines than their osmium counterparts, which could be explained by their lack of reactivity with 5'-GMP compared to ruthenium analogues, and lack of ease of hydrolysis.

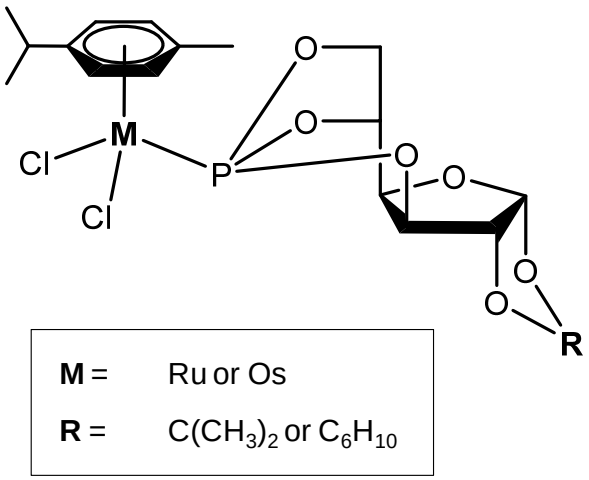

M =	Ru or Os
R =	$C(CH_3)_2$ or C_6H_{10}

Figure 1.24. Molecular structures of Ru(II) and Os(II) arene dichlorido complexes bearing glucose-derived monodentate ligands.

1.3.4.4.4. Os(VI) nitrido complexes

In the first of its kind, Tai-Chu Lau's group reported the synthesis of novel osmium(VI) nitrido octahedral anti-cancer complexes with azole ligands.[85] The Os≡N triple bond helps to stabilise the high oxidation state of Os(VI). The complexes are capable of forming 3 geometric isomers (see Figure 1.25). Many of the complexes have good cellular uptake into HeLa cervical cancer cell lines and a correlation between cellular uptake and cancer cell cytoxicity was observed, with IC_{50} values ranging between 9 - 82 μM over 4 different cancer cell lines. Cell cycle analysis showed S-phase arrest with the entry of cells from the G1-phase. Further *in vitro* DNA damage studies show that DNA is likely the primary target of these complexes.

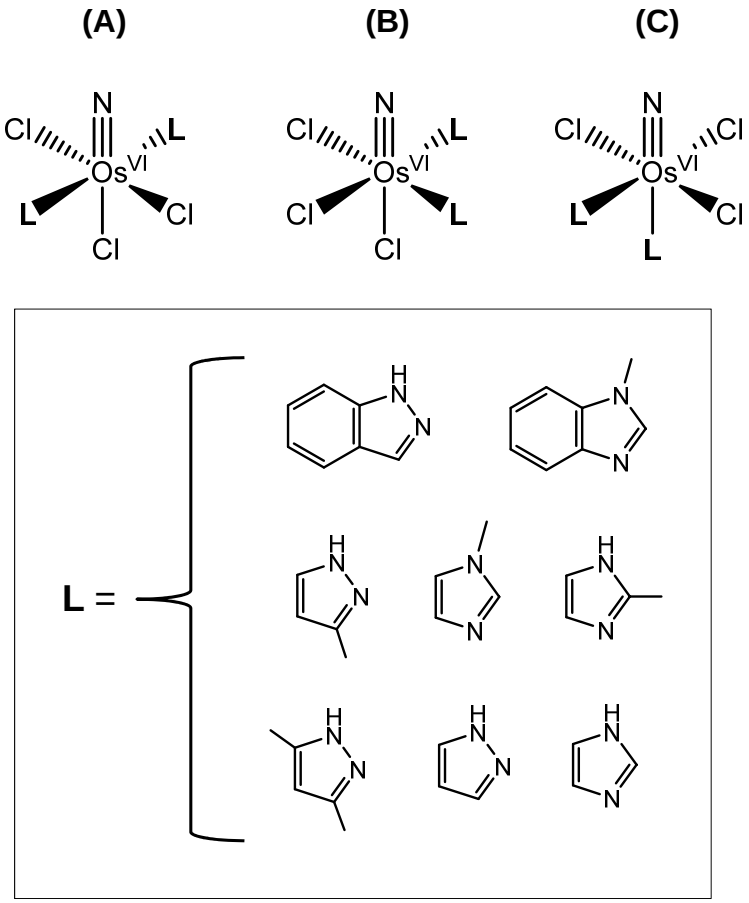

Figure 1.25. General structure of Os(VI) nitridohazole complexes. (A) *Trans*-isomer. (B) *Cis*-isomer with facial Cl ligands. (C) *Cis*-isomer with meridional Cl ligands.

1.4. Project aims

The general aim of this project was to synthesise and characterise novel osmium anti-cancer complexes with bidentate ligands containing an azo-bond. Then to undertake biological studies to determine their anti-cancer activities, structure-activity relationships, and further understand their mechanisms of activity. The more specific aims of this project are outlined below.

In terms of azo-ligand complexes, the Sadler group has previously explored only Os(II) and Ru(II) arene AZPY complexes in depth, with the exception of some Ru(II) arene phenylazopyrazole (AZPYZ) complexes that were featured in one publication.[54] There is an interest in exploring complexes of alternative azo-ligands to expand on our library of complexes, and gain a greater understanding of the properties of novel anti-cancer complexes. In **Chapter 3**, a new class of complexes is synthesised and their unique chemical properties are explored. The synthesis and exploration of Os(II) arene complexes with bidentate phenylazobenzothiazole (AZBTZ) ligands are described.

Chapter 4 describes the synthesis of further novel Os(II) arene AZPY anti-cancer complexes. This is undertaken utilising the structure-activity relationships that have already been established in Section **1.3.4.3**. One of the key challenges is to improve drug solubility in aqueous media, which is an inherent problem for this class of complexes. The attachment of water-solubilising glycol substituents to the AZPY ligands of complexes is explored. The trends in anti-proliferative activity, lipophilicity, cellular uptake and water solubility of new complexes are investigated, as well as the effect that key complexes have on the cell cycle and intracellular ROS levels of cancer cells.

The aim in **Chapter 5** is to label key Os(II) arene AZPY complexes with I-131 for the purpose of exploring intracellular activity. The most active species of this class contain a monodentate iodido ligand, which is replaced herein with the radioactive isotope, I-131. The subsequent radiotracers are used to study the stability of complexes in cell culture media, human blood serum and in the presence of MCF-7 cancer cells. These studies were designed to determine

whether the monodentate iodide ligand remains bound to the complex. It is easy to distinguish between complex-bound I-131 and free iodide-131 using radio-HPLC, and other gamma-ray detection techniques are utilised to determine the cellular accumulation of I-131.

Currently, little is known about the mechanism(s) by which Os(II) arene AZPY complexes increase ROS levels inside cancer cells. In **Chapter 6**, the mechanisms by which Os(II) arene AZPY complexes increase intracellular ROS levels are explored. Studies are carried out on **FY026**, [Os(η^6-p-cym)(AZPY-NMe_2)I]PF_6, and the new AZPY complexes synthesised in Chapter 4 to probe their intracellular interactions with biological targets: GSH, N-acetyl-*L*-cysteine (NAC), H_2O_2 and NADH.

1.5. References

(1) Scotting, P. *Cancer*; Oneworld Publications: Oxford, 2010.

(2) Pecorino, L. *Molecular Biology of Cancer*; *Second Ed.*; Oxford University Press: Oxford, 2008.

(3) http://www.cancerresearchuk.org

(4) http://www.macmillan.org.uk

(5) Fu, Y. Ph.D Thesis, University of Warwick, 2011.

(6) Parish, J. H. *Biochem. Educ.* **1990**, *18*, 157.

(7) Ma, Z.; Palermo, G.; Adhireksan, Z.; Murray, B. S.; von Erlach, T.; Dyson, P. J.; Rothlisberger, U.; Davey, C. A. *Angew. Chem. Int. Ed.* **2016**, *128*, 1.

(8) Sava, G.; Jaouen, G.; Hillard, E. A.; Bergamo, A. *Dalton Trans.* **2012**, *41*, 8226.

(9) Dyson, P. J.; Sava, G. *Dalton Trans.* **2006**, *16*, 1929.

(10) Ginzinger, W.; Mühlgassner, G.; Arion, V. B.; Jakupec, M. A.; Roller, A.; Galanski, M.; Reithofer, M.; Berger, W.; Keppler, B. K. *J. Med. Chem.* **2012**, *55*, 3398.

(11) Gridelli, C.; Bareschino, M. A.; Schettino, C.; Rossi, A.; Maione, P.; Ciardiello, F. *Oncologist* **2007**, *12*, 840.

(12) Lessene, G.; Czabotar, P. E.; Colman, P. M. *Nat. Rev. Drug. Discov.* **2008**, *7*, 989.

(13) Lessene, G.; Czabotar, P. E.; Sleebs, B. E.; Zobel, K.; Lowes, K. N.; Adams, J. M.; Baell, J. B.; Colman, P. M.; Deshayes, K.; Fairbrother, W. J.; Flygare, J. A.; Gibbons, P.; Kersten, W. J. A.; Kulasegaram, S.; Moss, R. M.; Parisot, J. P.; Smith, B. J.; Street, I. P.; Yang, H.; Huang, D. C. S.; Watson, K. G. *Nat. Chem. Biol.* **2013**, *9*, 390.

(14) Pelicano, H.; Carney, D.; Huang, P. *Drug Resist. Updat.* **2004**, *7*, 97.

(15) Jungwirth, U.; Kowol, C. R.; Keppler, B. K.; Hartinger, C. G.; Berger, W.; Heffeter, P. *Antioxid. Redox Sign.* **2011**, *15*, 1085.

(16) Lisanti, M. P.; Martinez-Outschoorn, U. E.; Lin, Z.; Pavlides, S.; Whitaker-Menezes, D.; Pestell, R. G.; Howell, A.; Sotgia, F. *Cell Cycle* **2011**, *10*, 2440.

(17) Noh, J.; Kwon, B.; Han, E.; Park, M.; Yang, W.; Cho, W.; Yoo, W.; Khang, G.; Lee, D. *Nat. Commun.* **2015**, *6*, 6907.

(18) López-Lázaro, M. *Cancer Lett.* **2007***, 252*, 1.

(19) Dougan, S. J.; Habtemariam, A.; McHale, S. E.; Parsons, S.; Sadler, P. J. *Proc. Natl. Acad. Sci. U.S.A.* **2008**, *105*, 11628.

(20) Balendiran, G. K.; Dabur, R.; Fraser, D. *Cell Biochem. Funct.* **2004**, *22*, 343.

(21) Wlassoff, W. A.; Albright, C. D.; Sivashinski, M. S.; Ivanova, A.; Appelbaum, J. G.; Salganik, R. I. *J. Pharm. Pharmacol.* **2007**, *59*, 1549.

(22) Meggers, E. *Chem. Commun.* **2009**, *9*, 1001.

(23) Fu, Y.; Habtemariam, A.; Basri, A. M. B. H.; Braddick, D.; Clarkson, G. J.; Sadler, P. J. *Dalton Trans.* **2011**, *40*, 10553.

(24) Pizarro, A.; Habtemariam, A.; Sadler, P.*Top Organomet. Chem.* **2010**, *32*, 21.

(25) Strohfeldt, K.; Tacke, M. *Chem. Soc. Rev.* **2008**, *37*, 1174.

(26) Kioseoglou, E.; Petanidis, S.; Gabriel, C.; Salifoglou, A. *Coord. Chem. Rev.* **2015**, *301*, 87.

(27) Romero-Canelón, I.; Sadler, P. J. *Inorg. Chem.* **2013**, *52*, 12276.

(28) Katsaros, N.; Anagnostopoulou, A. *Crit. Rev. Oncol. Hemat.* **2002**, *42*, 297.

(29) Dorcier, A.; Ang, W. H.; Bolaño, S.; Gonsalvi, L.; Juillerat-Jeannerat, L.; Laurenczy, G.; Peruzzini, M.; Phillips, A. D.; Zanobini, F.; Dyson, P. J. *Organometallics* **2006**, *25*, 4090.

(30) Budagumpi, S.; Haque, R. A.; Endud, S.; Rehman, G. U.; Salman, A. W. *Eur. J. Inorg. Chem.* **2013**, *2013*, 4367.

(31) Liu, Z.; Romero-Canelón, I.; Qamar, B.; Hearn, J. M.; Habtemariam, A.; Barry, N. P. E.; Pizarro, A. M.; Clarkson, G. J.; Sadler, P. J. *Angew. Chem. Int. Ed.* **2014**, *53*, 3941.

(32) Millett, A. J.; Habtemariam, A.; Romero-Canelón, I.; Clarkson, G. J.; Sadler, P. J. *Organometallics* **2015**, *34*, 2683.

(33) Zhang, J. J.; Lu , W.; Sun, R. W. Y.; Che, C. M. *Angew. Chem. Int. Ed.* **2012**, *51*, 4882.

(34) Chen, Z. F.; Liu, Y. C.; Peng, Y.; Hong, X.; Wang, H. H.; Zhang, M. M.; Liang, H. *J. Biol. Inorg. Chem.* **2012**, *17*, 247.

(35) Arnesano, F.; Natile, G. *Coord. Chem. Rev.* **2009**, *253*, 2070.

(36) Fenton, D. E. *Biocoordination Chemistry*; Oxford University Press: Oxford, 1995.

(37) Jung, Y.; Lippard, S. J. *Chem. Rev.* **2007**, *107*, 1387.

(38) Kasherman, Y.; Sturup, S.; Gibson, D. *J. Med. Chem.* **2009**, *52*, 4319.

(39) Fakih, S.; Munk, V. P.; Shipman, M. A.; Murdoch, P. S.; Parkinson, J. A.; Sadler, P. J. *Eur. J. Inorg. Chem.* **2003**, *2003*, 1206.

(40) Allen, O. R.; Croll, L.; Gott, A. L.; Knox, R. J.; McGowan, P. C. *Organometallics* **2004**, *23*, 288.

(41) Kelman, A., D; Clarke, M., J; Edmonds, S., D; Peresie, H., J *J. Clin. Hemat. Oncol.* **1977**, *7*, 274.

(42) Sava, G.; Zorzet, S.; Turrin, C.; Vita, F.; Soranzo, M.; Zabucchi, G.; Cocchietto, M.; Bergamo, A.; DiGiovine, S.; Pezzoni, G.; Sartor, L.; Garbisa, S. *Clin. Cancer Res.* **2003**, *9*, 1898.

(43) Hartinger, C. G.; Zorbas-Seifried, S.; Jakupec, M. A.; Kynast, B.; Zorbas, H.; Keppler, B. K. *J. Inorg. Biochem.* **2006**, *100*, 891.

(44) Yan, Y. K.; Melchart, M.; Habtemariam, A.; Sadler, P. J. *Chem. Commun.* **2005**, *38*, 4764.

(45) Ang, W. H.; Casini, A.; Sava, G.; Dyson, P. J. *J. Organomet. Chem.* **2011**, *696*, 989.

(46) Scolaro, C.; Bergamo, A.; Brescacin, L.; Delfino, R.; Cocchietto, M.; Laurenczy, G.; Geldbach, T. J.; Sava, G.; Dyson, P. J. *J. Med. Chem.* **2005**, *48*, 4161.

(47) Wang, F.; Chen, H.; Parsons, S.; Oswald, I. D. H.; Davidson, J. E.; Sadler, P. J. *Chem. Eur. J.* **2003**, *9*, 5810.

(48) Wang, F.; Xu, J.; Habtemariam, A.; Bella, J.; Sadler, P. J. *J. Am. Chem. Soc.* **2005**, *127*, 17734.

(49) Fernández, R.; Melchart, M.; Habtemariam, A.; Parsons, S.; Sadler, P. J. *Chem. Eur. J.* **2004**, *10*, 5173.

(50) Chen, H.; Parkinson, J. A.; Morris, R. E.; Sadler, P. J. *J. Am. Chem. Soc.* **2003**, *125*, 173.

(51) Yan, Y. K.; Melchart, M.; Habtemariam, A.; Peacock, A. F. A.; Sadler, P. J. *J. Biol. Inorg. Chem.* **2006**, *11*, 483.

(52) Soldevila-Barreda, J. J. Ph.D Thesis, University of Warwick, 2014.

(53) Soldevila-Barreda, J. J.; Romero-Canelón, I.; Habtemariam, A.; Sadler, P. J. *Nat. Commun.* **2015**, *6*, 1.

(54) Dougan, S. J.; Melchart, M.; Habtemariam, A.; Parsons, S.; Sadler, P. J. *Inorg. Chem.* **2006**, *45*, 10882.

(55) Romero-Canelon, I.; Salassa, L.; Sadler, P. J. *J. Med. Chem.* **2013**, *56*, 1291.

(56) Girolami, G. *Nat. Chem.* **2012**, *4*, 954.

(57) Arblaster, J., W.*Platin. Met. Rev.* **1995**, *39*, 164.

(58) https://www.webelements.com/osmium/isotopes.html

(59) McDonald, D. *Platin. Met. Rev.* **1961**, *5*, 146.

(60) http://www.rsc.org/chemistryworld/2014/08/osmium-tetraoxide-podcast

(61) Hinckley, C. C.; Bemiller, J. N.; Strack, L. E.; Russell, L. D. *Platinum, Gold, and Other Metal Chemotherapeutic Agents*; American Chemical Society: **1983**, *209*, 421.

(62) Housecroft, C. E.; Sharpe, A. G. *Inorganic Chemistry*, *First ed.*; Prentice Hall: New York, 2000.

(63) Clementi, E.; Raimondi, D. L.; Reinhardt, W. P. *J. Chem. Phys.* **1967**, *47*, 1300.

(64) Peacock, A. F. A.; Habtemariam, A.; Fernández, R.; Walland, V.; Fabbiani, F. P. A.; Parsons, S.; Aird, R. E.; Jodrell, D. I.; Sadler, P. J. *J. Am. Chem. Soc.* **2006**, *128*, 1739.

(65) Peacock, A. F. A.; Habtemariam, A.; Moggach, S. A.; Prescimone, A.; Parsons, S.; Sadler, P. J. *Inorg. Chem.* **2007**, *46*, 4049.

(66) Peacock, A. F. A.; Melchart, M.; Deeth, R. J.; Habtemariam, A.; Parsons, S.; Sadler, P. J. *Chem. Eur. J.* **2007**, *13*, 2601.

(67) Peacock, A. F. A.; Parsons, S.; Sadler, P. J. *J. Am. Chem. Soc.* **2007**, *129*, 3348.

(68) Kostrhunova, H.; Florian, J.; Novakova, O.; Peacock, A. F. A.; Sadler, P. J.; Brabec, V. *J. Med. Chem.* **2008**, *51*, 3635.

(69) Rijt, S. H. v.; Kostrhunova, H.; Brabec, V.; Sadler, P. J. *Bioconj. Chem.* **2011**, *22*, 218.

(70) Fu, Y.; Habtemariam, A.; Pizarro, A. M.; van Rijt, S. H.; Healey, D. J.; Cooper, P. A.; Shnyder, S. D.; Clarkson, G. J.; Sadler, P. J. *J. Med. Chem.* **2010**, *53*, 8192.

(71) van Rijt, S. H.; Romero-Canelon, I.; Fu, Y.; Shnyder, S. D.; Sadler, P. J. *Metallomics* **2014**, *6*, 1014.

(72) Jordan, M. A.; Wilson, L. *Nat. Rev. Cancer* **2004**, *4*, 253.

(73) Hearn, J. M.; Romero-Canelón, I.; Munro, A. F.; Fu, Y.; Pizarro, A. M.; Garnett, M. J.; McDermott, U.; Carragher, N. O.; Sadler, P. J. *Proc. Natl. Acad. Sci. U.S.A.* **2015**, *112*, 3800.

(74) Shnyder, S. D.; Fu, Y.; Habtemariam, A.; van Rijt, S. H.; Cooper, P. A.; Loadman, P. M.; Sadler, P. J. *Med. Chem. Comm.* **2011**, *2*, 666.

(75) Romero-Canelón, I.; Mos, M.; Sadler, P. J. *J. Med. Chem.* **2015**, *58*, 7874.

(76) Fu, Y.; Romero, M. J.; Habtemariam, A.; Snowden, M. E.; Song, L.; Clarkson, G. J.; Qamar, B.; Pizarro, A. M.; Unwin, P. R.; Sadler, P. J. *Chem. Sci.* **2012**, *3*, 2485.

(77) Cebrián-Losantos, B.; Krokhin, A. A.; Stepanenko, I. N.; Eichinger, R.; Jakupec, M. A.; Arion, V. B.; Keppler, B. K. *Inorg. Chem.* **2007**, *46*, 5023.

(78) Büchel, G. E.; Stepanenko, I. N.; Hejl, M.; Jakupec, M. A.; Keppler, B. K.; Arion, V. B. *Inorg. Chem.* **2011**, *50*, 7690.

(79) Atilla-Gokcumen, G. E.; Pagano, N.; Streu, C.; Maksimoska, J.; Filippakopoulos, P.; Knapp, S.; Meggers, E. *Chem. Bio. Chem.* **2008**, *9*, 2933.

(80) Pagano, N.; Maksimoska, J.; Bregman, H.; Williams, D. S.; Webster, R. D.; Xue, F.; Meggers, E. *Org. Biomol. Chem.* **2007**, *5*, 1218.

(81) Maksimoska, J.; Williams, D. S.; Atilla-Gokcumen, G. E.; Smalley, K. S. M.; Carroll, P. J.; Webster, R. D.; Filippakopoulos, P.; Knapp, S.; Herlyn, M.; Meggers, E. *Chemistry* **2008**, *14*, 4816.

(82) Vougioukalakis, G. C.; Grubbs, R. H. *Chem. Rev.* **2010**, *110*, 1746.

(83) Kilpin, K. J.; Crot, S.; Riedel, T.; Kitchen, J. A.; Dyson, P. J. *Dalton Trans.* **2014**, *43*, 1443.

(84) Hanif, M.; Nazarov, A. A.; Hartinger, C. G.; Kandioller, W.; Jakupec, M. A.; Arion, V. B.; Dyson, P. J.; Keppler, B. K. *Dalton Trans.* **2010**, *39*, 7345.

(85) Ni, W. X.; Man, W. L.; Yiu, S. M.; Ho, M.; Cheung, M. T. W.; Ko, C. C.; Che, C. M.; Lam, Y. W.; Lau, T. C. *Chem. Sci.* **2012**, *3*, 1582.

Chapter 2

Materials, Instrumentation and Experimental Methods

2.1. Materials and synthesis

2.1.1. Materials

2.1.1.1. Chemicals

$OsCl_3.3H_2O$ was purchased from either Sigma Aldrich or Heraeus (South Africa), $K_2[Os^{VI}O_2(OH)_4]$ from Alfa Aesar, and α-terpinene and biphenyl from Sigma Aldrich. Ammonium hexafluorophosphate, ammonium triflate and potassium iodate (counter ions for complexes) were all purchased from Sigma Aldrich. Magnesium sulphate (drying agent) and silica gel (particle size 40-63 Å) were purchased from Sigma Aldrich, and phosphorus pentoxide (vacuum desiccant) was purchased from VWR. Dry ethanol was produced by distilling absolute ethanol over Mg/I under a N_2 atmosphere. Synthesis grade deionised water was obtained from a Millipore Elix 5 purification system. Analysis grade doubly deionised water (18 MΩ cm^{-1}) was obtained from either a Millipore Simplicity UV, or an USF Elga UHQ PS purification system. The osmium ICP standard was 1000±10 µg/mL in 15% HCl (v/v) and purchased from Inorganic Ventures. All other solvents and reagents for synthesis and analysis were purchased from commercial suppliers and used as received.

Stock phosphate buffer solutions (600 mM) were prepared by dissolving monosodium phosphate monohydrate (1.56 g, 11.305 mmol) and disodium phosphate heptahydrate (13.1 g, 48.868 mmol) (both purchased from Fisher Scientific) together in doubly deionised water (100 mL). The pH of the phosphate buffer solution was measured using the pH bench top meter (Section **2.2.7.1**) and adjusted to pH 7.4(±0.1) using aqueous sodium hydroxide.

Phosphate-buffered D_2O solutions were prepared in a similar manner, adjusting the pH* to 7.4(±0.1) using sodium hydroxide in D_2O without correcting for the effect of deuterium on the glass electrode.

2.1.1.2. Cell culture

DMEM and RPMI-1640 cell culture media, penicillin/streptomycin mixture, foetal bovine serum, *L*-gutamine, phosphate buffered saline solution (PBS), AccuMax cell dissociation solution, trypsin and trypsin/EDTA were all purchased from PAA Laboratories GmbH. Cell culture media (500 mL) were supplemented with foetal bovine serum (50 mL), penicillin/streptomycin mixture (5 mL) and *L*-glutamine (5 mL). All cancer cell lines were purchased from the European Collection of Cell Cultures and Public Health England.

2.1.2. Synthesis of Os(II) dimers

Osmium dimers are vital precursors for the synthesis of osmium(II) arene 'piano-stool' complexes. A total of six dimers were synthesised; $[Os(\eta^6\text{-}p\text{-cym})Cl_2]_2$, $[Os(\eta^6\text{-}p\text{-cym})Br_2]_2$, $[Os(\eta^6\text{-}p\text{-cym})I_2]_2$, $[Os(\eta^6\text{-bip})Cl_2]_2$, $[Os(\eta^6\text{-bip})Br_2]_2$, $[Os(\eta^6\text{-bip})I_2]_2$. Reported traditional synthetic methods were utilised[1-3] and implemented to improve product yields. Also, new synthetic strategies involving microwave synthesis were developed.[4] The two principal synthetic routes for generating dimers from inorganic osmium compounds are summarised in Scheme 2.1.

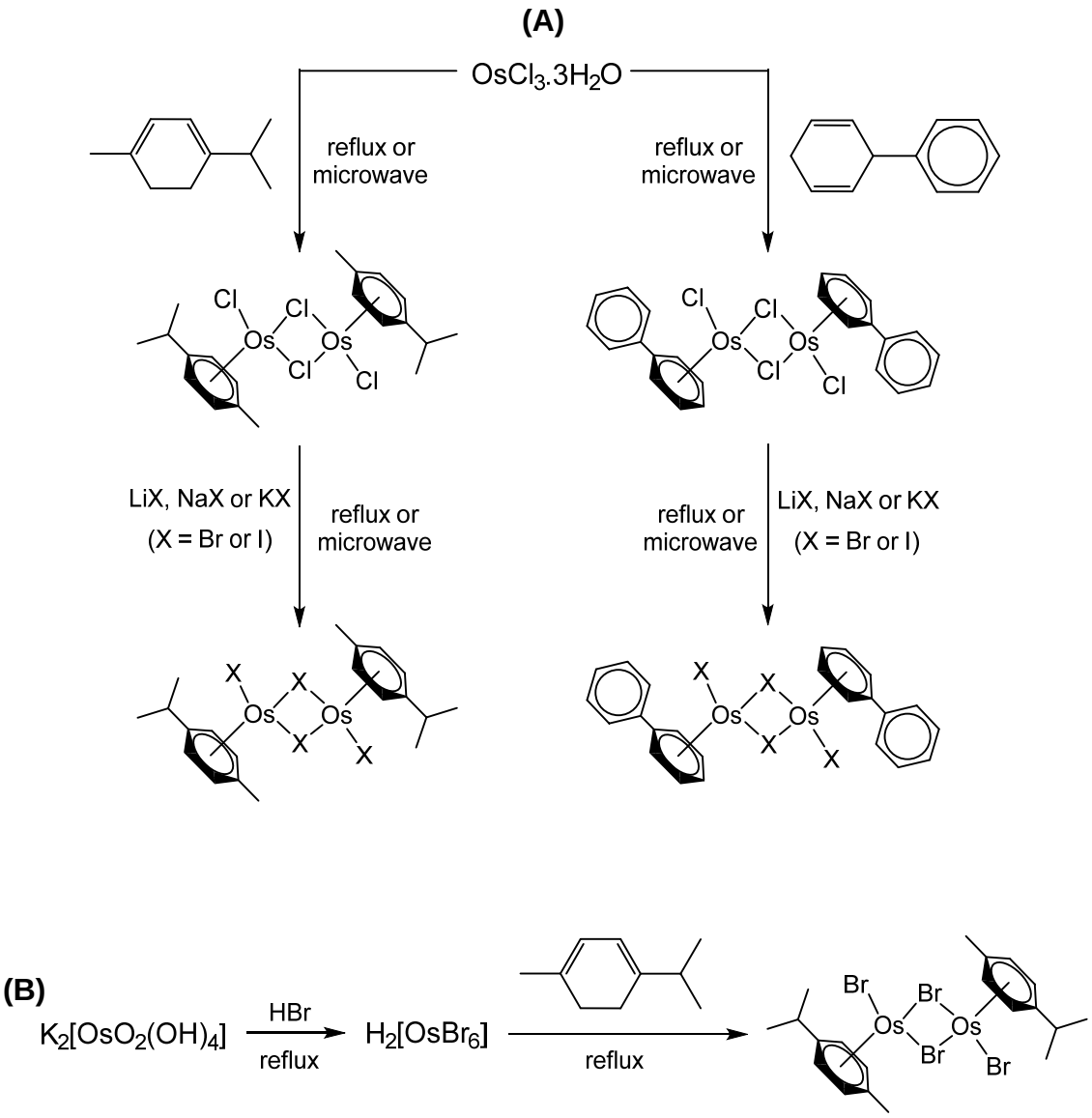

Scheme 2.1. Two methods of generating osmium(II) dimers. (A); starting from osmium trichloride, Os^{III}. (B); starting from potassium osmate, Os^{VI}.

2.1.2.1. Synthesis of $[Os(\eta^6\text{-}p\text{-cym})Cl_2]_2$[5,6]

Method 1. $OsCl_3.3H_2O$ (5.00 g, 14.26 mmol) was dissolved in dry freshly distilled EtOH (250 mL) and α-terpinene (32.16 g, 0.24 mol) was added drop-wise. The mixture was heated under reflux for 18 h under a N_2 atmosphere and the colour changed from black to dark orange. The mixture was hot-filtered to

remove a light brown precipitate. The filtrate was concentrated under reduced pressure and placed in the freezer overnight. An orange precipitate formed, which was collected *via* vacuum filtration and washed with ice-cold EtOH (2 x 5 mL) and Et_2O (2 x 5 mL). The product was dried overnight in a vacuum desiccator. Yield: 3.92 g, (70%).

Method 2. $OsCl_3.3H_2O$ (1.00 g, 2.85 mmol) and α-terpinene (1.84 g, 13.51 mmol) were dissolved in MeOH (10 mL) in a microwave reaction vessel. The mixture was irradiated with microwave radiation for 5 min at 150 °C. The mixture was placed in the freezer overnight, and the resulting orange precipitate was collected *via* vacuum filtration and washed with ice-cold EtOH (2 x 5 mL) and Et_2O (2 x 5 mL). The product was dried overnight in a vacuum desiccator. Yield: 1.02 g, (90%). ^{1}H NMR (400 MHz, $(CD_3)_2SO$): δ 6.07 (d, 4H, J = 6.0 Hz), 5.99 (d, 4H, J = 6.0 Hz), 2.74 (sept., 2H, J = 6.9 Hz), 2.13 (s, 6H), 1.19 (12H, d, J = 7.0 Hz).

2.1.2.2. Synthesis of $[Os(\eta^6\text{-}p\text{-cym})Br_2]_2$[2]

Method 1. $[Os(\eta^6\text{-}p\text{-cym})Cl_2]_2$ (200.0 mg, 0.25 mmol) and LiBr (10.98 g, 0.13 mol) were mixed in deionised water (50 mL). The solution was heated to 100 °C for 18 h and a brown precipitate was observed. The reaction mixture was cooled to room temperature then placed in the fridge for 2 h. The precipitate was filtered and washed with water (2 x 5 mL), ice-cold EtOH (2 x 5 mL) and Et_2O (2 x 5 mL). The product was dried overnight in a vacuum desiccator. Yield: 159.6 mg, (65%).

Method 2. $K_2[Os^{VI}O_2(OH)_4]$ (1.07 g, 2.90 mmol) was dissolved in absolute EtOH (20 mL) and 48% aqueous hydrobromic acid (10 mL) was added. The mixture was heated under reflux for 18 h under a N_2 atmosphere. α-Terpinene (5.52 g, 40.52 mmol) was added and the mixture was heated under reflux for a further 18 h under N_2. Deionised water (20 mL) was added and the product was extracted with DCM (3 x 20 mL). The combined DCM extracts were concentrated to 5-10 mL under reduced pressure and diethyl ether (5 mL) was added. The mixture was placed in the freezer overnight yielding brown crystalline needles, which were collected *via* vacuum filtration and washed with ice-cold EtOH (2 x 5 mL) and Et_2O (2 x 5 mL). The product was dried overnight in a vacuum desiccator. Yield: 0.57 g, (41%). ^{1}H NMR (400 MHz, $(CD_3)_2SO$): δ 6.10 (d, 4H, J = 6.0 Hz), 6.03 (d, 4H, J = 6.0 Hz), 2.82 (sept., 2H, J = 6.9 Hz), 2.22 (s, 6H), 1.20 (d, 12H, J = 7.0 Hz).

2.1.2.3. Synthesis of $[Os(\eta^6\text{-}p\text{-cym})I_2]_2$[3]

Method 1. A solution of LiI (55.64 g, 0.42 mol) in deionised water (100 mL) was prepared and N_2 was bubbled through for 20 min to remove molecular oxygen. $[Os(\eta^6\text{-}p\text{-cym})Cl_2]_2$ (657.4 mg, 0.83 mmol) was added and the solution was heated at 80 °C for 18 h under a N_2 atmosphere and a brown precipitate was observed. The reaction mixture was cooled to room temperature and the precipitate was collected *via* vacuum filtration, re-dissolved in DCM (20 mL) and filtered again to remove a black precipitate. The filtrate was concentrated to 5-10 mL under reduced pressure and placed in the freezer overnight, yielding a

red-brown precipitate. The product was collected *via* vacuum filtration, washed with ice-cold EtOH (2 x 5 mL) and Et_2O (2 x 5 mL), and dried overnight in a vacuum desiccator. Yield: 585.8 mg, (61%).

Method 2. $[Os(\eta^6\text{-}p\text{-cym})Cl_2]_2$ (602.9 mg, 0.76 mmol) was dissolved in MeOH (5 mL) in a microwave reaction vessel. A solution of KI (12.66 g, 76.27 mmol) in deionised water (10 mL) was added and the mixture was irradiated with microwave radiation for 5 min at 150 °C. The mixture was cooled in the fridge overnight, and the resulting red precipitate was collected *via* vacuum filtration and washed with water (2 x 5 mL), ice-cold EtOH (2 x 5 mL) and Et_2O (2 x 5 mL). The product was dried overnight in a vacuum desiccator. Yield: 707.5 mg, (80%). ^{1}H NMR (400 MHz, $(CD_3)_2SO$): δ 6.09 (d, 4H, J = 6.1 Hz), 6.04 (d, 4H, J = 6.1 Hz), 3.00 (sept., 2H, J = 6.9 Hz), 2.39 (s, 6H), 1.21 (12H, d, J = 6.9 Hz).

2.1.2.4. Synthesis of 1-phenyl-cyclohexa-2,5-diene[7]

All glassware was oven dried and purged with N_2 prior to use and the synthesis was carried out under anhydrous conditions. Biphenyl (15.43 g, 100.06 mmol) was dissolved in anhydrous THF (150 mL) in a 1L 3-necked flask. Liquid NH_3 (~200 mL) was condensed into a 2L 3-necked flask submerged in an acetone/dry ice bath (-78 °C). The biphenyl solution was transferred into the liquid NH_3 *via* a cannula and stirred with a mechanical stirrer. Lithium (1.85 g, 0.27 mol) was added to the stirring mixture, which turned blue, green, and finally red. The mixture was left to stir for a further 30 min. NH_4Cl (20.0 g, 0.37 mol) was added and the mixture was left to stir overnight at ambient

temperature. Deionised water (500 mL) was added and the mixture was adjusted to pH 1 with 6 M HCl. The crude product was extracted with Et_2O (3 x 300 mL), dried over $MgSO_4$, filtered, and the solvent was removed under reduced pressure. The product was purified by vacuum distillation (45 °C, 0.1 mbar). Yield: 12.8 g, (82%). ^{1}H NMR (400 MHz, $CDCl_3$): δ 7.23-7.22 (m, 2H), 7.14-7.13 (m, 3H), 5.75-5.74 (m, 2H), 5.66-5.65 (m, 2H), 3.88-3.87 (m, 1H), 2.68-2.67 (m, 2H).

2.1.2.5. Synthesis of $[Os(\eta^6\text{-bip})Cl_2]_2$[6]

Method 1. $OsCl_3.3H_2O$ (1.00 g, 2.85 mmol) was dissolved in dry freshly distilled EtOH (50 mL) and 1-phenyl-cyclohexa-2,5-diene (1.78 g, 11.41 mmol) was added drop-wise. The mixture was heated under reflux under a N_2 atmosphere for 72 hours. The resulting mixture contained a light brown precipitate, which was cooled down to room temperature. The precipitate was collected *via* vacuum filtration and washed with ice-cold EtOH (2 x 5 mL) and Et_2O (2 x 5 mL). The product was dried overnight in a vacuum desiccator. Yield: 1.02 g, (86%).

Method 2. $OsCl_3.3H_2O$ (1.00 g, 2.85 mmol) and 1-phenyl-cyclohexa-2,5-diene (1.58 g, 10.11 mmol) were dissolved in MeOH (5 mL) in a microwave reaction vessel, and the mixture was irradiated with microwave radiation for 10 min at 120 °C. After cooling to room temperature, an orange precipitate was collected *via* vacuum filtration and washed with ice-cold ethanol (2 x 5 mL) and Et_2O (2 x 5 mL). The product was dried overnight in a vacuum desiccator. Yield: 1.13 g,

(95%). ^{1}H NMR (400 MHz, $(CD_3)_2SO$): δ 7.71 (dd, 4H, J = 8.1, 1.4 Hz), 7.49-7.44 (m, 6H), 6.68 (d, 4H, 5.6 Hz), 6.38-6.31 (m, 6H).

2.1.2.6. Synthesis of $[Os(\eta^6\text{-bip})I_2]_2$[3]

$[Os(\eta^6\text{-bip})Cl_2]_2$ (500.0 mg, 0.60 mmol) was dissolved in MeOH (5 mL) in a microwave reaction vessel. A solution of KI (9.99 g, 60.18 mmol) in deionised water (10 mL) was added and the mixture was irradiated with microwave radiation for 3 min at 100 °C. The mixture was cooled in the fridge overnight, and a dark brown precipitate was collected *via* vacuum filtration and washed with water (2 x 5 mL), ice-cold EtOH (2 x 5 mL) and Et_2O (2 x 5 mL). The product was dried overnight in a vacuum desiccator. Yield: 520.4 mg, (72%). ^{1}H NMR (400 MHz, $(CD_3)_2SO$): δ 7.72 (dd, 4H, J = 8.1, 1.6 Hz), 7.50-7.41 (m, 6H), 6.82 (d, 4H, J = 6.0 Hz), 6.57-6.55 (m, 2H), 6.34-6.32 (m, 4H).

2.2. Instrumentation

2.2.1. NMR spectroscopy

^{1}H and ^{13}C NMR spectra were acquired in 5 mm NMR tubes at 298 K on either Bruker DPX-300 or 400, AV-400, or DRX-500 spectrometers. Data processing was carried out using TOPSPIN version 2.1 (Bruker U.K. Ltd). ^{1}H NMR chemical shifts were internally referenced to TMS *via* their residual solvent peaks: acetonitrile (δ = 1.94 ppm), acetone (δ = 2.05 ppm), methanol (δ = 3.31 ppm), water (δ = 4.79 ppm), chloroform (δ = 7.26 ppm), DMSO (δ = 2.50 ppm).[8]

Likewise for ^{13}C NMR chemical shifts: acetonitrile (δ = 118.26 ppm), acetone (δ = 206.26 ppm), methanol (δ = 49.00 ppm).[8] 1D ^{1}H NMR spectra were recorded using standard pulse sequences and 1D ^{13}C NMR spectra were recorded using a JMOD pulse sequence. Typically, ^{1}H data were acquired with 16 transients into 32 k data points over a spectral width of 14 ppm, and ^{13}C data with 256 transients into 64 k data points over a spectral width of 260 ppm.

2.2.2. Electrospray ionisation mass spectrometry (ESI-MS)

Positive and negative ion electrospray mass spectra were obtained using the Agilent 6130B single Quad (ESI) mass spectrometer. Samples of complexes were typically prepared in methanol, deionised water or acetonitrile and run in positive ion mode (500-1000 m/z) and negative ion mode (50-500 m/z). Likewise, samples submitted for high-resolution mass spectroscopy were carried out using a Bruker MaXis UHR-ESI-TOF by Phil Aston.

2.2.3. Elemental analysis

All purified complexes and ligands were analysed *via* elemental analysis. Analyses (carbon, hydrogen and nitrogen) were performed by Warwick Analytical Service using an Exeter Analytical elemental analyser (CE440).

2.2.4. UV-Vis spectroscopy

UV-Vis spectroscopy was used routinely as a means of characterising complexes and following chemical reactions. A Varian Cary 300 Bio or Varian Cary 300 Scan instrument was used with 1 cm path length quartz cuvettes, and a Varian Cary temperature controller. Unless otherwise stated, spectra were recorded at 25 °C between 800-200 nm at a scan rate of 600 nm/min with 1 nm intervals. Varian Cary WinUV software was used to record the spectra, using either Scan version 4.10(464), Scanning Kinetics version 4.10(461), or Kinetics version 4.10(461) mode, depending on the type of experiment. Commercially available solvents were used and any aqueous solutions were made using doubly deionised water. All spectra were processed using MS Excel 2010.

2.2.5. Microwave reactor

Microwave assistance was utilised for the synthesis of some Os(II) arene dimers. Microwave synthesis enables increased solvent molecular vibrations and for reactions to take place at higher temperatures than traditional heating apparatus. A CEM Discover-SP microwave reactor was used with the following settings: maximum power = 150 W, maximum pressure = 250 PSI. Reaction times and temperatures varied and are stated in the synthesis experimental (Section **2.1.2**).

2.2.6. Automated reverse-phase column chromatography

Sometimes Os(II) arene complexes required an alternative purification method when recrystallization methods were not viable. Complexes were purified using a Biotage Isolera one instrument with a Biotage KP-C18-HS 12g SNAP cartridge. The mobile phase consisted of; (A) H_2O + 0.1 %TFA, and (B) MeCN + 0.1 % TFA. The complex (≤100 mg) was dissolved in DCM, loaded onto ISOLUTE HM-N granules and installed onto the top of the column. The following solvent gradient was used with a 12 mL/min flow rate.

Start (%B)	End (%B)	Column volumes
0	0	1
0	10	1
10	80	20-30
80	80	6
80	10	1

The collected fractions were analysed by MS and the chosen fractions were combined. MeCN was removed under reduced pressure and the product was extracted with DCM (10-20 mL). The product was re-dissolved in EtOH and recombined with its original counter ion by adding the appropriate salt (e.g. ammonium hexafluorophosphate), then recrystallised in EtOH.

2.2.7. pH measurements

2.2.7.1. pH bench top meter

A Martini instruments Mi 150 pH/Temperature bench meter with a Mettler-Toledo U402-M3-S7/200 chloride pH probe was used. The instrumentation was calibrated with three Mettler-Toledo buffer solutions; pH 4.01±0.02, 7.00 ±0.02,

and 10.00±0.02. The probe was washed between measuring samples with deionised water, and stored in 1 M KCl when not in use. All pH meter readings were recorded at room temperature.

2.2.7.2. Portable pH meter device

A portable pH meter was specifically used for pH measurements when measuring the pK_a of a complex by ^1H NMR. A HACH H138 minilab instrument was used and calibrated using 3 buffer solutions that were supplied with the instrument; pH 4.01±0.02, 7.00±0.02, and 10.01±0.02. The probe was washed with deionised water between measuring samples. All pH meter readings were recorded at room temperature.

2.2.8. X-ray crystallography

All diffraction data were collected by Dr. Guy Clarkson using an Oxford Diffraction Gemini four-circle system with a Ruby CCD area detector. All structures were refined by full-matrix least squares against F^2 using SHELXL-97, and were solved by direct methods using SHELXS(TREF) with additional light atoms found by Fourier methods.[9] Hydrogen atoms were added at calculated positions and refined using a riding model. Anisotropic displacement parameters were used for all non-H atoms. H-atoms were given an isotropic displacement parameter equal to 1.2 (or 1.5 for methyl and NH H-atoms) times

the equivalent isotropic displacement parameter of the atom to which they are attached. The data were processed using Mercury 3.3.software.

2.2.9. High performance liquid chromatography (HPLC)

The HPLC analysis of complexes was carried out on an Agilent Technologies 1200 series HPLC instrument with a VWD and 100 µL loop, and an Agilent ZORBAX Eclipse Plus C18 250 x 4.6 mm column with a pore size of 5 µm was used. The mobile phase consisted of; (A) HPLC grade H_2O + 0.1 %TFA, and (B) HPLC grade MeCN + 0.1 % TFA. The following solvent gradient was used with a flow rate of 1 mL/min.

Time (min)	% (B)
0	10
30	80
40	80
41	10
45	10

Samples were typically prepared at 100 µM in H_2O (10% MeCN) using HPLC grade solvents and were filtered through Iso-Disc^{TM} filters (PTFE-4-4 4 mm x 0.45 µm). Sample volumes of 50µM were injected into the HPLC instrument and analysed at a detection wavelength of 254 nm with reference wavelengths set to 360 nm and 510 nm. Some samples also required a detection wavelength of 610 nm with a reference wavelength setting of 360 nm. The chromatograms were analysed using ChemStation software and any peaks greater than 10 mAU were integrated. Chromatograms were generated using MS Excel 2010.

2.2.10. Liquid chromatography-mass spectrometry (LC-MS)

A Bruker Amazon X+ instrument coupled with an Agilent Technologies 1200 series HPLC instrument was used. The same HPLC column, method and conditions were used as shown in Section 2.2.9. Sample injections were 20 µL and the mass spectrometer was operated in electrospray positive mode with a scan range of 50-2000 m/z.

2.2.11. Electrochemistry[10]

Electrochemical measurements were carried out by Dr. Nicolas P. E. Barry and Dr. Nichola Smith. All cyclic voltammogram (CV) experiments were carried out using a CH Instrument model 600D Electrochemical Analyzer/Workstation (Austin, TX). The electrochemical measurements were performed on compounds in an acetonitrile solution (1 mg/mL) containing tetrabutylammonium hexafluorophosphate (0.1 M) as supporting electrolyte. The solutions were degassed under nitrogen and cyclic voltammograms were typically scanned from -2.0 V to +2.0 V. In a typical experimental set up, a three-electrode system was used: a glassy carbon electrode as the working electrode, Ag/AgCl in 3.0 M KCl as the reference electrode (0.21 V versus NHE), and platinum wire as the counter electrode. For each electrode, CV was performed at a scan rate of 0.1 V/s.

2.2.12. Electron paramagnetic resonance (EPR)[11]

All EPR experiments were conducted by Dr. Carlos Sanchez-Cano. EPR spectra were recorded at room temperature on a Bruker EMX (X-band) spectrometer fitted with a cylindrical Tm110 mode cavity (Bruker 4103TM). Samples were contained in quartz capillary (I.D. 1.0 mm; O.D. 1.2 mm; Wilmad Labglass) sealed with T-BluTac®, and placed inside larger quartz tubes (O.D. 2.0 mm) to achieve easy and accurate positioning of the sample inside the resonator. Typical EPR spectrometer settings were; modulation amplitude 2.0 G, microwave power 0.63 mW, 1.0 x 10^5 receiver gain, conversion time 81.92 ms, time constant 81.92 ms, sweep width 200 G, and a repeated number of 10 X-scans with a resolution in Y of 5 or 9. Spin-trapping experiments of complexes were performed in aqueous solutions with an excess of spin trap (1 mM complex, 6 mM DEPMPO, 10 mM hydrogen peroxide, in 75 mM phosphate buffer, pH 7.4) in the presence or absence of ethanol. EPR spectra were analysed and simulated using the EASYSPIN software.[12]

2.2.13. Ion-coupled plasma optical emission spectroscopy (ICP-OES)[3,13]

ICP-OES analysis of osmium solutions were carried out on a Perkin Elmer (Optical Emission Spectrometer) Optima 5300 DV instrument. All samples and standards were prepared fresh on the day in doubly deionised water with distilled HNO_3 (3.2%). The osmium standard was diluted to the following concentrations for the calibration curve: 0, 25, 50, 100, 200, 400, 600, 800 and 1000 ppb. The samples were diluted by serial dilutions of typically 1 in 10 until their concentrations fitted within the calibration range and the % total dissolved

solids were below 0.2%. For samples in cell culture medium or containing sodium chloride, the standards were prepared containing the same amount of sodium chloride as the samples after dilution. Samples were made in triplicates and the optical emissions at 228.226 and 225.585 nm were detected and integrated.

2.2.14. Ion-coupled plasma mass spectrometry (ICP-MS)[3,13]

ICP-MS analysis of osmium solutions were carried out on an Agilent Technologies 7500 series ICP-MS instrument. All samples and standards were prepared fresh on the day in doubly deionised water with distilled HNO_3 (3.2%). The osmium standard was diluted to the following concentrations for the calibration curve: 0, 0.1, 0.2, 0.5, 1, 2, 4, 8, 10, 20,40, 60, 80 and 100 ppb. The samples were diluted by serial dilutions of typically 1 in 10 until their concentrations fitted within the calibration range and the % total dissolved solids were below 0.1%. For samples containing cell culture medium or sodium chloride, the standards were prepared containing the same amount of sodium chloride as the samples after dilution. Samples were made in triplicates and the isotope detected was ^{189}Os in no-gas mode.

2.3. Experimental methods

2.3.1. Cell culture

Cell cultures were grown in T-75 or T-175 culture flasks as adherent monolayers. The cells were passaged 2-3 times per week whenever confluence reached 80-90%, using 0.25% trypsin for A2780 or 0.25% trypsin/EDTA for all other cell lines. Cell cultures were stored in an incubator at 37 °C with a 5% CO_2 humidified atmosphere. Cells were used for experiments between 5-25 numbers of passages.

2.3.2. *In vitro* growth inhibition assay

IC_{50} values were determined by Dr. Isolda Romero-Canelón.[13] Approximately 5000 A2780 human ovarian cancer cells were seeded per well in 96-well plates. The cells were pre-incubated in drug-free media at 37 °C for 48 h before adding different concentrations of the complexes to be tested. Cells were exposed to complexes for 24 h at 37 °C. The supernatants were removed by suction and each well was washed with PBS. The cells were allowed to recover for 72 h in a drug-free medium at 37 °C. The SRB assay was used to determine cell viability. Absorbance measurements of the solubilised dye (on a BioRad iMark microplate reader using a 470 nm filter) allowed the determination of viable treated cells compared to untreated controls. IC_{50} values (the concentration at which 50% cell death occurs) were determined as triplicates of duplicates for each complex. ICP-MS was used to determine the osmium concentrations of the initial stock solutions of the complexes, and the IC_{50} value was corrected for ICP factor.

2.3.3. Determination of Partition coefficient (Log $P_{o/w}$)

The partition coefficient was determined using a modified version of the shake-flask method.[14,15] A 300 mM solution of NaI was prepared in doubly distilled water. Octanol-saturated water and water-saturated octanol were prepared by stirring octanol (100 mL) and 300 mM NaI solution (100 mL) together for 24 h, then separating the layers in a separating funnel. Complexes (0.5 – 3.0 mg) were dissolved in octanol-saturated water solution (3 mL) with plenty of stirring/shaking, then filtered. (NOTE: 300 mM NaI solution was used to supress the hydrolysis of complexes containing monodentate iodide ligands. For chlorido and bromido complexes, octanol-saturated water containing 300 mM NaCl or NaBr was prepared and used instead in the same manner). Saturated solutions of complexes in octanol-saturated water (1 mL) were combined with water-saturated octanol (1 mL), and placed on a Vibrax VXB basic shaker for 24 h at a speed of 500 g/min. After partition, the aqueous layers were collected for analysis, along with the aqueous solutions of complexes before partitioning. The osmium concentrations of samples were determined by either ICP-MS or ICP-OES, and the partition coefficient was calculated *via* the following equation; Log $P_{o/w}$ = Log ($[Os]_{octanol}/[Os]_{water}$). Experiments were performed in duplicates of triplicates in two independent experiments and at ambient temperature.

2.3.4. Cellular uptake

Cellular accumulation studies for osmium complexes were conducted by Dr. Isolda Romero-Canelón in A2780 ovarian cancer cells.[13] Approximately 4 x 10^6

cells were seeded into P100 Petri dishes. After 24 h of pre-incubation time in drug-free medium at 37°C in a 5% CO_2 humidified atmosphere, the complexes were added to give concentrations equal to $IC_{50}/3$ and 24 h of incubated drug exposure was allowed. Afterwards, the cells were treated with trypsin, counted, and the cell pellets were collected. The experiment also included a set of control samples with untreated cells. Cell pellets were digested overnight in 72% distilled nitric acid at 80 °C in Wheaton V-vials. The resulting solutions were diluted in a stabilisation solution of thiourea (10 mM) with ascorbic acid (0.1 g/L) in doubly deionised water, diluting the nitric acid content to 3.6%. Ascorbic acid acts as a reducing agent to reduce any OsO_4 that may have been generated during the digestion process, and thiourea acts as an osmium 'chelator'.[16] Osmium concentrations were determined by ICP-MS. Measurements were carried out in triplicate for each complex and cellular accumulation was calculated in units of ng Os /10^6 cells.

2.3.5. Cell cycle analysis

Cell cycle analyses were conducted by Dr. Isolda Romero-Canelón.[15] Briefly, 1.5 x 10^6 A2780 cells per well were seeded in a 6-well plate. Cells were pre-incubated in drug-free media at 37 °C for 24 h in a 5% CO_2 humidified atmosphere, then complexes were added to triplicates at 1x or 2x IC_{50} concentrations. This experiment included a set of control samples with untreated cells. After 24 h of incubated drug exposure the supernatants were removed by suction. The cells were washed with PBS and harvested using

trypsin. Cells were fixed with 70% ethanol and stored at -20 °C. DNA staining was achieved by re-suspending the cell pellets in PBS containing propidium iodide (PI) and RNase. Cell pellets were re-suspended in PBS before being analysed in a Becton Dickinson FACScan flow cytometer, using excitation of DNA-bound PI at 536 nm with emission at 617 nm. Data were processed using Flowjo software.

2.3.6. ROS experiments

Flow cytometry analysis of ROS/superoxide generation in A2780 cells caused by exposure to osmium complexes, was carried out using the Total ROS/Superoxide detection kit (Enzo-Life sciences) according to the supplier's instructions, by Dr. Isolda Romero-Canelón.[17] Briefly, 1.5 x 10^6 cells per well were seeded in a 6-well plate. Cells were pre-incubated in drug-free media at 37°C for 24 h in a 5% CO_2 humidified atmosphere, then complexes were added to triplicates at 1x and 2x IC_{50} concentrations. After 24 h of incubated drug exposure, the supernatants were removed by suction and cells were washed with PBS. Cells were harvested using trypsin and collected after centrifugation. This experiment included pyocyanin as a positive control and untreated cells as a negative control. Staining was achieved by re-suspending the cell pellets in buffer containing the orange/green fluorescent reagents. Cells were analysed on a Becton Dickinson FACScan Flow Cytometer using FL1 channel Ex/Em: 490/525 nm for the oxidative stress and FL2 channel Ex/Em: 550/620 nm for superoxide detection. Compensation adjustments were carried out using

pyocyanin-treated cells singly-stained with either fluorescent agent. Data were processed using Flowjo software.

2.3.7. Induction of Apoptosis

Flow cytometry analyses of apoptotic populations of A2780 cells caused by exposure to complexes were carried out using the Biovision Annexin V-FITC Apoptosis detection kit, according the suppliers instructions. These were carried out by Dr. Isolda Romero-Canelón.[13,17] Briefly, 1.5 x 10^6 cells per well were seeded in a 6-well plate. Cells were pre-incubated in drug-free media at 37°C for 24 h in a 5% CO_2 humidified atmosphere, then complexes were added to triplicates at 1x and 2x IC_{50} concentrations. After 24 h of incubated drug exposure, the supernatants were removed by suction and cells were washed with PBS. Cells were harvested using trypsin and collected after centrifugation. This experiment included a control with untreated cells. The cells were stained with Annexin V-FITC and PI and analysed using a Becton Dickinson FACScan flow cytometer, running Cell Quest software (20 000 events were collected from each sample).

2.4. Radiolabelling studies at Kings College London[18]

2.4.1. Iodine-131

Radiolabelling studies of osmium complexes required the use of sodium iodide-131. Iodine-131 is a ‘neutron rich’ 78-neutron nuclide that decays with a half-life

of 8.02 days into a stable xenon-131 nuclide. Its decay involves a two-step process involving a β^- emission, rapidly followed by a γ emission. Iodine-131 nuclides expend 971 keV of decay energy by a β^- emission of 606 keV (89% abundance), followed by a γ emission of 364 keV (82% abundance).[19] The decay process is shown in Figure. 2.1. One disintegration involves the conversion of one neutron into a proton, an electron and an anti-neutrino. As the nuclear excited state of the newly formed xenon-131 nuclide relaxes, a γ-ray is emitted. For the purposes of these studies, the method of detection involved γ-ray detection throughout because γ-emissions are more penetrating and easier to detect than β^- emissions.

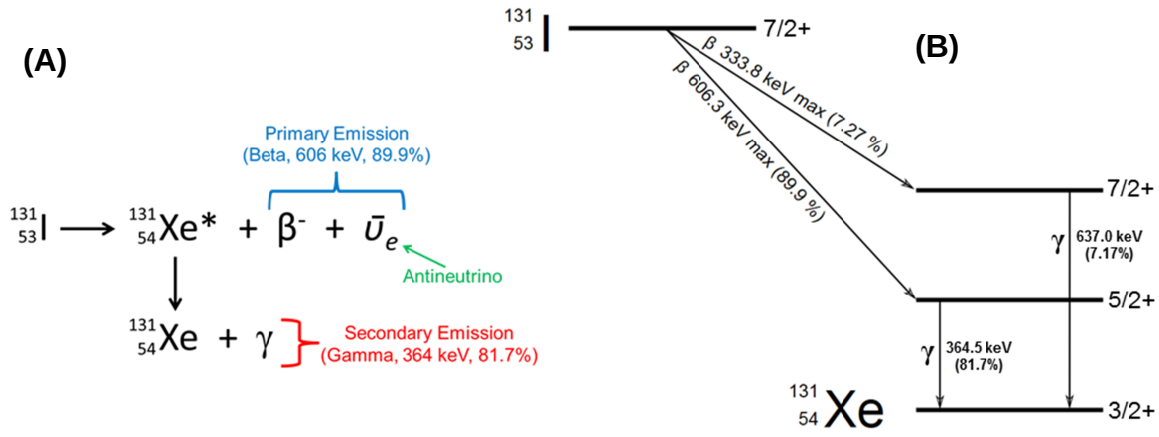

Figure 2.1. (A) Reaction scheme for the decay of an iodine-131 nuclide. (B) Iodine-131 decay schematic showing the nuclear excited states.

2.4.2. Laboratories and synthesis apparatus

All research involving the radioactive iodine-131 isotope was carried out at King's College London (KCL) at the Division of Imaging Sciences and

Biomedical Engineering in St Thomas's Hospital. Work was carried out in accordance with the Ionising Radiation Regulations 1999 (IRR99) and Local Rules, which required prior health and safety training. All manual handling of iodine-131 stock solutions, radio-chemical synthesis and reactions, were carried out in a radioactive work station inside a fume-hood. A typical work station consists of lead bricks walls and a 1-inch thick leaded glass safety screen as shown in Figure 2.2. Dosimeter badges and finger rings were worn at all times in the labs to monitor radioactive exposure. Radio-chemical syntheses were carried out 2 mL plastic sealable tubes and placed on a mechanical shaker/heater. All radioactive waste materials were monitored and disposed of appropriately according to local rules. Samples containing iodine-131 were stored in lead containers and samples in use were kept inside radioactivity work stations where ever possible to minimise exposure.

Figure 2.2. A photograph of a radioactivity safety workstation

2.4.3. Instrumentation

2.4.3.1. Radio-TLC[20]

TLC-sheets (12 x 100 mm, silica gel 60 F254, layer thickness 0.2 mm) were used. Plates were spotted with 3 µL of reaction mixture at the baseline and placed inside sealed plastic falcon tubes with eluent H_2O:MeOH (1:1) (700 µL). The solvent front was allowed to travel 90 mm from the baseline. Plates were scanned on a LabLogic MINI-SCAN TLC scanner with a LabLogic B-FC-3200 gamma probe at a scan rate of 0.25 mm/s. TLC chromatograms were analysed and integrated using Laura-TLC version 4.0.2.75 software.

2.4.3.2. Radio-HPLC[18,21]

An Agilent 1200 series instrument with a VWD (wavelength of detection 254 nm), a 200 µL loop, and an Agilent ZORBAX Eclipse Plus C_{18} 250 x 4.6 mm column with a pore size of 5 µm was used. The HPLC instrument was fitted with either a raytest Gabi Star gamma detector with a raytest NaI-detector 1x1`` Std gamma probe, or a LabLogic FLOW-COUNT gamma detector with a LabLogic B-FC-3200 gamma probe. The HPLC instrument was specially equipped with lead shielding. The mobile phase consisted of; (A) doubly deionised H_2O + 0.1 % TFA, and (B) HPLC grade MeCN + 0.1 % TFA. The HPLC gradient used was the same as shown in Section **2.2.9**. Non-radioactive samples were filtered, however, it was not possible to filter radioactive samples due to safety concerns. Samples were injected into the loop at volumes of up to 200 µL. HPLC chromatograms were analysed and integrated using GINA Star version

5.8, or Laura-HPLC version 4.0.2.75 software. All data were generated using MS Excel 2010. Preparative radio-HPLC was also used under the same conditions.

2.4.3.3. Gamma counter

Samples of low level radioactivity (>15 KBq) were analysed using a LKB Wallac 1282 Compugamma universal gamma counter with EdenTerm V1.21 software. The data were processed using MS Excel 2010.

2.4.3.4. Electronic cell counting

Cell counting was carried out using an Invitrogen countess automated cell counter with plastic disposable Invitrogen^{TM} hemocytometers, after staining cells with PI. The number of live cells and % cell viability were recorded.

2.4.4. Methods

2.4.4.1. Human blood serum stability assays

Stability assays were setup for both non-carrier added and carrier added experiments (NOTE: Carrier added conditions are where the non-radiolabelled complex is also added with the radio-tracer at a concentration comparable to the IC_{50} value). Non-carrier added; human blood serum (900 µL) was combined with radio-tracer complex (100 µL, ~500 KBq). Carrier added; human blood

serum (900 µL) was combined with radio-tracer complex (50 µL, ~250 KBq), and a solution of the non-radiolabelled carrier complex (50 µL, 5 µM), giving a carrier concentration of 0.25 µM. Samples were prepared in 2 mL plastic sealable disposable tubes, incubated at 37 ºC with 300 rpm stirring for 24 h, and analysed after 1 h and 24 h by radio-HPLC. The samples were firstly treated with 1 part MeCN and centrifuged for 5 min (>10000 rpm) to precipitate serum proteins before injection into the HPLC instrument.

2.4.4.2. Serum protein accumulation experiment

Samples were prepared in the same way as in Section **2.4.4.1** and incubated for 24 h. One part MeCN was added to the samples before centrifuging for 5 min (>10000 rpm) to produce serum protein pellets. The supernatants were collected into plastic test tubes, and the pellets were digested in 1 M NaOH and collected into separate tubes. The fractions were analysed using the gamma counter and the % iodine uptake into serum proteins was calculated.

2.4.4.3. *In vitro* stability assays

Approximately 1 x 10^6 MCF-7 cells were seeded per well in a 24-well plate. A well was assigned for each time point measurement, then pre-incubated in drug free media for 24 h in a 5% CO_2 humidified atmosphere. The supernatants were removed by suction and fresh media was added: non-carrier added experiments; 900 µL of medium + 100 µL of radio-tracer complex (~500KBq),

carrier added experiments; 900 µL of medium dosed with non-radiolabelled carrier complex + 100 µL tracer (~500 KBq), giving a carrier concentration of IC_{50}/3. A second 24-well plate was prepared in exactly the same manner for the control experiments, where no cells were added (Figure 2.3). The well plates were incubated for 24 h and supernatants from wells were removed at different time points: 2, 4, 8 and 24 h. Supernatants were combined with 1 part MeCN and centrifuged for 5 min (>10000 rpm) to remove cell culture proteins/dead cells, then analysed by radio-HPLC.

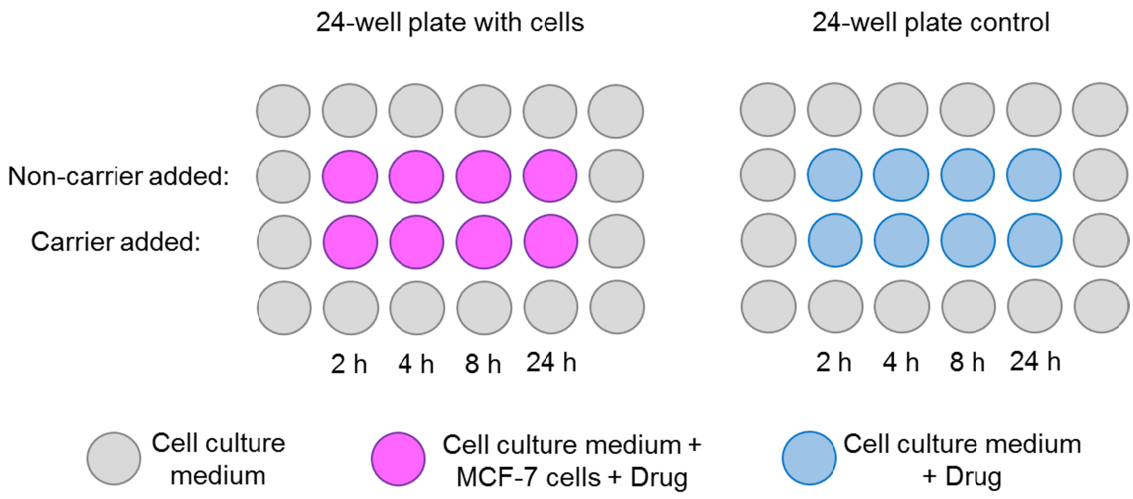

Figure 2.3. Diagram of the set-up of well plates for the *in vitro* stability assay.

2.4.4.4. Cellular accumulation assays[21]

Approximately 1 x 10^6 MCF-7 cells were seeded into borosilicate glass culture tubes (12 x 75 mm) with 1 mL cell culture medium, and radio-tracer complex (30 µL, 15-17 KBq). Control experiments were carried out in the same way but no cells were seeded. The samples were incubated for certain time periods (5, 10, 30, 60, 180, 360 min) in quadruplets. The tubes were cooled in ice/water,

centrifuged at 10 ºC/1000 rpm for 3 min, and the supernatants were removed by pipette and collected. The cells were then washed twice with refrigerated PBS solution (1 mL) and the washings were combined with the supernatant fractions. The cell pellets were digested in NaOH solution (1 M, 1 mL) at 37 °C for 30 min and collected separately. The tubes were washed with twice with PBS solution (1 mL) and residues were combined with digested cell fractions. Control experiments were carried out in the same manner. The CPM of the supernatant and digested cell fractions were measured using the gamma counter. The number of cells in each digested cell sample was measured using a cell calibration curve in Chapter 5, Section **5.2.3.2**. The data were processed using MS excel 2010 to obtain the % cell uptake of I-131 /10^6 cells.

2.5. References

(1) Stahl, S.; Werner, H. *Organometallics* **1990**, *9*, 1876.

(2) Clayton, H. S.; Makhubela, B. C. E.; Su, H.; Smith, G. S.; Moss, J. R. *Polyhedron* **2009**, *28*, 1511.

(3) Fu, Y. Ph.D Thesis, University of Warwick, 2011.

(4) Tönnemann, J.; Risse, J.; Grote, Z.; Scopelliti, R.; Severin, K. *Eur. J. Inorg. Chem.* **2013**, *2013*, 4558.

(5) Cabeza, J. A.; Maitlis, P. M. *J. Chem. Soc., Dalton Trans.* **1985**, *3*, 573.

(6) Peacock, A. F. A.; Habtemariam, A.; Fernández, R.; Walland, V.; Fabbiani, F. P. A.; Parsons, S.; Aird, R. E.; Jodrell, D. I.; Sadler, P. J. *J. Am. Chem. Soc.* **2006**, *128*, 1739.

(7) Lindow, D. F.; Cortez, C. N.; Harvey, R. G. *J. Am. Chem. Soc.* **1972**, *94*, 5406.

(8) Gottlieb, H. E.; Kotlyar, V.; Nudelman, A. *J. Org. Chem.* **1997**, *62*, 7512.

(9) Sheldrick, G. *Acta Crystallogr. Sect. A* **1990**, *46*, 467.

(10) Liu, Z.; Romero-Canelón, I.; Qamar, B.; Hearn, J. M.; Habtemariam, A.; Barry, N. P. E.; Pizarro, A. M.; Clarkson, G. J.; Sadler, P. J. *Angew. Chem. Int. Ed.* **2014**, *53*, 3941.

(11) Butler, J. S. Ph.D Thesis, University of Warwick, 2014.

(12) Stoll, S.; Schweiger, A. *J. Magn. Reson.* **2006**, *178*, 42.

(13) Romero-Canelón, I.; Salassa, L.; Sadler, P. J. *J. Med. Chem.* **2013**, *56*, 1291.

(14) Henczi, M.; Nagy, J.; Weaver, D. F. *J. Liq. Chromatogr.* **1994**, *17*, 2605.

(15) van Rijt, S. H.; Romero-Canelon, I.; Fu, Y.; Shnyder, S. D.; Sadler, P. J. *Metallomics* **2014**, *6*, 1014.

(16) Venzago, C.; Popp, M.; Kovac, J.; Kunkel, A. *J. Anal. At. Spectrom.* **2013**, *28*, 1125.

(17) Romero-Canelón, I.; Mos, M.; Sadler, P. J. *J. Med. Chem.* **2015**, *58*, 7874.

(18) Ma, M. T.; Meszaros, L. K.; Paterson, B. M.; Berry, D. J.; Cooper, M. S.; Ma, Y.; Hider, R. C.; Blower, P. J. *Dalton Trans.* **2015**, *44*, 4884.

(19) http://www.oseh.umich.edu/radiation/I131.shtml

(20) Torres Martin de Rosales, R.; Tavaré, R.; Paul, R. L.; Jauregui-Osoro, M.; Protti, A.; Glaria, A.; Varma, G.; Szanda, I.; Blower, P. J. *Angew. Chem. Int. Ed.* **2011**, *50*, 5509.

(21) Chiotellis, A.; Mu, L.; Müller, A.; Selivanova, S. V.; Keller, C.; Schibli, R.; Krämer, S. D.; Ametamey, S. M. *Eur. J. Med. Chem.* **2013**, *70*, 768.

Chapter 3

Osmium(II) Arene Complexes of Phenylazobenzothiazoles

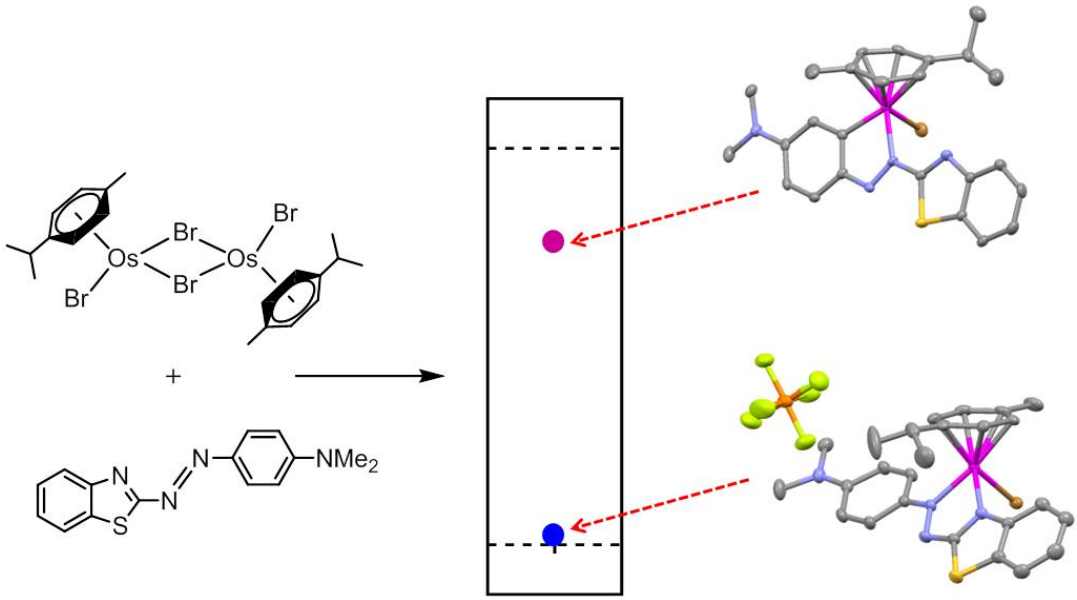

3.1. Introduction

Os(II) arene complexes with *N,N*- chelating phenylazopyridine (AZPY) ligands have been previously reported by the Sadler group.[1,2] Such complexes show very promising anti-cancer properties with IC_{50} values against various cancer cell lines in the nano-molar range, and novel mechanisms of action. Following the success of these complexes, there is particular interest to explore Os(II) complexes of alternative azo-ligands in order to expand our library and gain more understanding of the properties of novel anti-cancer complexes. One group of azo-ligands of potential interest are phenylazobenzothiazoles (AZBTZs). Interestingly, AZBTZs have strong applications in the field of dyes and pigments, owing to their intense red colourations.[3] They can also be utilised as probes for *in vivo* radio-imaging of neurofibrillary tangles in Alzheimer's disease brains, as they show promising selective binding towards β-amyloid peptides and hyper phosphorylated tau proteins associated with Alzheimer's disease.[4]

AZBTZs are analogous to AZPY ligands, whereby the pyridine is substituted by a benzothiazole moiety (Figure 3.1). Benzothiazole is a bicyclic ring system consisting of a benzene ring fused to a 5-membered 1,3-thiazole ring. Because of their pronounced biological and pharmacological activities they are of great interest for medicinal applications. Numerous benzothiazole compounds have shown promising anticancer activity and have been reported frequently in the Journal of Medicinal Chemistry,[5-9] making benzothiazole a desirable functional group to include in our study of osmium anti-cancer complexes. Furthermore, there are also studies highlighting organometallic complexes bearing

benzothiazole groups with anti-proliferative activities,[10,11] and DNA binding capabilities.[12] Most notable are the Os(II) and Ru(II) complexes reported by Keppler *et al* with benzothiazole and benzimidazole pharmacophoric protein kinase inhibitor sites.[11] AZBTZs exhibit several coordination sites for which binding to a metal centre is possible, and within this chapter we explore the binding of AZBTZs in Os(II) arene complexes.

Figure 3.1. (A) A phenylazopyridine ligand with pyridine moiety, compared to (B) a phenylazobenzothiazole ligand with a benzothiazole moiety.

3.2. Experimental

3.2.1. Materials

Osmium dimers ($[Os(\eta^6\text{-}p\text{-cym})X_2]_2$ where X= Cl, Br or I) were prepared as shown in Chapter 2, Section **2.1.2**. *N,N*-Dimethylaniline, 3,5-dimethylaniline, 2-aminobenzothiazole, sodium nitrite, sulphuric acid (>95%) and glacial acetic acid were purchased from Fisher Scientific. All organic solvents were purchased from commercial suppliers and used as received. Deionised water was prepared as described in Chapter 2, Section **2.1.1.1**. Deuterated solvents used for NMR spectroscopy were purchased from Cambridge Isotope Laboratories Inc. and Sigma Aldrich.

3.2.2. Synthesis

3.2.2.1. Synthesis of AZBTZ ligands

4-(2-Benzothiazolylazo)-*N,N*-dimethylaniline (L). 2-Aminobenzothiazole (500.0 mg, 3.33 mmol) was mixed with glacial acetic acid (20 mL) and cooled to 0 °C in a water/ice bath. Sulphuric acid (>95%, 7 mL) was then added. A solution of $NaNO_2$ (252.7 mg, 3.66 mmol) in deionised water (10 mL) was added drop-wise to the stirring mixture, and it instantaneously turned yellow/orange. The mixture was stirred for 2 h at 0°C. An ice-cold solution of *N,N*-dimethylaniline (425 µL, 3.33 mmol) in MeOH (34 mL) was added drop-wise and the mixture turned dark purple. The mixture was stirred for a further 18 h, allowing it to warm to ambient temperature, then was combined with water (200 mL) and DCM (100 mL), and the layers were separated. The aqueous layer was washed with DCM (2 x 50 mL), and the combined DCM extracts were washed with water (2 x 50 mL), dried over $MgSO_4$, filtered, and the solvent was removed under reduced pressure yielding a dark precipitate. The crude product was re-crystallised from a minimum amount of chloroform, giving a dark green precipitate. The product was collected by filtration, washed with ice-cold Et_2O (2x 5 mL), and dried overnight in a vacuum desiccator. Yield: 585.6 mg, (62%). ^{1}H NMR (400 MHz, $CDCl_3$): δ 8.07 (d, 1H, J = 7.8 Hz), 8.00 (d, 2H, J = 9.1 Hz), 7.84 (d, 1H, J = 7.8 Hz), 7.47-7.46 (m, 1H), 7.38-7.37 (m, 1H), 6.77 (d, 2H, J = 9.4 Hz), 3.17 (s, 6H). ESI-MS calculated for $C_{15}H_{14}N_4S + H^+$: m/z 283.1. Found: 283.1. CHN analysis: Found: C, 63.22%; H, 4.92%; N, 19.67%. Calculated for $C_{15}H_{14}N_4S$: C, 63.81%; H, 5.00%; N, 19.84%.

***para*-(2-Benzothiazolylazo)-3,5-dimethylaniline (L*).** The synthesis follows the same preparation as above, where 3,5-dimethylaniline (457 µL, 3.66 mmol) was used instead of *N,N*-dimethylaniline. The crude product was purified *via* flash column chromatography (SiO_2, 1:2 acetone:n-hexane, R_f = 0.33). Due to low solubility of the crude product in the mobile phase, it was only possible to purify a portion of the crude product. The collected fractions containing product were combined and the solvent was removed under reduced pressure to yield a dark red precipitate, which was dried overnight in a vacuum desiccator. Yield: 53.2 mg. ^{1}H NMR (400 MHz, $CDCl_3$): δ 8.08 (d, 1H, J = 8.0 Hz), 7.81 (d, 1H, J = 8.0 Hz), 7.46-7.45 (m, 1H), 7.37-7.36 (m, 1H), 6.43 (s, 2H), 4.33 (s. br, 2H), 2.64 (s, 6H). ESI-MS calculated for $C_{15}H_{14}N_4S$ + H^+: m/z 283.1. Found: 282.8.CHN analysis: Found: C, 63.35%; H, 5.00%; N, 19.60%. Calculated for $C_{15}H_{14}N_4S$: C, 63.81%; H, 5.00%; N, 19.84%.

3.2.2.2. Synthesis of Os(II) arene AZBTZ complexes

[Os(η^6-*p*-cym)(*N,N*-AZBTZ-NMe$_2$)Cl]PF$_6$ (1a). [Os(η^6-*p*-cym)Cl$_2$]$_2$ (50.0 mg, 63.2 µmol) and 4-(2-benzothiazolylazo)-*N,N*-dimethylaniline (37.5 mg, 132.8 µmol) were dissolved in EtOH (20 mL). The mixture was stirred at 50 °C for 2 h and the colour turned dark blue. The mixture was left to stir for 18 h at ambient temperature and NH_4PF_6 (103.1 mg, 0.63 mmol) was added. The volume was reduced under reduced pressure to ~2 mL, and the mixture was placed in the freezer overnight. The resulting dark blue precipitate was collected by filtration. The precipitate was dissolved in chloroform (10 mL), stirred for 1 h, and filtered.

The filtrate was collected and the solvent was removed under reduced pressure. The resulting dark blue precipitate was re-crystallised from a minimum amount of EtOH. The product was collected by filtration and washed with ice-cold EtOH (2 x 1 mL) and Et_2O (2 x 5 mL). The product was dried overnight in a vacuum desiccator. Yield: 44.9 mg, (45%). ^{1}H NMR (400 MHz, CD_3OD): δ 8.28-8.27 (m, 2H), 8.15-8.14 (m, 2H), 7.83-7.82 (m, 1H), 7.75-7.74 (m, 1H), 7.06-7.05 (m, 2H), 6.59-6.58 (m, 1H), 6.55-6.54 (m, 1H), 6.25-6.24 (m, 1H), 6.21-6.20 (m, 1H), 3.53 (s, 6H), 2.48 (s, 3H), 2.18 (sept., 1H, J = 6.9 Hz), 0.87 (d, 3H, J = 6.9 Hz), 0.76 (d, 3H, J = 6.9 Hz). ESI-MS calculated for $C_{25}H_{28}ClN_4OsS^+$: m/z 643.1. Found: 643.0. CHN analysis: Found: C, 37.67%; H, 3.42%; N, 6.91%. Calculated for $C_{25}H_{28}ClF_6N_4OsPS$: C, 38.14%; H, 3.59%; N, 7.12%.

Os(η^6-*p*-cym)(*N,C*-AZBTZ-NMe$_2$)Cl (1b). [Os(η^6-*p*-cym)Cl$_2$]$_2$ (50.0 mg, 63.2 μmol) and 4-(2-benzothiazolylazo)-*N,N*-dimethylaniline (37.5 mg, 132.8 μmol) were dissolved in EtOH (20 mL). The mixture was stirred at 50 °C for 2 h and the colour turned dark blue. The mixture was left to stir for 18 h at ambient temperature, then the solvent was removed under reduced pressure. The product was purified *via* flash column chromatography (SiO_2, 50:1 DCM:MeOH, R_f = 0.34). The collected fractions containing product were combined and the solvent was removed under reduced pressure to give a dark purple precipitate. The precipitate was recrystallized from a minimum amount of EtOH. The product was collected by filtration and washed with ice-cold EtOH (2 x 1 mL) and Et_2O (2 x 5 mL), then dried in a vacuum desiccator overnight. Yield: 14.9 mg, (18%). ^{1}H NMR (400 MHz, $(CD_3)_2CO$): δ 8.10 (m, 1H), 8.08 (d, 1H, J = 9.4

Hz), 7.96-7.95 (m, 1H), 7.60-7.59 (m, 2H), 7.47-7.46 (m, 1H), 6.94 (dd, 1H, J = 9.4, 2.7 Hz), 6.24-6.23 (m, 1H), 6.14-6.13 (m, 1H), 6.03-6.02 (m, 1H), 5.46-5.45 (m, 1H), 3.45 (s, 6H), 2.32 (sept., 1H, J = 6.9 Hz), 2.25 (s, 3H), 1.04 (d, 3H, J = 6.9 Hz), 0.79 (d, 3H, J = 6.9 Hz). ESI-MS calculated for $C_{25}H_{27}ClN_4OsS + H^+$: m/z 643.1. Found: 643.0. CHN analysis: Found: C, 46.67%; H, 4.39%; N, 8.34%. Calculated for $C_{25}H_{27}ClN_4OsS$: C, 46.83%; H, 4.24%; N, 8.74%.

[Os(η^6-*p*-cym)(*N,N*-AZBTZ-NMe$_2$)Br]PF$_6$ (2a) and Os(η^6-*p*-cym)(*N,C*-AZBTZ-NMe$_2$)Br (2b). [Os(η^6-*p*-cym)Br$_2$]$_2$ (70.0 mg, 72.3 μmol) and 4-(2-benzothiazolylazo)-*N,N*-dimethylaniline (40.8 mg, 144.6 μmol) were dissolved in EtOH (20 mL). The mixture was stirred at 50 °C for 2 h and the colour turned dark blue/purple. The mixture was left to stir for 18 h at ambient temperature and NH_4PF_6 (103.1 mg, 0.63 mmol) was added. The solvent was removed under reduced pressure and the dark blue residue was re-dissolved in chloroform (20 mL) and stirred for 1 h. The mixture was filtered giving a precipitate predominantly containing **2b**, and filtrate predominantly containing **2a**.

2a. The filtrate was concentrated under reduced pressure to ~1-2 mL, combined with a small amount of Et_2O (<1 mL), and placed in the freezer overnight. The resulting dark blue precipitate was collected by filtration, washed with ice-cold EtOH (1 mL) and Et_2O (2 x 5 mL), and dried overnight in a vacuum desiccator. Yield: 9.9 mg, (8%). ^{1}H NMR (400 MHz, $(CD_3)_2CO$): δ 8.36 (d, 2H, J = 9.6 Hz), 8.23-8.22 (m, 2H), 7.80-7.79 (m, 2H), 7.07 (d, 2H, J = 9.7 Hz), 6.80-6.79 (m, 1H), 6.75-6.74 (m, 1H), 6.46-6.45 (m, 1H), 6.41-6.40 (m, 1H), 3.58 (s, 6H), 2.66 (s, 3H), 2.26 (sept., 1H, J = 6.9 Hz), 0.94 (d, 3H, J = 6.9 Hz), 0.85 (d, 3H, J =

6.9 Hz). ESI-MS calculated for $C_{25}H_{28}BrN_4OsS^+$: m/z 687.1. Found: 687.1. No CHN analysis due to low yield and impure sample.

2b. The precipitate was dissolved in a minimum amount of MeOH and purified *via* flash column chromatography (SiO_2, MeOH, R_f = 0.74). The selected fractions containing product were combined and the solvent was removed under reduced pressure to give a dark purple solid, which was dried overnight in a vacuum desiccator. Yield: 20.2 mg, (20%). ^{1}H NMR (400 MHz, $(CD_3)_2SO$): δ 7.98-7.91 (m, 1H), 7.96 (d, 1H, J = 9.3 Hz), 7.48-7.47 (m, 1H), 7.43 (d, 1H, J = 2.6 Hz), 7.35-7.34 (m, 1H), 6.85 (dd, 1H, J = 9.3, 2.6 Hz), 6.15-6.14 (m, 2H), 5.81-5.80 (m, 1H), 5.49-5.48 (m, 1H), 3.34 (s, 6H, *hidden under water peak*), 2.31 (sept., 1H, J = 6.9 Hz), 2.16 (s, 3H), 0.99 (d, 3H, J = 6.9 Hz), 0.70 (d, 3H, J = 6.9 Hz). ESI-MS calculated for $C_{25}H_{27}BrN_4OsS + H^+$ and $C_{25}H_{27}BrN_4OsS + Na^+$: m/z 687.1 and 709.1. Found: 687.0 and 708.9. CHN analysis: Found: C, 42.68%; H, 3.84%; N, 8.00 %. Calculated for $C_{25}H_{27}BrN_4OsS + ⅓CH_2Cl_2$: C, 42.61%; H, 3.91%; N, 7.85%.

Os(η^6-*p*-cym)(*N,C*-AZBTZ-NMe$_2$)I (3b). $[Os(\eta^6\text{-}p\text{-cym})I_2]_2$ (50.0 mg, 43.2 μmol) and 4-(2-benzothiazolylazo)-*N,N*-dimethylaniline (24.4 mg, 86.5 μmol) were dissolved in EtOH (20 mL). The mixture was stirred at 50 °C for 2 h and the colour turned dark blue/purple. The mixture was left to stir for 18 h at ambient temperature, then the volume was reduced under reduced pressure to ~2 mL. The mixture was placed in the freezer overnight resulting in a dark brown precipitate, which was collected by filtration and washed with ice-cold EtOH (2 x 1 mL) and Et_2O (2 x 5 mL). The product was dried overnight in a vacuum desiccator. Yield: 48.6 mg, (77%). ^{1}H NMR (700 MHz, $CDCl_3$): δ 8.11 (d, 1H, J

= 9.2 Hz), 7.93 (d, 1H, J = 8.0 Hz), 7.76 (d, 1H, J = 7.9 Hz), 7.42-7.41 (m, 1H), 7.30-7.29 (m, 1H), 7.27 (d, 1H, J = 2.5 Hz), 6.71 (dd, 1H, J = 9.2, 2.5 Hz), 5.99-5.98 (m, 1H), 5.87-5.86 (m, 1H), 5.67-5.66 (m, 1H), 5.36-5.35 (m, 1H), 3.32 (s, 6H), 2.58 (sept., 1H, J = 6.9 Hz), 2.41 (s, 3H), 1.13 (d, 3H, 6.9 Hz), 0.83 (d, 3H, 6.9 Hz). ESI-MS calculated for $C_{25}H_{27}IN_4OsS + H^+$ and $C_{25}H_{27}IN_4OsS + Na^+$: m/z 735.1 and 757.1. Found: 735.0 and 756.9. CHN analysis: Found: C, 38.75%; H, 3.39%; N, 7.17%. Calculated for $C_{25}H_{27}IN_4OsS + ½CHCl_3$: C, 38.65%; H, 3.50%; N, 7.07%.

[Os(η^6-*p*-cym)(*N,N*-AZBTZ*-NH$_2$)Cl]PF$_6$ (4). [Os(η^6-*p*-cym)Cl$_2$]$_2$ (30.0 mg, 37.9 µmol) was stirred in EtOH (10 mL), and a solution of *para*-(2-benzothiazolylazo)-3,5-dimethylaniline (22.5 mg, 79.7 µmol) in EtOH (5 mL) was added drop-wise to the stirring mixture. The mixture was stirred for 2 h at 50 °C and the colour turned dark blue/purple. The mixture was left to stir for 18 h at ambient temperature, then NH_4PF_6 (61.8 mg, 0.38 mmol) was added. The mixture was concentrated under reduced pressure and placed in the freezer overnight. The resulting dark purple precipitate was collected by filtration and washed with ice-cold EtOH (2 x 1 mL) and Et_2O (2 x 5 mL). The product was dried overnight in a vacuum desiccator. Yield: 41.0 mg (69%). ^{1}H NMR (400 MHz, $CDCl_3$): δ 8.22 (d, 1H, J = 8.3 Hz), 8.06-7.99 (m, 2H), 7.92-7.91 (m, 1H), 6.90-6.89 (m, 1H), 6.60-6.59 (m, 1H), 6.48-6.47 (m, 1H), 6.05-6.04 (m, 1H), 5.90-5.89 (m, 1H), 5.65-5.64 (m, 1H), 4.20 (s. br, 2H), 2.49 (s, 3H), 2.34 (s, 3H), 2.28 (sept., 1H, J = 6.9 Hz), 1.92 (s, 3H), 1.11 (d, 3H, J = 6.9 Hz), 0.91 (d, 3H, J = 6.9 Hz). ESI-MS calculated for $C_{25}H_{28}ClN_4OsS^+$: m/z 643.1. Found: 643.2.

CHN analysis: Found: C, 38.14%; H, 3.59%; N, 7.12%. Calculated for $C_{25}H_{28}F_6ClN_4OsPS$: C, 37.54%; H, 3.46%; N, 7.13%.

[Os(η^6-*p*-cym)(*N,N*-AZBTZ*-NH$_2$)I]PF$_6$ (5). [Os(η^6-*p*-cym)I$_2$]$_2$ (23.1 mg, 20.0 µmol) was stirred in EtOH (10 mL), and a solution of *para*-(2-benzothiazolylazo)-3,5-dimethylaniline (11.3 mg, 39.9 µmol) in EtOH (5 mL) was added drop-wise to the stirring mixture. The mixture was stirred for 2 h at 50 °C and the colour turned dark blue/purple. The mixture was left to stir for 18 h at ambient temperature, then NH_4PF_6 (32.6 mg, 0.20 mmol) was added. The mixture was concentrated under reduced pressure and placed in the freezer overnight. The resulting dark purple precipitate was collected by filtration and washed with ice-cold EtOH (2 x 1 mL) and Et_2O (2 x 5 mL). The product was dried overnight in a vacuum desiccator. Yield: 20.4 mg, (58%). ^{1}H NMR (400 MHz, $CDCl_3$): δ 8.22 (d, 1H, J = 8.3 Hz), 8.02-7.96 (m, 2H), 7.89-7.88 (m, 1H), 6.82-6.81 (m, 1H), 6.58-6.57 (m, 1H), 6.48-6.47 (m, 1H,), 6.08-6.07 (m, 1H), 5.94-5.93 (m, 1H), 5.74-5.73 (m, 1H), 4.13 (s. br, 2H), 2.69 (s, 3H), 2.62 (s, 3H), 2.53 (sept., 1H, J = 6.9 Hz), 1.86 (s, 3H), 1.05 (d, 3H, J = 6.9 Hz), 1.01 (d, 3H, J = 6.9 Hz). ESI-MS calculated for $C_{25}H_{28}IN_4OsS^+$: m/z 735.1. Found: 735.0. CHN analysis: Found: C, 31.26%; H, 2.93%; N, 6.14%. Calculated for $C_{25}H_{28}F_6IN_4OsPS + CHCl_3$: C, 31.29%; H, 2.93%; N, 5.61%.

3.2.3. Growing single crystals for X-ray crystallography

Single crystals **1a** and **2b** crystals were obtained by diffusion of n-hexane into an acetone solution at ambient temperature. Crystals of **2a** were obtained by

slow evaporation of a MeOH solution at ambient temperature. Crystals of **3a** were obtained by slow evaporation of a chloroform solution at ambient temperature.

3.2.4. 1D ^{1}H sel-NOE NMR

A solution of complex **5** was prepared in $CDCl_3$. A 1D ^{1}H sel-NOE experiment was conducted using a 600 mHz instrument, targeting the ^{1}H resonance at 6.84 ppm. The ^{1}H NMR spectrum was then superimposed to view the ^{1}H resonances that are in close proximity through space to the resonance at 6.84 ppm. (The greater the intensity of the NOE peak, the closer the distance in space).

3.2.5. ^{1}H NMR kinetic experiment

Solutions of complex **2b** (1.13 mg, 1.648 μmol) in methanol-d_4 (700 μL), and 0.889 M HBr in methanol-d_4 were prepared. HBr (9.27 μL, 5 mol. equiv.) was combined with the complex and the ^{1}H NMR spectrum was collected every 30 min for 16 h at 25 °C on a 400 MHz NMR instrument.

3.2.6. Aqueous solution chemistry

Solutions of complexes **1a** and **1b** were prepared in H_2O:MeOH (1:1, v/v) at concentrations of 50 μM. The UV-Vis spectrum was measured at 25 °C every 1

h for 24 h. Also carried out was a 50 μM solution of complex **1a** in H_2O:MeOH (1:1, v/v) with 100 mM NaCl.

3.2.7. Calculation of partial charges

The Mulliken partial charges of complex **2b** were calculated by Dr. Nicolas P. E. Barry from the optimised gas phase geometry, using Gaussian 03 program and employing the DFT method and PBE1PBE functionals. A LanL2DZ basis set and effective core potential was used for the osmium atom, and 6-31G**+ basis set was used for all other atoms.

3.3. Results

3.3.1. Synthesis of AZBTZ ligands

The bidentate phenylazobenzothiazole ligand, AZBTZ-NMe_2 (**L**), was synthesised *via* a diazotisation coupling reaction[3] (Scheme 3.1). Step (a): nitrosation of the primary amine in 2-aminobenzothiazole occurs when the nitrosonium cation is generated *in situ* from sodium nitrite and sulfuric acid, leading to the formation of a reactive diazonium salt intermediate. Step (b): on addition of *N,N*-dimethylaniline, the electrophilic diazonium salt reacts at the *para*- position of the aniline ring to form the highly coloured ligand, **L**. Reactivity at the *ortho*- position of the ring is blocked by the presence of tertiary amine methyl groups. Similarly, a second ligand, AZBTZ*-NH_2 (**L***), was synthesised *via* the same reaction. Step (c): when *3,5*-dimethylaniline is added to the

diazonium salt, there are no methyl groups situated on the amine group to prevent electrophilic addition occurring at the *ortho*-position. An *ortho*-substituated impurity was found at 18% by ^{1}H NMR and the product was purified by SiO_2 column chromatography. Full mechanistic details of the diazotisation coupling reaction are shown in Scheme 3.2.

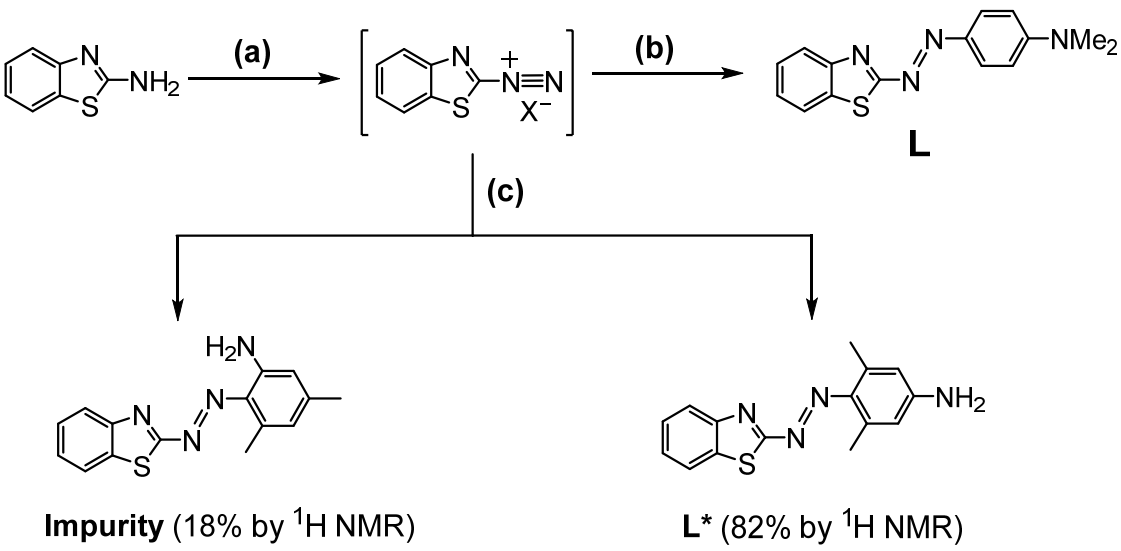

Scheme 3.1. Diazotisation coupling reactions used for the synthesis of **L** and **L***. (a) Glacial acetic acid:water:concentrated H_2SO_4 (6:3:2), $NaNO_2$, 0°C. (b) *N,N*-Dimethylaniline, MeOH, 0 °C. (c) 3,5-Dimethylaniline, MeOH, 0 °C.

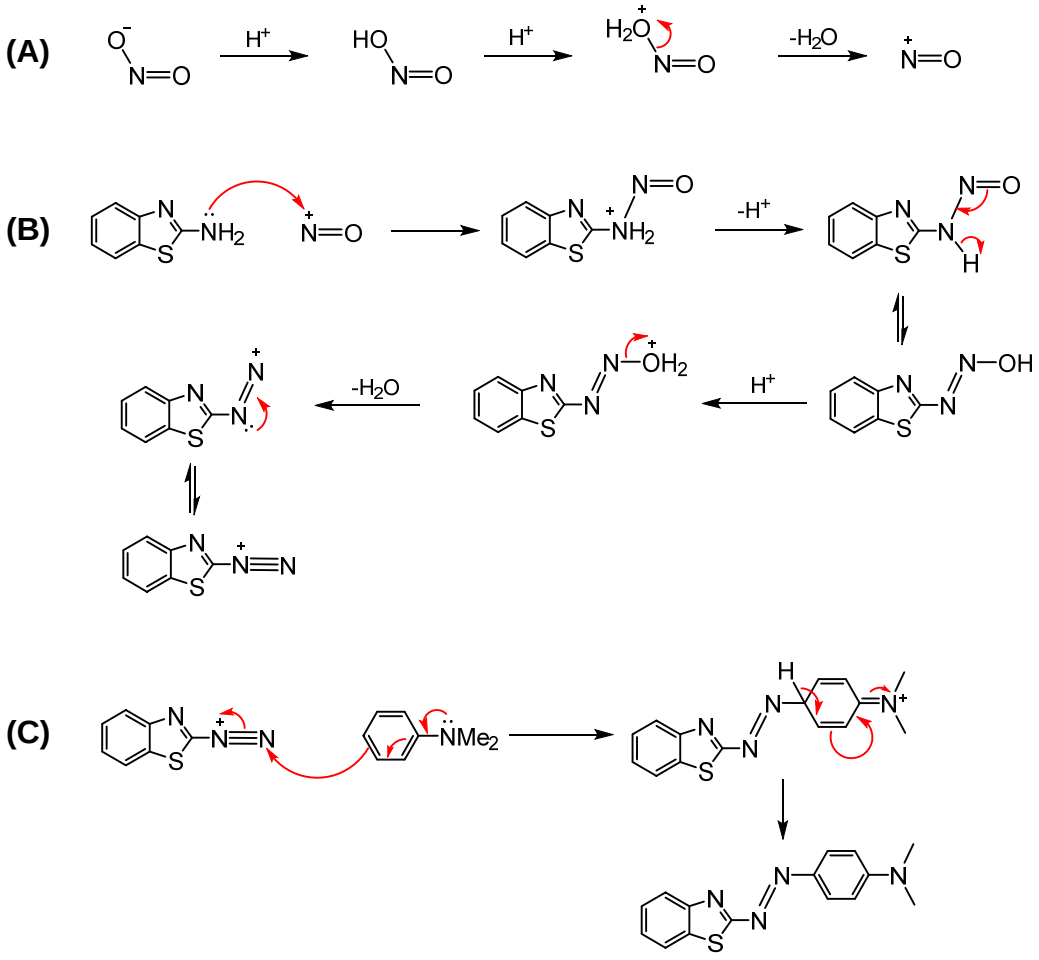

Scheme 3.2. Reaction mechanism for the synthesis of ligand **L**. Showing (A) *in situ* generation of the nitrosonium cation from sodium nitrite under strong acid conditions, (B) formation of the diazonium salt reactive intermediate, and (C) addition of *N,N*-dimethylaniline, yielding **L**.

3.3.2. Synthesis of Os(II) arene AZBTZ complexes

Os(II) arene AZBTZ complexes were synthesised by stirring 2 mol. equiv. of **L** with an Os(II) *p*-cym dimer; $[Os(\eta^6\text{-}p\text{-cym})X_2]_2$ (where X = Cl, Br or I), in EtOH at ambient temperature. All three dimers react with **L** to form both a positively charged *N,N*-coordinated complex, **A**, and a neutral cyclo-metalated *N,C*-coordinated complex, **B**, in varying ratios (Scheme 3.3). These were observed

in reaction mixtures *via* SiO_2 thin layer chromatography (TLC), using MeOH as the eluent. Positively charged *N,N*-complexes exhibit strong affinities for SiO_2 and do not move far from the TLC plate baseline. In contrast, *N,C*-complexes travel with the mobile phase with R_f values ranging between 0.70-0.74.

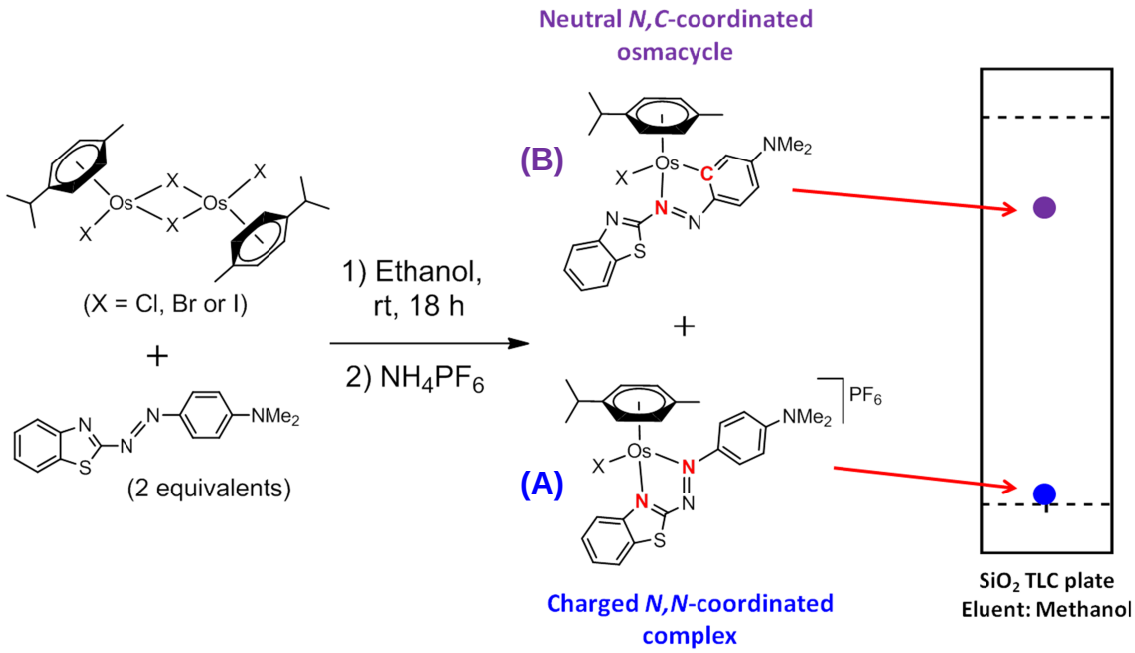

Scheme 3.3. Synthesis of charged *N,N*-coordinated complexes, **A**, and neutral *N,C*-coordinated complexes, **B**.

The percentages of **A** and **B** formed were determined for each dimer by observing a ^{1}H NMR spectrum of the reaction mixture after 18 h of stirring, and measuring the integrals of the aliphatic *p*-cym doublets, which correspond to CH_3 groups (Figure 3.2). It was observed that for *N,N*-coordinated complexes, these doublets lie significantly closer together to one another (0.09-0.11 ppm

distance apart), in comparison to *N,C*-coordinated complexes, in which they lie 0.25-0.30 ppm apart.

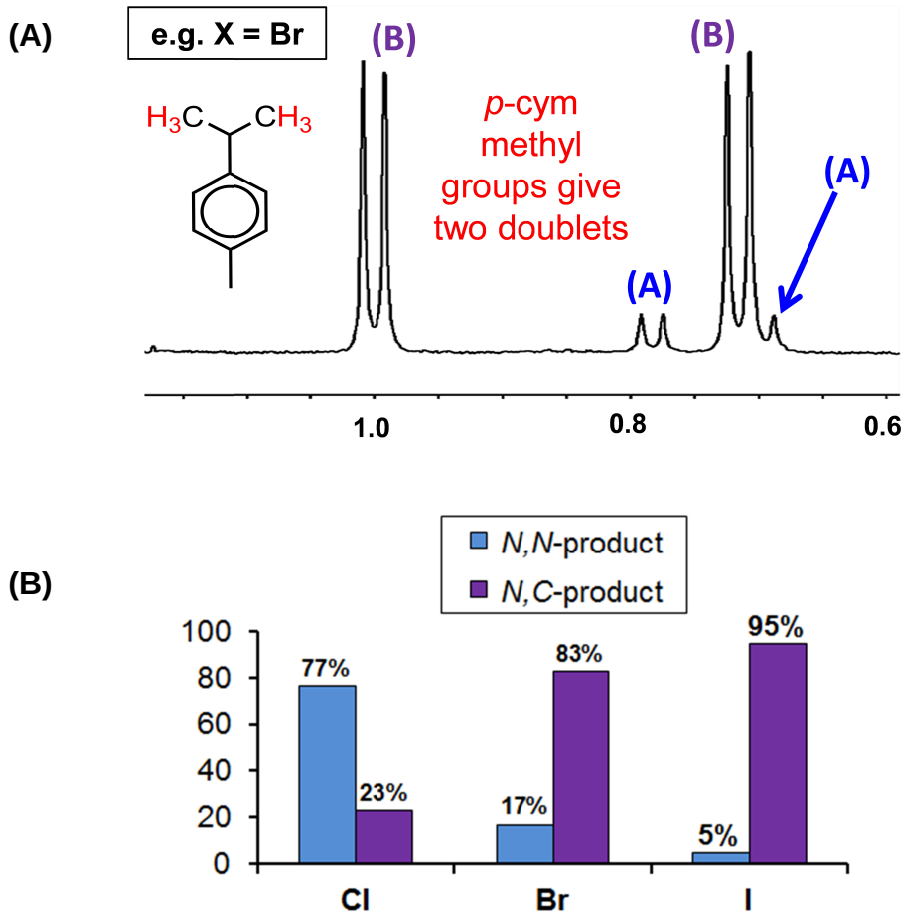

Figure 3.2. (A) The ^{1}H NMR spectrum (aliphatic region, 400 MHz, DMSO-d_6) after a 24 h reaction of $[Os(\eta^6\text{-}p\text{-cym})Br_2]_2$ with **L**, showing two doublets for the *p*-cym methyl groups of complexes **A** (*N,N*-coordination), and **B** (*N,C*-coordination). (B) The percentages of **A** and **B** formed when different dimers ($[Os(\eta^6\text{-}p\text{-cym})X_2]_2$, where X = Cl, Br or I) were reacted with **L**.

When X = Cl or Br, both the charged complexes (**1a** and **2a**), and neutral complexes (**1b** and **2b**) were isolated (Figure 3.3). However, when X = I, only neutral complex **3b** was isolated as the major product. Complexes **1b**, **2b** and **3b** can be easily purified *via* silica flash column chromatography, which was not

possible for charged complexes **1a** and **2a** due to their high affinities for SiO_2. Unfortunately a pure bulk sample of **2a** was not obtained after re-crystallisation, but a pure single crystal suitable for an X-ray crystallography study was grown in MeOH.

(A)

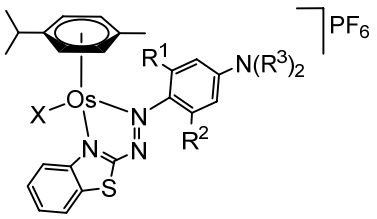

Complex	X	R^1	R^2	R^3
****1a**	Cl	H	H	Me
****2a**	Br	H	H	Me
3a	I	H	H	Me
***4**	Cl	Me	Me	H
***5**	I	Me	Me	H

(B)

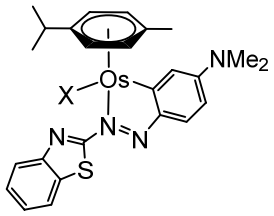

Complex	X
***1b**	Cl
****2b**	Br
****3b**	I

* product has been isolated
** product has been isolated and X-ray structure determined

Figure 3.3. Complexes formed from ligands **L** and **L***. Complexes **1** - **3** were formed using **L**, and **4** and **5** using **L***. Complexes **1a**, **2a**, **3a**, **4** and **5** are *N,N*-coordinated species. Complexes **1b**, **2b** and **3b** are *N,C*-coordinated osmacycles.

The reaction conditions were altered to see if the formation of a *N,N*-coordinated species can be favoured over *N,C*-coordination; when the reaction between $[Os(\eta^6\text{-}p\text{-cym})I_2]_2$ was carried out with **L** in the aprotic and weakly coordinating solvent DCM, formation of the *N,N*-coordinated species (**3a**) was still disfavoured. Furthermore, carrying out the reaction between $[Os(\eta^6\text{-}p\text{-cym})Br_2]_2$ and **L** in the presence of HBr did not prevent deprotonation of the

phenyl ring, hence prevent formation of the *N,C*-coordinated species. Even when the reaction was carried out with 50 mol. equiv. HBr per 1 mol. equiv. of **L**. Ligand **L*** has methyl groups situated at the R^1 and R^2 positions on the aniline ring (Figure 3.3), hence preventing cyclo-metalation and the formation of a *N,C*-coordinated species from occurring. When $[Os(\eta^6\text{-}p\text{-cym})I_2]_2$ was reacted with 2 mol. equiv. of **L***, the reaction took notably longer for the initial colour change but was successful in yielding complex **5**. Complex **4** was also synthesised *via* the same reaction using $[Os(\eta^6\text{-}p\text{-cym})Cl_2]_2$. The molecular structures of all the complexes synthesised in this chapter are shown in the Appendices, Section **8.1**.

3.3.3. Characterisation of complexes

The ^{1}H NMR spectrum of the aromatic region of **1a** is shown in Figure 3.4. There are 12 aromatic protons and characterisation was confirmed by 2D COSY ^{1}H NMR. In contrast, the ^{1}H NMR spectrum of complex **3b** reveals a species containing 11 rather than 12 aromatic protons (Figure 3.5). It was confirmed that the missing proton is from the 3-position of the aniline ring, which is bonded to osmium giving a neutral osmacycle structure. This structure is characterised by the doublet of doublets, proton e (J = 9.2, 2.5 Hz), which has short range coupling to proton f (^3J = 9.2 Hz) and long range coupling to proton g (^4J =2.5 Hz).

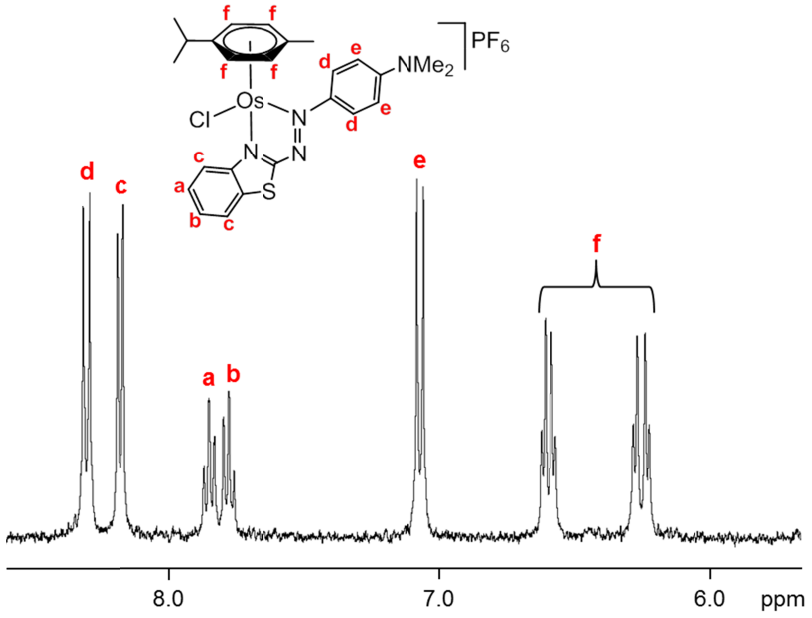

Figure 3.4. ^{1}H NMR spectrum of the aromatic region of complex **1a** in methanol-d_4 recorded at 400 MHz, with assignments.

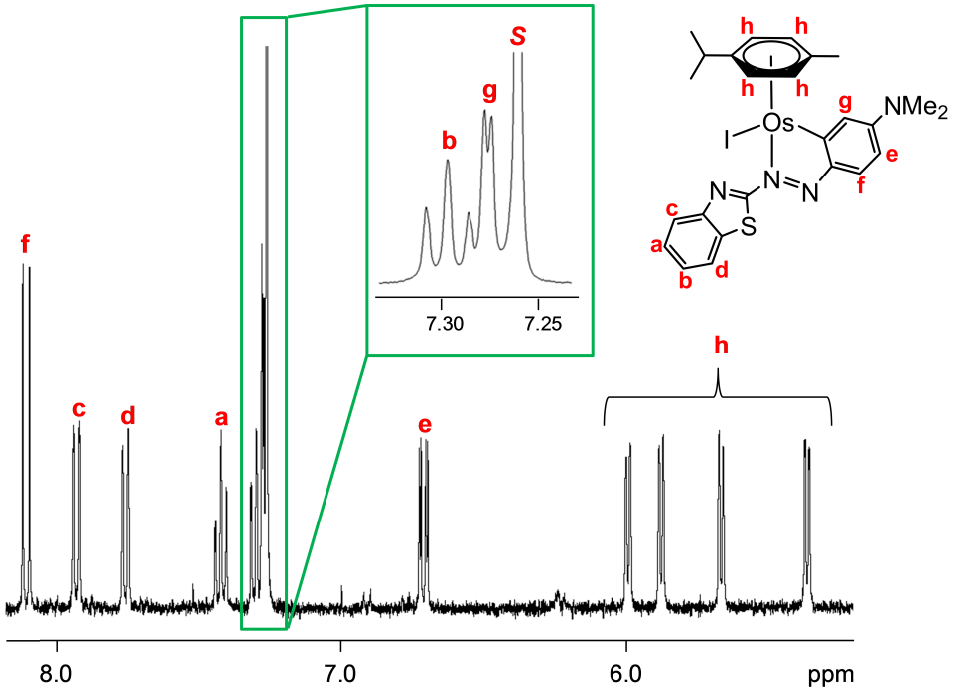

Figure 3.5. ^{1}H NMR spectrum of the aromatic region of complex **3** in chloroform-d_1 recorded at 400 MHz. The assignment of 11 aromatic protons is shown. The region 7.35 – 7.25 ppm was recorded at 700 MHz to improve the resolution between peaks b and g and the overlapping residual solvent peak, *S*.

The ^{1}H NMR spectrum of complex **5** consists of 10 aromatic protons, four of which correspond to the *p*-cym ligand. It was noted that the chemical shift of one of these multiplets is abnormally more de-shielded than the others; three protons reside between 6.09 – 5.72 ppm, whilst one resides at 6.82 ppm. A ^{1}H sel-NOE experiment was conducted, where a 1D NOE is used to irradiate a specific resonance (at 6.82 ppm) and show other resonances in close proximity through space. Figure 3.6 shows the spectrum obtained for the ^{1}H sel-NOE with the ^{1}H NMR spectrum aligned above, and an assignment of the neighbouring protons. The de-shielded arene proton (a) is neighbouring another aromatic *p*-cym proton (c), a methyl group on the arene (d), and interestingly, it is in close proximity to the proton at the 8-position on the benzothiazole group (b). In comparison, the chlorido complex (**4**) also shows the same trend with a de-shielded *p*-cym proton residing at 6.90 ppm.

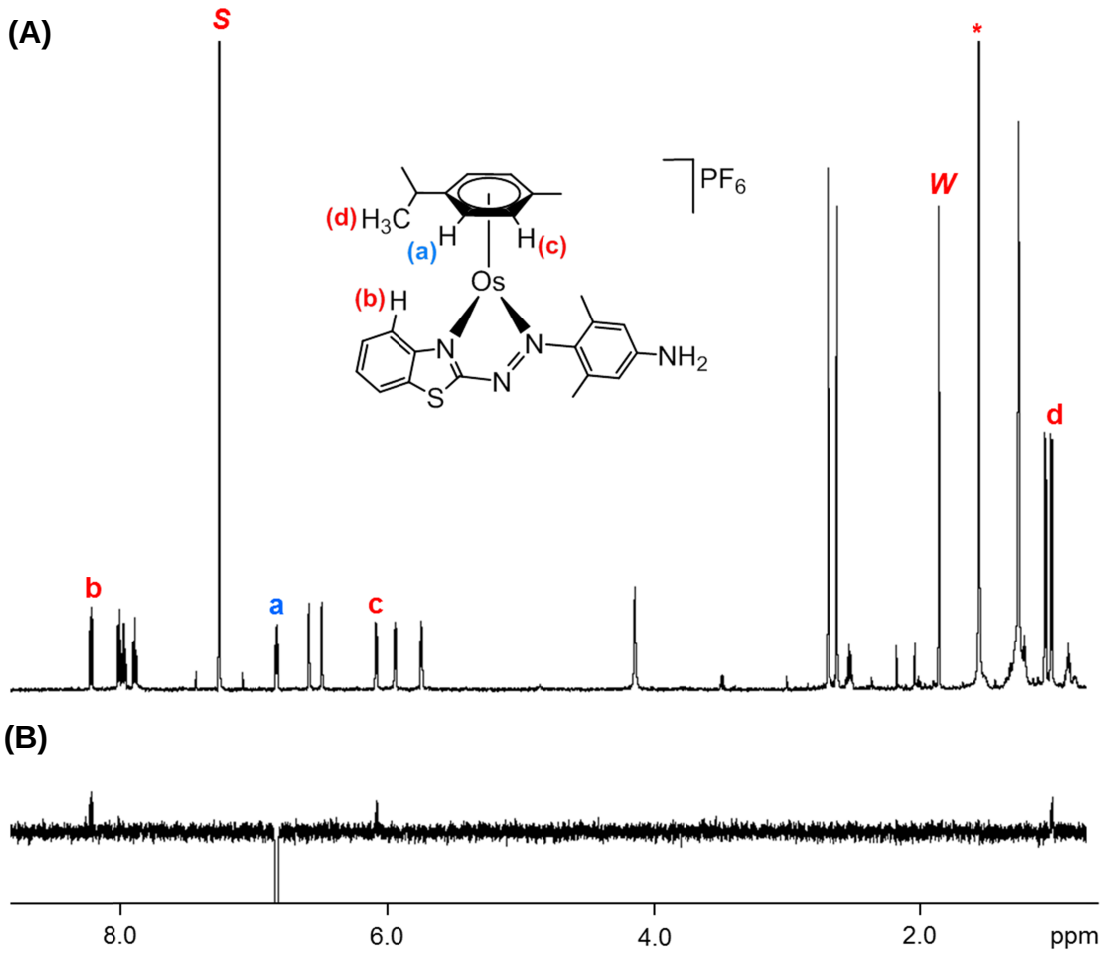

Figure 3.6. (A) ^{1}H NMR spectrum of **5** in chloroform-d_1, and shown above, (B) the corresponding ^{1}H sel-NOE spectrum. The de-shielded resonance at 6.84 ppm, 'a', was irradiated. Protons in the spectrum that interact with 'a' through space are labelled above. Residual solvent peak, *S*, residual water peak, *W*, and an artefact found in the chloroform-d_1 solvent, *, have been highlighted. The iodido monodentate ligand in the structure is pointing into the plane of the page for clarity. The experiment was carried out using a 600 MHz instrument.

ESI-MS analysis of the charged *N,N*-coordinated complexes (**1a**, **2a**, **3a**, **4** and **5**) revealed m/z peaks that correspond to the cationic species without their counter anions (M - PF_6). Alternatively, neutral *N,C*-coordinated complexes (**1b**, **2b** and **3b**) were observed as neutral species with either a H^+ or Na^+ cation (M

+ H^+ and M + Na^+). For example, complex **2a**; $C_{25}H_{28}BrN_4OsS^+$: m/z 687.1, and complex **2b**; $C_{25}H_{27}BrN_4OsS$ + H^+: m/z 687.1, and $C_{25}H_{27}BrN_4OsS$ + Na^+:708.9.

3.3.4. X-ray crystal structures

The molecular structures of complexes **1a**, **2a**, **2b**, and **3b** were determined by single crystal X-ray diffraction (Figure 3.7). The crystallographic data are shown in Table 3.1 and selected bond lengths, bond angles, torsion angles, and atom to atom distances are summarised in Table 3.2. The complexes adopt the familiar *pseudo*-octahedral three-legged piano-stool geometry that is common to all Os(II) η^6-arene structures, where the Os(II) centre is π-bonded to the arene ligand. The Os(II) centre is also coordinated to a monodentate halide ligand and the bidentate ligand, **L**, *via* either *N,N* or *N,C* atoms, which constitute the three legs of the piano stool. All complexes exhibit a five-membered chelate ring with **L**; N1-C9-N10-N11-Os1 for **1a** and **2a**, and N10-N11-C12-C17-Os1 for **2b** and **3b**. They all crystallise as racemates, owing to the presence of a chiral Os(II) centre. Complexes **1a** and **2a** have PF_6^- counter-ions in their X-ray crystal structures, whereas complexes **2b** and **3b** incorporate molecules of acetone and chloroform in their crystal lattice, respectively, at a 2:1 ratio of complex: solvent.

Table 3.1. Crystallographic data for complexes **1a**, **2a**, **2b** and **3b**

	1a	**2a**	**2b**·0.5C_3H_6O	**3b**·0.5$CHCl_3$
Formula	$C_{25}H_{28}ClF_6N_4OsPS$	$C_{25}H_{28}BrF_6N_4OsPS$	$C_{25}H_{27}BrN_4OsS·0.5C_3H_6O$	$C_{25}H_{27}IN_4OsS·0.5CHCl_3$
Molar mass /g mol^{-1}	787.19	831.65	714.72	792.35
Density /mg m^{-3}	1.869	2.011	1.876	2.021
Crystal system	Monoclinic	Monoclinic	Monoclinic	Monoclinic
Crystal dimensions /mm	0.20 x 0.16 x 0.10	0.20 x 0.16 x 0.12	0.55 x 0.30 x 0.15	0.40 x 0.10 x 0.01
Space group	C2/c	P2(1)/c	P2(1)/c	P2(1)/c
Crystal character	purple block	blue block	black block	brown plate
a/Å	15.13119(10)	14.5035(3)	8.6795(3)	8.7369(5)
b/Å	14.67057(10)	8.02511(14)	26.5519(10)	26.6425(12)
c/Å	25.80898(15)	24.5348(5)	11.6929(5)	11.8741(8)
α/deg	90	90	90	90
β/deg	102.3937(6)	105.828(2)	110.116(4)	109.544(7)
γ/deg	90	90	90	90
T/K	100(2)	150(2)	150(2)	100(2)
Z	8	4	4	4
R [F> 4σ(F)]	0.0260	0.0292	0.0560	0.0701
R_w	0.0665	0.0685	0.1010	0.1782
GOF	1.106	1.066	1.255	1.087
Δρ max and min /e$Å^{-3}$	1.397 & -0.862	3.098 & -0.989	2.967 & -3.209	3.646 & -2.888

Table 3.2. Selected bond lengths (Å), atom to atom distances (Å), and bond/torsion angles (°), observed in the X-ray crystal structures of complexes **1**, **2a**, **2b**·0.5C_3H_6O and **3b**·0.5$CHCl_3$. X = Cl, Br or I.

Bond length (Å)	**1a**	**2a**	**2b**·0.5C_3H_6O	**3b**·0.5$CHCl_3$
Os1-X1	2.3785(6)	2.5243(3)	2.5530(8)	2.7115(9)
Os1-N1	2.072(2)	2.055(2)	N/A	N/A
Os1-N10	N/A	N/A	2.073(5)	2.081(9)
Os1-N11	2.079(3)	2.089(2)	N/A	N/A
Os1-C17	N/A	N/A	2.020(7)	2.038(10)
N10-N11	1.334(4)	1.336(3)	1.325(8)	1.304(13)
Os1-Arene Centroid	1.705	1.705	1.723	1.725
Atom to atom distance (Å)	**1a**	**2a**	**2b**·0.5C_3H_6O	**3b**·0.5$CHCl_3$
H3⋯24	2.041	2.379	N/A	N/A
H13⋯H22	2.144	2.238	N/A	N/A
H16⋯24	N/A	N/A	2.441	2.290
S1⋯S1	N/A	N/A	3.229	3.252
Bond angle (°)	**1a**	**2a**	**2b**·0.5C_3H_6O	**3b**·0.5$CHCl_3$
$\theta_{X1\text{-}Os1\text{-}N1}$	84.55(7)	85.72(7)	N/A	N/A
$\theta_{N1\text{-}Os1\text{-}N11}$	75.01(10)	74.66(9)	N/A	N/A
$\theta_{N11\text{-}Os1\text{-}X1}$	85.56(7)	85.87(7)	N/A	N/A
$\theta_{X1\text{-}Os1\text{-}N10}$	N/A	N/A	84.86(16)	85.8(3)
$\theta_{N10\text{-}Os1\text{-}C17}$	N/A	N/A	75.8(2)	75.9(4)
$\theta_{C17\text{-}Os1\text{-}X1}$	N/A	N/A	86.2(2)	85.4(3)
Torsion angle (°)	**1a**	**2a**	**2b**·0.5C_3H_6O	**3b**·0.5$CHCl_3$
$\theta_{N1\text{-}C9\text{-}N10\text{-}N11}$	-1.63	0.66	N/A	N/A
$\theta_{N10\text{-}N11\text{-}C12\text{-}C17}$	-17.00	14.16	1.08	-5.57
$\theta_{S8\text{-}C9\text{-}N10\text{-}N11}$	N/A	N/A	0.42	0.03

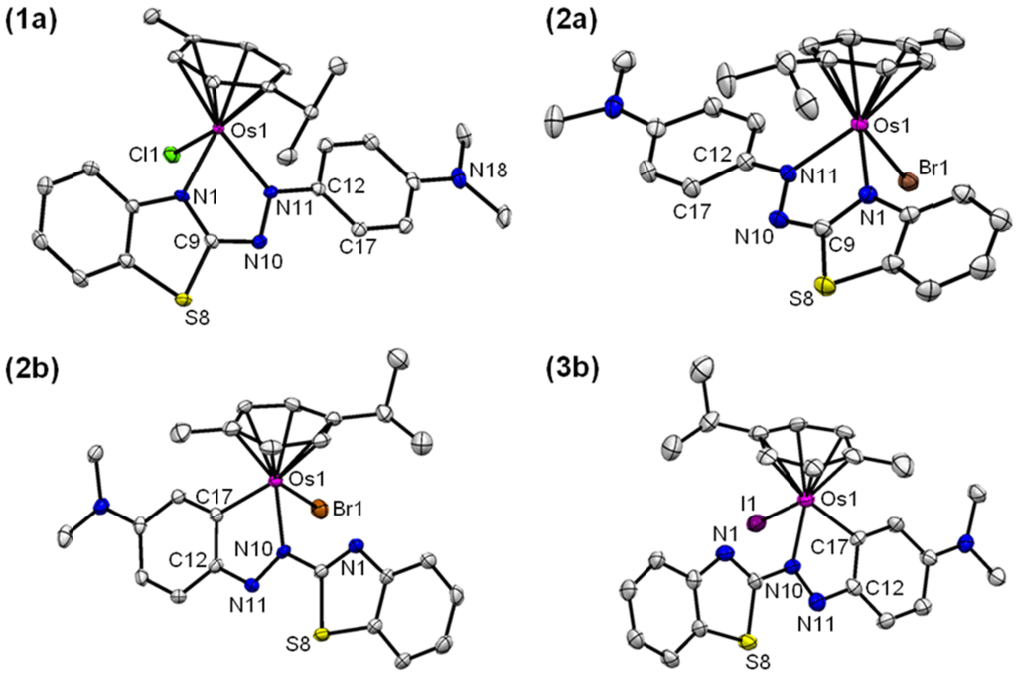

Figure 3.7. ORTEP diagrams of complexes **1a**, **2a**, **2b**·0.5C_3H_6O and **3b**·0.5$CHCl_3$. Ellipsoids are shown at the 50% probability level and all hydrogens, counter ions and solvent molecules have been omitted for clarity.

The X-ray crystal structures of *N,N*-coordinated complexes **1a** and **2a**, confirm that ligand **L** is bound to the Os(II) centre *via* the N-atom of the benzothiazole group, N1, and N11 of the azo-bond. Weak π-π interactions between aniline rings (3.46 Å, centroid-to-centroid) were observed for **1a** (Figure 3.8). Short H···H distances are present between aromatic hydrogens on the *p*-cym ligand and bidentate ligand **L**; H13···H22 and H3···H24 for complexes **1a** and **2a**. The torsion angle, $\theta_{N1\text{-}C9\text{-}N10\text{-}N11}$, serves as a measure of distortion of the chelate ring from planarity and values of -1.63° and 0.66° were calculated, respectively, for complexes **1a** and **2a**. The torsion angle $\theta_{N10\text{-}N11\text{-}C12\text{-}C17}$ describes the angle between the chelate ring and the aniline ring. With values of -17.00° and 14.16° for **1a** and **2a**, respectively, ligand **L** is not aligned flat within the structure. In

contrast, *N,C*-coordinated complexes **2b** and **3b** exhibit fewer H···H clashes between the *p*-cym ligand and ligand **L** (H16···H24). The torsion angle, $\theta_{S8\text{-}C9\text{-}N10\text{-}N11}$, which serves as the angle between the chelate ring and the benzothiazole moiety for complexes **2b** and **3b**, are very small (0.42° and 0.03°, respectively). This results in strong planarity of ligand **L** which is observable in the crystal structures. The torsion angles serving as a measure of distortion of the chelate ring from planarity for **2b** and **3b** ($\theta_{N10\text{-}N11\text{-}C12\text{-}C17}$) are 1.08° and -5.57°, respectively. Also observed in **2b** and **3b** are intermolecular S···S bridges, mediated through the free and uncoordinated benzothiazole groups with outwardly pointing S-atoms (Figure 3.8).

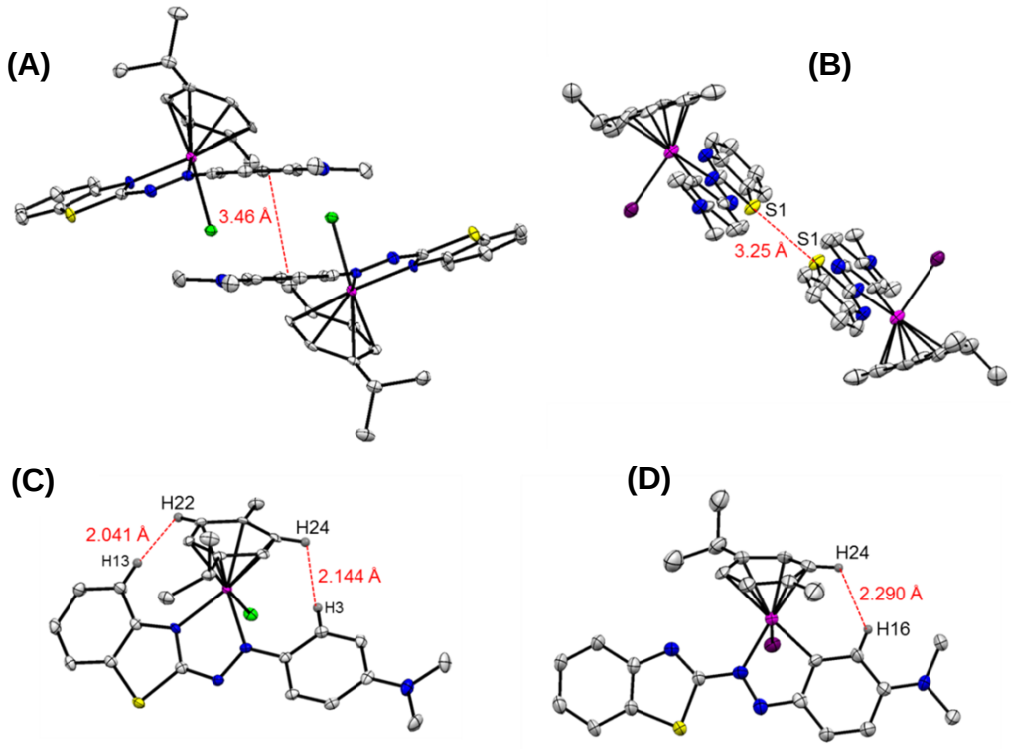

Figure 3.8. (A) Weak π-π interactions between aniline rings of complex **1a** (distances are centroid-to-centroid). (B) S···S bridging in complex **3b**·0.5$CHCl_3$. (C) H13···H22 and H3···H24 atom-atom distances in complex **1a**. (D) H16···H24 atom-atom distances in complex **3b**·0.5$CHCl_3$.

3.3.5. Aqueous solubility and stability

All complexes isolated in this chapter are too insoluble in water and cell culture media for biological studies and stability testing in D_2O by ^1H NMR. The stabilities of **1a** and **1b** in MeOH:H_2O (1:1, v/v) were monitored over a 24 h period by UV-Vis spectroscopy at 25 °C (Figure 3.9).

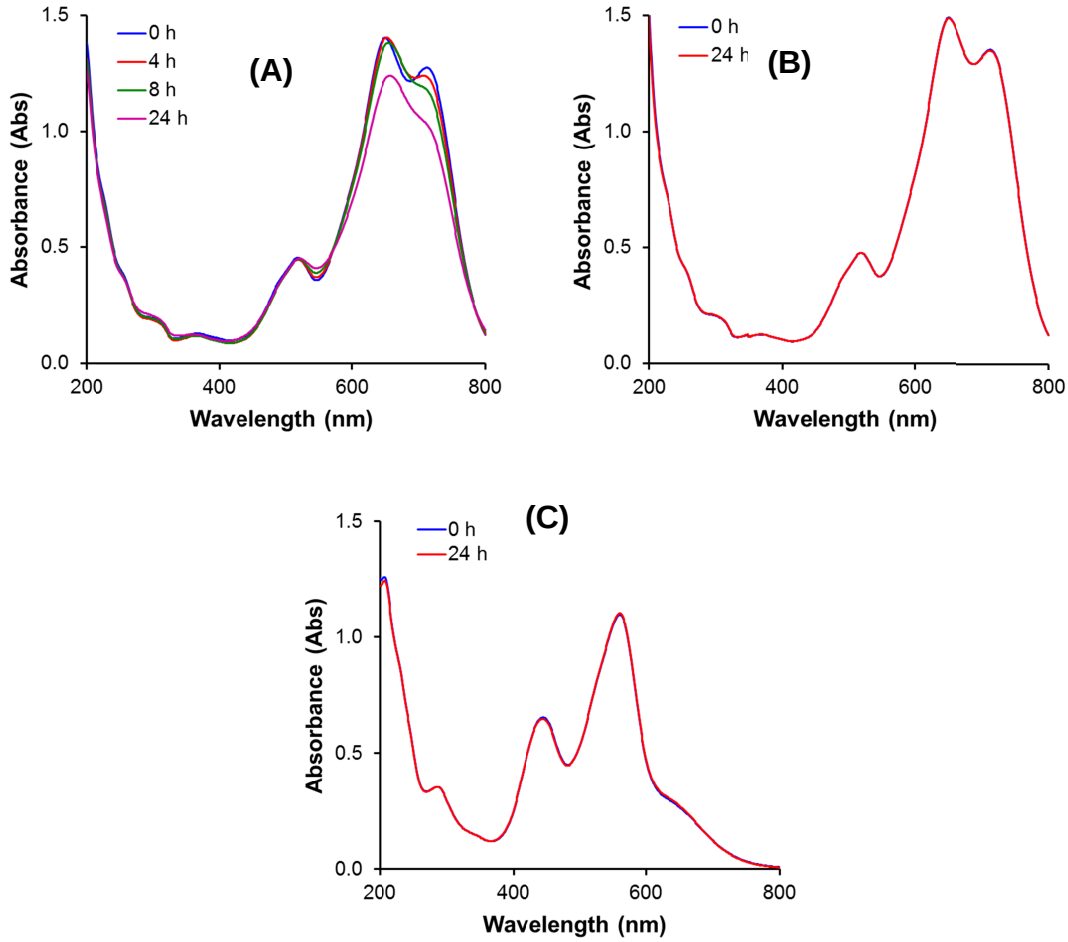

Figure 3.9. UV-Vis spectra in MeOH:H_2O (1:1, v/v) at 25 °C. (A) 50 μM complex **1a**. (B) 50 μM complex **1a** with 100 mM NaCl. (C) 50 μM complex **3b**.

Changes in the UV-Vis absorption spectra of **1a** was observed over 24 h, and a decline in intensity of the absorption peaks at 653 and 716 nm was noted.

Repeating the experiment in the presence of 100 mM NaCl inhibited any changes to the spectra over 24 h. In contrast, no decomposition of **1b** was observed over a 24 h period in MeOH:H_2O (1:1, v/v). Two stable maxima were observed at 447 and 562 nm.

3.3.6. Acid stability and regio-specific aniline ring deuteration of 2b

When complex **2b** was stirred with 100 mol. equiv. HBr in MeOH, no conversion to the *N,N*-coordinated species, **2a**, was observed by ^{1}H NMR. It was only after heating under reflux for two days that a new set of small aliphatic *p*-cym proton peaks started to emerge in the ^{1}H NMR spectrum. TLC analysis in MeOH revealed a small blue spot residing close to the base-line, likely indicating the presence of a charged *N,N*-coordinated species. Further experiments showed that carrying out reactions between $[Os(\eta^6\text{-}p\text{-cym})Br_2]_2$ and **L** in the presence of HBr did not influence the ratio of products **2a** and **2b**, as observed by ^{1}H NMR. The ratio of **2a**:**2b** formed remained unchanged even when the reaction was carried out in the presence of 100 mol. equiv. HBr.

Complex **2b** was combined with 3 mol. equiv. HBr in methanol-d_4 and studied by ^{1}H NMR. The aromatic hydrogen which lies next to the Os-C bond (H_a, 7.58 ppm) disappears over time, showing almost complete disappearance after 15 h. The disappearance of this peak in the ^{1}H NMR spectrum also coincides with a loss of long-range proton coupling to H_b (^4J = 2.5 Hz, 7.26 ppm, see Figure 3.10).

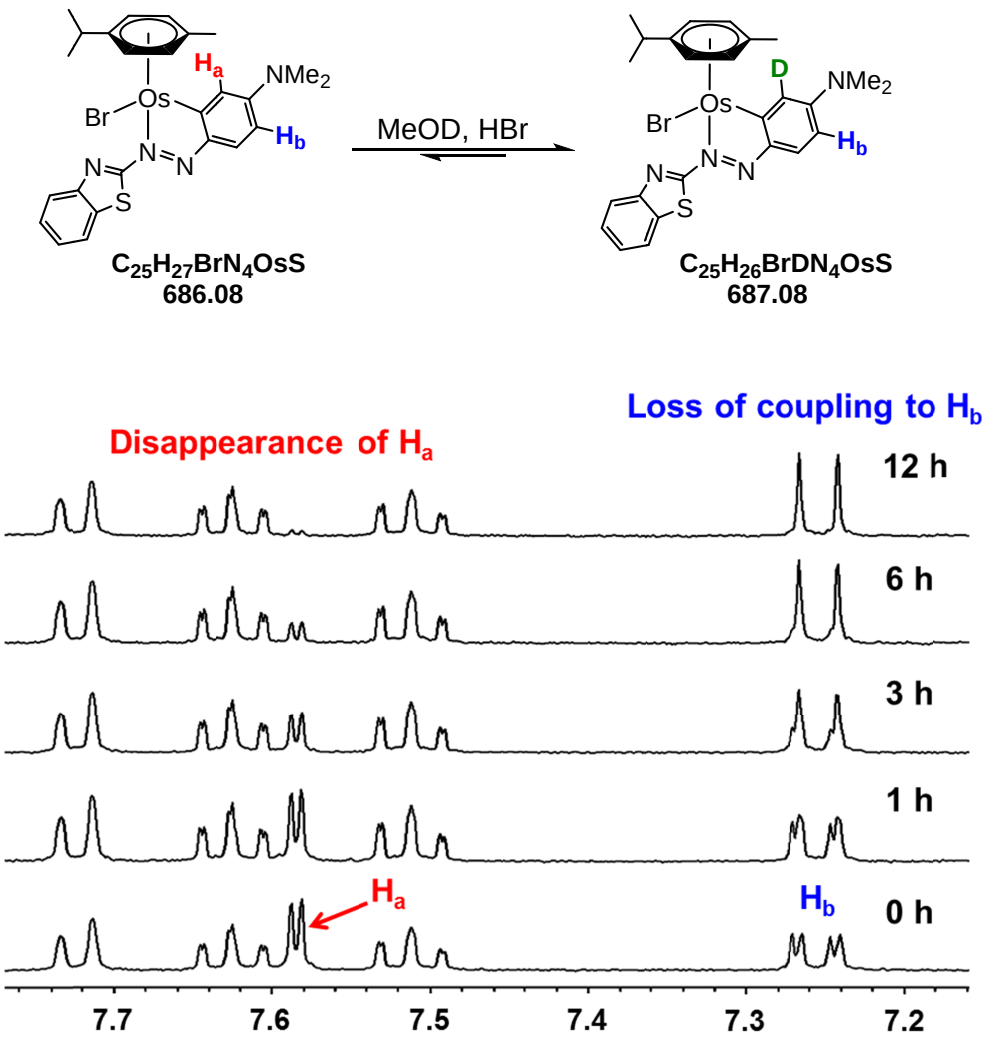

Figure 3.10. ^{1}H NMR spectra of complex **2b** with 3 mol. equiv. HBr in methanol-d_4 showing the disappearance of proton H_a (7.58 ppm), accompanied by the loss of long-range coupling between protons H_b and H_a (^{4}J = 2.5 Hz). Spectra were collected on a 400 MHz instrument.

The substitution at this position occurs only in the presence of an acid. High resolution mass spectrometry reveals the presence of the deuterated complex after treatment with HBr; exact masses of 688.0876 and 710.0696 m/z, which correspond to the formulas $C_{25}H_{26}BrDN_4OsS + H^+$ and $C_{25}H_{26}BrDN_4OsS + Na^+$, respectively, (see Figure 3.11). A kinetic ^{1}H NMR study was conducted at

25 °C, where a spectrum was collected every 30 min to observe the disappearance of H_a (measured by proton peak integration using TOPSPIN version 2.1 software). The reaction shows first order rate kinetics for deuteration of the phenyl ring with a rate constant of 5.78 x 10^{-5} s^{-1} and half-life 1.04 x 10^3 s (Figure 3.12).

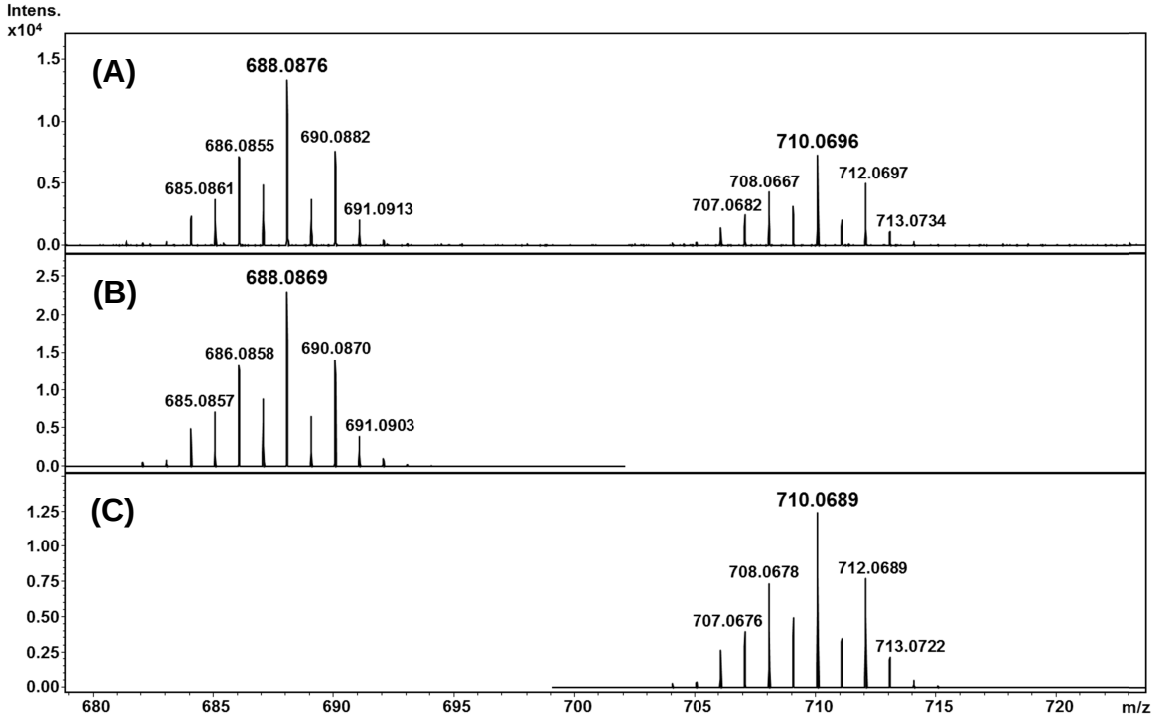

Figure 3.11. High resolution mass spectrum of complex **2b** after deuterium exchange of H_a. (A) Experimental spectrum, (B) calculated spectrum for $C_{25}H_{26}BrDN_4OsS + H^+$, (C) calculated spectrum for $C_{25}H_{26}BrDN_4OsS + Na^+$.

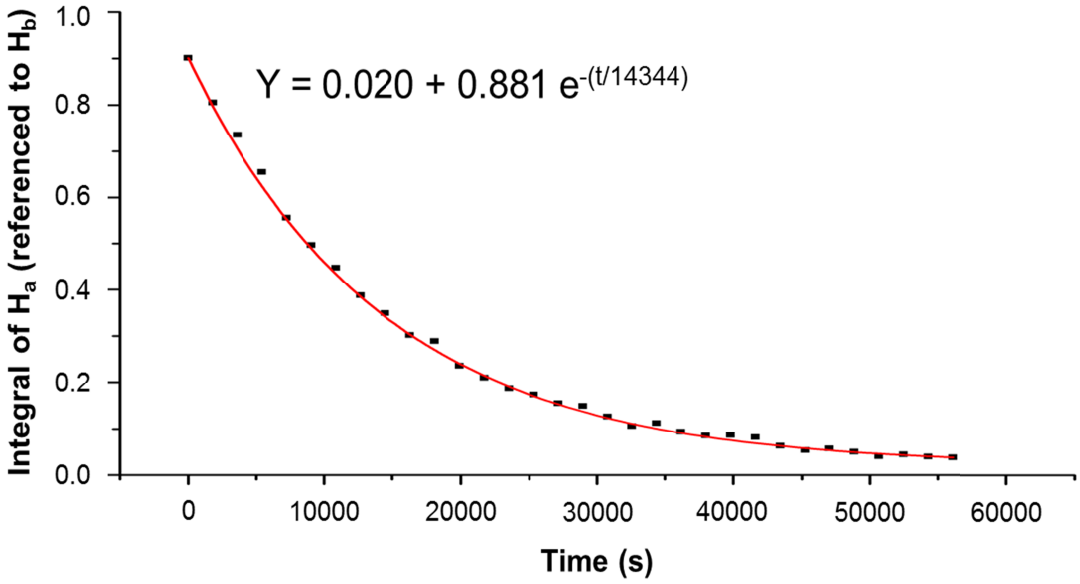

Figure 3.12. Time dependent disappearance of the NMR resonance, H_a (7.58 ppm) in complex **2b** at 25 °C. k = 5.78 x 10^{-5} s^{-1} and $t_{1/2}$ = 1.04 x 10^{3} s.

3.3.7. Mulliken partial charges of 2b

The Mulliken partial charge calculations for complex **2b** was carried out by Dr. Nicolas P. E. Barry and is shown in Figure 3.13. Carbon C1 (the site where regio-specific deuteration occurs) is significantly more negatively charged than the other carbon atoms making up the aniline ring. Furthermore, the aniline ring exhibits disrupted aromaticity with only two C=C bonds present; C1=C2 and C4=C5, which have calculated bond lengths of 1.384 Å and 1.363 Å, respectively. These are consistent with the X-ray crystal structure, which have bond lengths of 1.386(9) Å and 1.345(9) Å, respectively. In contrast, the bond lengths of C2-C3 and C5-C6 are 1.478 Å and 1.470 Å in the calculated structure, and 1.433(9) Å and 1.434(10) Å in the crystal structure, respectively.

The structure also exhibits CH_3 carbons with significantly high negative charges.

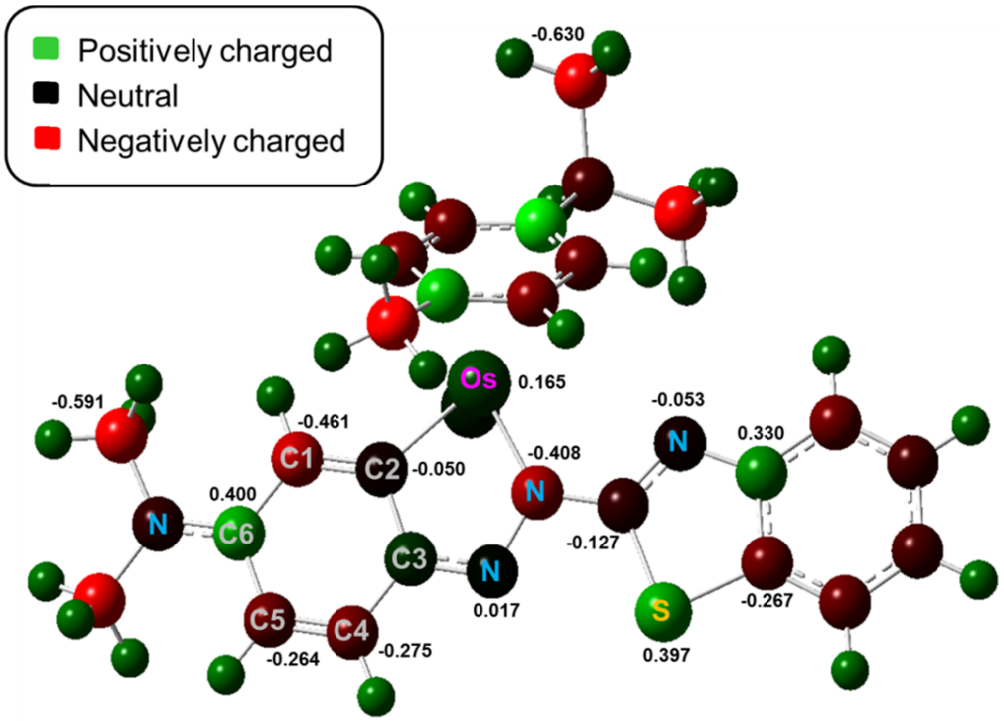

Figure 3.13. The Mulliken partial charges of complex **2b** showing the partial charges of selected atoms.

3.4. Discussion

3.4.1. Intramolecular C-H bond activation and cyclo-metalation

Reactions between Os(II) *p*-cym dimers and **L** were expected to yield *N,N*-coordinated cationic species, analogous to AZPY complexes previously reported in our group.[1,2] To our surprise, mixtures containing both *N,N*- and *N,C*-coordinated complexes were yielded. Formation of the *N,C*-cyclo-metalated complex requires C-H bond activation, a challenging step that involves

deprotonation of the aniline ring at the *ortho* position. There are several literature examples of ruthenium, rhodium, osmium and iridium metallocycles formed *via* direct arylation of ligands such as 2-phenyl-substituated pyridines.[13-17] Metalation of the phenyl ring in these examples invariably occurs at the *ortho* position and results in five-membered chelate rings. Older synthetic routes utilise a trans-metalation pathway involving *ortho*-mercurated species, eliminating the need for C-H activation.[18-21] However, direct metalation of 2-phenylpyridine (2-PhPy) is also possible in the presence of a suitable base such as acetate and is controlled by the nitrogen-containing directing group (pyridine), which initially binds to the metal centre. In the synthesis between $[Os(\eta^6\text{-}p\text{-cym})X_2]_2$ (X = Cl, Br or I) and **L**, direction occurs *via* initial coordination to the azo-bond nitrogen and C-H activation occurs spontaneously and remarkably in the absence of an additional base. Cerón-Camacho *et al*, report on the successful electrophilic cyclo-osmation of bidentate ligands; 2-PhPy and *N,N*-dimethylbenzylamine.[22] The latter of which was also achieved in the absence of a base, and the ligand is believed to act as both a substrate and base for its own C-H bond cleavage. Similarly to *N,N*-dimethylbenzylamine, **L** possess a basic amine group which could be responsible for assisting C-H bond cleavage at the *ortho* position of the aniline.

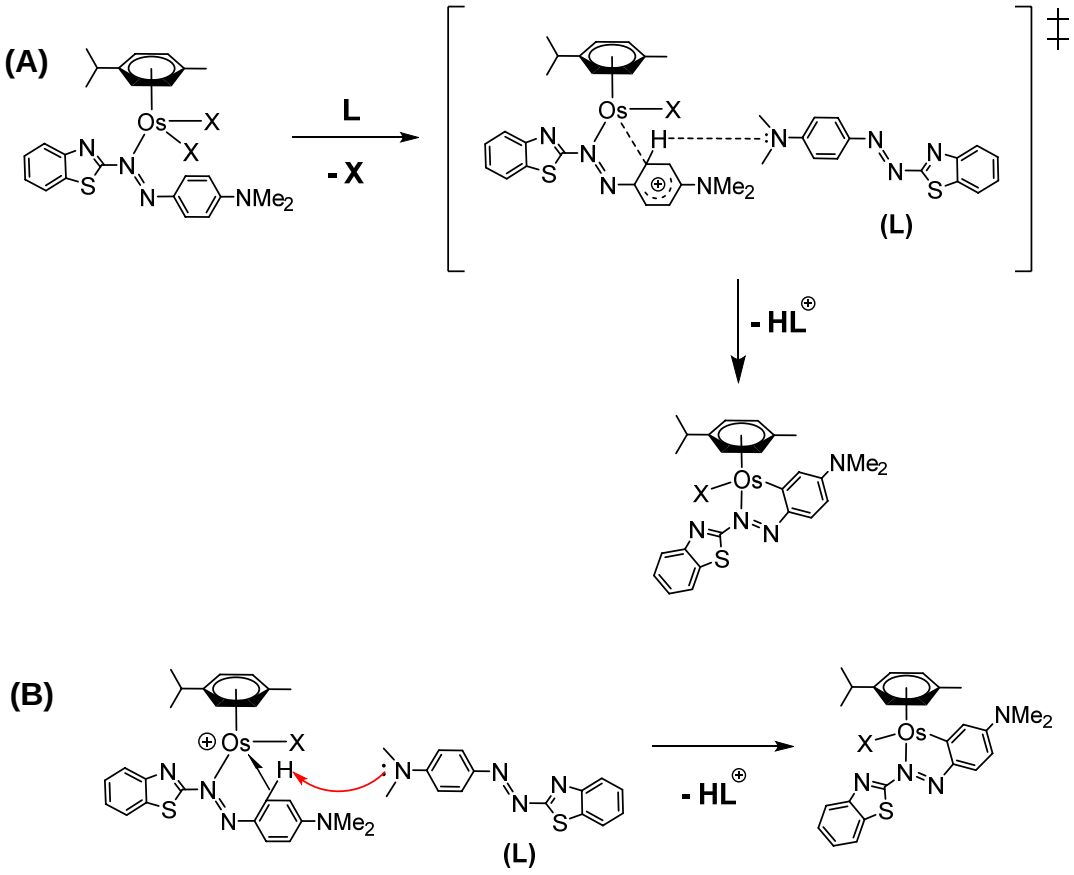

Scheme 3.4. Two possible mechanisms for *ortho* C-H bond deprotonation. (A) S_E3 mechanism. (B) An alternative mechanism involving an agnostic *ortho* Os(C-H) bond.

The mechanism of C-H activation might be elucidated in more detail with detailed computational and kinetic analyses, however a review of the literature suggests a likely mechanism may involve base-assisted S_E3 electrophilic cyclo-metalation.[23,24] Alternatively, a mechanism involving an agostic *ortho* Os(C-H) bond cannot be ruled out either[24,25] (Scheme 3.4). Both mechanisms require the nucleophilic -NMe_2 group on **L** playing a role as a proton acceptor during C-H bond activation. Such mechanisms have been previously proposed for the cyclo-metalation of 2-PhPy with ruthenium η^6-arene complexes.

3.4.2. Selectivity towards *N,C*-osmacycle formation over *N,N*-coordination

It was initially anticipated that ligand **L** may coordinate to the metal centre *via* the S-atom of the benzothiazole group. However, to the best of our knowledge there are no literature reports of benzothiazoles coordinating to metal centres through the S-atom.[26] The benzothiazole group of **L** favours N-binding in our complexes as confirmed by X-ray crystal structures of complexes **1a** and **2a**.

N,C-coordination is the preferred geometry formed when X = Br or I, but for X = Cl, *N,N*-coordination is preferred. From crystallographic observations, it is most likely that the ratio of products formed is dependent on steric considerations. Assessment of the crystal structures shows that *N,N*-coordinated species (**1a** and **2a**) exhibit more steric hindrance in the form of H···H clashes between *p*-cym and **L**, than do *N,C*-coordinated species (**2b** and **3b**). *N,N*-coordinated species also show greater torsion angles in ligand **L**, than do *N,C*-coordinated species where **L** is very much planar. The torsion of **L** in **1a** and **2a** appears to show the aniline ring twisting to reduce clashing with the *p*-cym ligand. It is most likely that when X = Br or I, *N,N*-coordination is more difficult due to the increased halide size, hence producing greater steric crowding around the metal centre, pushing the organic ligands closer together. Increased steric crowding may entice coordination to occur *via* the cyclo-metalation route (Figure 3.14).

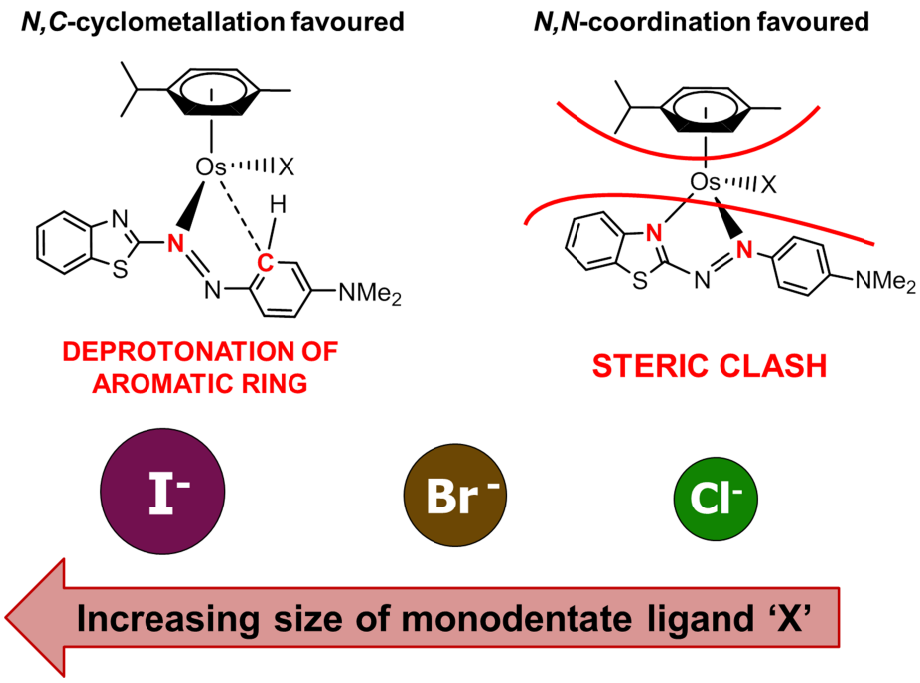

Figure 3.14. Diagram to illustrate how steric effects might dictate the ratios of products formed. *N,N*-coordination results in steric clashes between *p*-cym and **L**, and so is less viable when the monodentate ligand is large. *N,C*-coordination is preferred to relieve steric tension and involves spontaneous deprotonation of aromatic ring.

Preferential binding *via* cyclo-metalation could also be influenced by the weaker binding capability of benzothiazole in comparison to pyridine. The complex **FY026**, synthesised previously by Sadler's group contains an AZPY ligand analogous to **L** with distinct *N,N*-coordination[2] (Figure 3.15). Pyridine (the binding moiety in AZPY) is a good π-acceptor moiety because of strong aromaticity around the 6-membered ring; hence greater back-donation of electron density from the metal centre into the π*-orbitals of N. However, benzothiazole (the binding moiety of AZBTZ) is a weaker π-acceptor due to lack of aromaticity around the 5-membered ring, hence weaker back-donation into

π*-orbitals. Both moieties, pyridine and benzothiazole, are weak σ-donors, but the reduced π-acceptor capability of benzothiazole may also account for preferential *N,C*-coordination, as well as steric factors.

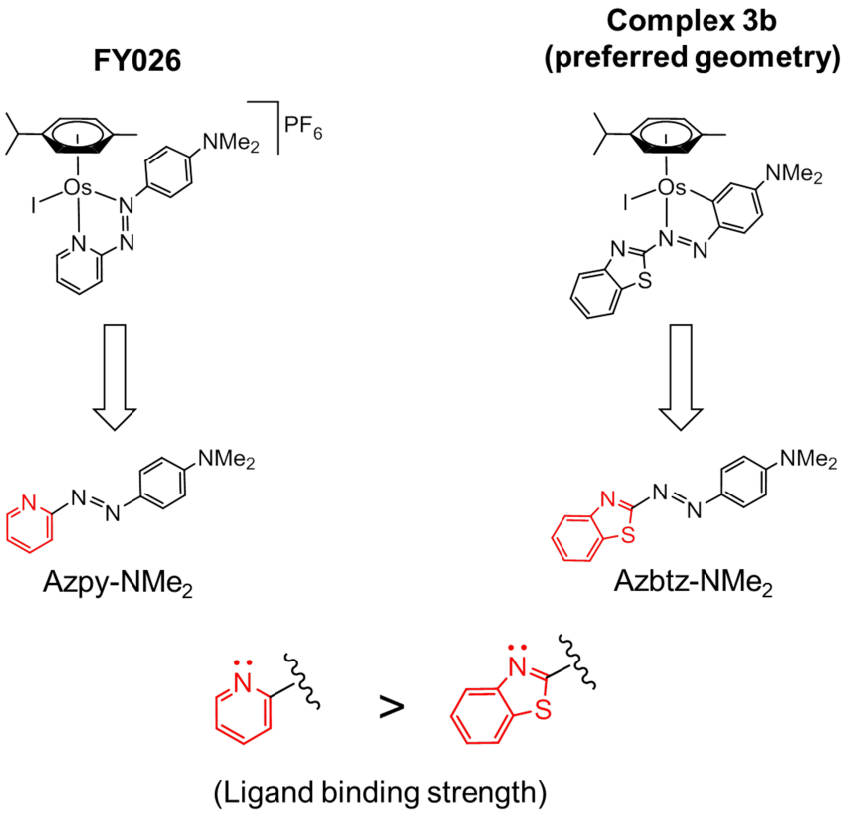

Figure 3.15. Comparison between **FY026** and **3b** in their preferred coordination geometries.

UV-Vis studies in aqueous media shows that the *N,N*-coordinated complex **1a**, undergoes a chemical change over a 24 h period, which is prevented in the presence of NaCl (100 mM). This indicates that the chemical change involves loss of the monodentate chloride ligand, and is likely a hydrolysis reaction. In contrast, *N,C*-coordinated complex **1b** shows no sign of decompostion over 24 h and exhibits a very stable Os-Cl bond.

3.4.3. Hindered arene rotation of 5

The iodido complex, **5**, was shown to possess a de-shielded aromatic hydrogen belonging to the *p*-cym ligand. A ^{1}H sel-NOE study confirmed that this proton is pushed in close proximity to an aromatic proton belonging to **L***. The steric crowding is likely a result of *N,N*-coordination, which in this case is forced due to blocking of the *ortho* positions on the aniline ring (preventing cyclo-metalation). It was also found that the chlorido complex **4** exhibited the same trend, with a de-shielded aromatic hydrogen on *p*-cym. *N,N*-coordinated structures that were formed with ligand **L** (**1a** and **2a**) do not exhibit the same trend. It is therefore likely that hindered rotation may also play some role in the de-shielding of the protons observed. The methyl groups at positions R^1 and R^2 in complexes **4** and **5** (Figure 3.3) may play a role in locking the *p*-cym ligand in a fixed orientation, hence hindering its rotation. No X-ray crystal structure was obtained for **4** or **5**, and further temperature-controlled ^{1}H NMR studies would be required confirm the presence of hindered *p*-cym rotation.[27]

3.4.4. Regio-specific aniline ring deuteration of 2b

Remarkably, complex **2b** undergoes deuteration of the aniline ring at the position next to the Os-C bond (*meta* H_a), but only in the presence of acid (HBr). On addition of 3 mol. equiv. of HBr the ^{1}H NMR signal of H_a disappeared along with its coupling to H_b, following first-order kinetics. The Mulliken partial charge calculations showed that the same carbon where deuteration occurs carries a greater negative partial charge (-0.461) than the other CH carbons making up

the aniline ring (-0.264 and -0.275). This may account for the acidic nature of H_a. Interestingly, its exchange with deuterium occurs under acidic conditions suggesting an associative mechanism of exchange (see Scheme 3.5). To the best of my knowledge, there are no literature examples of other complexes that undergo 'self-deuteration' by aromatic hydrogen exchange under acidic conditions. There are however examples of catalytic osmium complexes capable of deuterating organic molecules that undergo temporary binding to the osmium metal centre.[28,29]

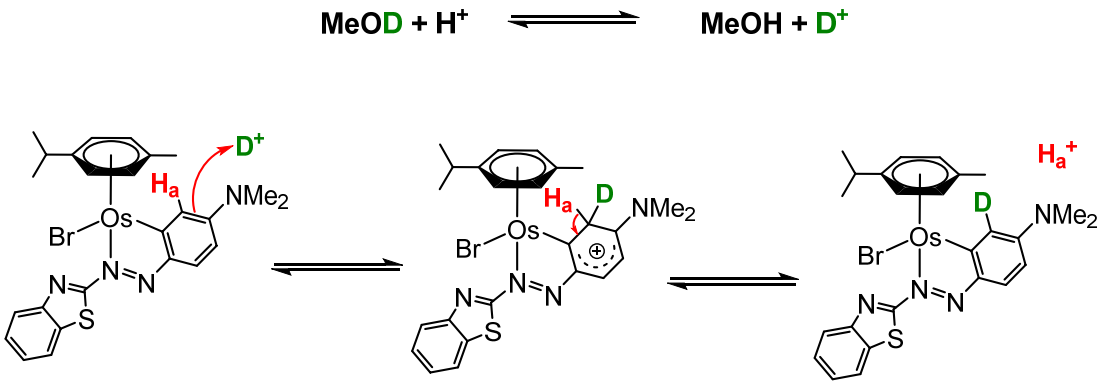

Scheme 3.5. Proposed mechanism for the associative exchange of H_a with deuterium in complex **2b** under acidic conditions in methanol-d_4.

3.5. Summary

This chapter has explored the novel synthesis of Os(II) *p*-cym phenylazobenzothiazole complexes, which adopt two different coordination geometries: *N,N*-coordination and *N,C*-coordination. Exploration of the crystallographic data suggests that *N,N*-coordination geometry leads to steric crowding around the metal centre, and so is formed as a minor product when

the halide monodentate ligand is large (X = I or Br). *N,C*-coordination requires C-H bond activation to form an osmacycle and occurs spontaneously in the absence of a base, most likely owing to the presence of the basic -NMe_2 group assisting in aromatic deprotonation. The mechanism of cyclo-metalation is not clear, but a S_E3 mechanism is speculated. Furthermore, *N,N*-coordinated species, **1a**, was shown to be unstable in aqueous media over 24 h, but stable over 24 h in the presence of 100 mM NaCl, indicating that the decomposition of **1a** involves loss of the monodentate ligand and likely relates to hydrolysis. In contrast, the *N,C*-coordinated analogue (**2b**) was stable over 24 h.

Complexes **4** and **5** were synthesised with intentional blocking of the C-H activation sites with methyl groups to force formation of *N,N*-coordinated geometries. This led to complexes with an unusually de-shielded aromatic *p*-cym proton. Upon analysis by ^{1}H sel-NOE the de-shielded proton in **5** was found to be in close proximity to a proton on the benzothiazole group, thus providing further evidence of steric crowding in *N,N*-coordinated species.

Unusual properties were also found for the *N,C*-coordinated complex, **2b**. In the presence of acid (HBr) in methanol-d_4, the *meta* H (neighbouring the Os-C bond) exchanges with deuterium and this was explored kinetically. Calculations of the Mulliken partial charges showed that an increased negative partial charge on the *meta* C may provide a reasonable explanation for this phenomenon.

The chemistry of novel complexes presented in this chapter has been explored in some depth. Unfortunately, due to the complexes very poor solubility in

aqueous media, it was not possible to progress with anti-cancer screening and other biological evaluations.

3.6. References

(1) Fu, Y.; Habtemariam, A.; Basri, A. M. B. H.; Braddick, D.; Clarkson, G. J.; Sadler, P. J. *Dalton Trans.* **2011**, *40*, 10553.

(2) Fu, Y.; Habtemariam, A.; Pizarro, A. M.; van Rijt, S. H.; Healey, D. J.; Cooper, P. A.; Shnyder, S. D.; Clarkson, G. J.; Sadler, P. J. *J. Med. Chem.* **2010**, *53*, 8192.

(3) Wang, M.; Funabiki, K.; Matsui, M. *Dyes Pigments* **2003**, *57*, 77.

(4) Matsumura, K.; Ono, M.; Hayashi, S.; Kimura, H.; Okamoto, Y.; Ihara, M.; Takahashi, R.; Mori, H.; Saji, H. *Med. Chem. Commun.* **2011**, *2*, 596.

(5) Shi, D. F.; Bradshaw, T. D.; Wrigley, S.; McCall, C. J.; Lelieveld, P.; Fichtner, I.; Stevens, M. F. G. *J. Med. Chem.* **1996**, *39*, 3375.

(6) Chua, M. S.; Shi, D. F.; Wrigley, S.; Bradshaw, T. D.; Hutchinson, I.; Shaw, P. N.; Barrett, D. A.; Stanley, L. A.; Stevens, M. F. G. *J. Med. Chem.* **1999**, *42*, 381.

(7) Hutchinson, I.; Jennings, S. A.; Vishnuvajjala, B. R.; Westwell, A. D.; Stevens, M. F. G. *J. Med. Chem.* **2001**, *45*, 744.

(8) Mortimer, C. G.; Wells, G.; Crochard, J. P.; Stone, E. L.; Bradshaw, T. D.; Stevens, M. F. G.; Westwell, A. D. *J. Med. Chem.* **2005**, *49*, 179.

(9) Mortimer, C. G.; Wells, G.; Crochard, J.-P.; Stone, E. L.; Bradshaw, T. D.; Stevens, M. F. G.; Westwell, A. D. *J. Med. Chem.* **2006**, *49*, 179.

(10) Hussein, B. H. M.; Azab, H. A.; El-Azab, M. F.; El-Falouji, A. I. *Eur. J. Med. Chem.* **2012**, *51*, 99.

(11) Ginzinger, W.; Mühlgassner, G.; Arion, V. B.; Jakupec, M. A.; Roller, A.; Galanski, M.; Reithofer, M.; Berger, W.; Keppler, B. K. *J. Med. Chem.* **2012**, *55*, 3398.

(12) Spillane, C. B.; Dabo, M. N. V.; Fletcher, N. C.; Morgan, J. L.; Keene, F. R.; Haq, I.; Buurma, N. J. *J. Inorg. Biochem.* **2008**, *102*, 673.

(13) Oi, S.; Fukita, S.; Hirata, N.; Watanuki, N.; Miyano, S.; Inoue, Y. *Org. Lett.* **2001**, *3*, 2579.

(14) Ryabov, A. D.; Soukharev, V. S.; Alexandrova, L.; Le Lagadec, R.; Pfeffer, M. *Inorg. Chem.* **2003**, *42*, 6598.

(15) Davies, D. L.; Donald, S. M. A.; Al-Duaij, O.; Macgregor, S. A.; Pölleth, M. *J. Am. Chem. Soc.* **2006**, *128*, 4210.

(16) Boutadla, Y.; Al-Duaij, O.; Davies, D. L.; Griffith, G. A.; Singh, K. *Organometallics* **2009**, *28*, 433.

(17) Li, B.; Roisnel, T.; Darcel, C.; Dixneuf, P. H. *Dalton Trans.* **2012**, *41*, 10934.

(18) Abbenhuis, H. C. L.; Pfeffer, M.; Sutter, J. P.; de Cian, A.; Fischer, J.; Ji, H. L.; Nelson, J. H. *Organometallics* **1993**, *12*, 4464.

(19) Clark, A. M.; Rickard, C. E. F.; Roper, W. R.; Wright, L. J. *Organometallics* **1999**, *18*, 2813.

(20) Fernandez, S.; Pfeffer, M.; Ritleng, V.; Sirlin, C. *Organometallics* **1999**, *18*, 2390.

(21) Djukic, J. P.; Berger, A.; Duquenne, M.; Pfeffer, M.; de Cian, A.; Kyritsakas-Gruber, N.; Vachon, J.; Lacour, J. *Organometallics* **2004**, *23*, 5757.

(22) Cerón-Camacho, R.; Morales-Morales, D.; Hernandez, S.; Le Lagadec, R.; Ryabov, A. D. *Inorg. Chem.* **2008**, *47*, 4988.

(23) Ferrer Flegeau, E.; Bruneau, C.; Dixneuf, P. H.; Jutand, A. *J. Am. Chem. Soc.* **2011**, *133*, 10161.

(24) Ackermann, L. *Chem. Rev.* **2011**, *111*, 1315.

(25) Baya, M.; Eguillor, B.; Esteruelas, M. A.; Lledós, A.; Oliván, M.; Oñate, E. *Organometallics* **2007**, *26*, 5140.

(26) Zhang, Z.; Di, D.; Zhai, J.; Wu, L.; Zhu, Q.; Xu, Y.; Huang, R. *Chem. Res. Chin. Univ.* **2014**, *30*, 185.

(27) Carrión, M. C.; Sepúlveda, F.; Jalón, F. A.; Manzano, B. R.; Rodríguez, A. M. *Eur. J. Inorg. Chem.* **2013**, *2013*, 217.

(28) Bossi, G.; Putignano, E.; Rigo, P.; Baratta, W. *Dalton Trans.* **2011**, *40*, 8986.

(29) Eguillor, B.; Esteruelas, M. A.; García-Raboso, J.; Oliván, M.; Oñate, E. *Organometallics* **2009**, *28*, 3700.

Chapter 4

Osmium(II) Arene Complexes of Phenylazopyridines

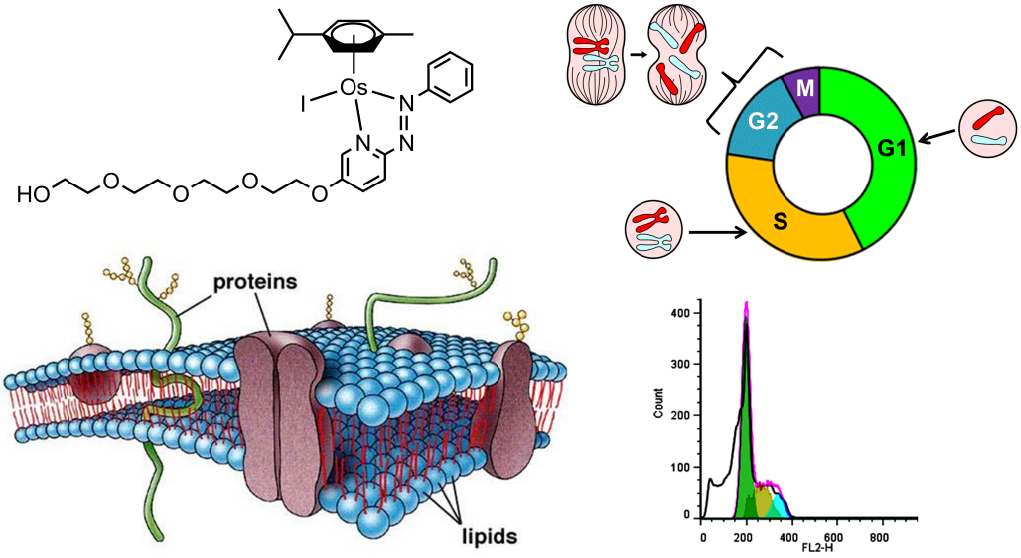

4.1. Introduction

The synthesis and chemistry of azobenzenes and pyridine-based azobenzenes (see Figure 1.1) has been a matter of scientific interest for many years. Traditionally, azobenzene was synthesised by an azo-coupling condensation reaction between aniline and nitrosobenzene, which can be catalysed by acidic or basic conditions.[1-4] However, there are now multiple strategies for forming azo-bonds between two aryl groups.[5-7] Interestingly, azobenzenes and pyridine based azobenzenes can be cleanly photo-isomerised from their *trans* to *cis* configuration, and the reverse process can be induced either by visible light or thermally. Such processes have proved useful in applications such as photo-switchable ion-channel blockers, photo-control of the activity of enzymes, switchable catalysts and liquid crystals.[7,8]

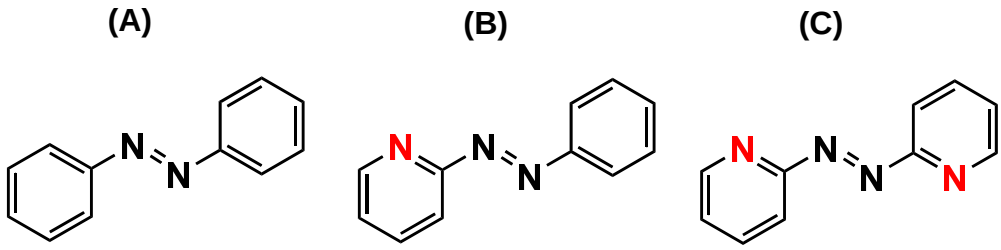

Figure 1.1. The structures of (A) azobenzene, (B) phenyazopyridine (AZPY), and (C) azo*bis*pyridine (ABPY).

The first AZPY complexes of Ru(II) were synthesized in 1979 and were shown to exhibit strong dπ-pπ interactions, which produced a stabilising effect towards Ru(II).[9] The stabilising effects of AZPY ligands were later utilised by the Sadler group in Ru(II) and Os(II) arene anti-cancer complexes (see Chapter 1,

Sections **1.3.3.2** and **1.3.4.3**) Interestingly, Os(II) arene complexes of ABPY[10] and Ru(II) arene complexes of AZPY[11] have unique redox properties. Using cyclic voltammetry, two reduction potentials were observed that are attributed to the reduction of the azo-bond.[10] The azo-bond contains a low lying π*-orbital which can receive two electrons (see Scheme 4.1). This is described in greater detail for Ru(II) arene AZPY complexes in Chapter 1, Section **1.3.3.2**.

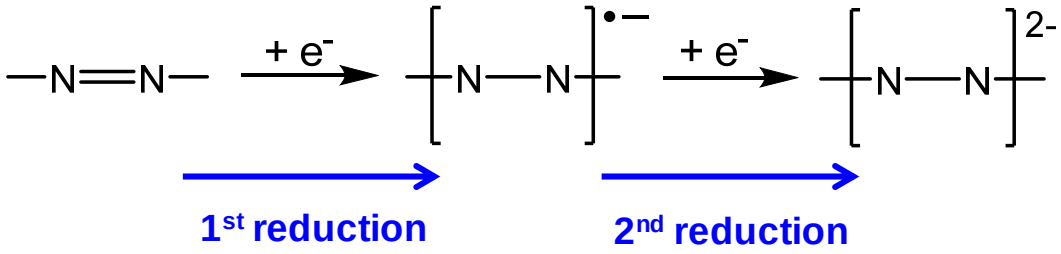

Scheme 4.1. Two successive one-electron reductions of the azo-bond.

Piano-stool Os(II) arene AZPY complexes with monodentate halide ligands exhibit some of the most potent anti-proliferative activities of all osmium complexes within the Sadler group. Their mechanism(s) of activation differ greatly from earlier Os(II) arene complexes with σ-donor bidentate ligands, which rely primarily on monodentate ligand dissociation followed by DNA binding.[12] In contrast, the strong π-acceptor character of AZPYs produces different characteristics in their complexes, such as resistance towards hydrolysis and mechanism(s) of action that involve raising intracellular levels of ROS.[13,14]

The main aim of the work in this chapter was to synthesise new Os(II) arene AZPY complexes, expand on our library of complexes, and improve on anti-cancer activity and drug characteristics such as aqueous solubility, based on the structure-activity relationships (SARs) that have already determined for complexes of this class.[15] Monodentate iodide ligands are known to improve anti-cancer activity drastically over chloride ligands. Bip arene ligands enhance activity over *p*-cym ligands, and substituents on the AZPY ligand positioned on the pyridyl and phenyl moieties *para* to the azo-bond also maximise activity. One of the key issues to resolve is poor drug solubility in aqueous media, which is an inherent issue for Os(II) arene AZPY complexes. This could hinder the administration of drugs to patients, hence their progress into clinical trials. Tackling solubility issues needs to be overcome ideally without drastically compromising anti-cancer activity. There are 3 main methods in which drug solubility can be improved: (1) The addition of polar substituents on the AZPY ligand. (2) Reducing crystal lattice energies of complexes by changing the counter anion. (3) Disrupting molecular planarity/symmetry and crystal packing by re-positioning substituents or changing substituents for bulkier groups. The last approach has proved useful for increasing the solubility of small molecule drugs, whilst maintaining their lipophilicity.[16]

Lipinski's 'rule of five' (Ro5) is a general rule of thumb, formulated by Christopher A. Lipinski in 1997 to determine whether a drug candidate has particular pharmacological properties that make it suitable for absorption, distribution, metabolism and excretion within the human body.[17] Ro5 predicts that good absorption and permeation is more likely when the molecular

structure has ≤5 H-bond donors, ≤10 H-bond acceptors, a molecular weight of ≤500 g/mol, and a Log $P_{o/w}$ of ≤5. Ignoring counter-ions such as PF_6, Os(II) arene AZPY complexes comply with Ro5 specifications except for their high molecular masses, which are typically higher than 500 g/mol due to the presence of Os and I atoms. The reasons for lower drug absorption when the molecular mass is ≥500 g/mol are not fully understood and it is purely observational. However, there are outliers such as vitamin B_{12} (1355.37 g/mol), which like Os(II) arene AZPY drugs is also a metal complex.[18] A variation to the Ro5 states that the effective range of Log $P_{o/w}$ is -0.4 to 5.6 with an average value of 2.52.[19] Furthermore, an excessive number of H-bond donor or acceptor groups can impair permeability across the cell membrane.

Herein, a novel synthesis is outlined for the attachment of alkoxy and water solubilising glycolic side-chains to AZPY ligands. A new range of Os(II) arene AZPY complexes were synthesized and the SARs were explored for anti-cancer activity against A2780 cells, aqueous solubility in 100 mM $NaCl_{(aq)}$, HPLC capacity factor, and cellular uptake. Furthermore, variation of the counter anion was explored as a method of improving aqueous solubility, and the monodentate ligand was varied with alternatives (Br^-, N_3^- and SCN^-) to determine if anticancer activity can be improved upon. Figure 4.2 lists all of the Os(II) arene AZPY complexes synthesised (**6**-**35**). Selected complexes were further tested against other cell lines (MCF-7, SUNE1, OE19 and MRC-5), and their ability to induce apoptosis, ROS elevation, and cell cycle arrest in A2780 cells was explored.

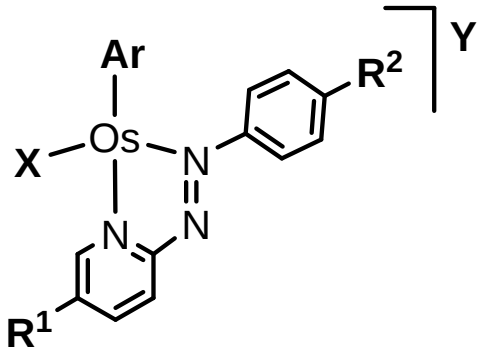

Complex	X	R^1	R^2	Ar	Y	AZPY ligand	Max solubility in 100 mMNaCl (µM)	IC_{50} against A2780 cells (µM)	Capacity factor (*K*)	Cell uptake in A2780 cells (ng Os /10^6)
6	I	MeO	H	*p*-cym	PF_6^-	**L1**	9±2	n.d.	n.d.	n.d.
7	I	MeO	H	*p*-cym	$CF_3SO_3^-$	**L1**	405±19	0.5±0.1	2.61±0.09	8±2
8	Cl	EtO	H	*p*-cym	PF_6^-	**L2**	118±7	15.1±0.5	1.94±0.06	11.0±0.8
9	Br	EtO	H	*p*-cym	PF_6^-	**L2**	124±8	14.1±0.9	2.61±0.09	19±1
10	I	EtO	H	*p*-cym	PF_6^-	**L2**	52±2	0.92±0.02	3.81±0.09	31±2
11	I	EtO	H	*p*-cym	$CF_3SO_3^-$	**L2**	185±9	0.9±0.2	4.0±0.1	30±2
12	I	EtO	H	*p*-cym	IO_3^-	**L2**	341±3	1.6±0.3	n.d.	n.d.
13	I	EtO	H	bip	$CF_3SO_3^-$	**L2**	26±2	0.51±0.02	3.7±0.1	21±1
14	I	^{n}PrO	H	*p*-cym	PF_6^-	**L3**	14.9±0.7	0.33±0.02	6.0±0.1	10±2
15	I	^{i}PrO	H	*p*-cym	PF_6^-	**L4**	75±2	0.30±0.09	5.4±0.1	n.d.
16	I	^{n}BuO	H	*p*-cym	PF_6^-	**L5**	1.7±0.3	10.2±0.7	9.4±0.2	n.d.

17	Cl	$HOCH_2CH_2O$	H	*p*-cym	PF_6^-	**L6**	1686±63	>140	0.57±0.03	3.93±0.09
18	Br	$HOCH_2CH_2O$	H	*p*-cym	PF_6^-	**L6**	640±4	>130	0.74±0.03	3.00±0.08
19	I	$HOCH_2CH_2O$	H	*p*-cym	PF_6^-	**L6**	412±19	20.7±0.1	1.04±0.03	12±2
20	I	$HOCH_2CH_2O$	H	bip	PF_6^-	**L6**	93±2	2.37±0.09	0.99±0.07	n.d.
21	I	$H(OCH_2CH_2)_2O$	H	*p*-cym	PF_6^-	**L7**	721±17	2.04±0.06	1.09±0.02	n.d.
22	I	$Me(OCH_2CH_2)_2O$	H	*p*-cym	PF_6^-	**L10**	239±5	1.80±0.09	2.63±0.03	n.d.
23	I	$Et(OCH_2CH_2)_2O$	H	*p*-cym	PF_6^-	**L12**	132±6	0.68±0.03	0.74±0.03	n.d.
24	I	$Et(OCH_2CH_2)_2O$	H	bip	$CF_3SO_3^-$	**L12**	61±3	1.9±0.2	3.53±0.06	n.d.
25	I	$H(OCH_2CH_2)_3O$	H	*p*-cym	PF_6^-	**L8**	680±13	12±1	1.11±0.02	n.d.
26	I	$Me(OCH_2CH_2)_3O$	H	*p*-cym	PF_6^-	**L11**	359±31	2.1±0.2	2.52±0.04	n.d.
27	I	$Et(OCH_2CH_2)_3O$	H	*p*-cym	PF_6^-	**L13**	232±8	2.6±0.4	3.59±0.06	n.d.
28	I	$H(OCH_2CH_2)_4O$	H	*p*-cym	PF_6^-	**L9**	656±26	7.6±0.6	1.11±0.02	n.d.
29	Cl	Br	OH	*p*-cym	PF_6^-	**L14**	n.d.	2.0±0.2	n.d.	n.d.
30	Br	Br	OH	*p*-cym	PF_6^-	**L14**	n.d.	1.2±0.1	n.d.	n.d.
31	I	Br	OH	*p*-cym	PF_6^-	**L14**	n.d.	0.54±0.02	n.d.	n.d.
32	Cl	F_3C	OH	*p*-cym	PF_6^-	**L15**	n.d.	1.4±0.1	n.d.	n.d.
33	Br	F_3C	OH	*p*-cym	PF_6^-	**L15**	n.d.	0.74±0.08	n.d.	n.d.
34A	*S*-SCN	EtO	H	*p*-cym	PF_6^-	**L2**	n.d.	>50	n.d.	n.d.
34B	*N*-SCN	EtO	H	*p*-cym	PF_6^-	**L2**	n.d.	25-50	n.d.	n.d.
35	N_3	EtO	H	*p*-cym	PF_6^-	**L2**	n.d.	1.2±0.2	n.d.	n.d.

***Highlited green:** Complexes with sub micro-molar IC_{50} values against A2780 cells.

Figure 4.2. List of all the Os(II) arene AZPY complexes synthesised, **6**-**35**, using **L1**-**L15**, and their properties.

4.2. Experimental

4.2.1. Materials

Osmium dimers, $[Os(\eta^6\text{-arene})X_2]_2$, (where X= Cl, Br or I and arene = *p*-cym or bip) were prepared as described in Chapter 2, Section **2.1.2**. 2-Amino-5-fluoropyridine, nitrosobenzene, 5-bromo-2-hydrazinopyridine, 2-hydrazinyl-5-trifluoromethylpyridine, *p*-benzoquinone, benzene, and 70% perchloric acid were purchased from Sigma Aldrich, and sodium hydroxide from Fisher Scientific. The alcohols and glycols used to synthesise RO-AZPY ligands were purchased from Sigma Aldrich, with the exception of ethylene glycol and diethylene glycol, which were obtained from Alfa Aesar. Deionised water was prepared as described in Chapter 2, Section **2.1.1.1**. Deuterated NMR solvents were purchased from Cambridge Isotope Laboratories Inc. and Sigma Aldrich. Phosphate buffer solution was prepared as described in Chapter 2, Section **2.1.1.1**.

4.2.2. Synthesis

2-(Phenylazo)-5-fluoropyridine (5-F-AZPY).[15] 2-Amino-5-fluoropyridine (1.00 g, 8.92 mmol) was stirred in a 1:4 mixture of benzene (5 mL) and water (20 mL). Sodium hydroxide (4.28 g, 0.11 mol) was added and the mixture was left to stir for 10 min at 50 ºC under N_2. Nitrosobenzene (0.96 g, 8.96 mmol) was added to the stirring mixture and an instant colour change to green was observed. The mixture was heated at 100 ºC overnight under N_2, and turned dark red-brown. The layers were separated and the aqueous layer was washed with toluene (3 x

50 mL). The combined organic extracts were washed with water (3 x 30 mL), dried over $MgSO_4$, and filtered. The solvent was removed under reduced pressure to yield an oily red precipitate. The precipitate was then dissolved in a minimum amount of DCM and purified *via* flash column chromatography (SiO_2, DCM, R_f = 0.52). The selected fractions were combined and the solvent was removed under reduced pressure to yield an orange precipitate. The product was dried overnight in a vacuum desiccator. Yield: 469.1 mg, (26%). ^{1}H NMR (400 MHz, $CDCl_3$): δ 8.52 (d, 1H, J = 2.9 Hz), 7.98-7.96 (m, 2H), 7.83 (dd, 1H, J = 8.8, 4.3 Hz), 7.55-7.54 (m, 1H), 7.49-7.46 (m, 3H). ESI-MS calculated for $C_{11}H_8N_3F + H^+$: m/z 202.1. Found: 202.1. CHN analysis: Found: C, 65.39%; H, 3.90%; N, 20.71%. Calculated for $C_{11}H_8N_3F$: C, 65.66%; H, 4.01%; N, 20.88%.

4.2.2.1. General procedure for synthesis of RO-AZPY ligands

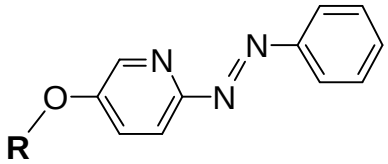

2-(Phenylazo)-5-fluoropyridine (100.00 mg, 0.50 mmol) was dissolved in ROH (20 mL) and an aqueous potassium hydroxide solution (5 mol. equiv.) was added. The mixture was either heated to reflux or heated at 120 °C (depending on b.p. of ROH) for 18 h. The product was extracted with DCM (20 mL) and washed with water (3 x 20 mL). The DCM extract was dried over $MgSO_4$, filtered, and the solvent was removed under reduced pressure. Some reaction mixtures required vacuum distillation to remove excess ROH. Purification was

usually carried out by either re-crystallisation or SiO_2 column chromatography. The product was dried overnight on a vacuum line.

5-MeO-AZPY (L1). (ROH = methanol). The crude product was purified *via* flash column chromatography (SiO_2, Et_2O, R_f = 0.40). The selected fractions were combined and the solvent was removed under reduced pressure to give a pale orange precipitate. Yield: 62.1 mg, (59%). ^{1}H NMR (400 MHz, $CDCl_3$): δ 8.33 (d, 1H, J = 3.0 Hz), 7.96-7.93 (m, 2H), 7.81 (d, 1H, J = 8.8 Hz), 7.47-7.40 (m, 3H), 7.30 (dd, 1H, J = 8.8, 3.0 Hz), 3.88 (s, 3H). ESI-MS calculated for $C_{12}H_{11}N_3O$ + H^+: m/z 214.1. Found: 214.0. CHN analysis: Found: C, 67.01%; H, 5.19%; N, 19.31%. Calculated for $C_{12}H_{11}N_3O$: C, 67.59%; H, 5.20%; N, 19.71%.

5-EtO-AZPY (L2). (ROH = ethanol). The crude product was re-crystallised from a minimum amount of hot Et_2O. Orange crystals were collected *via* vacuum filtration and washed with ice-cold Et_2O. Yield: 78.1 mg, (69%). ^{1}H NMR (400 MHz, $CDCl_3$): δ 8.31 (d, 1H, J = 3.0 Hz), 7.95-7.92 (m, 2H), 7.79 (d, 1H, J = 8.8 Hz), 7.47-7.39 (m, 3H), 7.27 (dd, 1H, J = 8.8, 3.0 Hz), 4.10 (q, 2H, J = 7.0 Hz), 1.40 (t, 3H, J = 7.0 Hz). ESI-MS calculated for $C_{13}H_{13}N_3O$ + H^+: m/z 228.1. Found: 228.0. CHN analysis: Found: C, 68.47%; H, 5.72%; N, 18.39%. Calculated for $C_{13}H_{13}N_3O$: C, 68.70%; H, 5.77%; N, 18.49%.

5-^{n}PrO-AZPY (L3). (ROH = n-propanol). The crude product was purified *via* flash column chromatography (SiO_2, Et_2O:n-hexane 1:1, R_f = 0.30). The selected fractions were combined and the solvents were removed under reduced pressure to give an orange precipitate. Yield: 102.1 mg, (85%). ^{1}H NMR (400 MHz, $CDCl_3$): δ 8.30 (d, 1H, J = 3.0 Hz), 7.94-7.91 (m, 2H), 7.76 (d,

1H, J = 8.8 Hz), 7.44-7.38 (m, 3H), 7.24 (dd, 1H, J = 8.8, 3.0 Hz), 3.95 (t, 2H, J = 6.5 Hz), 1.81-1.72 (m, 2H), 0.97 (t, 3H, J = 7.4 Hz). ESI-MS calculated for $C_{14}H_{15}N_3O + H^+$: m/z 242.1. Found: 242.1. CHN analysis: Found: C, 69.50%; H, 6.24%; N, 17.25%. Calculated for $C_{14}H_{15}N_3O$: C, 69.69%; H, 6.27%; N, 17.41%.

5-^{i}PrO-AZPY (L4). (ROH = isopropanol). The crude product was purified *via* flash column chromatography (SiO_2, Et_2O:n-hexane 1:1, R_f = 0.29). The selected fractions were combined and the solvents were removed under reduced pressure to give an orange viscous oil. Yield: 42.6 mg, (35%). ^{1}H NMR (400 MHz, $CDCl_3$): δ 8.30 (d, 1H, J = 3.0 Hz), 7.96-7.93 (m, 2H), 7.79 (d, 1H, J = 8.8 Hz), 7.47-7.40 (m, 3H), 7.27 (dd, 1H, J = 8.8, 3.0 Hz), 4.63 (sept., 1H, J = 6.1 Hz), 1.35 (d, 6H, J = 6.1 Hz). ESI-MS calculated for $C_{14}H_{15}N_3O + H^+$: m/z 242.1. Found: 242.1.

5-^{n}BuO-AZPY (L5). (ROH = n-butanol). Excess ROH was removed by vacuum distillation. The crude product was dissolved in Et_2O and filtered. The filtrate was collected and the solvent removed under reduced pressure, resulting in an orange precipitate. Yield: 102.4 mg, (81%). ^{1}H NMR (400 MHz, $CDCl_3$): δ 8.29 (d, 1H, J = 2.9 Hz), 7.94-7.91 (m, 2H), 7.76 (d, 1H, J = 8.8 Hz), 7.45-7.37 (m, 3H), 7.23 (dd, 1H, J = 8.8, 3.0 Hz), 3.97 (t, 2H, J = 6.5 Hz), 1.71-1.70 (m, 2H), 1.41-1.40 (m, 2H), 0.89 (t, 3H, J = 7.4 Hz). ESI-MS calculated for $C_{15}H_{17}N_3O + H^+$: m/z 256.1. Found: 256.1.

5-$HOCH_2CH_2O$-AZPY (L6). (ROH = ethylene glycol). The crude product was dissolved in a minimum amount of hot DCM and the product was re-crystallised upon adding Et_2O. An orange precipitate was collected *via* vacuum filtration and

washed with ice-cold Et_2O. Yield: 64.7 mg, (54%). ^1H NMR (400 MHz, $CDCl_3$): δ 8.45 (d, 1H, J = 2.9 Hz), 8.04-8.01 (m, 2H), 7.89 (d, 1H, J = 8.8 Hz), 7.55-7.48 (m, 3H), 7.43 (dd, 1H, J = 8.8, 3.0 Hz), 4.26-4.24 (m, 2H), 4.06-4.04 (m, 2H). ESI-MS calculated for $C_{13}H_{13}N_3O_2$ $+Na^+$: m/z 266.1. Found: 266.0. CHN analysis: Found: C, 63.95%; H, 5.35%; N, 17.03%. Calculated for $C_{13}H_{13}N_3O_2$: C, 64.19%; H, 5.39%; N, 17.27%.

5-HO(CH_2CH_2O)$_2$-AZPY (L7). (ROH = diethylene glycol). The crude product was re-crystallised from a minimum amount of hot DCM. An orange precipitate was collected *via* vacuum filtration and washed with ice-cold Et_2O. Yield: 51.3 mg, (36%). ^1H NMR (400 MHz, $CDCl_3$): δ 8.46 (d, 1H, J = 2.9 Hz), 8.04-8.01 (m, 2H), 7.89 (d, 1H, J = 8.8 Hz), 7.55-7.48 (m, 3H), 7.43 (dd, 1H, J = 8.8, 3.0 Hz), 4.32-4.30 (m, 2H), 3.95-3.93 (m, 2H), 3.81-3.79 (m, 2H), 3.71-3.69 (m, 2H). ESI-MS calculated for $C_{15}H_{17}N_3O_3 + H^+$: m/z 288.1. Found: 288.1.

5-HO(CH_2CH_2O)$_3$-AZPY (L8). (ROH = triethylene glycol). The crude product was dissolved in Et_2O and filtered. The filtrate was collected and the solvent removed under reduced pressure, resulting in an orange viscous oil. Yield: 132.9 mg, (81%). ^1H NMR (400 MHz, $CDCl_3$): δ 8.32 (d, 1H, J = 2.9 Hz), 7.92-7.88 (m, 2H), 7.74 (d, 1H, J = 8.8 Hz), 7.43-7.36 (m, 3H), 7.29 (dd, 1H, J = 8.8, 3.0 Hz), 4.16-4.14 (m, 2H), 3.79-3.77 (m, 2H), 3.65-3.61 (m, 4H), 3.58-3.56 (m, 2H), 3.51-3.49 (m, 2H). ESI-MS calculated for $C_{17}H_{21}N_3O_4 + H^+$: m/z 332.2. Found: 332.1.

5-HO(CH_2CH_2O)$_4$-AZPY (L9). (ROH = tetraethylene glycol). The crude product was dissolved in Et_2O and filtered. The filtrate was collected and the solvent

removed under reduced pressure, resulting in an orange viscous oil. Yield: 151.3 mg, (81%). ^{1}H NMR (400 MHz, $CDCl_3$): δ 8.35 (d, 1H, J = 3.0 Hz), 7.95-7.92 (m, 2H), 7.79 (d, 1H, J = 8.8 Hz), 7.44-7.39 (m, 3H), 7.33 (dd, 1H, J = 8.8, 3.0 Hz), 4.22-4.20 (m, 2H), 3.84-3.82 (m, 2H), 3.68-3.58 (m, 11H), 3.53-3.51 (m, 2H). ESI-MS calculated for $C_{19}H_{25}N_3O_5$ + Na^+: m/z 398.2. Found: 398.2.

5-MeO(CH_2CH_2O)$_2$-AZPY (L10). (ROH = diethylene glycol monomethyl ether). The crude product was dissolved in MeOH and decanted, removing a white oily substance. Excess ROH was removed by vacuum distillation and the product was dried, resulting in an orange viscous oil. Yield: 148.0 mg, (99%). ^{1}H NMR (400 MHz, $CDCl_3$): δ 8.41 (d, 1H, J = 3.0 Hz), 8.01-7.98 (m, 2H), 7.85 (d, 1H, J = 8.8 Hz), 7.52-7.46 (m, 3H), 7.38 (dd, 1H, J = 8.8, 3.0 Hz), 4.28-4.25 (m, 2H), 3.90-3.88 (m, 2H), 3.72-3.70 (m, 2H), 3.57-3.55 (m, 2H), 3.37 (s, 3H). ESI-MS calculated for $C_{16}H_{19}N_3O_3$ + Na^+: m/z 324.1. Found: 324.1.

5-MeO(CH_2CH_2O)$_3$-AZPY (L11). (ROH = triethylene glycol monomethyl ether). Excess ROH was removed by vacuum distillation. The crude product was dissolved in Et_2O and filtered. The filtrate was collected and the solvent removed under reduced pressure, resulting in an orange viscous oil. Yield: 154.0 mg, (90%). ^{1}H NMR (400 MHz, $CDCl_3$): δ 8.38 (d, 1H, J = 2.9 Hz), 7.98-7.96 (m, 2H), 7.82 (d, 1H, J = 8.8 Hz), 7.50-7.44 (m, 3H), 7.35 (dd, 1H, J = 8.8, 2.9 Hz), 4.23-4.21 (m, 2H), 3.87-3.85 (m, 2H), 3.71-3.69 (m, 2H), 3.65-3.60 (m, 4H), 3.51-3.49 (m, 2H), 3.33 (s, 3H). ESI-MS calculated for $C_{18}H_{23}N_3O_4$ + H^+: m/z 368.1. Found: 368.1.

5-EtO(CH_2CH_2O)$_2$-AZPY (L12). (ROH = diethylene glycol monoethyl ether). Excess ROH was removed by vacuum distillation. The crude product was dissolved in Et_2O and filtered. The filtrate was collected and the solvent removed under reduced pressure, resulting in an orange viscous oil. Yield: 135.1 mg, (86%). ^{1}H NMR (400 MHz, $CDCl_3$): δ 8.33 (d, 1H, J = 3.0 Hz), 7.93-7.90 (m, 2H), 7.76 (d, 1H, J = 8.8 Hz), 7.44-7.36 (m, 3H), 7.29 (dd, 1H, J = 8.8, 3.0 Hz), 4.18-4.16 (m, 2H), 3.82-3.80 (m, 2H), 3.64-3.62 (m, 2H), 3.53-3.51 (m, 2H), 3.43 (q, 2H, J = 7.0 Hz), 1.12 (t, 3H, J = 7.0 Hz). ESI-MS calculated for $C_{17}H_{22}N_3O_3 + H^+$: m/z 316.2. Found: 316.1.

5-EtO(CH_2CH_2O)$_3$-AZPY (L13). (ROH = triethylene glycol monoethyl ether). Excess ROH was removed by vacuum distillation. The crude product was dissolved in Et_2O and filtered. The filtrate was collected and the solvent removed under reduced pressure, resulting in an orange viscous oil. Yield: 170.8 mg, (96%). ^{1}H NMR (400 MHz, $CDCl_3$): δ 8.33 (d, 1H, J = 2.9 Hz), 7.94-7.91 (m, 2H), 7.77 (d, 1H, J = Hz), 7.46-7.39 (m, 3H), 7.30 (dd, 1H, J = 8.8, 2.9 Hz), 4.18-4.15 (m, 2H), 3.82-3.79 (m, 2H), 3.67-3.48 (m, 6H), 3.42 (q, 2H, J = 7.0 Hz), 1.11 (t, 3H, J = 7.0 Hz). ESI-MS calculated for $C_{19}H_{25}N_3O_4 + H^+$: m/z 382.2. Found: 382.1.

5-bromo-2-(4-hydroxyphenylazo)pyridine (Br-AZPY-OH) (L14). *p*-Benzoquinone (316.0 mg, 2.93 mmol) was dissolved in deionised water (50 mL) and perchloric acid (70% v/v, 2.6 mL) was added. A solution of 5-bromo-2-hydrazinopyridine (500.0 mg, 2.66 mmol) in MeOH (10 mL) was added drop-wise to the stirring mixture. The mixture turned red-brown and was stirred for 18 h at ambient temperature. The pH was neutralised with the drop-wise addition

of aqueous sodium hydroxide (6 M). The product was extracted with ethyl acetate (3 x 50 mL) and washed with water (3 x 50 mL). The mixture was concentrated under reduced pressure and placed in the freezer overnight. The resulting brown precipitate was collected *via* vacuum filtration and washed with ice-cold EtOH (2 x 1 mL) and Et_2O (2 x 5 mL). Yield: 495.5 mg (67%). ^{1}H NMR (400 MHz, CD_3OD): δ 8.73 (d, 1H, J = 2.4 Hz), 8.19 (dd, 1H, J = 8.6, 2.4 Hz), 7.93-7.92 (m, 2H), 7.76 (d, 1H, J = 8.6 Hz), 6.96-6.94 (m, 2H). ESI-MS calculated for $C_{11}H_8BrN_3O + H^+$: m/z 278.0. Found: 277.9. CHN analysis: Found: C, 47.28%; H, 2.80%; N, 14.82%. Calculated for $C_{11}H_8BrN_3O$: C, 47.51%; H, 2.90%; N, 15.11%.

5-trifluoromethyl-2-(4-hydroxyphenylazo)pyridine (F_3C-AZPY-OH) (L15). *p*-Benzoquinone (343.0 mg, 3.2 mmol) was dissolved in deionised water (50 mL) and perchloric acid (70% v/v, 2.6 mL) was added. A solution of 2-hydrazinyl-5-trifluoromethylpyridine (511.3 mg, 22.9 mmol) in MeOH (10 mL) was added drop-wise to the stirring mixture. The mixture turned dark red and was stirred for 18 h at ambient temperature. The pH was neutralised with the drop-wise addition of aqueous sodium hydroxide (6 M). The product was extracted with ethyl acetate (3 x 50 mL) and washed with water (3 x 50 mL). The mixture was concentrated under reduced pressure and placed in the freezer overnight. The resulting brown precipitate was collected *via* vacuum filtration and washed with ice-cold EtOH (2 x 1 mL) and Et_2O (2 x 5 mL). Yield: 266.2 mg (34%). ^{1}H NMR (400 MHz, CD_3OD): δ 8.97-8.96 (m, 1H), 8.33 (dd, 1H, J = 8.6, 2.3 Hz), 7.99-7.94 (m, 3H), 6.98-6.96 (m, 2H). ESI-MS calculated for $C_{12}H_8F_3N_3O + Na^+$: m/z

290.1. Found: 290.0. CHN analysis: Found: C, 53.14%; H, 2.88%; N, 15.19%. Calculated for $C_{12}H_8F_3N_3O$: C, 53.94%; H, 3.02%; N, 15.73%.

4.2.2.2. General procedure for synthesis of Os(II) arene AZPY complexes

$[Os(\eta^6\text{-arene})X_2]_2$ (where X = Cl, Br or I, and arene = *p*-cym or bip) was dissolved in EtOH (10 mL), and a solution of the AZPY ligand (2.1 mol. equiv.) in EtOH (5 mL) was added drop-wise. The mixture was stirred for 18 h at ambient temperature, then filtered through glass microfibre to remove a black precipitate and NH_4PF_6, $NH_4CF_3SO_3$ or KIO_3 (10 mol. equiv.) were added. Complexes were isolated using either method 1 or 2. Method 1 involves obtaining the product *via* re-crystallisation. Some complexes were difficult to re-crystallise and hence method 2 was employed.

Method 1. The mixture was concentrated under reduced pressure to ~3 mL and placed in the freezer overnight. A dark crystalline precipitate formed, which was collected *via* vacuum filtration, and washed with ice-cold EtOH (2 x 1 mL) and Et_2O (2 x 5 mL), and dried overnight in a vacuum desiccator.

Method 2. The mixture was concentrated under reduced pressure to ~3 mL, a small amount of n-hexane was added (~1 mL), and the mixture was placed in the freezer overnight forming a dark residue. The solvents were decanted out and the resulting residue was washed with Et_2O (3 x 5 mL). The brown residue was dissolved in DCM (3 mL) and transferred into a pre-weighed vial, and dried overnight on a vacuum line.

[Os(η^6-*p*-cym)(5-MeO-AZPY)I]PF$_6$ (6). [Os(η^6-*p*-cym)I$_2$]$_2$ (50.0 mg, 43.2 μmol), 5-MeO-AZPY (19.4 mg, 90.8 μmol), NH_4PF_6 (70.5 mg, 0.43 mmol), and Isolation method 1. Yield: 54.6 mg (78%). ^{1}H NMR (400 MHz, $(CD_3)_2CO$): δ 9.23 (d, 1H, J = 2.7 Hz), 8.95 (d, 1H, J = 9.1 Hz), 8.13-8.10 (m, 2H), 8.08 (dd, 1H, J = 9.1, 2.7 Hz), 7.78-7.74 (m, 1H), 7.72-7.67 (m, 2H), 6.73-6.72 (m, 1H), 6.41-6.40 (m, 1H), 6.29-6.28 (m, 1H), 6.21-6.20 (m, 1H), 4.23 (s, 3H), 2.76 (s, 3H), 2.59 (sept., 1H, J = 6.9 Hz), 0.98 (d, 3H, J = 6.9 Hz), 0.97 (d, 3H, J = 6.9 Hz). ESI-MS calculated for $C_{22}H_{25}IN_3OOs^+$: m/z 666.1. Found: 666.1. CHN analysis: Found: C, 32.15%; H, 3.12%; N, 5.22%. Calculated for $C_{22}H_{25}F_6IN_3OOsP$: C, 32.64%; H, 3.11%; N, 5.19%.

[Os(η^6-*p*-cym)(5-MeO-AZPY)I]CF$_3$SO$_3$ (7). [Os(η^6-*p*-cym)I$_2$]$_2$ (50.0 mg, 43.2 μmol), 5-MeO-AZPY (19.4 mg, 90.8 μmol), $NH_4CF_3SO_3$ (72.3 mg, 0.43 mmol), and Isolation method 1. Yield: 57.1 mg (81%). ^{1}H NMR (400 MHz, CD_3OD): δ 9.09 (d, 1H, J = 2.7 Hz), 8.86 (d, 1H, J = 9.1 Hz), 8.03-8.02 (m, 2H), 7.97 (dd, 1H, J = 9.1, 2.7 Hz), 7.74-7.70 (m, 1H), 7.67-7.64 (m, 2H), 6.49-6.48 (m, 1H), 6.18-6.17 (m, 1H), 6.05-6.04 (m, 1H), 5.98-5.97 (m, 1H), 4.18 (s, 3H), 2.71 (s, 3H), 2.46 (sept., 1H, J = 6.9 Hz), 0.93 (d, 3H, J = 6.9 Hz), 0.92 (d, 3H, J = 6.9 Hz). ESI-MS calculated for $C_{22}H_{25}IN_3OOs^+$: m/z 666.1. Found: 665.9. CHN analysis: Found: C, 33.24%; H, 3.09%; N, 5.27%. Calculated for $C_{23}H_{25}F_3IN_3O_4OsS$: C, 33.95%; H, 3.10%; N, 5.16%.

[Os(η^6-*p*-cym)(5-EtO-AZPY)Cl]PF$_6$ (8). [Os(η^6-*p*-cym)Cl$_2$]$_2$ (50.0 mg, 63.2 μmol), 5-EtO-AZPY (30.2 mg, 132.8 μmol), NH_4PF_6 (103.0 mg, 0.63 mmol), and Isolation method 1. Yield: 81.4 mg (88%). ^{1}H NMR (400 MHz, $(CD_3)_2CO$): δ 9.91 (d, 1H, J = 2.7 Hz), 8.90 (d, 1H, J = 9.1 Hz), 8.10-8.06 (m, 3H), 7.77-7.70

(m, 3H), 6.76-6.75 (m, 1H), 6.39-6.38 (m, 1H), 6.22-6.21 (m, 2H), 4.59-4.47 (m, 2H), 2.47 (sept., 1H, J = 6.9 Hz), 2.43 (s, 3H), 1.53 (t, 3H, J = 7.0 Hz), 0.95 (d, 3H, J = 7.0 Hz), 0.92 (d, 3H, J = 7.0 Hz). ESI-MS calculated for $C_{23}H_{27}ClN_3OOs^+$: m/z 588.2. Found: 588.0. CHN analysis: Found: C, 37.43%; H, 3.55%; N, 5.69%. Calculated for $C_{23}H_{27}ClF_6N_3OOsP$: C, 37.73%; H, 3.72%; N, 5.74%.

[Os(η^6-*p*-cym)(5-EtO-AZPY)Br]PF$_6$ (9). [Os(η^6-*p*-cym)Br$_2$]$_2$ (50.0 mg, 51.6 µmol), 5-EtO-AZPY (24.6 mg, 108.4 µmol), NH_4PF_6 (84.2 mg, 0.52 mmol), and Isolation method 1. Yield: 61.8 mg (77%). ^{1}H NMR (400 MHz, $(CD_3)_2CO$): δ 9.20 (d, 1H, J = 2.7 Hz), 8.91 (d, 1H, J = 9.1 Hz), 8.10-8.06 (m, 3H), 7.76-7.70 (m, 3H), 6.75-6.74 (m, 1H), 6.41-6.40 (m, 1H), 6.25-6.21 (m, 2H), 4.59-4.47 (m, 2H), 2.56 (s, 3H), 2.51 (sept., 1H, J = 6.9 Hz), 1.53 (t, 3H, J = 7.0 Hz), 0.97 (d, 3H, J = 7.0 Hz), 0.94 (d, 3H, J = 7.0 Hz). ESI-MS calculated for $C_{23}H_{27}BrN_3OOs^+$: m/z 632.1. Found: 631.9. CHN analysis: Found: C, 35.25%; H, 3.32%; N, 5.34%. Calculated for $C_{23}H_{27}BrF_6N_3OOsP$: C, 35.57%; H, 3.50%; N, 5.41%.

[Os(η^6-*p*-cym)(5-EtO-AZPY)I]PF$_6$ (10). [Os(η^6-*p*-cym)I$_2$]$_2$ (100.0 mg, 86.5 µmol), 5-EtO-AZPY (41.3 mg, 181.6 µmol), NH_4PF_6 (140.9 mg, 0.86 mmol), and isolation method 1. Yield: 119.6 mg (84%). ^{1}H NMR (400 MHz, CD_3OD): δ 9.07 (d, 1H, J = 2.6 Hz), 8.84 (d, 1H, J = 9.1 Hz), 8.04-8.01 (m, 2H), 7.94 (dd, 1H, J = 9.1, 2.6 Hz), 7.73-7.63 (m, 3H), 6.47-6.46 (m, 1H), 6.16-6.15 (m, 1H), 6.03-6.02 (m, 1H), 5.96-5.95 (m, 1H), 4.50-4.38 (m, 2H), 2.70 (s, 3H), 2.45 (sept., 1H, J = 6.9 Hz), 1.55 (t, 3H, J = 7.0 Hz), 0.94-0.92 (2x d, 6H, J = 6.9 Hz). ESI-MS calculated for $C_{23}H_{27}IN_3OOs^+$: m/z 680.1. Found: 679.9. CHN analysis: Found:

C, 33.30%; H, 3.26%; N, 4.98%. Calculated for $C_{23}H_{27}F_6IN_3OOsP$: C, 33.54%; H, 3.30%; N, 5.10%.

[Os(η^6-*p*-cym)(5-EtO-AZPY)I]CF_3SO_3 (11). $[Os(\eta^6\text{-}p\text{-cym})I_2]_2$ (50.0 mg, 43.2 µmol), 5-EtO-AZPY (20.6 mg, 90.8 µmol), $NH_4CF_3SO_3$ (72.3 mg, 0.43 mmol), and isolation method 1. Yield: 66.8 mg (93%). ^{1}H NMR (400 MHz, CD_3OD): δ 9.07 (d, 1H, J = 2.6 Hz), 8.84 (d, 1H, J = 9.1 Hz), 8.05-8.01 (m, 2H), 7.94 (dd, 1H, J = 9.1, 2.6 Hz), 7.74-7.69 (m, 1H), 7.68-7.63 (m, 2H), 6.47-6.46 (m, 1H), 6.17-6.16 (m, 1H), 6.03-6.02 (m, 1H), 5.96-5.95 (m, 1H), 4.51-4.38 (m, 2H), 2.71 (s, 3H), 2.45 (sept., 1H, J = 6.9 Hz), 1.55 (t, 3H, J = 7.0 Hz), 0.94-0.92 (2x d, 6H, J = 6.9 Hz). ESI-MS calculated for $C_{23}H_{27}IN_3OOs^+$: m/z 680.1. Found: 680.0. CHN analysis: Found: C, 34.74%; H, 3.26%; N, 5.01%. Calculated for $C_{24}H_{27}F_3IN_3O_4OsS$: C, 34.83%; H, 3.29%; N, 5.08%.

[Os(η^6-*p*-cym)(5-EtO-AZPY)I]IO_3 (12). $[Os(\eta^6\text{-}p\text{-cym})I_2]_2$ (50.0 mg, 43.2 µmol), 5-EtO-AZPY (20.6 mg, 90.8 µmol), KIO_3 (92.5 mg, 0.43 mmol), and isolation method 1. Yield: 39.2 mg (53%). ^{1}H NMR (400 MHz, CD_3OD): δ 9.07 (d, 1H, J = 2.6 Hz), 8.84 (d, 1H, J = 9.1 Hz), 8.04-8.02 (m, 2H), 7.94 (dd, 1H, J = 9.1, 2.6 Hz), 7.72-7.71 (m, 1H), 7.65-7.64 (m, 2H), 6.48-6.47 (m, 1H), 6.17-6.16 (m, 1H), 6.04-6.03 (m, 1H), 5.96-5.95 (m, 1H), 4.51-4.38 (m, 2H), 2.71 (s, 3H), 2.46 (sept., 1H, J = 6.9 Hz), 1.55 (t, 3H, J = 7.0 Hz), 0.94 (d, 6H, J = 6.9 Hz), 0.93 (d, 6H, J = 6.9 Hz). ESI-MS calculated for $C_{23}H_{27}IN_3OOs^+$: m/z 680.1. Found: 680.0. CHN analysis: Found: C, 33.40%; H, 3.33%; N, 4.98%. Calculated for $C_{23}H_{27}I_2N_3O_4Os + C_2H_6O$: C, 33.38%; H, 3.70%; N, 4.67%.

[Os(η^6-bip)(5-EtO-AZPY)I]CF_3SO_3 (13). [Os(η^6-bip)I_2]$_2$ (50.0 mg, 41.8 μmol), 5-EtO-AZPY (19.9 mg, 87.8 μmol), $NH_4CF_3SO_3$ (69.8 mg, 0.42 mmol), and isolation method 1. Yield: 59.2 mg (84%). ^{1}H NMR (400 MHz, CD_3OD): δ 8.77 (d, 1H, J = 9.1 Hz), 8.61 (d, 1H, J = 2.6 Hz), 7.89-7.87 (m, 2H), 7.83 (dd, 1H, J = 9.1, 2.6 Hz), 7.63-7.62 (m, 1H), 7.53-7.48 (m, 3H), 7.42-7.36 (m, 4H), 6.92-6.91 (m, 1H), 6.71-6.70 (m, 1H), 6.56-6.55 (m, 1H), 6.42-6.35 (m, 2H), 4.21-4.07 (m, 2H), 1.44 (t, 3H, J = 7.0 Hz). ESI-MS calculated for $C_{25}H_{23}IN_3OOs^+$: m/z 700.1. Found: 700.0. CHN analysis: Found: C, 36.85%; H, 2.84%; N, 4.84%. Calculated for $C_{26}H_{23}F_3IN_3O_4OsS$: C, 36.84%; H, 2.74%; N, 4.96%.

[Os(η^6-*p*-cym)(5-^{n}PrO-AZPY)I]PF_6 (14). [Os(η^6-*p*-cym)I_2]$_2$ (50.0 mg, 43.2 μmol), 5-^{n}PrO-AZPY (21.9 mg, 90.8 μmol), NH_4PF_6 (70.5 mg, 0.43 mmol), and isolation method 2. Yield: 69.3 mg (73%). ^{1}H NMR (400 MHz, CD_3OD): δ 9.08 (d, 1H, J = 2.6 Hz), 8.84 (d, 1H, J = 9.1 Hz), 8.05-8.02 (m, 2H), 7.95 (dd, 1H, J = 9.1, 2.6 Hz), 7.73-7.63 (m, 3H), 6.48-6.47 (m, 1H), 6.18-6.17 (m, 1H), 6.04-6.03 (m, 1H), 5.96-5.95 (m, 1H), 4.40-4.29 (m, 2H), 2.71 (s, 3H), 2.45 (sept., 1H, J = 7.0 Hz), 2.00-1.92 (m, 2H), 1.15 (t, 3H, J = 7.5 Hz), 0.94-0.91 (2x d, 6H, J = 7.0 Hz). ESI-MS calculated for $C_{24}H_{29}IN_3OOs^+$: m/z 694.1. Found: 694.1. CHN analysis: Found: C, 34.32%; H, 3.40%; N, 4.98%. Calculated for $C_{24}H_{29}F_6IN_3OOsP$: C, 34.41%; H, 3.49%; N, 5.02%.

[Os(η^6-*p*-cym)(5-^{i}PrO-AZPY)I]PF_6(15). [Os(η^6-*p*-cym)I_2]$_2$ (50.0 mg, 43.2 μmol), 5-^{i}PrO-AZPY (21.9 mg, 90.8 μmol), NH_4PF_6 (70.5 mg, 0.43 mmol), and isolation method 2. Yield: 58.9 mg (81%). ^{1}H NMR (400 MHz, CD_3OD): δ 9.04 (d, 1H, J = 2.6 Hz), 8.83 (d, 1H, J = 9.1 Hz), 8.04-8.01 (m, 2H), 7.95 (dd, 1H, J = 9.1, 2.6 Hz), 7.73-7.63 (m, 3H), 6.46-6.45 (m, 1H), 6.15-6.14 (m, 1H), 6.04-6.03 (m, 1H),

5.96-5.95 (m, 1H), 5.07 (sept., 1H, J = 6.0 Hz), 2.68 (s, 3H), 2.46 (sept., 1H, J = 6.9 Hz), 1.49 (t, 6H, J = 6.3 Hz), 0.95 (d, 3H, J = 6.9 Hz), 0.94 (d, 3H, J = 6.9 Hz). ESI-MS calculated for $C_{24}H_{29}IN_3OOs^+$: m/z 694.1. Found: 694.1.

[Os(η^6-*p*-cym)(5-^{n}BuO-AZPY)I]PF$_6$(16). [Os(η^6-*p*-cym)I$_2$]$_2$ (50.0 mg, 43.2 μmol), 5-^{n}BuO-AZPY (23.2 mg, 90.8 μmol), NH_4PF_6 (70.5 mg, 0.43 mmol), and isolation method 2. Yield: 69.0 mg (94%). ^{1}H NMR (400 MHz, $(CD_3)_2CO$): δ 9.25 (d, 1H, J = 2.7 Hz), 8.94 (d, 1H, J = 9.1 Hz), 8.13-8.10 (m, 2H), 8.07 (dd, 1H, J = 9.1, 2.7 Hz), 7.78-7.67 (m, 3H), 6.73-6.72 (m, 1H), 6.42-6.41 (m, 1H), 6.28-6.27 (m, 1H), 6.20-6.19 (m, 1H), 4.52-4.41 (m, 2H), 2.77 (s, 3H), 2.58 (sept., 1H, J = 6.9 Hz), 1.94-1.87 (m, 2H), 1.61-1.51 (m, 2H), 1.01 (t, 3H, J = 7.4 Hz), 0.98 (d, 3H, J = 6.9 Hz), 0.96 (d, 3H, J = 6.9 Hz). ESI-MS calculated for $C_{25}H_{31}IN_3OOs^+$: m/z 708.1. Found: 708.1.

[Os(η^6-*p*-cym)(5-HOCH$_2$CH$_2$O-AZPY)Cl]PF$_6$ (17). [Os(η^6-*p*-cym)Cl$_2$]$_2$ (50.0 mg, 63.2 μmol), 5-$HOCH_2CH_2O$-AZPY (32.3 mg, 132.8 μmol), NH_4PF_6 (103.0 mg, 0.63 mmol), and isolation method 2. Yield: 78.5 mg (83%). ^{1}H NMR (400 MHz, CD_3OD): δ 9.05 (d, 1H, J = 2.7 Hz), 8.77 (d, 1H, J = 9.1 Hz), 8.00-7.97 (m, 3H), 7.71-7.66 (m, 3H), 6.49-6.48 (m, 1H), 6.13-6.12 (m, 1H), 5.98-5.97 (m, 2H), 4.55-4.42 (m, 2H), 4.01 (t, 2H, J = 4.5 Hz), 2.36 (s, 3H), 2.34 (sept., 1H, J = 6.9 Hz), 0.91 (d, 3H, J = 6.9 Hz), 0.88 (d, 3H, J = 6.9 Hz). ESI-MS calculated for $C_{23}H_{27}ClN_3O_2Os^+$: m/z 604.1. Found: 604.0. CHN analysis: Found: C, 36.95%; H, 3.54%; N, 5.41%. Calculated for $C_{23}H_{27}ClF_6N_3O_2OsP$: C, 36.93%; H, 3.64%; N, 5.62%.

[Os(η^6-*p*-cym)(5-HOCH$_2$CH$_2$O-AZPY)Br]PF$_6$ (18). [Os(η^6-*p*-cym)Br$_2$]$_2$ (50.0 mg, 51.6 μmol), 5-HOCH$_2$CH$_2$O-AZPY (26.4 mg, 108.4 μmol), NH_4PF_6 (84.2 mg, 0.52 mmol), and isolation method 1. Yield: 70.1 mg (86%). ^{1}H NMR (400 MHz, CD_3OD): δ 9.04 (d, 1H, J = 2.6 Hz), 8.78 (d, 1H, J = 9.1 Hz), 8.03-7.99 (m, 2H), 7.96 (dd, 1H, J = 9.1, 2.7 Hz), 7.72-7.65 (m, 3H), 6.46-6.45 (m, 1H), 6.00-5.99 (m, 1H), 6.13-6.12 (m, 1H), 5.97-5.96 (m, 1H), 4.54-4.41 (m, 2H), 4.01 (t, 2H, J = 4.5 Hz), 2.46 (s, 3H), 2.39 (sept., 1H, J = 6.9 Hz), 0.93 (d, 3H, J = 6.9 Hz), 0.90 (d, 3H, J = 6.9 Hz). ESI-MS calculated for $C_{23}H_{27}BrN_3O_2Os^+$: m/z 648.1. Found: 647.9. CHN analysis: Found: C, 34.51%; H, 3.33%; N, 5.19%. Calculated for $C_{23}H_{27}ClF_6N_3O_2OsP$: C, 34.85%; H, 3.43%; N, 5.30%.

[Os(η^6-*p*-cym)(5-HOCH$_2$CH$_2$O-AZPY)I]PF$_6$ (19). [Os(η^6-*p*-cym)I$_2$]$_2$ (100.0 mg, 86.5 μmol), 5-HOCH$_2$CH$_2$O-AZPY (44.2 mg, 181.6 μmol), NH_4PF_6 (140.9 mg, 0.87 mmol), and isolation method 1. Yield: 128.6 mg (89%). ^{1}H NMR (400 MHz, CD_3OD): δ 9.03 (d, 1H, J = 2.6 Hz), 8.78 (d, 1H, J = 9.1 Hz), 8.04-8.00 (m, 2H), 7.92 (dd, 1H, J = 9.1, 2.7 Hz), 7.71-7.62 (m, 3H), 6.45-6.44 (m, 1H), 6.12-6.11 (m, 1H), 6.03-6.02 (m, 1H), 5.94-5.93 (m, 1H), 4.53-4.39 (m, 2H), 4.00 (t, 2H, J = 4.4 Hz), 2.64 (s, 3H), 2.46 (sept., 1H, J = 6.9 Hz), 0.95-0.91 (2x d, 6H, J = 6.9 Hz). ESI-MS calculated for $C_{23}H_{27}IN_3O_2Os^+$: m/z 696.1. Found: 695.9. CHN analysis: Found: C, 32.19%; H, 3.19%; N, 4.82%. Calculated for $C_{23}H_{27}F_6IN_3O_2OsP$: C, 32.90%; H, 3.24%; N, 5.00%.

[Os(η^6-bip)(5-HOCH$_2$CH$_2$O-AZPY)I]PF$_6$ (20). [Os(η^6-bip)I$_2$]$_2$ (39.8 mg, 33.3 μmol), 5-HOCH$_2$CH$_2$O-AZPY (17.0 mg, 69.9 μmol), NH_4PF_6 (54.2 mg, 0.33 mmol), and isolation method 1. Yield: 30.7 mg (54%). ^{1}H NMR (400 MHz, $(CD_3)_2CO$): δ 8.94 (d, 1H, J = 2.3 Hz), 8.87 (d, 1H, J = 9.1 Hz), 8.00 (dd, 1H, J =

9.1, 2.3 Hz), 7.90-7.88 (m, 2H), 7.66-7.64 (m, 1H), 7.54-7.41 (m, 7H), 7.08-7.07 (m, 1H), 6.94-6.93 (m, 1H), 6.78-6.77 (m, 1H), 6.71-6.70 (m, 1H), 6.63-6.62 (m, 1H), 4.31-4.30 (m, 2H), 3.95-3.94 (m, 2H). ESI-MS calculated for $C_{25}H_{23}IN_3O_2Os^+$: m/z 716.1. Found: 716.1. CHN analysis: Found: C, 34.71%; H, 2.61%; N, 4.86%. Calculated for $C_{25}H_{23}F_6IN_3O_2OsP$: C, 34.93%; H, 2.70%; N, 4.89%.

[Os(η^6-*p*-cym)(5-HO{CH_2CH_2O}$_2$-AZPY)I]PF_6 (21). [Os(η^6-*p*-cym)I_2]$_2$ (50.0 mg, 43.2 μmol), 5-HO(CH_2CH_2O)$_2$-AZPY (26.1 mg, 90.8 μmol), NH_4PF_6 (70.5 mg, 0.43 mmol), and isolation method 2. Yield: 70.3 mg (92%). ^{1}H NMR (400 MHz, CD_3OD): δ 9.13 (d, 1H, J = 2.6 Hz), 8.84 (d, 1H, J = 9.1 Hz), 8.05-8.02 (m, 2H), 7.99 (dd, 1H, J = 9.1, 2.7 Hz), 7.74-7.63 (m, 3H), 6.49-6.48 (m, 1H), 6.18-6.17 (m, 1H), 6.04-6.03 (m, 1H), 5.96-5.95 (m, 1H), 4.60-4.51 (m, 2H), 3.97 (t, 2H, J = 4.4 Hz), 3.74-3.71 (m, 2H), 3.68-3.65 (m, 2H), 2.71 (s, 3H), 2.45 (sept., 1H, J = 6.9 Hz), 0.94-0.91 (2x d, 6H, J = 6.9 Hz). ESI-MS calculated for $C_{25}H_{31}IN_3O_3Os^+$: m/z 740.1. Found: 740.1. CHN analysis: Found: C, 34.09%; H, 3.42%; N, 4.80%. Calculated for $C_{25}H_{31}F_6IN_3O_3OsP$: C, 33.98%; H, 3.54%; N, 4.76%.

[Os(η^6-*p*-cym)(5-MeO{CH_2CH_2O}$_2$-AZPY)I]PF_6 (22). [Os(η^6-*p*-cym)I_2]$_2$ (75.0 mg, 64.8 μmol), 5-MeO(CH_2CH_2O)$_2$-AZPY (41.0 mg, 136.2 μmol), NH_4PF_6 (105.7 mg, 0.65 mmol), and isolation method 2. The product was purified using the Biotage Isolera instrument (Chapter 2, Section **2.2.6**). Yield: 99.4 mg (85%). ^{1}H NMR (400 MHz, CD_3OD): δ 9.11 (d, 1H, J = 2.6 Hz), 8.83 (d, 1H, J = 9.1 Hz), 8.04-8.02 (m, 2H), 7.98 (dd, 1H, J = 9.1, 2.6 Hz), 7.74-7.63 (m, 3H), 6.48-6.47 (m, 1H), 6.17-6.16 (m, 1H), 6.04-6.03 (m, 1H), 5.96-5.95 (m, 1H),

4.59-4.50 (m, 2H), 3.96 (t, 2H, J = 4.3 Hz), 3.74-3.72 (m, 2H), 3.60-3.57 (m, 2H), 3.37 (s, 3H), 2.71 (s, 3H), 2.46 (sept., 1H, J = 6.9 Hz), 0.95-0.92 (2x d, 6H, J = 6.9 Hz). ESI-MS calculated for $C_{26}H_{33}IN_3O_3Os^+$: m/z 754.1. Found: 754.1. CHN analysis: Found: C, 34.78%; H, 3.61%; N, 4.53%. Calculated for $C_{26}H_{33}F_6IN_3O_3OsP$: C, 34.79%; H, 3.71%; N, 4.68%.

[Os(η^6-*p*-cym)(5-EtO{CH_2CH_2O}$_2$-AZPY)I]PF_6 (23). [Os(η^6-*p*-cym)I_2]$_2$ (100.0 mg, 86.5 μmol), 5-EtO(CH_2CH_2O)$_2$-AZPY (57.3 mg, 181.6 μmol), NH_4PF_6 (140.9 mg, 0.87 mmol), and isolation method 2. Yield: 150.5 mg (96%). ^{1}H NMR (400 MHz, CD_3OD): δ 9.12 (d, 1H, J = 2.6 Hz), 8.83 (d, 1H, J = 9.1 Hz), 8.05-8.02 (m, 2H), 7.98 (dd, 1H, J = 9.1, 2.6 Hz), 7.74-7.70. (m, 1H), 7.78-7.63 (m, 2H), 6.48-6.47 (m, 1H), 6.17-6.16 (m, 1H), 6.04-6.03 (m, 1H), 5.96-5.95 (m, 1H), 4.60-4.50 (m, 2H), 3.97 (t, 2H, J = 4.4 Hz), 3.74-3.72 (m, 2H), 3.64-3.61 (m, 2H), 3.54 (q, 2H, J = 7.0 Hz), 2.71 (s, 3H), 2.46 (sept., 1H, J = 6.9 Hz), 1.19 (t, 3H, J = 7.0 Hz), 0.95-0.92 (2x d, 6H, J = 6.9 Hz). ESI-MS calculated for $C_{27}H_{35}IN_3O_3Os^+$: m/z 768.1. Found: 768.0. CHN analysis: Found: C, 34.90%; H, 3.68%; N, 4.49%. Calculated for $C_{27}H_{35}F_6IN_3O_3OsP$: C, 35.57%; H, 3.87%; N, 4.61%.

[Os(η^6-bip)(5-EtO{CH_2CH_2O}$_2$-AZPY)I]CF_3SO_3 (24). [Os(η^6-*p*-cym)I_2]$_2$ (50.0 mg, 41.8 μmol), 5-EtO(CH_2CH_2O)$_2$-AZPY (27.7 mg, 87.8 μmol), $NH_4CF_3SO_3$ (69.8 mg, 0.42 mmol), and isolation method 2. The product was purified using the Biotage Isolera instrument (Chapter 2, Section **2.2.6**). Yield: 68.1 mg (87%). ^{1}H NMR (400 MHz, CD_3OD): δ 8.77 (d, 1H, J = 9.1 Hz), 8.71 (d, 1H, J = 2.3 Hz), 7.90-7.85 (m, 3H), 7.62-7.61 (m, 1H), 7.52-7.48 (m, 3H), 7.41-7.36 (m, 4H), 6.92-6.91 (m, 1H), 6.73-6.71 (m, 1H), 6.59-6.58 (m, 1H), 6.44-6.39 (m,

2H), 4.31-4.21 (m, 2H), 3.87 (t, 2H, J = 4.2 Hz), 3.71-3.69 (m, 2H), 3.63-3.61 (m, 2H), 3.55 (q, 2H, J = 7.0 Hz), 1.20 (t, 3H, J = 7.0 Hz). ESI-MS calculated for $C_{29}H_{31}IN_3O_3Os^+$: m/z 788.1. Found: 788.1. CHN analysis: Found: C, 37.85%; H, 3.20%; N, 4.81%. Calculated for $C_{30}H_{31}F_3IN_3O_6OsS$: C, 38.51%; H, 3.34%; N, 4.49%.

[Os(η^6-*p*-cym)(5-HO{CH_2CH_2O}$_3$-AZPY)I]PF_6 (25). [Os(η^6-*p*-cym)I_2]$_2$ (50.0 mg, 43.2 μmol), 5-HO(CH_2CH_2O)$_3$-AZPY (30.1 mg, 90.8 μmol), NH_4PF_6 (70.5 mg, 0.43 mmol), and isolation method 2. Yield: 79.3 mg (99%). ^{1}H NMR (400 MHz, CD_3CN): δ 8.95 (d, 1H, J = 2.6 Hz), 8.75 (d, 1H, J = 9.1 Hz), 8.00-7.97 (m, 2H), 7.86 (dd, 1H, J = 9.1, 2.7 Hz), 7.74-7.63 (m, 3H), 6.33-6.32 (m, 1H), 6.06-6.05 (m, 1H), 5.96-5.95 (m, 1H), 5.86-5.85 (m, 1H), 4.49-4.48 (m, 2H), 3.91-3.90 (m, 2H), 3.70-3.67 (m, 2H), 3.64-3.59 (m, 4H), 3.52-3.50 (m, 2H), 2.66 (s, 3H), 2.42 (sept., 1H, J = 6.9 Hz), 0.88 (d, 3H, J = 6.9 Hz), 0.87 (d, 3H, J = 6.9 Hz). ESI-MS calculated for $C_{27}H_{35}IN_3O_4Os^+$: m/z 784.1. Found: 784.1. CHN analysis: Found: C, 33.87%; H, 3.65%; N, 4.68%. Calculated for $C_{27}H_{35}F_6IN_3O_4OsP$ + ½CH_2Cl_2: C, 34.05%; H, 3.74%; N, 4.33%.

[Os(η^6-*p*-cym)(5-MeO{CH_2CH_2O}$_3$-AZPY)I]PF_6 (26). [Os(η^6-*p*-cym)I_2]$_2$ (50.0 mg, 43.2 μmol), 5-MeO(CH_2CH_2O)$_3$-AZPY (31.4 mg, 90.8 μmol), NH_4PF_6 (70.5 mg, 0.43 mmol), and isolation method 2. The product was purified using the Biotage Isolera instrument (Chapter 2, Section **2.2.6**). Yield: 76.4 mg (94%). ^{1}H NMR (400 MHz, CD_3OD): δ 9.12 (d, 1H, J = 2.5 Hz), 8.84 (d, 1H, J = 9.1 Hz), 8.04-8.03 (m, 2H), 7.99 (dd, 1H, J = 9.1, 2.5 Hz), 7.71-7.70 (m, 1H), 7.67-7.63 (m, 2H), 6.48-6.47 (m, 1H), 6.18-6.17 (m, 1H), 6.04-6.03 (m, 1H), 5.96-5.95 (m, 1H), 4.60-4.50 (m, 2H), 3.97 (t, 2H, J = 4.3 Hz), 3.74-3.73 (m, 2H), 3.68-3.62

(m, 4H), 3.55-3.53 (m, 2H), 3.35 (s, 3H), 2.71 (s, 3H), 2.46 (sept., 1H, J = 6.9 Hz), 0.95-0.92 (2x d, 6H, J = 6.9 Hz). ^{13}C NMR ($(CD_3)_2CO$): δ 161.95 (*C*), 159.46 (*C*), 158.81 (*C*), 143.97 (*C*H), 134.21 (*C*H), 130.31 (*C*H), 129.93 (*C*H), 126.99 (*C*H), 126.52 (*C*H), 105.99 (*C*), 104.96 (*C*), 85.13 (*C*H), 83.41 (*C*H), 81.03 (*C*H), 72.77 (CH_2), 71.53 (CH_2), 71.34 (CH_2), 71.16 (CH_2), 71.11 (CH_2), 70.09 (CH_2), 58.91 (CH_3), 32.59 (*C*H), 22.44 (CH_3), 22.34 (CH_3), 21.35 (CH_3). ESI-MS calculated for $C_{28}H_{37}IN_3O_4Os^+$: m/z 798.1. Found: 798.0.

[Os(η^6-*p*-cym)(5-EtO{CH_2CH_2O}$_3$-AZPY)I]PF_6 (27). [Os(η^6-*p*-cym)I_2]$_2$ (50.0 mg, 43.2 μmol), 5-EtO(CH_2CH_2O)$_3$-AZPY (32.6 mg, 90.8 μmol), NH_4PF_6 (70.5 mg, 0.43 mmol), and isolation method 2. The product was purified using the Biotage (Chapter 2, Section **2.2.6**). Yield: 77.2 mg (93%). ^{1}H NMR (400 MHz, $(CD_3)_2CO$): δ 9.26 (d, 1H, J = 2.6 Hz), 8.94 (d, 1H, J = 9.1 Hz), 8.13-8.09 (m, 3H), 7.78-7.74 (m, 1H), 7.72-7.67 (m, 2H), 6.76-6.75 (m, 1H), 6.46-6.45 (m, 1H), 6.30-6.29 (m, 1H), 6.20-6.19 (m, 1H), 4.66-4.56 (m, 2H), 3.97 (t, 2H, J = 4.4 Hz), 3.71-3.69 (m, 2H), 3.66-3.63 (m, 2H), 3.61-3.58 (m, 2H), 3.55-3.52 (m, 2H), 3.47 (q, 2H, J = 7.0 Hz), 2.79 (s, 3H), 2.58 (sept., 1H, J = 6.9 Hz), 1.13 (t, 3H, J = 7.0 Hz), 0.98 (d, 3H, J = 6.9 Hz), 0.96 (d, 3H, J = 6.9Hz). ESI-MS calculated for $C_{29}H_{39}IN_3O_4Os^+$: m/z 812.2. Found: 812.1.CHN analysis: Found: C, 35.30%; H, 4.00%; N, 4.36%. Calculated for $C_{29}H_{39}F_6IN_3O_4OsP$ + ½CH_2Cl_2: C, 35.50%; H, 4.04%; N, 4.21%.

[Os(η^6-*p*-cym)(5-HO{CH_2CH_2O}$_4$-AZPY)I]PF_6 (28). [Os(η^6-*p*-cym)I_2]$_2$ (50.0 mg, 43.2 μmol), 5-HO(CH_2CH_2O)$_4$-AZPY (34.1 mg, 90.8 μmol), NH_4PF_6 (70.5 mg, 0.43 mmol), and isolation method 2. Yield: 82.8 mg (98%). ^{1}H NMR (400 MHz, CD_3OD): δ 9.12 (d, 1H, J = 2.6 Hz), 8.84 (d, 1H, J = 9.1 Hz), 8.04-8.02 (m, 2H),

7.99 (dd, 1H, J = 9.1, 2.6 Hz), 7.74-7.64 (m, 3H), 6.48-6.47 (m, 1H), 6.18-6.17 (m, 1H), 6.04-6.03 (m, 1H), 5.96-5.65 (m, 1H), 4.60-4.51 (m, 2H), 3.97 (t, 2H, J = 4.4 Hz), 3.76-3.73 (m, 2H), 3.70-3.63 (m, 8H), 3.58-3.55 (m, 2H), 2.71 (s, 3H), 2.46 (sept., 1H, J = 6.9 Hz), 0.94 (d, 3H, J = 6.9 Hz), 0.93 (d, 3H, J = 6.9 Hz). ESI-MS calculated for $C_{29}H_{39}IN_3O_5Os^+$: m/z 828.2. Found: 828.1. CHN analysis: Found: C, 34.54%; H, 4.00%; N, 4.62%. Calculated for $C_{29}H_{39}F_6IN_3O_5OsP + 2H_2O$: C, 34.56%; H, 4.30%; N, 4.17%.

[Os(η^6-*p*-cym)(5-Br-AZPY-OH)Cl]PF$_6$ (29). [Os(η^6-*p*-cym)Cl$_2$]$_2$ (50.0 mg, 63.2 μmol), 5-Br-AZPY-OH (36.9 mg, 132.8 μmol), NH_4PF_6 (103.1 mg, 0.63 mmol), and isolation method 1. Yield: 89.6 mg (91%). ^{1}H NMR (400 MHz, $(CD_3)_2CO$): δ 9.66 (d, 1H, J = 2.1 Hz), 8.75 (d, 1H, J = 8.7 Hz), 8.56 (dd, 1H, J = 8.7, 2.1 Hz), 8.15-8.11 (m, 2H), 7.15-7.11 (m, 2H), 6.82-6.81 (m, 1H), 6.53-6.52 (m, 1H), 6.40-6.35 (m, 2H), 2.47 (sept., 1H, J = 6.9 Hz), 2.43 (s, 3H), 0.97 (d, 3H, J = 6.9 Hz), 0.91 (d, 3H, J = 6.9 Hz). ESI-MS calculated for $C_{21}H_{22}BrClN_3OOs^+$: m/z 638.0. Found: 637.9. CHN analysis: Found: C, 31.87%; H, 2.70%; N, 5.16%. Calculated for $C_{21}H_{22}BrClF_6N_3OOsP$: C, 32.21%; H, 2.83%; N, 5.37%.

[Os(η^6-*p*-cym)(5-Br-AZPY-OH)Br]PF$_6$ (30). [Os(η^6-*p*-cym)Br$_2$]$_2$ (50.0 mg, 51.6 μmol), 5-Br-AZPY-OH (30.2 mg, 108.4 μmol), NH_4PF_6 (84.2 mg, 0.52 mmol), and isolation method 1. Yield: 78.1 mg (91%). ^{1}H NMR (400 MHz, $(CD_3)_2CO$): δ 9.66 (d, 1H, J = 2.1 Hz), 8.78 (d, 1H, J = 8.7 Hz), 8.53 (dd, 1H, J = 8.7, 2.1 Hz), 8.16-8.12 (m, 2H), 7.15-7.11 (m, 2H), 6.82-6.81 (m, 1H), 6.55-6.54 (m, 1H), 6.42-6.39 (m, 2H), 2.56 (s, 3H), 2.51 (sept., 1H, J = 6.9 Hz), 0.99 (d, 3H, J = 6.9 Hz), 0.92 (d, 3H, J = 6.9 Hz). ESI-MS calculated for $C_{21}H_{22}Br_2N_3OOs^+$: m/z

682.0. Found: 681.9. CHN analysis: Found: C, 30.19%; H, 2.60%; N, 4.98%. Calculated for $C_{21}H_{22}Br_2F_6N_3OOsP$: C, 30.48%; H, 2.68%; N, 5.08%.

[Os(η^6-*p*-cym)(5-Br-AZPY-OH)I]PF$_6$ (31). [Os(η^6-*p*-cym)I$_2$]$_2$ (100.0 mg, 86.5 µmol), 5-Br-AZPY-OH (50.5 mg, 181.6 µmol), NH_4PF_6 (140.9 mg, 0.87 mmol), and isolation method 1. Yield: 76.7 mg (51%). ^{1}H NMR (400 MHz, CD_3OD): δ 9.10-9.09 (m, 1H), 8.12-8.08 (m, 2H), 8.02-8.01 (m, 2H), 6.43-6.39 (m, 2H), 7.15-7.11 (m, 2H), 6.20-6.19 (m, 1H), 6.07-6.06 (m, 1H), 6.03-6.02 (m, 1H), 5.97-5.96 (m, 1H), 2.73 (s, 3H), 2.39 (sept., 1H, J = 6.9 Hz), 0.97 (d, 3H, J = 6.9 Hz), 0.89 (d, 3H, J = 6.9 Hz). ESI-MS calculated for $C_{21}H_{22}BrIN_3OOs^+$: m/z 730.0. Found: 729.8. CHN analysis: Found: C, 28.62%; H, 2.63%; N, 4.73%. Calculated for $C_{21}H_{22}BrF_6IN_3OOsP$: C, 28.85%; H, 2.54%; N, 4.81%.

[Os(η^6-*p*-cym)(5-F$_3$C-AZPY-OH)Cl]PF$_6$ (32). [Os(η^6-*p*-cym)Cl$_2$]$_2$ (40.0 mg, 50.6 µmol), 5-F$_3$C-AZPY-OH (28.4 mg, 106.2 µmol), NH_4PF_6 (82.5 mg, 0.51 mmol), and isolation method 1. Yield: 69.2 mg (89%). ^{1}H NMR (400 MHz, $(CD_3)_2CO$): δ 9.78-9.77 (m, 1H), 9.03 (d, 1H, J = 8.5 Hz), 8.68 (dd, 1H, J = 8.5, 2.0 Hz), 8.21-8.17 (m, 2H), 7.18-7.14 (m, 2H), 6.88-6.87 (m, 1H), 6.62-6.61 (m, 1H), 6.48-6.47 (m, 1H), 6.44-6.43 (m, 1H), 2.48 (sept., 1H, J = 6.9 Hz), 2.42 (s, 3H), 0.97 (d, 3H, J = 6.9 Hz), 0.91 (d, 3H, J = 6.9 Hz). ESI-MS calculated for $C_{22}H_{22}ClF_3N_3OOs^+$: m/z 628.1. Found: 628.0. CHN analysis: Found: C, 34.71%; H, 3.18%; N, 5.17%. Calculated for $C_{22}H_{22}ClF_9N_3OOsP$: C, 34.22%; H, 2.87%; N, 5.44%.

[Os(η^6-*p*-cym)(5-F$_3$C-AZPY-OH)Br]PF$_6$ (33). [Os(η^6-*p*-cym)Br$_2$]$_2$ (50.0 mg, 51.6 µmol), 5-F$_3$C-AZPY-OH (29.0 mg, 108.4 µmol), NH_4PF_6 (84.2 mg, 0.52 mmol),

and isolation method 1. The product was purified using the Biotage Isolera instrument (Chapter 2, Section **2.2.6**). Yield: 70.9 mg (84%). ^{1}H NMR (400 MHz, $(CD_3)_2CO$): δ 9.78-9.77 (m, 1H), 9.06 (d, 1H, J = 8.6 Hz), 8.66 (dd, 1H, J = 8.6, 1.9 Hz), 8.22-8.18 (m, 2H), 7.19-7.15 (m, 2H), 6.89-6.88 (m, 1H), 6.64-6.63 (m, 1H), 6.49-6.48 (m, 2H), 2.56 (s, 3H), 2.53 (sept., 1H, J = 6.9 Hz), 0.99 (d, 3H, J = 6.9 Hz), 0.92 (d, 3H, J = 6.9 Hz). ESI-MS calculated for $C_{22}H_{22}BrF_3N_3OOs^+$: m/z 672.1. Found: 672.0. CHN analysis: Found: C, 32.30%; H, 2.62%; N, 5.06%. Calculated for $C_{22}H_{22}BrF_9N_3OOsP$: C, 32.36%; H, 2.72%; N, 5.15%.

[Os(η^6-*p*-cym)(5-EtO-AZPY)(*S*-SCN)]PF_6 (34A) and [Os(η^6-*p*-cym)(5-EtO-AZPY)(*N*-SCN)]PF_6 (34B). $[Os(\eta^6\text{-}p\text{-cym})Cl_2]_2$ (50.0 mg, 63.2 μmol) was dissolved in EtOH (10 mL) and a solution of 5-EtO-AZPY (30.2 mg, 132.8 μmol) in EtOH (5 mL) was added drop-wise. The mixture was stirred for 18 h at ambient temperature then filtered through glass micro-fibre to remove a black precipitate. The solvent was removed under reduced pressure and a solution of KSCN (6.15 g, 63.24 mmol) in MeOH:H_2O (1:1 v/v, 12 mL) was added to the brown residue. The mixture was heated to reflux for 18 h. The product was extracted with DCM (2 x 10 mL), washed with water (2 x 10 mL), dried over $MgSO_4$, and filtered. The solvent was removed under reduced pressure and the product was re-dissolved in a minimum amount of hot EtOH, and NH_4PF_6 (103.1 mg, 0.63 mmol) was added. Isolation method 2 was used. Yield: 60.6 mg (64%). ^{1}H NMR (400 MHz, $(CD_3)_2CO$): Major isomer; δ 9.05 (d, 1H, J = 2.6 Hz), 8.89 (d, 1H, J = 9.1 Hz), 8.06-8.00 (m, 3H), 7.74-7.72 (m, 3H), 6.88-6.87 (m, 1H), 6.53-6.52 (m, 1H), 6.38-6.37 (m, 1H), 6.33-6.32 (m, 1H), 4.68-4.51 (m, 2H), 2.54 (sept., 1H, J = 6.9 Hz), 2.49 (s, 3H), 1.53 (t, 3H, J = 7.0 Hz), 1.01 (d,

3H, J = 6.9 Hz), 0.96 (d, 3H, J = 6.9 Hz). Minor isomer; δ 9.35 (d, 1H, J = 2.6 Hz), 8.94 (d, 1H, J = 9.1 Hz), 8.15 (dd, 1H, J = 9.1, 2.6 Hz), 8.11-8.08 (m, 2H), 7.79-7.77 (m, 3H), 6.91-6.90 (m, 1H), 6.57-6.56 (m, 1H), 6.74-6.73 (m, 1H), 6.42-6.41 (m, 1H), 4.68-4.61 (m, 2H), 2.46 (s, 3H), 1.55 (t, 3H, J = 7.0 Hz), 1.00 (d, 3H, J = 6.9 Hz), 0.97 (d, 3H, J = 6.9 Hz). ESI-MS calculated for $C_{24}H_{27}N_4OOsS^+$: m/z 611.2. Found: 611.1.

[Os(η^6-*p*-cym)(5-EtO-AZPY)N$_3$]PF$_6$ (35). [Os(η^6-*p*-cym)Cl$_2$]$_2$ (50.0 mg, 63.2 μmol) was dissolved in a solution of MeOH:H_2O (2:1 v/v, 10 mL) and a solution of $AgNO_3$ (20.10 mg/mL, 4 mol. equiv.) in water was added. A white precipitate immediately formed and the solute turned yellow. The precipitate was removed by filtration and 5-EtO-AZPY (30.2 mg, 132.8 μmol), then NaN_3 (41.1 mg, 0.63 mmol) were added. The mixture was heated to 50 °C for 2 h. Isolation method 1 was used. Yield: 34.8 mg (37%). The product was impure and a portion was purified by preparative HPLC. ^{1}H NMR (400 MHz, CD_3OD): δ 9.08 (d, 1H, J = 2.5 Hz), 8.83 (d, 1H, J = 9.1 Hz), 8.01 (dd, 1H, J = 9.1, 2.5 Hz), 7.95-7.93 (m, 2H), 7.73-7.71 (m, 3H), 6.56-6.55 (m, 1H), 6.16-6.15 (m, 1H), 6.01-5.98 (m, 2H), 4.56-4.43 (m, 2H), 2.35 (s, 3H), 2.30 (sept., 1H, J = 6.9 Hz), 1.57 (t, 3H, J = 7.0 Hz), 0.88 (d, 3H, J = 6.9 Hz), 0.84 (d, 3H, J = 6.9 Hz). ^{13}C NMR ($(CD_3)_2CO$): δ161.89 (*C*), 160.67 (*C*), 157.96 (*C*), 142.67 (*C*H), 134.16 (*C*H), 130.66 (*C*H), 130.19 (*C*H), 126.69 (*C*H), 125.61 (*C*H), 110.30 (*C*), 105.80 (*C*), 85.87 (*C*H), 85.40 (*C*H), 80.71 (*C*H), 79.96 (*C*H), 67.6 (CH_2), 32.30 (*C*H), 22.94 (CH_3), 22.80 (CH_3), 18.64 (CH_3), 14.82 (CH_3). ESI-MS calculated for $C_{23}H_{27}N_6OOs^+$: m/z 595.2. Found: 595.1.

4.2.3. Growing single crystals for X-ray crystallography

Single crystals of **6**, **10**, **32**, **33** and **FY026** were obtained by cooling MeOH or EtOH solutions of approximately 1-2 mg/mL in a freezer at -20 °C. Crystals of **13A** were obtained by slow evaporation of a MeOH solution at ambient temperature.[20]

4.2.4. Measuring the pK_a of 31

A solution of **31** (100 µM) in water was prepared and divided into 34x 1mL aliquots in glass vials. The pH of the aliquots were individually adjusted by the addition of 1-10 µL of either KOH or $HClO_4$ (0.01, 0.1, 1, 2, 3, 4, 6, 8 or 10 M), and measured over a range of 1.9 - 12.8 using a pH bench top meter. Changes in the UV-Vis absorption spectra were then recorded at different pH values using disposable polystyrene semi-micro 1.6 mL cuvettes, ensuring no further contact with glass after the pH measurements (contact with glass affects pH). The change in intensity of the absorption at 588 nm with pH was fitted to the Henderson-Hasselbalch equation using Origin 8.5.

4.2.5. Aqueous stability testing

The stability after 24 h in D_2O was determined by ^1H NMR for all complexes. A more detailed assessment was conducted by HPLC for complexes **8**, **9** and **10**, which explored stability after 37°C incubation with different concentrations of

NaCl in phosphate buffer solution. No precautions were made to protect samples from light or air.

4.2.5.1. ^{1}H NMR spectroscopy

Saturated solutions of complexes were prepared by dissolving 1-2 mg in DMSO-d_6 (50 µL) followed by drop-wise addition of D_2O (950 µL), accompanied with vigorous stirring and shaking. The solutions were then filtered and transferred into NMR tubes. ^{1}H NMR spectra were collected straight after sample preparation (10-20 min) and after 24 h, leaving the sample at ambient temperature. Spectra were collected on a 400 or 500 MHz instrument.

4.2.5.2. HPLC

Solutions of complexes **8**, **9** and **10** (100 µM) were prepared with phosphate buffer (9.5 mM, pH 7.4), 5% DMSO, and NaCl at concentrations of either 23 or 103 mM. Samples were incubated for 0, 2, 12 and 24 h at 37 °C and placed in a freezer at -20 °C for storage, before running HPLC analysis (see Chapter 2, Section **2.2.9** for HPLC conditions).

4.2.6. Aqueous solubility testing

Saturated solutions of complexes were prepared in triplicates by combining 1-3 mg of complex with 100 mM NaCl solution (1 mL) and shaking samples for 24 h

on a mechanical shaker. If all the solids fully dissolve then more were added to ensure a saturated solution. The solutions were filtered using Iso-Disc^{TM} filters (PTFE-4-4 4 mm x 0.45 μm) and the concentrations of osmium were determined using either ICP-OES or ICP-MS (see Chapter 2, Sections **2.2.13** and **2.2.14**). The experiments were repeated to obtain duplicates of triplicates.

4.2.7. Measuring HPLC capacity factors

The isocratic HPLC analysis of complexes and uracil was carried out using the same instrument and column described in Chapter 2, Section **2.2.9**. The mobile phase consisted of H_2O:MeCN (1:1, v/v) with 50 mM NaCl with no solvent gradient (HPLC grade materials used). The temperature of the column was kept constant at 25 °C. Samples of the complexes and uracil (500 μM) were prepared in H_2O:MeCN (1:1, v/v) and were analysed in triplicates on three separate days (50 μL injection volume). The capacity factors were calculated using the following equations, where t_R is the retention time of the retained complex, t_0 is the retention time of an unretained compound (uracil), R_F is the retention factor, and *K* is the capacity factor.[21-23]

$$R_F = (t_R - t_0) \quad (1)$$

$$K = R_F/t_0 \quad (2)$$

4.2.8. Preparative HPLC

Preparative HPLC was used to purify **34** and **35** using the same instrument, mobile phase, solvent gradient and wavelengths of detection described in Chapter 2, Section **2.2.9**, with a flow rate of 2 mL/min. An Agilent ZORBAX Eclipse XDB-C18 250 x 9.4 mm column with a pore size of 5 μm was used with a 1mL loop. Samples were prepared in MeCN:H_2O (1:9, v/v) at concentrations of 500 μM and filtered through Iso-Disc^{TM} filters (PTFE-4-4 4 mm x 0.45 μm). Aliquots of 0.45-0.50 mL were injected at a time and fractions were collected from the waste line. Selected fractions were combined and MeCN was removed under reduced pressure. The sample was then freeze dried to remove the residual water and TFA. Complex **35** was re-dissolved in EtOH and recombined with excess ammonium hexafluorophosphate (100 mg). The solvent was then removed under reduced pressure and the resulting precipitate was re-dissolved in DCM, filtered into a pre-weighed vial, and dried under vacuum.

4.2.9. Stability testing of the structural isotopes of 34

After the isotopes of **34** were separated by preparative HPLC and freeze dried, the samples were re-dissolved in DMSO (50 μL) and PBS solution (950 μL), filtered through Iso-Disc^{TM} filters (PTFE-4-4 4 mm x 0.45 μm), and incubated at 37 °C for 24 h. The samples were then analysed using HPLC as described in Chapter 2, Section **2.2.9**.

4.3. Results

4.3.1. Synthesis of AZPY ligands

Two different types of AZPY ligand were synthesised. Ligands with alkoxy or glycolic side chains situated on the pyridine moiety, *para* to the azo-bond (RO-AZPY, see Scheme 4.2). Ligands with two substituents: an electron-withdrawing substituent on the pyridine ring and an electron-donating OH group on the phenyl ring, both situated *para* to the azo-bond (R-AZPY-OH, see Scheme 4.4).

4.3.1.1. RO-AZPY ligands

Phenylazopyridine (AZPY) ligands functionalised with alkoxy or glycolic side chains were synthesised *via* a two-step process detailed in Scheme 4.2. Step 1 is a condensation reaction that generates an azo-bond when 2-amino-5-fluoropyridine is reacted with nitrosobenzene in the presence of a base, forming 5-F-AZPY. This reaction is well understood for the synthesis of azobenzene.[3,4] Step 2 is an aromatic nucleophilic substitution reaction, whereby the reagent also behaves as a solvent matrix for the reaction to take place. The mechanism occurs *via* an addition-elimination process (Scheme 4.3), where the nucleophile (RO^-) is generated *in situ* under basic conditions and attacks the electropositive fluorinated carbon.[24] The π* orbital of the azo-bond provides a platform for electrons to occupy temporarily, making the addition process accessible.

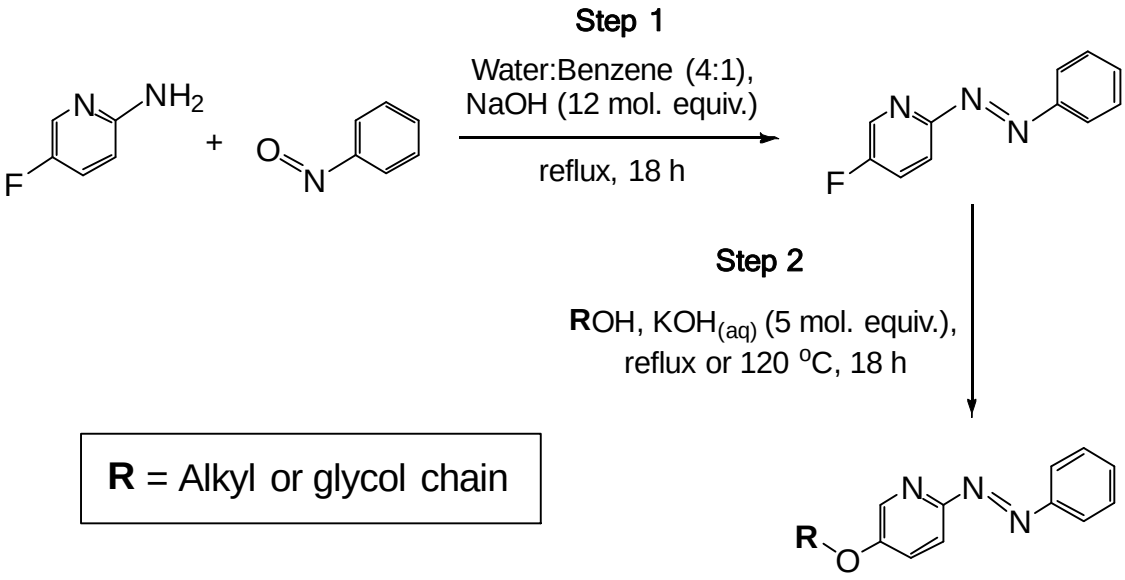

Scheme 4.2. Two-step synthesis of AZPY ligands with *para* alkoxy/glycol substituents (RO-AZPYs).

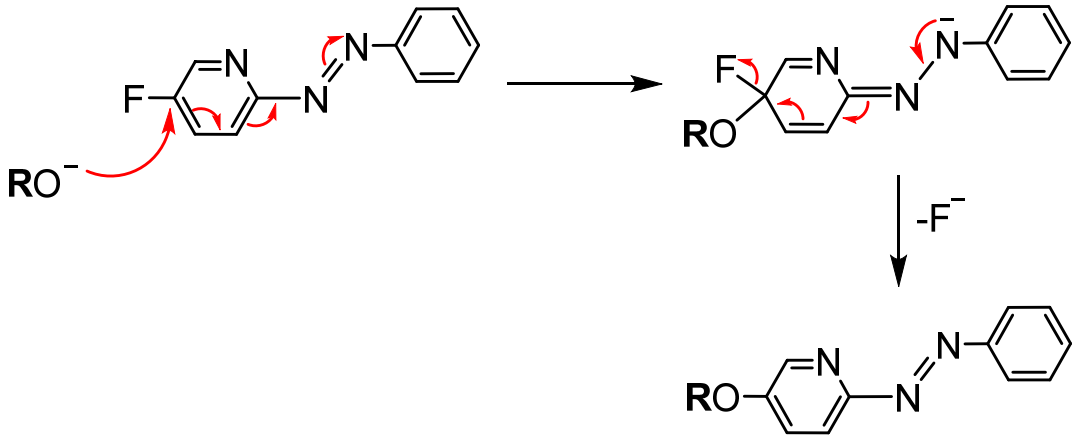

Scheme 4.3. Reaction mechanism for the nucleophilic addition-elimination of 5-F-AZPY, where the addition of nucleophile RO^- leads to the elimination of F^-.[24]

A total of 13 ligands were synthesised utilising a variety of alcohols and glycols with different chain lengths. Table 4.1 summarises all the ligands that were synthesised and the solvent/reagent (ROH) used to make them.

Table 4.1. List of all RO-AZPY ligands synthesized.

Ligand	ROH	Structure
L1 5-MeO-AZPY	Methanol	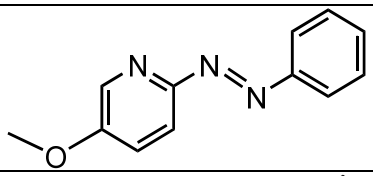
L2 5-EtO-AZPY	Ethanol	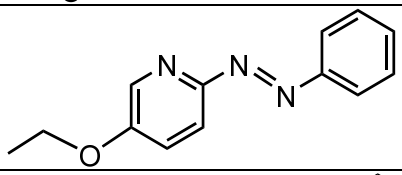
L3 5-^{n}PrO-AZPY	n-propanol	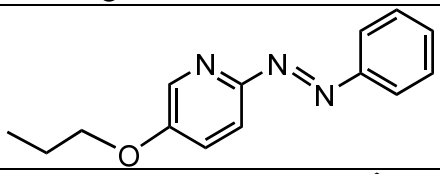
L4 5-^{i}PrO-AZPY	Isopropanol	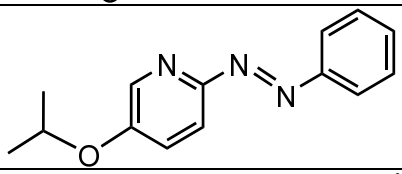
L5 5-^{n}BuO-AZPY	n-butanol	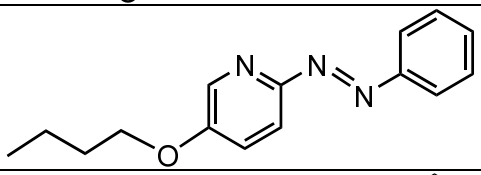
L6 5-HOCH$_2$CH$_2$O-AZPY	ethylene glycol	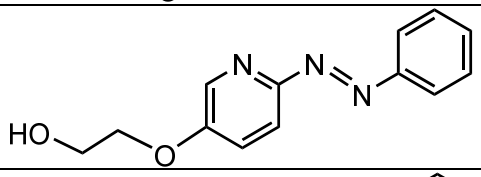
L7 5-HO(CH$_2$CH$_2$O)$_2$-AZPY	diethylene glycol	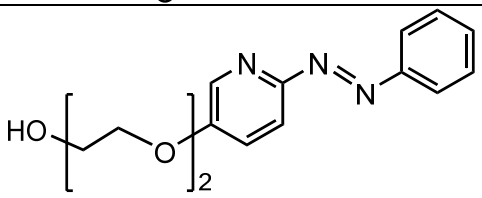

L8 5-HO(CH_2CH_2O)$_3$-AZPY	triethylene glycol	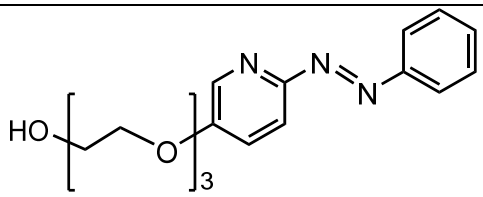
L9 5-HO(CH_2CH_2O)$_4$-AZPY	tetraethylene glycol	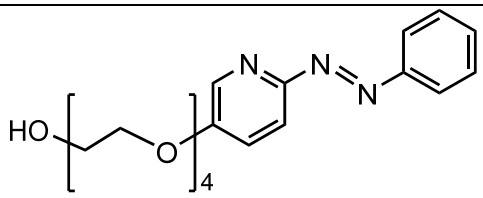
L10 5-MeO(CH_2CH_2O)$_2$-AZPY	diethylene glycol monomethyl ether	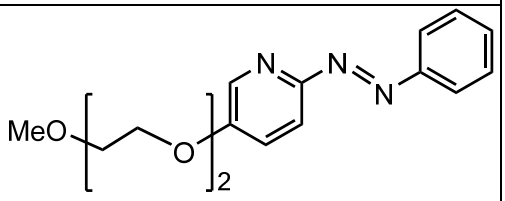
L11 5-MeO(CH_2CH_2O)$_3$-AZPY	triethylene glycol monomethyl ether	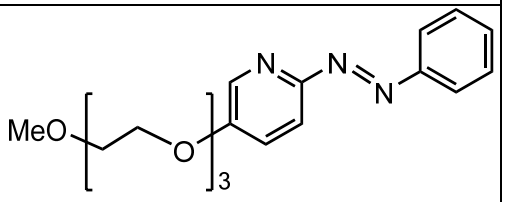
L12 5-EtO(CH_2CH_2O)$_2$-AZPY	diethylene glycol monoethyl ether	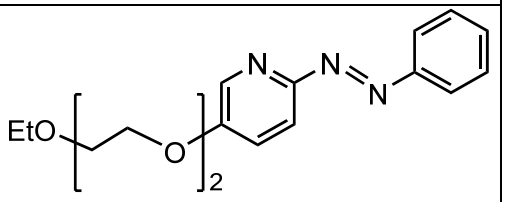
L13 5-EtO(CH_2CH_2O)$_3$-AZPY	triethylene glycol monoethyl ether	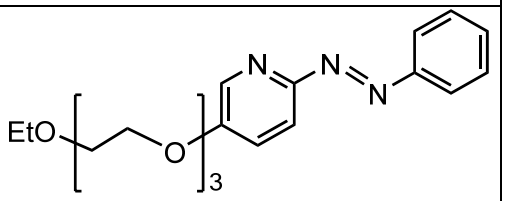

4.3.1.2. R-AZPY-OH ligands

The synthesis of AZPY ligands baring two substituents *para* to the azo-bond posed a significant challenge. There are many reported azo-coupling reactions

in the literature.[1-6] However, azo-couplings are sensitive to the presence of multiple electron donating/withdrawing substituents, hindering formation of the azo-bond. The synthesis of such ligands was attempted using a variety of different strategies and only one methodology proved to be successful producing significant yields (Scheme 4.4).[7] Two ligands were synthesised using this protocol, **L14** and **L15**.

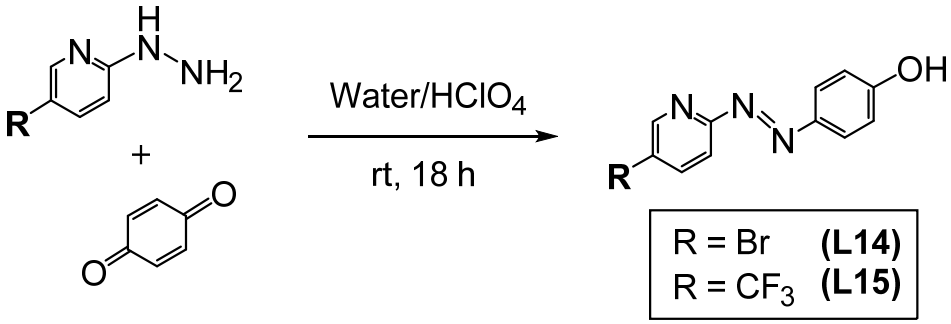

Scheme 4.4. One step synthesis of R-AZPY-OH ligands with a *para* electron withdrawing substituent on the pyridine ring and *para* hydroxyl substituent on the phenyl ring.

4.3.2. Synthesis of Os(II) arene AZPY complexes

Shown in Scheme 4.5 is the general synthesis protocol of Os(II) arene AZPY complexes baring halido monodentate ligands (**6**-**33**). The reaction involved stirring $[Os(\eta^6\text{-}p\text{-cym})X_2]_2$ (where X = Cl, Br or I) in ethanolic solution with 2.1 mol. equiv. of an AZPY ligand (**L1**-**L15**). The reactions occurred readily at ambient temperature, forming a cationic complex of +1 charge. Reactions involving $[Os(\eta^6\text{-bip})I_2]_2$, required further heating at reflux for 1 h. The second step of the synthesis involved exchanging the I^- counter-ion for an anion of choice (PF_6^-, $CF_3SO_3^-$ or IO_3^-) by adding 10 mol. equiv. of either NH_4PF_6,

$NH_4CF_3SO_3$ or KIO_3. When ESI-MS analysis of the complexes was acquired in positive mode, a m/z peak was observed that corresponds to the positively charged complex without its counter-ion (M - Y). When run in negative mode a m/z peak corresponding to the anion was observed (145.0 and 149.0 for PF_6^- and $CF_3SO_3^-$ respectively). IO_3^- was not observed by ESI-mass spectrometry.

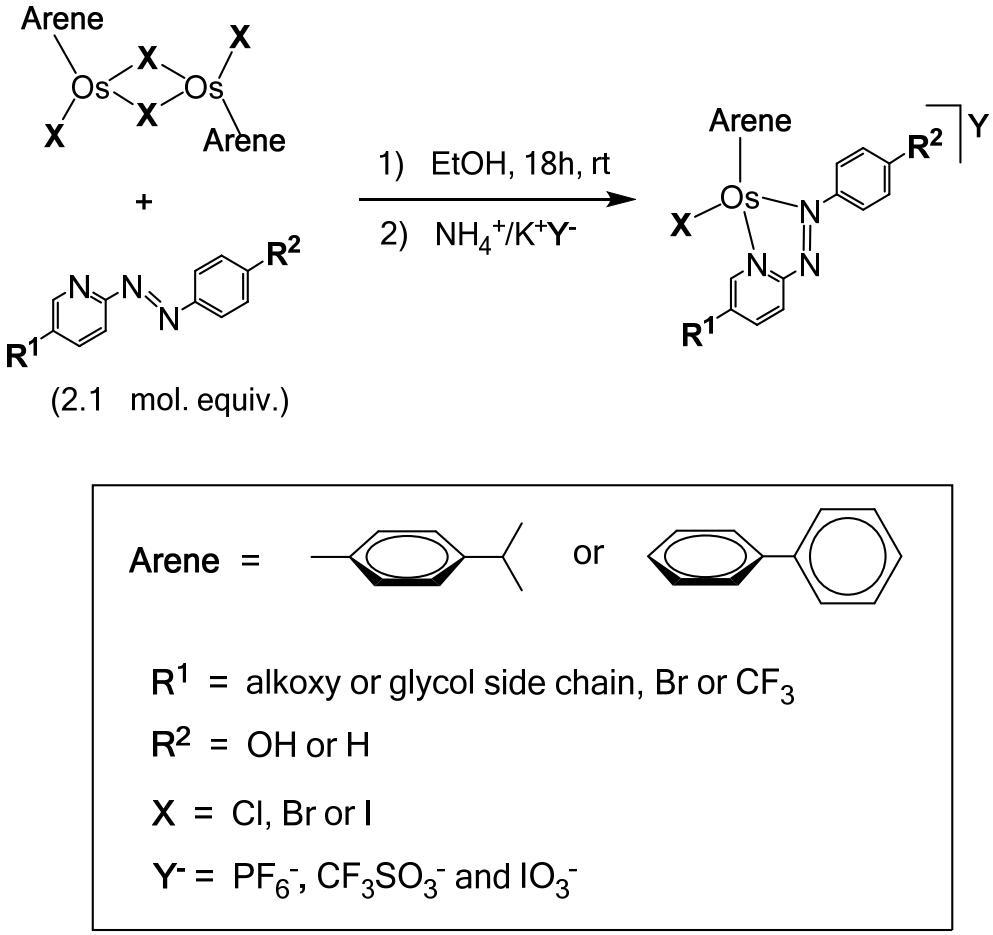

Scheme 4.5. General scheme for the synthesis of Os(II) arene AZPY complexes bearing monodentate halide ligands.

The synthesis of complexes bearing *pseudo*-halide ligands required different strategies. For thiocyanato complex (**34**), the first step involved reacting the

chloride dimer, $[Os(\eta^6\text{-}p\text{-cym})Cl_2]_2$, with 2.1 mol.equiv. of 5-EtO-AZPY to form a chlorido Os(II) arene AZPY complex *in situ*. The complex was then heated for 18 h under reflux with 500 mol. equiv. of KSCN and the chloride ligand was displaced by the *pseudo*-halide anion (see Scheme 4.6, A). The reaction formed a mixture of two different structural isomers (see Section **4.3.11**). The chloride dimer was selected because chloride is more labile and easier displace than bromide or iodide. Finally, the counter anion was changed to PF_6^- by adding NH_4PF_6 (10 mol. equiv.) to an ethanolic solution of the complex. Drying the mixtures and filtering them after re-dissolving in DCM was a process used to remove excess salts, as DCM does not solubilise KSCN or NH_4PF_6.

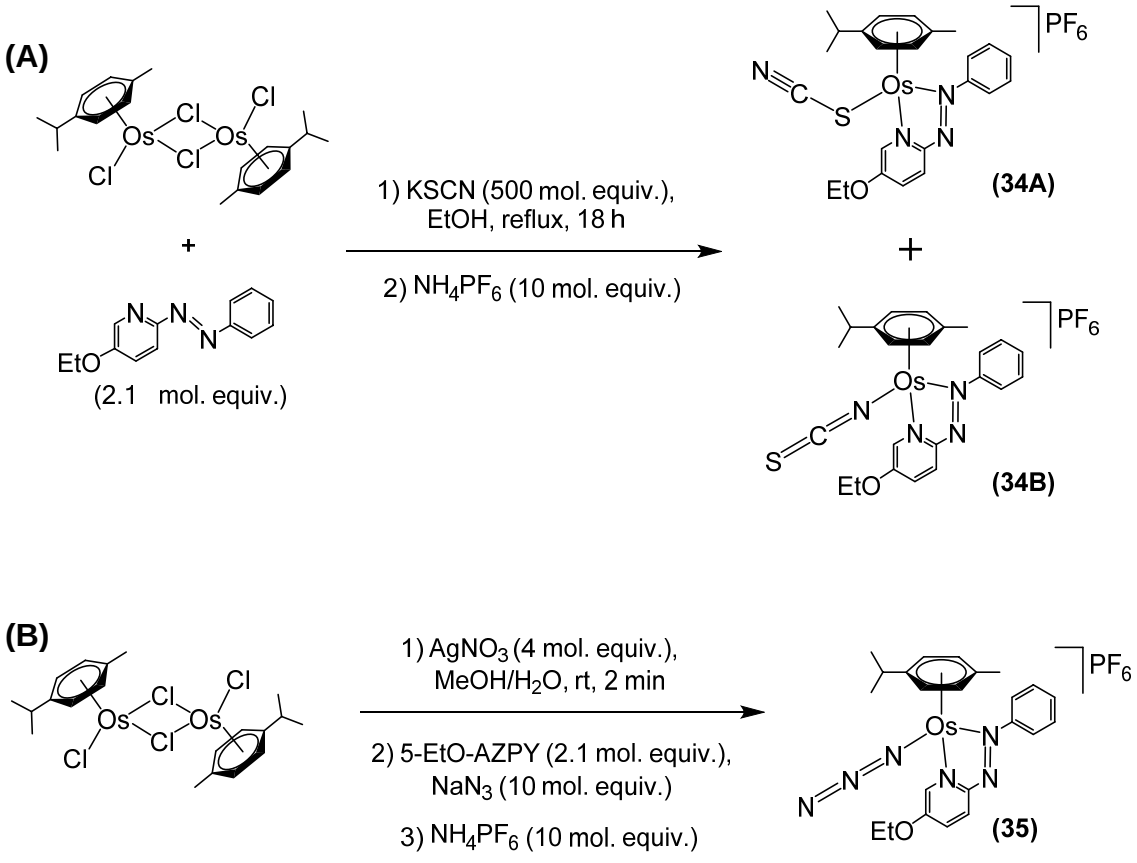

Scheme 4.6. Protocols for the synthesis of Os(II) *p*-cym 5-EtO-AZPY complexes bearing; (A) a SCN^- monodentate ligand, and (B) a N_3^- monodentate ligand.

Because of the dangers associated with azides, the method was altered to prevent using excessive amounts NaN_3 when synthesising **35**. $[Os(\eta^6\text{-}p\text{-cym})Cl_2]_2$ was reacted with $AgNO_3$ (4 mol. equiv.) to remove the chloride ligands and the resulting aqua-species was reacted with 2.1 mol. equiv. 5-EtO-AZPY and 10 mol. equiv. of NaN_3 (see Scheme 4.6, B).

All complexes were characterised by ^1H NMR, ESI-MS and CHN analysis. Some complexes proved to be unsuitable for CHN analysis and were instead characterised by ^{13}C NMR. Their purities were analysed *via* HPLC and complexes were only used for biological studies after ensuring a purity of >97%. Impure complexes were purified by either re-crystallisation, preparative HPLC, or automated reverse-phase column chromatography. The molecular structures of all the complexes synthesised in this chapter are shown in the Appendices, Section **8.2**.

4.3.3. X-ray crystal structures

The molecular structures of complexes **6**, **10**, **13A**, **32**, **33** and **FY026** were determined by single crystal X-ray diffraction (Figure 4.3). Selected bond lengths are summarised in Table 4.2 and the crystallographic data are shown in Table 4.3. Complex **13A** is analogous to **13** with a PF_6^- anion in place of $CF_3SO_3^-$. Complex **FY026** is described in greater detail in Chapter 1, Section **1.3.4.3**, and is studied in Chapters 5 and 6 herein.[25] All the complexes adopt the familiar *pseudo*-octahedral three-legged piano-stool geometry, where the Os(II) centre is π-bonded to the arene ligand. The Os(II) centre is also coordinated to

a halide ligand and the bidentate AZPY ligand, which constitute the three legs of the piano-stool. The complexes crystallise as racemates owing to their chiral metal centres and contain PF_6^- counter ions in their X-ray crystal structures. Complexes **10**, **32** and **33** also incorporate solvent molecules in their crystal lattices. Complex **10** incorporates half of a EtOH molecule, and **32** and **33** both incorporate a MeOH molecule that is involved in hydrogen bonding between the OH substituent of the AZPY ligand and the PF_6^- anion (Figure 4.4).

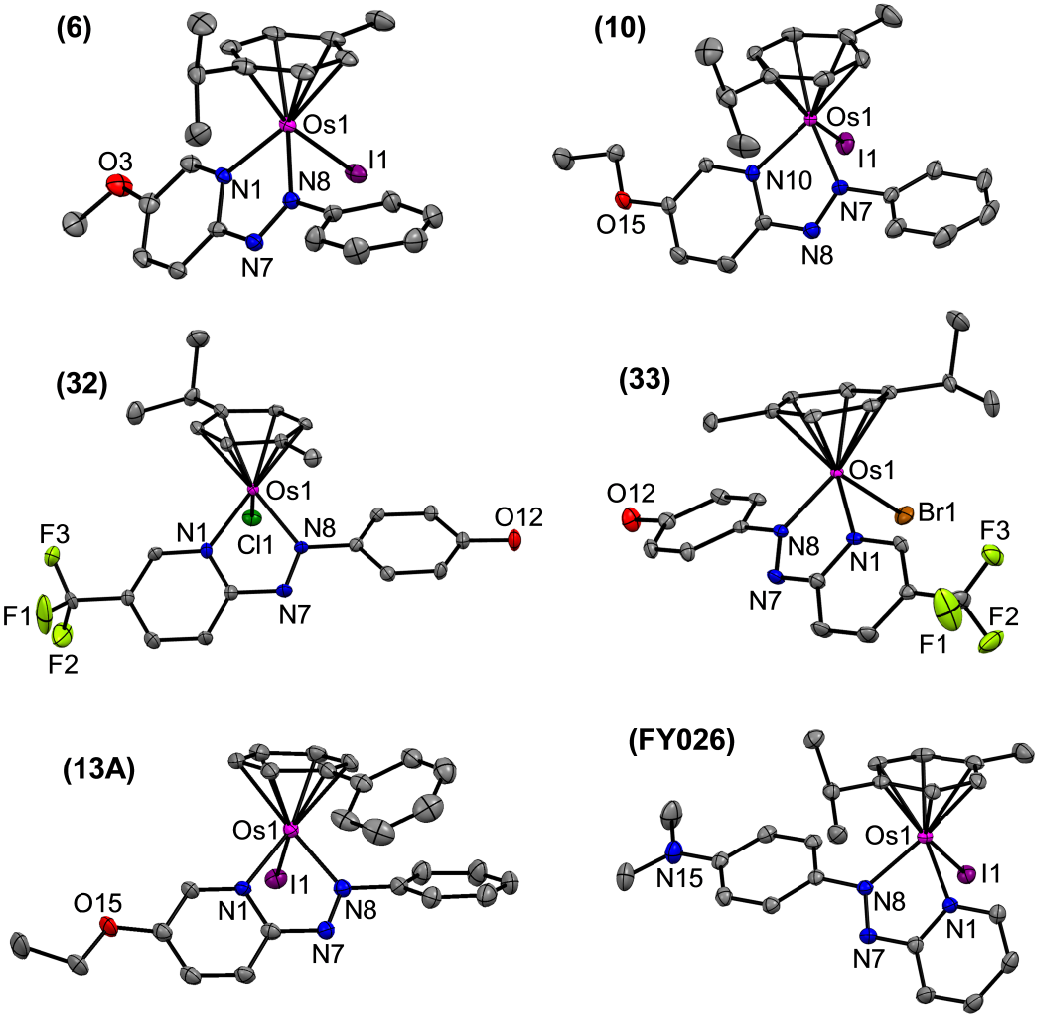

Figure 4.3. ORTEP diagrams for complexes **6**, **10**.0.5C_2H_6O, **32**.CH_4O, **33**.CH_4O, **13A** and **FY026**. Ellipsoids are shown at the 50% probability level and all hydrogens, counter ions and solvent molecules have been omitted for clarity.

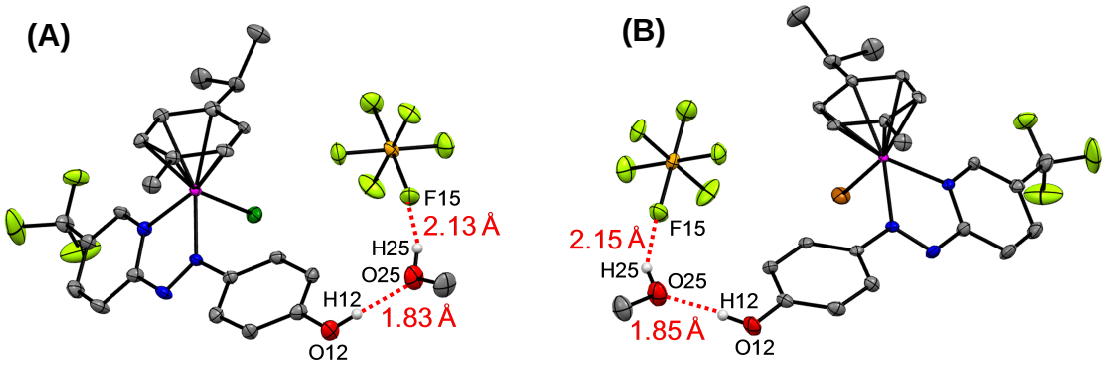

Figure 4.4. Hydrogen bonding interactions within the crystal structures of (A) **32**.CH_4O, and (B) **33**.CH_4O, occurring between the OH substituent, a molecule of MeOH, and the PF_6^- anion.

Table 4.2. Selected bond lengths (Å) observed in the X-ray crystal structures of complexes **6**, **10**.0.5C_2H_6O, **13A**, **32**.CH_4O, **33**.CH_4O and **FY026**. X = Cl, Br or I (monodentate halide ligand).

Bond length (Å)	**6**	**10**.0.5C_2H_6O	**13A**	**32**.CH_4O	**33**.CH_4O	**FY026**
Os1-X1	2.7099(2)	2.6974(2)	2.6918(3)	2.379(2)	2.4926(7)	2.7124(2)
Os1-N1/N10	2.060(3)	2.052(2)	2.059(3)	2.051(8)	2.051(5)	2.058(2)
Os1-N8/N7	2.023(3)	2.022(2)	2.029(4)	2.019(8)	2.013(5)	2.041(2)
N7-N8	1.286(4)	1.289(3)	1.279(5)	1.291(12)	1.300(8)	1.302(3)
Os1-Arene Centroid	1.728	1.712	1.704	1.711	1.711	1.714

Table 4.3. Crystallographic data for complexes **6**, **10**, **13A**, **32**, **33** and **FY026**.

	6	**10**.0.5C_2H_6O	**13A**	**32**.CH_4O	**33**.CH_4O	**FY026**
Formula	$C_{22}H_{25}F_6IN_3OOsP$	$C_{24}H_{30}F_6IN_3O_{1.5}OsP$	$C_{25}H_{23}F_6IN_3OOs$ P	$C_{23}H_{26}ClF_9N_3O_2OsP$	$C_{23}H_{26}BrF_9N_3O_2OsP$	$C_{23}H_{28}F_6IN_4OsP$
Molar mass /g mol^{-1}	809.52	846.58	843.53	804.09	848.55	822.56
Density /mg m^{-3}	2.138	2.021	2.137	1.963	2.040	2.077
Crystal system	Monoclinic	Monoclinic	Monoclinic	Orthorhombic	Orthorhombic	Monoclinic
Crystal dimensions /mm	0.4 x 0.3 x 0.2	0.52 x 0.38 x 0.28	0.20 x 0.08 x 0.02	0.4 x 0.1 x 0.08	0.2 x 0.2 x 0.1	0.6 x 0.18 x 0.1
Space group	P2(1)/c	P2(1)/c	P2(1)/c	Pna2(1)	Pna2(1)	P2(1)/c
Crystal character	Brown block	Brown block	Brown block	Brown block	Brown block	Purple block
a/Å	12.45801(8)	10.6922(3)	18.2542(6)	7.85520(7)	7.99294(7)	14.0452(3)
b/Å	13.88211(9)	12.2890(4)	7.2404(2)	20.50602(14)	20.44259(15)	10.7594(3)
c/Å	14.54312(11)	21.1818(6)	21.4614(6)	16.88981(11)	16.91178(14)	17.5925(4)
α/deg	90	90	90	90	90	90
β/deg	91.2934(6)	90.775(3)	112.418(4)	90	90	98.405(2)
γ/deg	90	90	90	90	90	90
T/K	150(2)	150(2)	150(2)	150(2)	150(2)	150(2)
Z	4	4	4	4	4	4
R [F> 4σ(F)]	0.0279	0.0311	0.0383	0.0435	0.0286	0.0306
R_w	0.0680	0.0600	0.0915	0.1120	0.0677	0.0554
GOF	1.105	1.052	1.079	1.072	1.077	1.084
Δρ max and min /e$Å^{-3}$	1.16 & -1.24	0.98 & -1.37	2.383 & -2.804	1.81 & -1.22	1.76 & -1.70	1.38 & -1.37

4.3.4. pK_a of complex 31

Complex **31** exhibits a Br-AZPY-OH ligand and the hydroxyl substituent on its phenyl ring that is capable of deprotonation (Scheme 4.7). Utilising UV-Vis spectroscopy, the intensity of the absorption at 588 nm was measured at various pH values (see Figure 4.5) and the data were fitted to the Henderson-Hasselbalch equation (Figure 4.6). The pK_a was determined as 6.41±0.02 and the error was obtained as a computer fitting error using Origin 8.5. When pH = pK_a the colour of the complex was brown. Interestingly, at high pH the complex was a deep blue colour and when adjusted to a low pH the complex was orange with a major absorption peak at 446 nm. Under physiological conditions (pH 7.4), the complex was blue and will predominantly exist in a zwitterionic form.

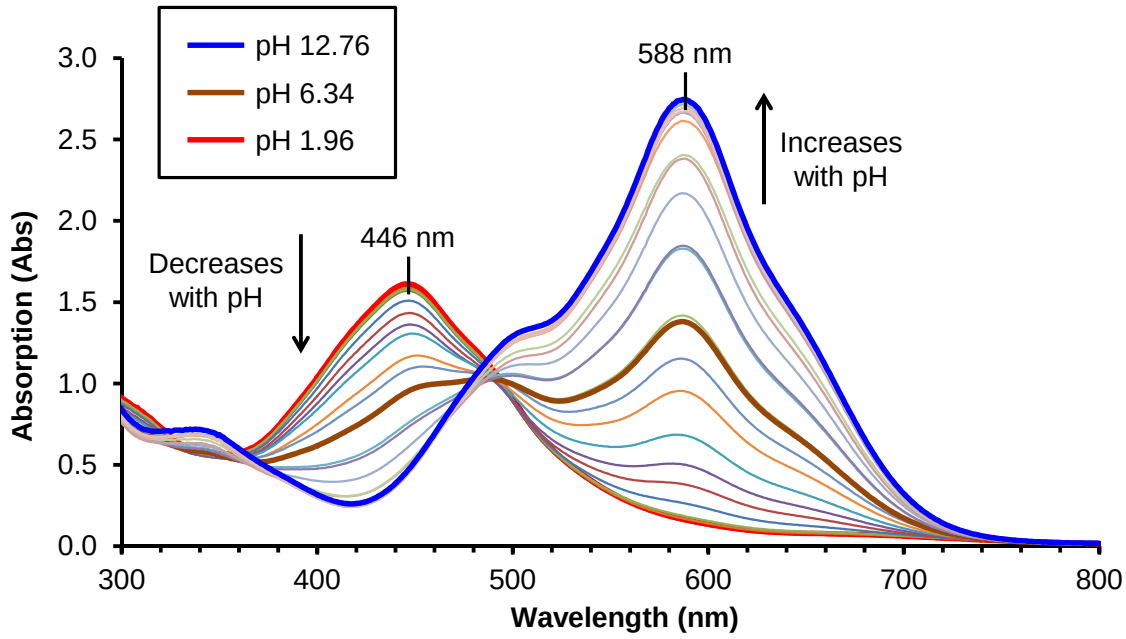

Figure 4.5. UV-Vis spectra of complex **31** (100 µM) in water at different pH levels. Absorption bands at 588 nm (high pH) and 446 nm (low pH) were observed.

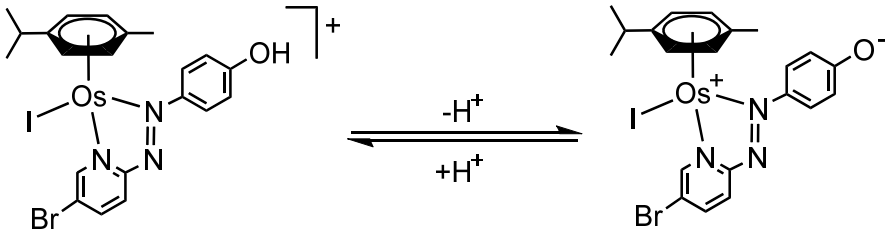

Scheme 4.7. Protonation and deprotonation of **31** under acid and basic conditions, respectively.

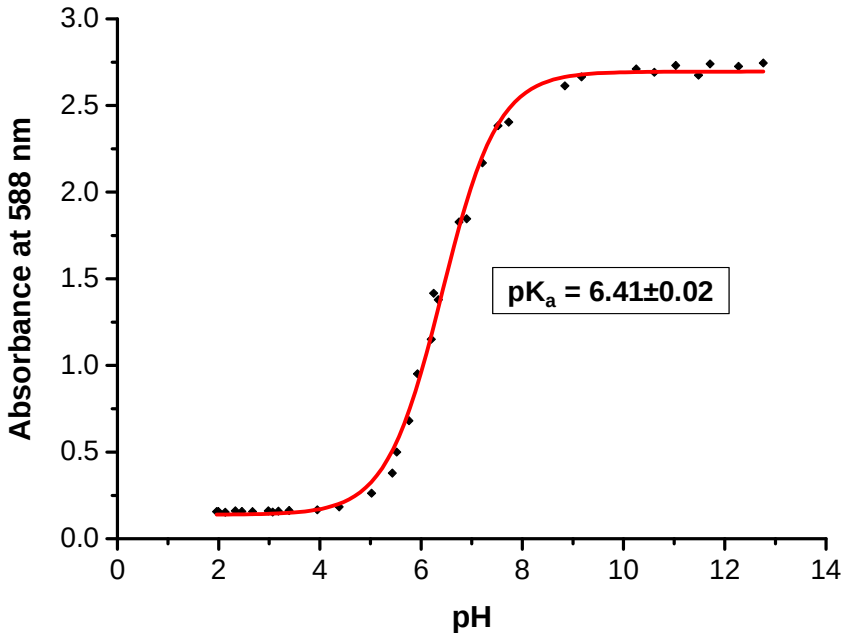

Figure 4.6. Variation of the absorbance at 588 nm for **31** with pH. The red line represents a computer fit to the Henderson-Hasselbalch equation.

4.3.5. Extent of hydrolysis of complexes in aqueous media

4.3.5.1. ^{1}H NMR spectroscopy

The extent of hydrolysis after 24 h was determined for all complexes in D_2O (5% DMSO-d_6) at ambient temperature *via* ^{1}H NMR. Figure 4.7 shows the ^{1}H

NMR spectrum of **8** straight after sample preparation (10-20 min) and 24 h later as an example. A new set of peaks that correspond to the aqua/hydroxido-adduct was visible after sample preparation and increases in intensity after 24 h. The red box highlights a region corresponding to *p*-cym CH_3 groups (2x 3H doublets) and their integrals were used to calculate the %hydrolysis. Interestingly, when the experiment was repeated in the presence of 100 mM NaCl, hydrolysis was significantly suppressed with only 7% hydrolysis occurring after 24 h.

The extent of hydrolysis of analogous complexes **8**, **9** and **10** (with chlorido, bromido and iodido ligands, respectively) was 23%, 7% and 0% after 24 h. Likewise, analogous complexes **17**, **18**, and **19** baring chlorido, bromido and iodido ligands show 20%, 15% and 0% hydrolysis, respectively. In general, the susceptibility of a complex towards hydrolysis follows the order Cl>Br>I. The extent of hydrolysis of all the other complexes was measured in the same manner (the majority of which are iodido complexes) and are as follows after 24 h: Complexes **6**-**13**, **20**, **21**, **23**, **24**, **29**-**35** were stable, complexes **14**, **15**, **25** and **28** showed <2% hydrolysis, and complexes **22**, **26** and **27** showed 10-15% hydrolysis. It is worth noting that this crude measurement may not give results that are comparable with one another as the concentrations used in the experiment were not fixed and resemble saturated solutions in D_2O. Some complexes have very poor solubility in D_2O which may lead to greater extents of hydrolysis. The pH of the solutions were not measured or controlled with a buffer.

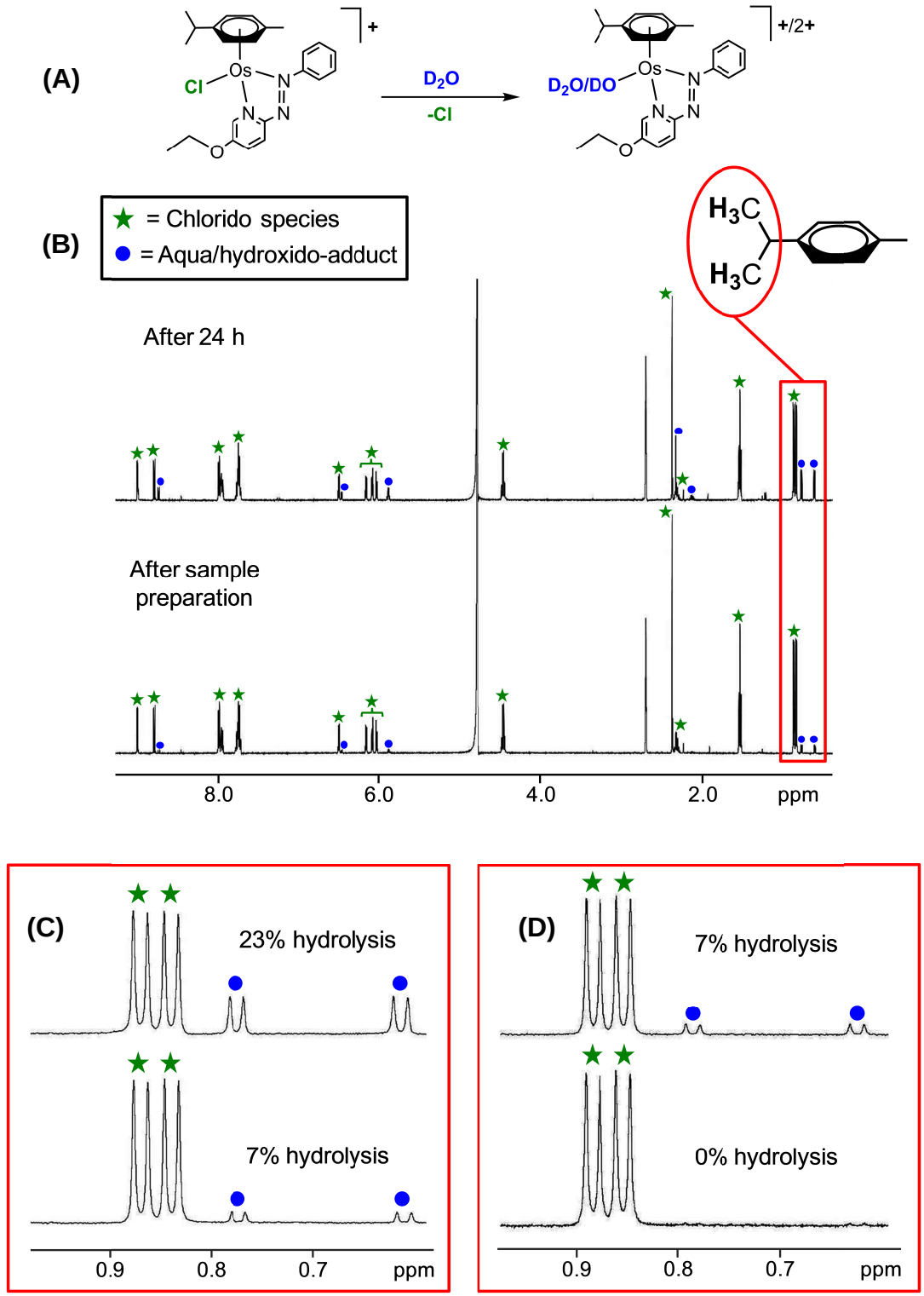

Figure 4.7. (A) Reaction scheme for the hydrolysis of **8** in D_2O. (B) ^1H NMR spectrum of **8** immediately after sample preparation and 24 h later. (C) Expansion of the ^1H NMR spectrum showing the *p*-cym CH_3 groups. (D) The same expansion but in the presence of 100 mM NaCl, showing the suppression of hydrolysis. Spectra were collected on a 500 MHz instrument.

4.3.5.2. HPLC

The extent of hydrolysis of **8**, **9** and **10** was also determined by HPLC at a fixed concentration (100 μM) after 0, 2, 12 and 24 h incubation at 37 °C. They were solubilised in phosphate buffer (95 mol. equiv., pH 7.4) with 5% DMSO and different concentrations of NaCl; 23 mM (intracellular conditions) and 103 mM (extracellular conditions). The chromatograms are shown in Figure 4.8. Chlorido and bromido complexes (**8** and **9**) show significant levels of hydrolysis after 24 h incubation in 23 mM NaCl, with 85% and 84% of the aqua/hydroxido species (**10-OH**) present, respectively. Incubation in 103 mM NaCl partially suppresses the hydrolysis of **8** and **9** with 61% and 58% occurring, respectively. For the bromido complex (**9**), formation of the chlorido species (**8**) was also observed in the presence of NaCl, occurring at 8% and 27%, respectively for 23 mM and 103 mM NaCl. In contrast, the iodido complex (**10**) is much more resilient towards hydrolysis, showing only 7% and 4% hydrolysis after 24 h incubation in the presence of 23 mM and 103 mM NaCl, respectively. Formation of the chlorido species (**8**) was also observed in small amounts when **10** was incubated for 24 h (1% and 2% was observed for 23 mM and 103 mM NaCl, respectively).

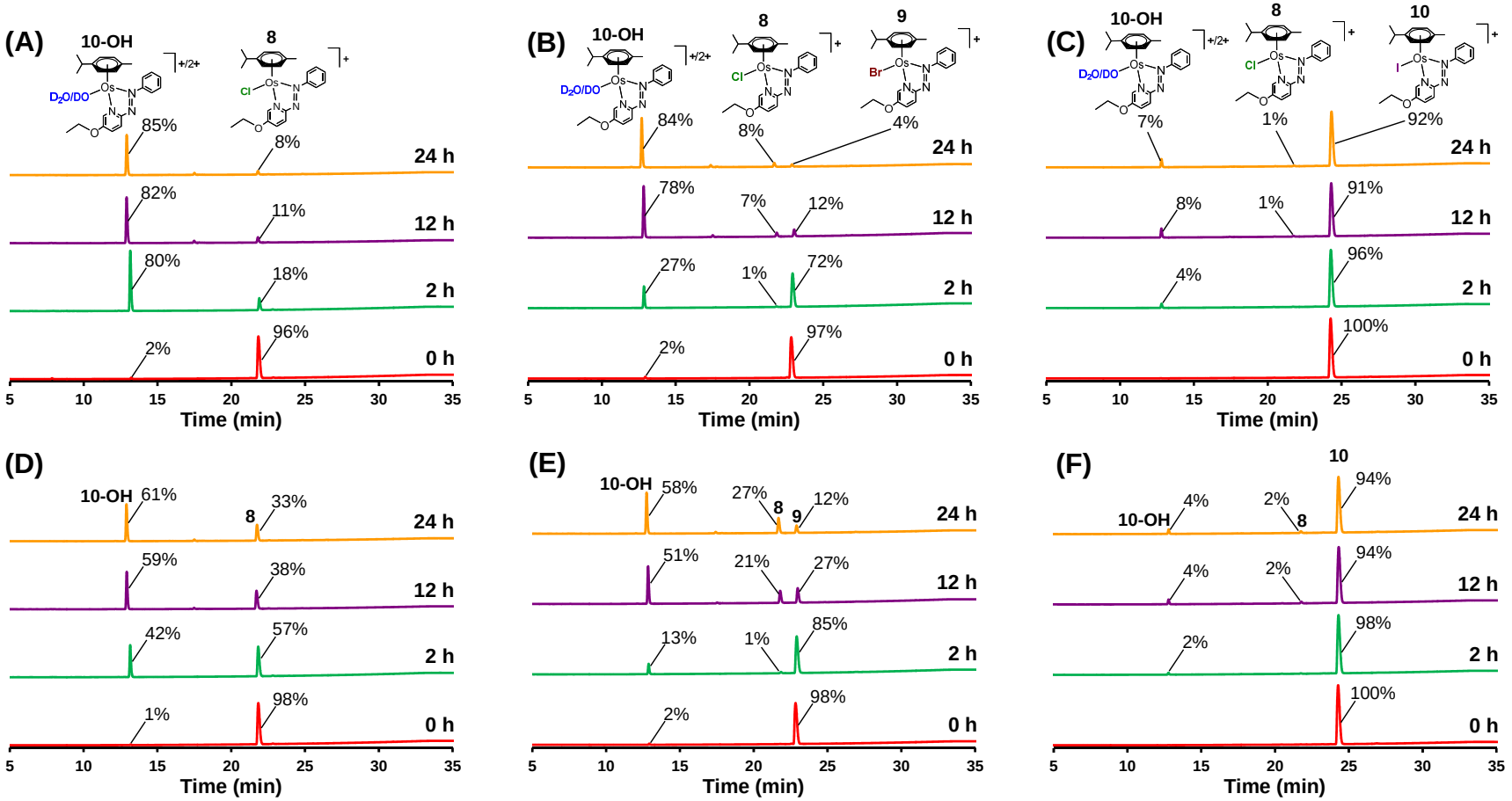

Figure 4.8. HPLC traces for complexes **8**, **9** and **10** (100 μM) after incubation in phosphate buffer solution (pH 7.4) and different concentrations of NaCl, for 0, 2, 12 and 24 h at 37 °C. (A) **8** in 23 mM NaCl. (B) **9** in 23 mM NaCl. (C) **10** in 23 mM NaCl. (D) **8** in 103 mM NaCl. (E) **9** in 103 mM NaCl. (F) **10** in 103 mM NaCl. Details of the HPLC conditions are shown in Chapter 2, Section **2.2.9**.

4.3.6. Solubility of complexes in aqueous media

The thermodynamic solubility of complexes **6**-**28** at ambient temperature was determined in 100 mM NaCl, resembling physiological extracellular conditions. This series of complexes consists of those with RO-AZPY ligands containing alkoxy and glycol side chains. Thermodynamic solubility requires an equilibrium to be reached, whereby a maximum quantity of a substance is completely dissolved at a given pressure and temperature and is thermodynamically valid as long as a solid phase exists in equilibrium with the solution phase.[17,26,27] The trends in solubility are shown in Figures 4.9- 4.11.

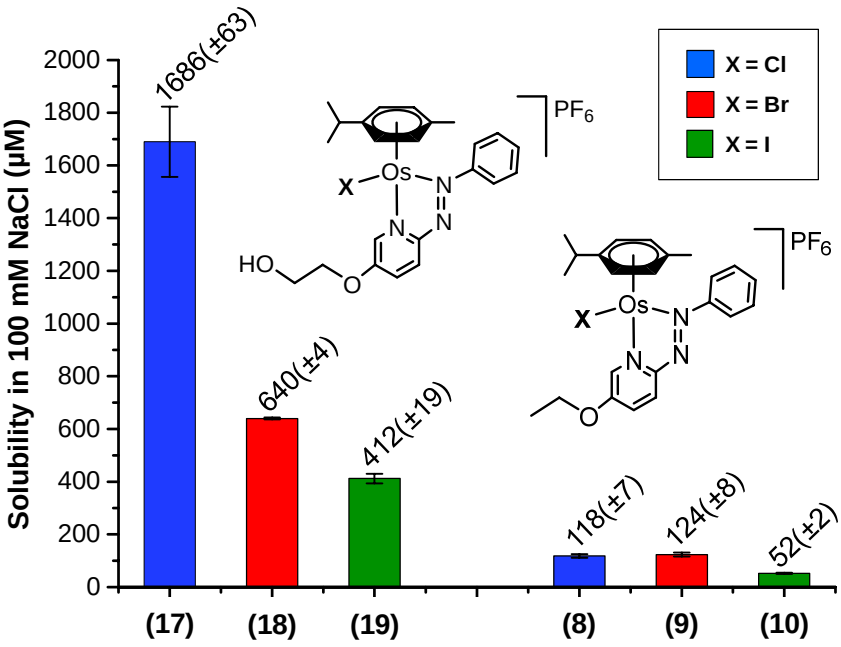

Figure 4.9. Trends in solubility for complexes **17**-**19** and **8**-**10** in 100 mM NaCl.

In Figure 4.9, the solubility trends between **17**-**19** and **8**-**10** show that chlorido and bromido complexes are considerably more soluble than their iodido

analogues. The observed trend follows Cl>Br>I where chlorido complexes are the most soluble with the exception of **8**, which has around the same solubility as bromido complex **9**. Furthermore, the addition of a terminal OH group at the end of the ethoxy substituent leads to a 14-fold, 5-fold and 8-fold increase in solubility for the chlorido, bromido and iodido complexes respectively.

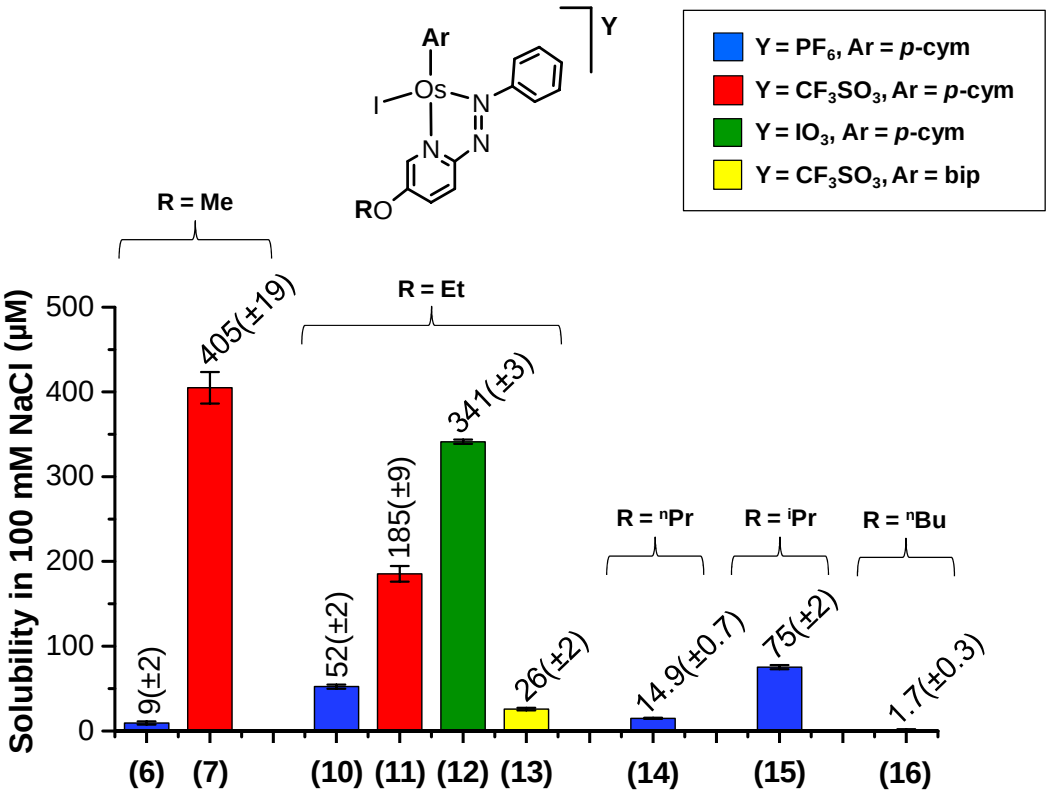

Figure 4.10. Trends in solubility for complexes **6**, **7** and **10**-**16** in 100 mM NaCl.

Figure 4.10 shows the solubility trends for complexes bearing alkoxy side-chains. The trends between **6** and **7**, and **10**-**12** highlight that solubility can be vastly improved by changing the counter anion from PF_6^- to either $CF_3SO_3^-$ or IO_3^-, with the trend following the order IO_3^->$CF_3SO_3^-$>PF_6^-. Most notably, changing the PF_6^- anion in **6** to $CF_3SO_3^-$ leads to 45-fold increase in solubility.

The trend between **11** and **13** shows that changing the arene from *p*-cym to bip leads to a 7-fold decrease in solubility. The solubility trend between **6**, **10**, and **14**-**16**, where the R-substituent is varied follows a more complicated order: ^{i}Pr>Et>^{n}Pr>Me>^{n}Bu.

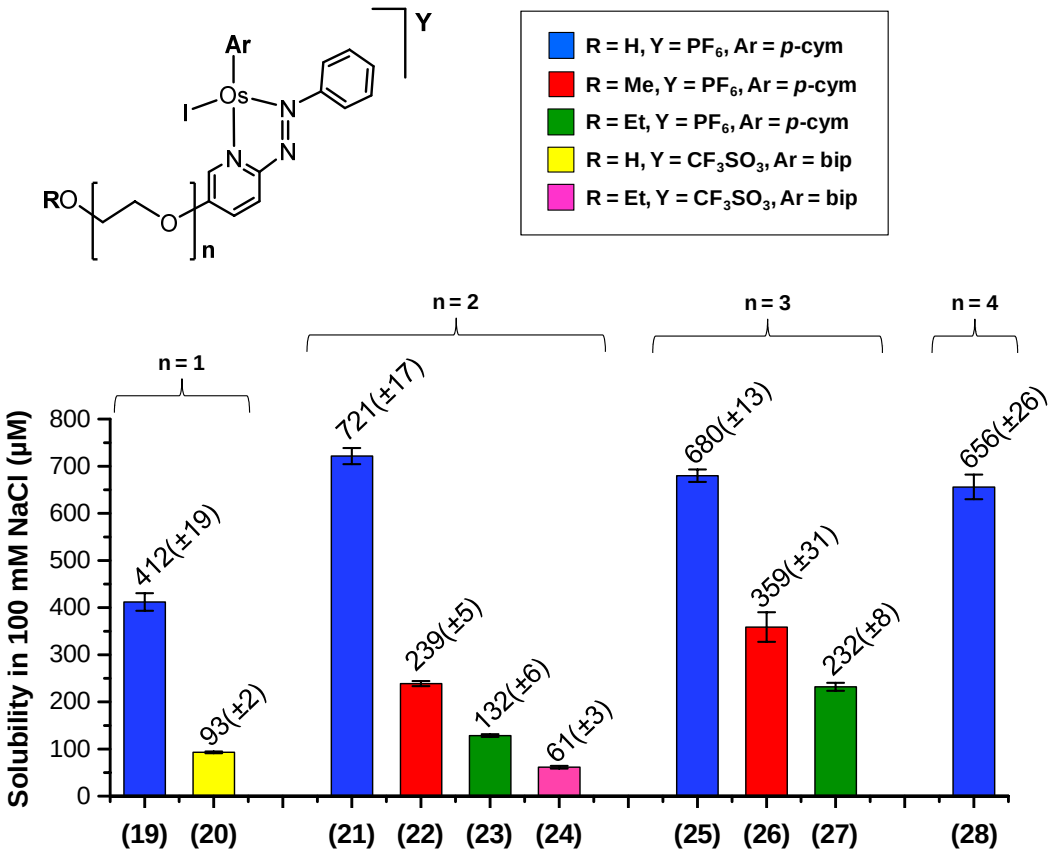

Figure 4.11. Trends in solubility for complexes **19**-**28** in 100 mM NaCl.

Figure 4.11 shows the solubility trends for complexes with glycolic side-chains. The trend between **19**, **21**, **25** and **28** shows how glycol chain length impacts on solubility when R= H. The poorest solubility was observed for **19**, bearing the monoethylene glycol substituent, and a notable solubility increase was

observed when the chain length was varied in the order n= 2>3>4>1. Changing the terminal R-substituent has an even greater impact on solubility as shown by **21**-**23** and **25**-**27**, and follows the order H>>Me>Et. Furthermore, **20** and **24** show that changing the arene from *p*-cym to bip leads to a decrease in solubility, despite containing a more solubilising counter anion.

The samples were further analysed by HPLC to determine whether they remained stable in solution after the 24 h solubilisation process. The vast majority of complexes remained >95% intact. However some complexes, particularly those with very low aqueous solubility were less stable. Samples of **6**, **14**, **16** and **20** remained 88%, 95%, 85% and 91% intact, respectively after solubilisation. There is potential for complexes to form aqua/hydroxido- species, and chlorido-species in small amounts due to the presence of NaCl.

4.3.7. Anti-proliferative activity

The IC_{50} values of all the complexes were measured against A2780 cells by Dr. Isolda Romero-Canelón using the protocol outlined in Chapter 2, Section **2.3.2**. The IC_{50} values of **8**-**10**, **17**-**19** and **35** are shown in Figure 4.12. The trend shows that placement of a terminal OH group at the end of the ethoxy substituent is deactivating towards anti-cancer activity. Furthermore, complexes with monodentate iodide ligands are considerably more active than their chloride and bromide counter-parts. The *pseudo*-halide, N_3, also provides improved reactivity. The observed trend follows $I>N_3>>Br\geq Cl$.

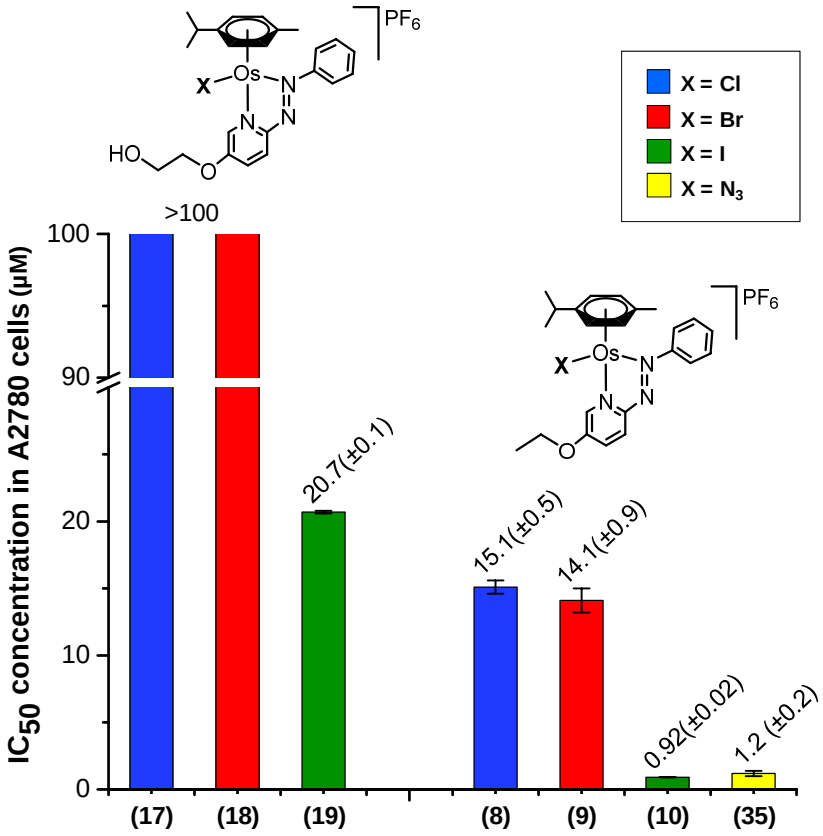

Figure 4.12. Trends in IC_{50} values against A2780 cells for complexes **8**-**10**, **17**-**19** and **35**.

In Figure 4.13, the trend between **10**-**12** shows that changing the anion has no impact on anti-cancer activity with the exception of **12** (IO_3^- counter-ion), which is slightly less active than the others. The trend between **11** and **13** shows that changing the arene from *p*-cym to bip increases activity. Furthermore, the trend between **7**, **10**, **14**, **15** and **16** where the R-substituent is varied follows the order $^{i}Pr>^{n}Pr>Me>Et>^{n}Bu$.

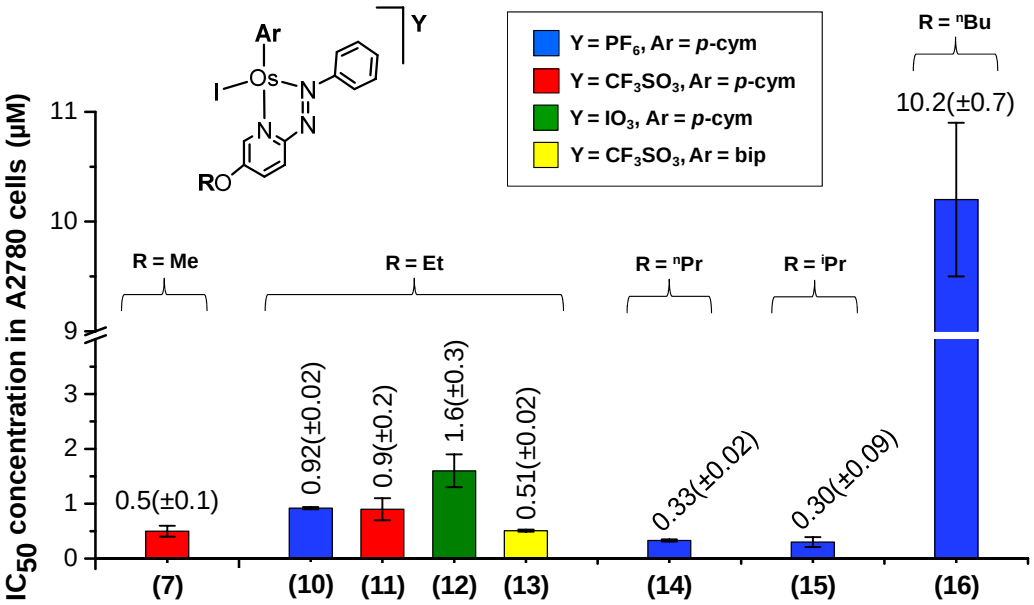

Figure 4.13. Trends in IC_{50} values against A2780 cells for complexes **7**, **10**-**13** and **14**-**16**.

In Figure 4.14, the trend between **19** and **20** (where R= H and n= 1) shows that changing the arene from *p*-cym to bip results in a large increase in anti-cancer activity. In contrast, the trend between complex **23** and **24** (R= H and n= 2) shows that the same change actually leads to a small decrease in activity. Changing the terminal group at the end of the glycol side chain from H to either Me or Et leads to an increase in activity, as seen by the trends in **21**-**23** and **25**-**27**. Furthermore, the differences in activity between **19**, **21**, **25** and **28** where the glycol chain length is varied (R= H) does not follow an obvious trend: n= 2>4>3>1. When R= Me or Et, increasing the glycol chain length from n= 2 to n= 3 produces a decrease in activity.

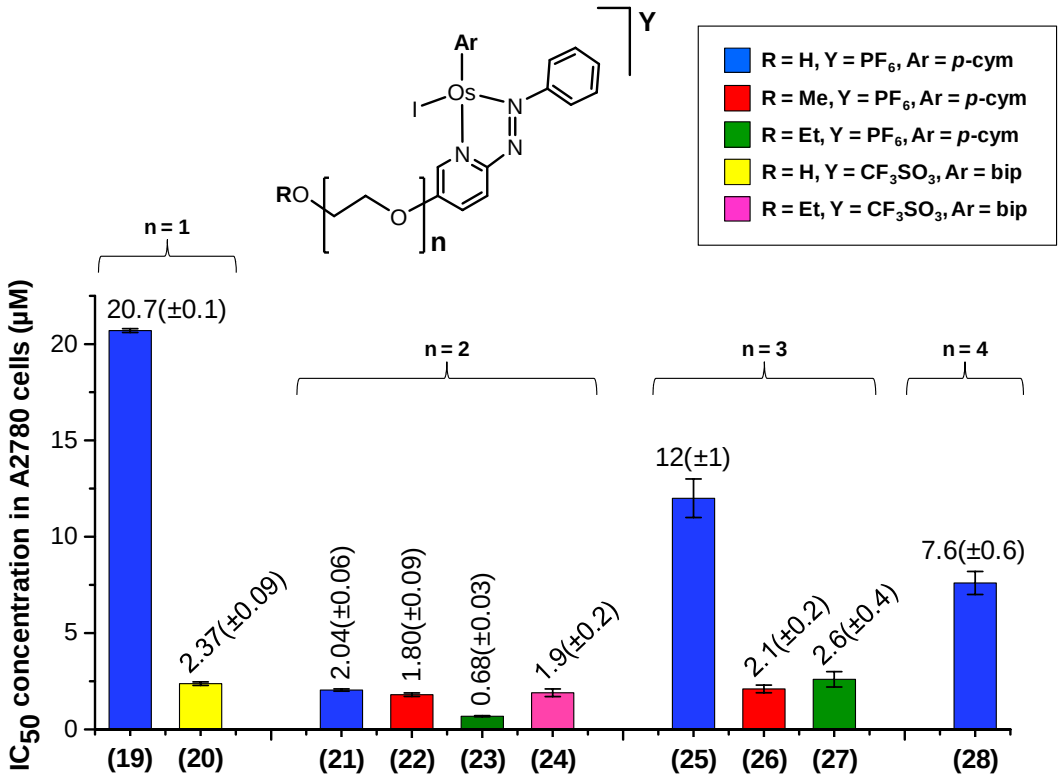

Figure 4.14. Trends in IC_{50} values against A2780 cells for complexes **19**-**28**.

The anti-cancer activity trends between **29**-**33** are shown in Figure 4.15. These complexes exhibit R-AZPY-OH ligands. It is shown again that iodido complexes are the most active complexes and the activity trend follows I>Br>Cl. Furthermore, greater activity is observed when the R-substituent is CF_3 over analogous complexes containing a Br substituent.

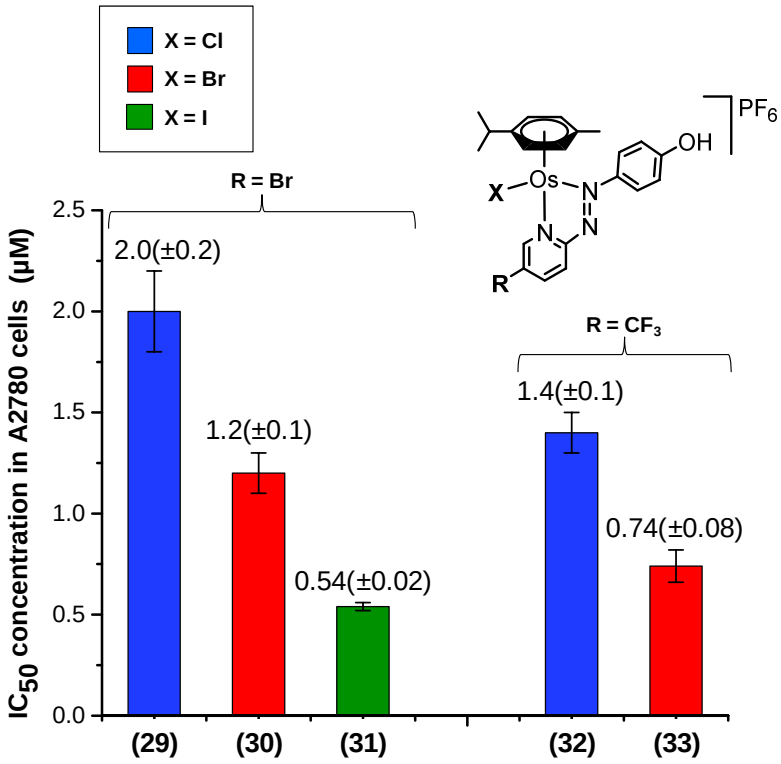

Figure 4.15. Trends in IC_{50} values against A2780 cells for complexes **29**-**33**.

Table 4.4 shows the IC_{50} values of key complexes in various cancer cell lines: A2780 ovarian cancer, MCF-7 breast cancer, SUNE1 nasopharyngeal cancer, OP19 oesophageal cancer, and normal cell line: MRC-5 lung fibroblast cells. Their selectivity factors (SFs) have been calculated for IC_{50}-MRC-5/IC_{50}-A2780. With the exception of complex **23**, all complexes that were tested against SUNE1 cells show very potent sub micro-molar activity. Complexes **10**, **13** and **23** exhibit exceptionally potent activity against OE19 cells. Particularly **13** which has an IC_{50} value of 96 nM. Complex **15** exhibits the best activity against A2780 cells (the most widely used cell line in the Sadler group), and **13** exhibits the best anti-cancer profile amongst all the tested cell lines, and has the highest SF.

In contrast, **31**, which exhibits potent activity against A2780 cells has very poor selectivity towards A2780 cancer cells over MRC-5 normal cells.

Table 4.4. The IC_{50} values of key complexes **10**, **13**, **15**, **22**, **23** and **31**, against various cancer cell lines and normal MRC-5 cells. Selectivity factors are calculated as a ratio of IC_{50}-MRC-5/IC_{50}-A2780. IC_{50} values are shown in μM.

	A2780	**MCF-7**	**SUNE1**	**OE19**	**MRC-5**	**Selectivity Factor**
10	0.92(±0.02)	1.2(±0.2)	0.86(±0.06)	0.20(±0.03)	2.2(±0.2)	2.4
13	0.51(±0.02)	n.d.	0.31(±0.02)	0.096(±0.004)	6.1(±0.1)	12.0
15	0.30(±0.09)	n.d.	n.d.	n.d.	1.99(±0.07)	6.6
22	1.80(±0.09)	n.d.	n.d.	n.d.	7.4(±0.8)	4.1
23	0.68(±0.03)	n.d.	1.7(±0.1)	0.42(±0.01)	3.6(±0.3)	5.3
31	0.54(±0.02)	n.d.	n.d.	n.d.	0.62(±0.01)	1.1

4.3.8. Cellular accumulation

The cellular accumulation of complexes into A2780 cells was measured using the protocol outlined in Chapter 2, Section **2.3.4** by Dr.Isolda Romero-Canelón, and the amount of accumulated ng of Os /10^6 cells was determined using ICP-MS. Figure 4.16 shows the cell uptake for complexes **7**-**11**, **13**, **14** and **17**-**19**. The trend between **8**-**10** and **17**-**19** shows that iodido complexes have greater cellular uptake than their chlorido and bromido analogues, and it follows the same order as anti-cancer activity (I>Br>Cl). It also shows that the presence of

a terminal OH group leads to lowered cell uptake, likely owing to lowered lipophilicity. The trends between **10**, **11** and **13** shows that the anion has no impact on cell uptake (similarly to anti-cancer activity), and switching the arene from *p*-cym to bip leads to an unexpected decrease in cell uptake. When the R-substituent is varied there is no obvious trend and cell uptake follows the order Et>^{n}Pr>Me, as observed between **7**, **10**, **11** and **14**.

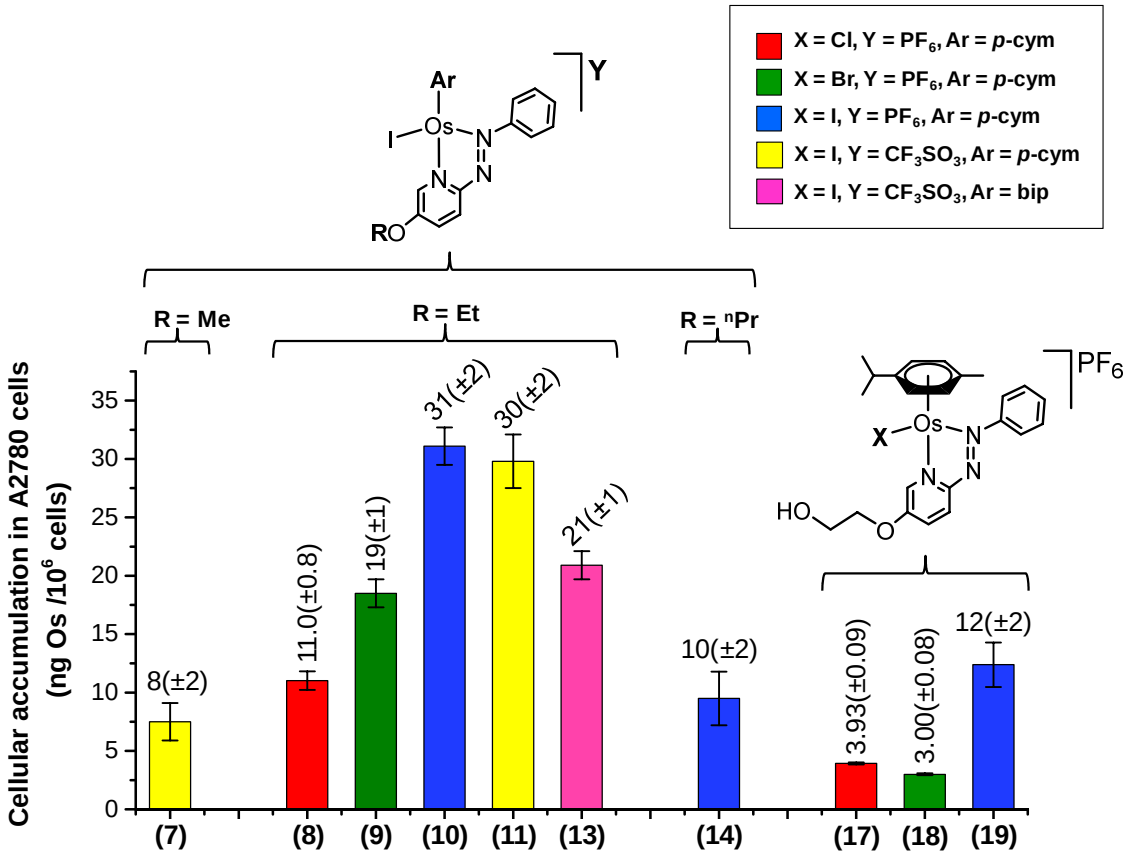

Figure 4.16. Trends in cellular accumulation for complexes **7**-**11**, **13**, **14** and **17**-**19**.

4.3.9. Capacity factors

The capacity factor (*K*) was determined for complexes **7**-**11** and **13**-**28** using an isocratic HPLC method at 25 °C. The mobile phase was H_2O:MeCN (1:1, v/v) with 50 mM NaCl, and the stationary was a reverse-phase C18 column (250 x 4.6 mm column with a pore size of 5 µm). The capacity factor provides a measure of affinity towards the stationary phase, hence provides a measure of the relative lipophilicity of a complex. The greater the retention time (hence *K*), the greater the lipophilicity of the complex. The trends in *K* are shown in Figures 4.17- 4.19.

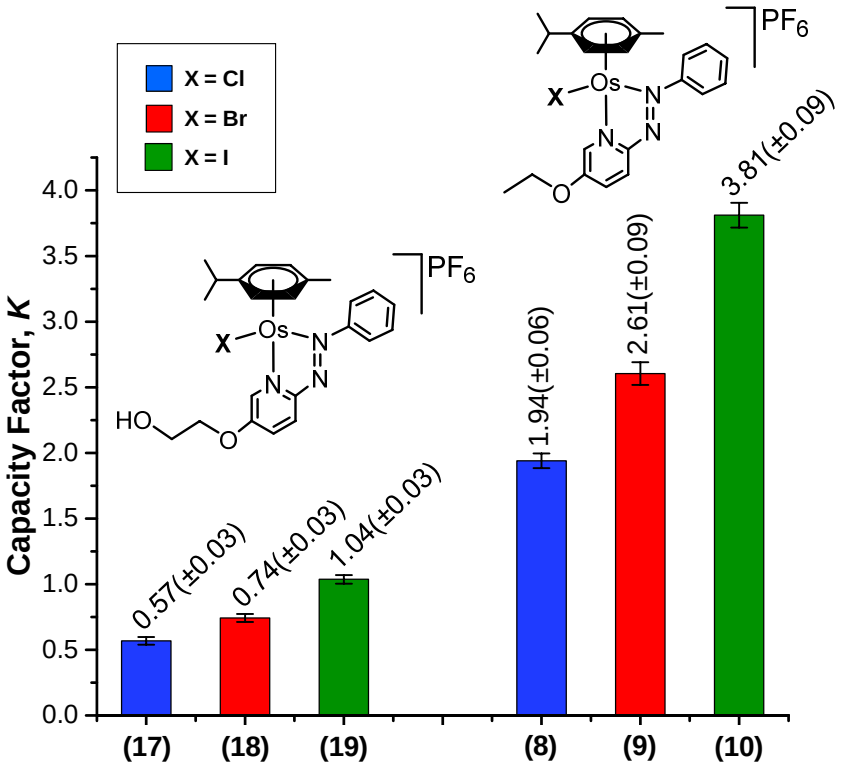

Figure 4.17. Trends in capacity factor for complexes **17**-**19** and **8**-**10**.

The capacity factors of **17**-**19** and **8**-**10** shown in Figure 4.17 show the opposite trend to their water solubility. Generally, *K* is larger for iodido complexes than

their chlorido and bromido analogues. The order follows I>Br>Cl, where iodido complexes are the most lipophilic and chlorido complexes are the least. Likewise, lower *K*-values were observed for complexes with a terminal OH group at the end of the ethoxy substituent, indicating they are less lipophilic.

Figure 4.18 shows the trends in *K* for complexes with alkoxy side-chains. The trend between **10** and **11** shows that varying the counter anion has little effect on lipophilicity, and the trend between **11** and **13** shows that changing the arene from *p*-cym to bip reduces lipophilicity. Moreover, the trend between **7**, **10**, and **14**-**16**, where only the R-substituent is varied follows the order ^{n}Bu>^{n}Pr>^{i}Pr>Et>Me. Lipophilicity increases with alkyl chain length of the substituent.

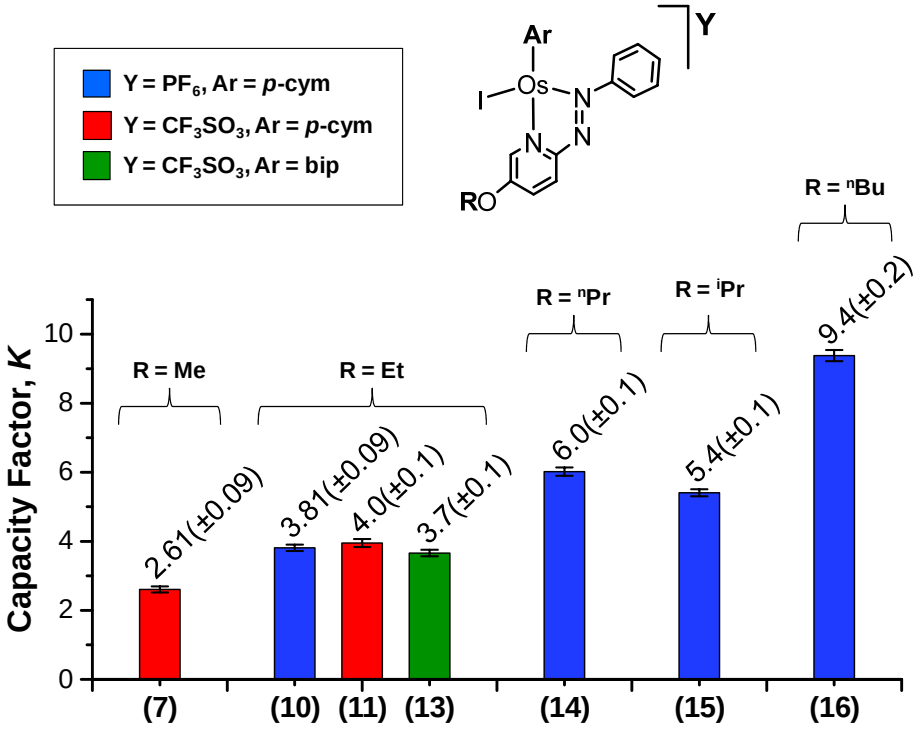

Figure 4.18. Trends in capacity factor for complexes **7** and **10**-**16**.

Figure 4.19 shows the trends in *K* for complexes bearing glycolic side-chains. The trend between **19**, **21**, **25** and **28**, where R= H shows that increasing the glycol side-chain length does not have much impact on lipophilicity. When R= Me or Et, increasing the glycol side-chain length slightly decreases the lipophilicity of the complex, as shown by the trends between **22**, **26**, **23** and **27**. Changing the arene from *p*-cym to bip reduces the lipophilicity by a small increment, which is shown by **19**, **20**, **23** and **24**. Moreover, the clearest trend is the effect of changing the terminal substituent, R. There are notable increases in lipophilicity associated with varying R, occurring in the following order H>Me>Et.

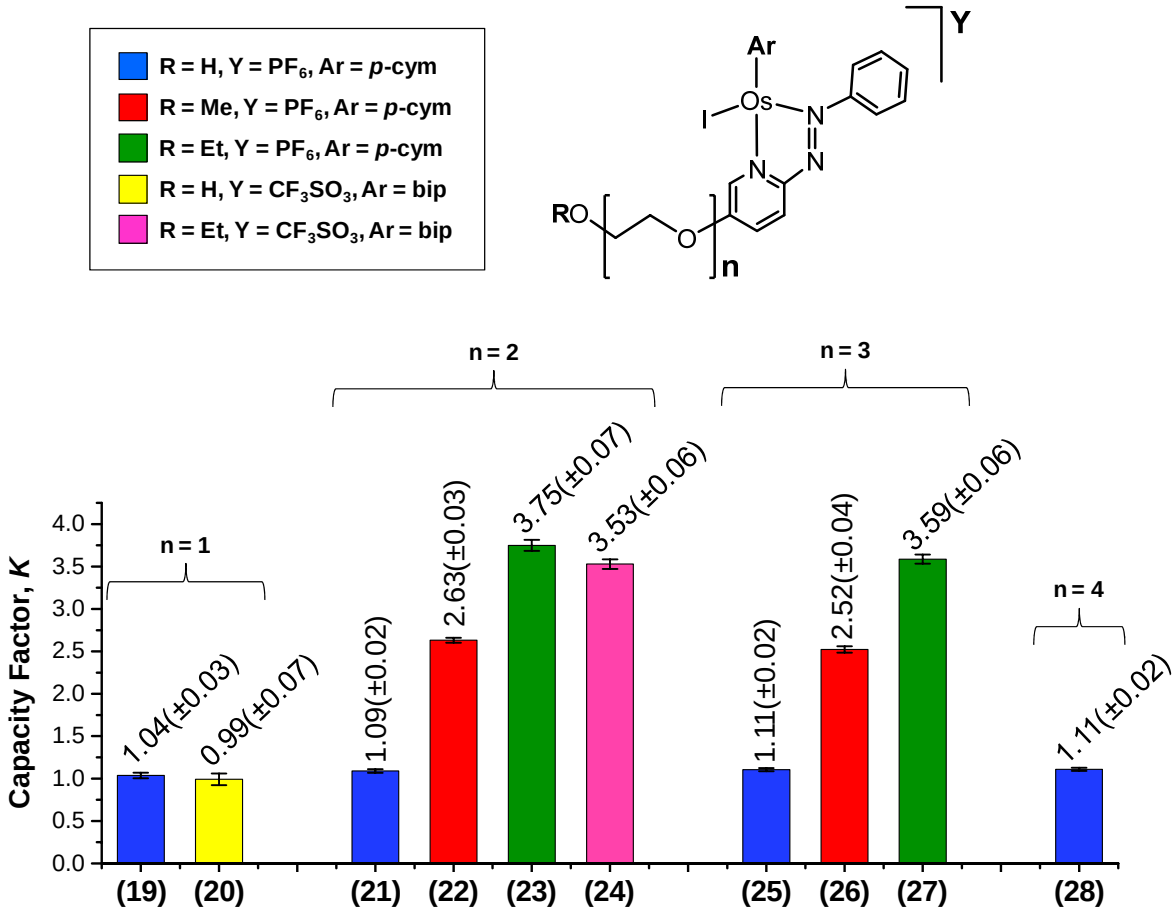

Figure 4.19. Trends in capacity factor for complexes **19**-**28**.

4.3.10. Octanol/water partition coefficients

The octanol/water partition coefficient ($P_{o/w}$) of complexes were measured in triplicate using a modified version of the shake-flask method,[21,28] described in Chapter 2, Section **2.3.3**. The octanol-saturated water contained 300 mM of NaX, where X = Cl, Br or I and was used to suppress the hydrolysis of chlorido, bromido and iodido complexes, respectively. Due to the time consuming nature of this method, Log $P_{o/w}$ was only determined for complexes **9**, **17**, **19**, **20**, **22**, **23** and **25**. It was not possible to measure the Log $P_{o/w}$ of complexes with very poor aqueous solubility using the shake-flask method, due to Os concentrations being below the limit of ICP-MS detection after partitioning.

A HPLC method for determining Log P_{HPLC} was adopted.[23] Using the *K*-values determined previously, a calibration curve was produced by plotting Log $P_{o/w}$ vs. Log *K* for complexes **9**, **17**, **19**, **20**, **22**, **23** and **25** (see Figure 4.20). The linear equation of the plot is: y = 2.4(±0.6)x + 1.2(±0.2). Using the measured *K*-values of the complexes and the calibration curve, their Log P_{HPLC} values were determined. However, due to a relatively weak correlation in the calibration curve (correlation coefficient = 0.743), the Log P_{HPLC} values have large errors ranging from ±0.2 to ±0.8, and could only be determined to one decimal place (see Table 4.4). Furthermore, the Log *K* values of complexes **10**, **11** and **14**-**16** fall outside the calibration range of the plot and their Log P_{HPLC} values were estimated by extrapolating the calibration curve.

Table 4.4. List of Log *K* values of complexes **7**-**11** and **13**-**28**, their determined Log P_{HPLC} values, and the Log $P_{o/w}$ values of **9**, **17**, **19**, **20**, **22**, **23** and **25**, which were measured using the shake-flask method.

Complex	Log (*K*)	Log ($P_{o/w}$)	Log (P_{HPLC})
7	0.42(±0.02)		2.1(±0.5)
8	0.29(±0.01)		1.8(±0.4)
9	0.42(±0.01)	1.59(±0.03)	2.1(±0.5)
10*	0.58(±0.01)		2.5(±0.6)
11*	0.60(±0.01)		2.6(±0.6)
13	0.56(±0.01)		2.5(±0.6)
14*	0.779(±0.009)		3.0(±0.7)
15*	0.733(±0.008)		2.9(±0.7)
16*	0.972(±0.007)		3.5(±0.8)
17	-0.25(±0.02)	0.11(±0.02)	0.6(±0.4)
18	-0.13(±0.02)		0.8(±0.3)
19	0.02(±0.02)	1.87(±0.05)	1.2(±0.2)
20	0.00(±0.03)	1.10(±0.04)	1.1(±0.2)
21	0.038(±0.009)		1.2(±0.2)
22	0.420(±0.005)	2.29(±0.04)	2.1(±0.5)
23	0.574(±0.007)	2.6(±0.2)	2.5(±0.6)
24	0.548(±0.007)		2.4(±0.5)
25	0.044(±0.007)	1.41(±0.04)	1.3(±0.2)
26	0.402(±0.006)		2.1(±0.5)
27	0.555(±0.006)		2.5(±0.6)
28	0.045(±0.007)		1.3(±0.2)

*Complexes Log (*K*) value is outside the calibration range

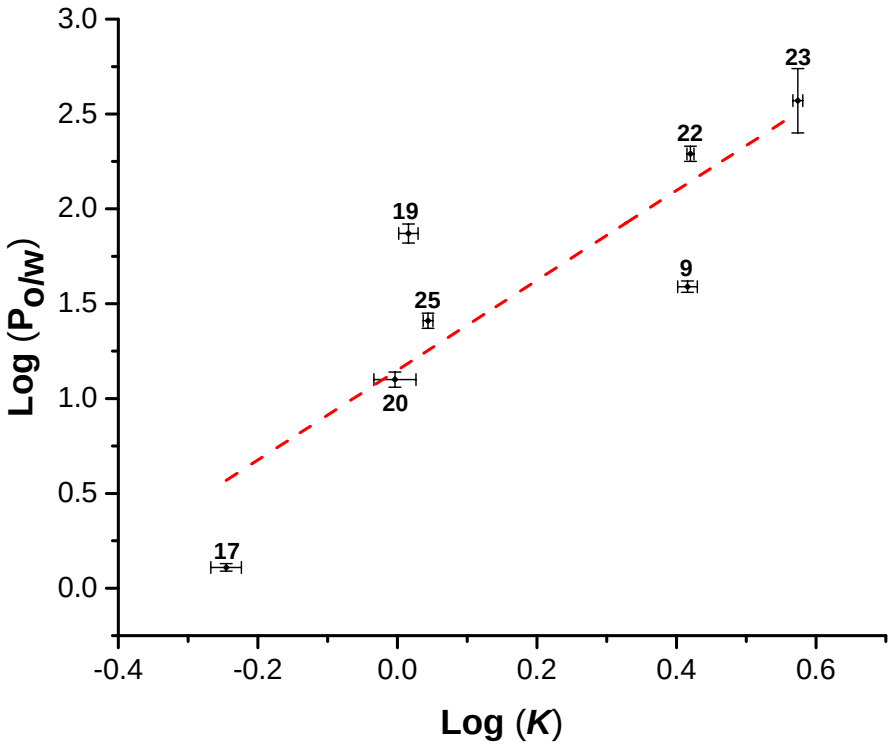

Figure 4.20. Plot of Log ($P_{o/w}$) vs. Log (*K*) for complexes **9**, **17**, **19**, **20**, **22**, **23** and **25**.

4.3.11. Separation of structural isomers 34A and 34B

The synthesis of **34** with *pseudo*-halide monodentate ligand, SCN^-, led to the formation of two structural isomers; *S*-bound SCN^- ([Os(η^6-*p*-cym)(5-EtO-AZPY)(*S*-SCN)]PF_6, **34A**) and *N*-bound SCN^- ([Os(η^6-*p*-cym)(5-EtO-AZPY)(*N*-SCN)]PF_6, **34B**), see Figure 4.21. HPLC analysis of the product showed two peaks in the chromatogram, corresponding to the two isomers with retention times of 20.42 and 22.52 min (88.5% and 14.0%, respectively, see Figure 4.22). Although no further analysis was carried out to characterise the isomers, it is believed that the more hydrophilic peak (a) is the *S*-bound isomer. Sulfur has preferential binding to osmium over nitrogen according to the Pearson acid-base concept and peak (a) is the major peak. Furthermore, the *S*-bound isomer

(which has the shorter retention time) has a H-bond acceptor group (-C≡N) pointing out into the solvent matrix (H_2O/MeCN), which is likely to make it the more hydrophilic of the two isomers, hence a shorter retention time.

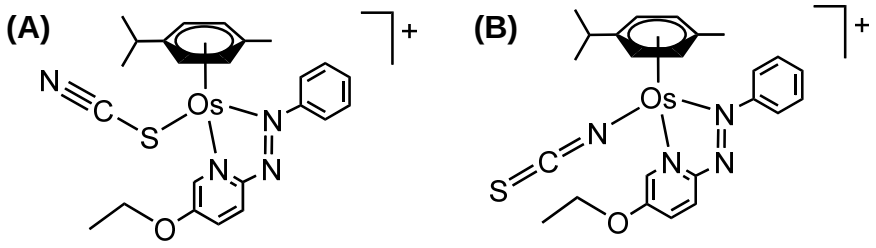

Figure 4.21. Two structural isomers of complex **34**. (A) with a *S*-bound SCN ligand (**34A**), and (B) with a *N*-bound SCN ligand (**34B**).

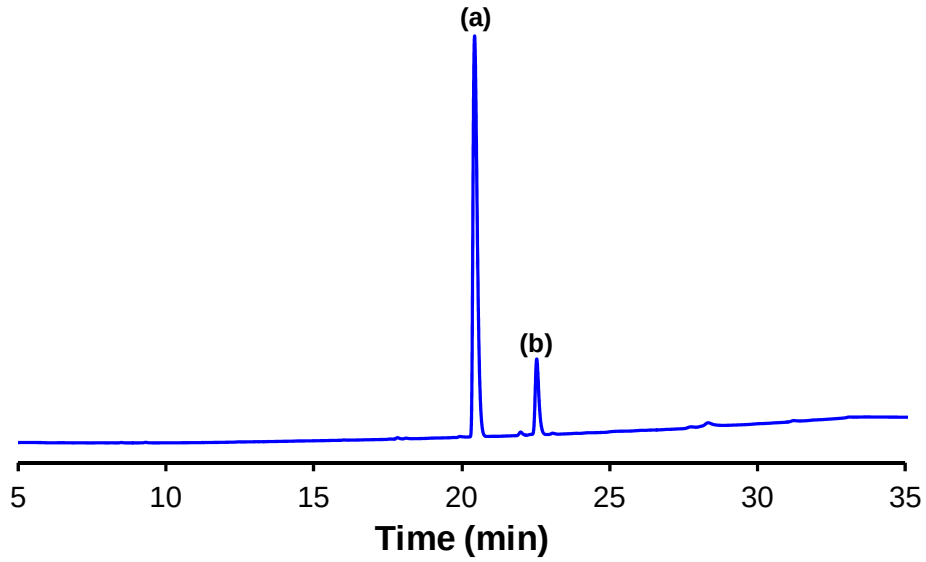

Figure 4.22. HPLC chromatogram of **34** with two structural isomers (a) 88.5% and (b) 14.0%, with retention times of 20.42 and 22.52 min, respectively. Details of the HPLC conditions are shown in Chapter 2, Section **2.2.9**.

The isomers were separated and isolated by preparative HPLC and their stabilities were tested in PBS solution over 24 h at 37 °C to determine whether the isomers were inter-convertible. After incubation the samples were analysed by HPLC. The chromatograms show that isomer (a) was the most stable with 98.7% purity after incubation. Isomer (b) on the other hand was only 84.4% pure after incubation. No inter-conversion between isomers was observed (see Figure 4.23).

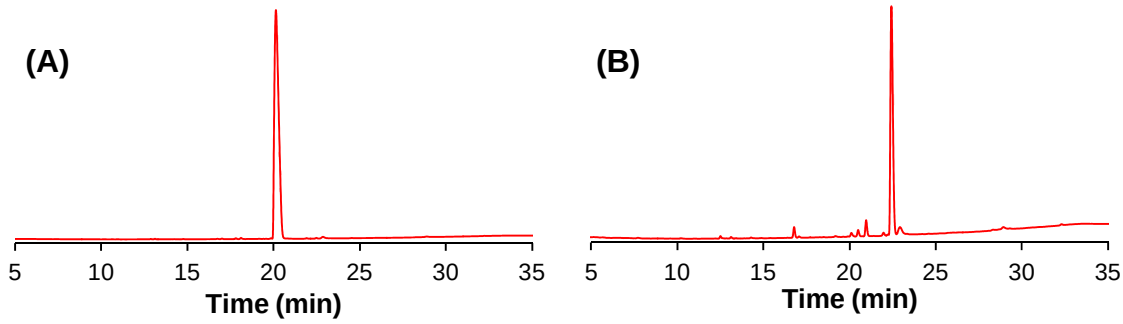

Figure 4.23. Chromatograms showing the purity of isomers (a) and (b) after 24 h incubation in PBS at 37 °C. (A) isomer (a), and (B) isomer (b). Details of the HPLC conditions are shown in Chapter 2, Section **2.2.9**.

The anti-proliferative activity of isomers (a) and (b) against A2780 cells was measured. Interestingly, the structural arrangement of the SCN^- ligand leads to complexes with different anti-cancer activities. Isomer (b) was the most active species, with an IC_{50} value between 25-50 µM, whereas isomer (a) was inactive (IC_{50}>50µM), see Figure 4.24.

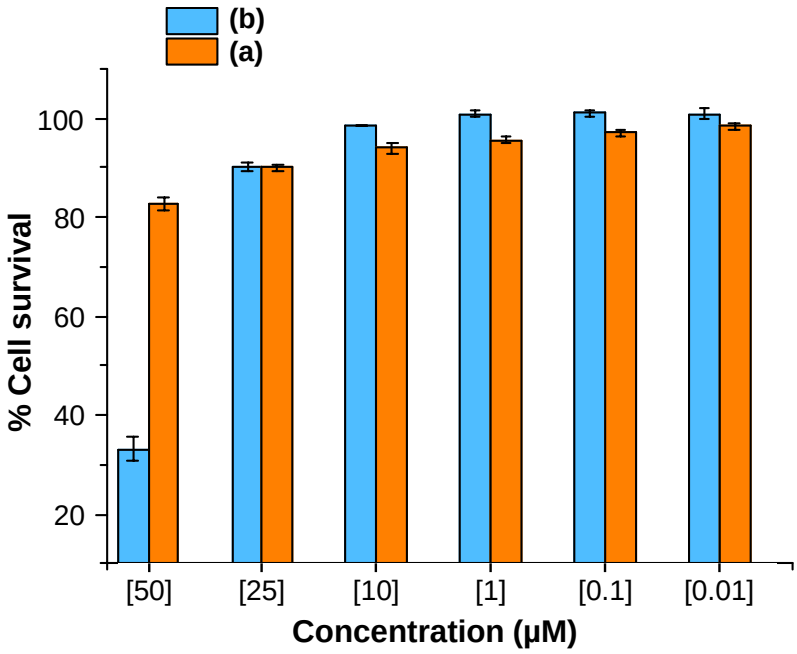

Figure 4.24. Cell viability studies of the structural isomers of complex **34**, (a) and (b), against A2780 cancer cells. The %cell survival was determined at different concentrations of the isomers.

4.3.12. Cyclic voltammetry of 10

Cyclic voltammetry analysis was carried out by Dr. Nicolas P. E. Barry for key active iodido complex **10**. A 1 mg/mL solution of the complex in MeCN with tetrabutylammonium hexafluorophosphate (0.1 M) as a supporting electrolyte was prepared. The sample was scanned between -2.0 V to +2.0 V in both directions. The cyclic voltammogram (CV) contains two reduction potentials at -0.26 and -0.81 V, one of which (-0.26 V) falls within the biologically relevant region (see Figure 4.25).[29] These were assigned to reduction of the azo-bond, which can accept two electrons into its π*-orbital.

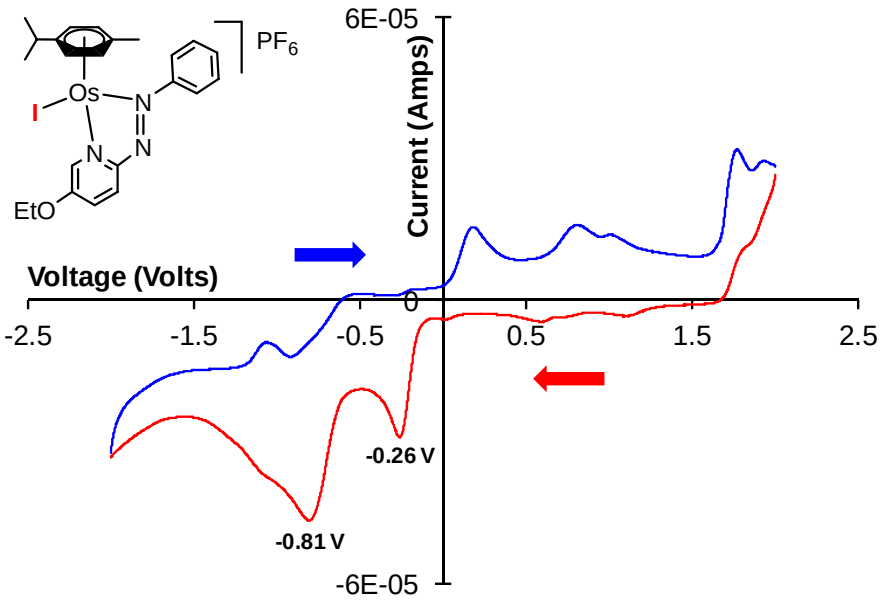

Figure 4.25. Cyclic voltammogram of **10** (1 mg/mL) in MeCN with 0.1 M tetrabutylammonium hexafluorophosphate. The red line represents the first segment where the voltage was scanned from +2.0 to -2.0 V. The blue line represents the second segment where the voltage was scanned back to +2.0 V. Identified are two reduction potentials at -0.26 and -0.81 V.

4.3.13. Cell cycle analysis

Changes in the cell cycle phase distribution of A2780 cells after incubation with complexes **10**, **13**, **15**, **19**, **23** and **31** at 37 °C for 24 h, were monitored using flow cytometry (see Chapter 2, Section **2.3.5**). This work was undertaken by Dr. Isolda Romero-Canelón. The histograms for the control experiment (no complex added), and complex **10** at three different concentrations (1x, 2x and 3x IC_{50}) are shown in Figure 4.26. Cells that are in the G1-phase contain two sets of DNA (2N). Those in the G2/M-phase contain four sets (4N), and any cells inbetween are in the process of DNA replication (S-phase). The experiment

shows that complex **10** causes S-phase arrest at 1x its IC_{50}. At higher concentrations there is a rise in sub-diploid cells. These are damaged non-viable cells that contain amounts of DNA equalling <2N, due to a compromised cell membrane and leakage of their DNA content.

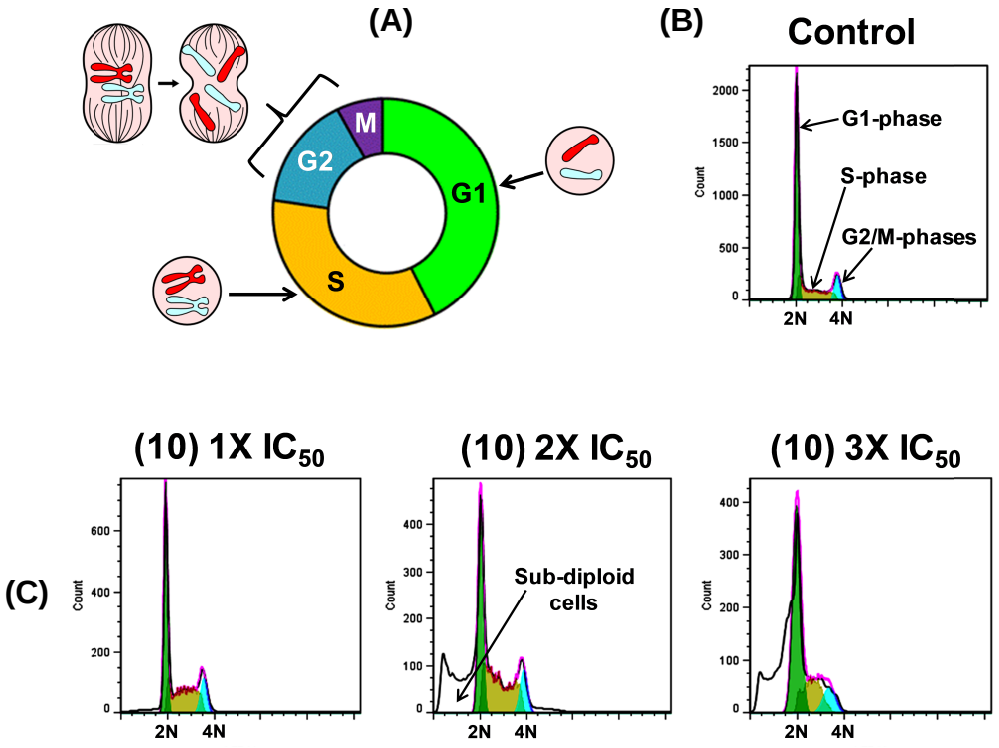

Figure 4.26. (A) Diagram of the cell cycle depicting the G1-phase with cells containing one DNA pair, the S-phase where DNA synthesis takes place, and the G2/M-phase where cells contain two DNA pairs and mitosis takes place. Histograms showing cell cycle distributions of A2780 cells after 24 h incubation at 37 °C with (B) no complex added (control), and (C) different concentrations of **10** (1x, 2x and 3x IC_{50} values).

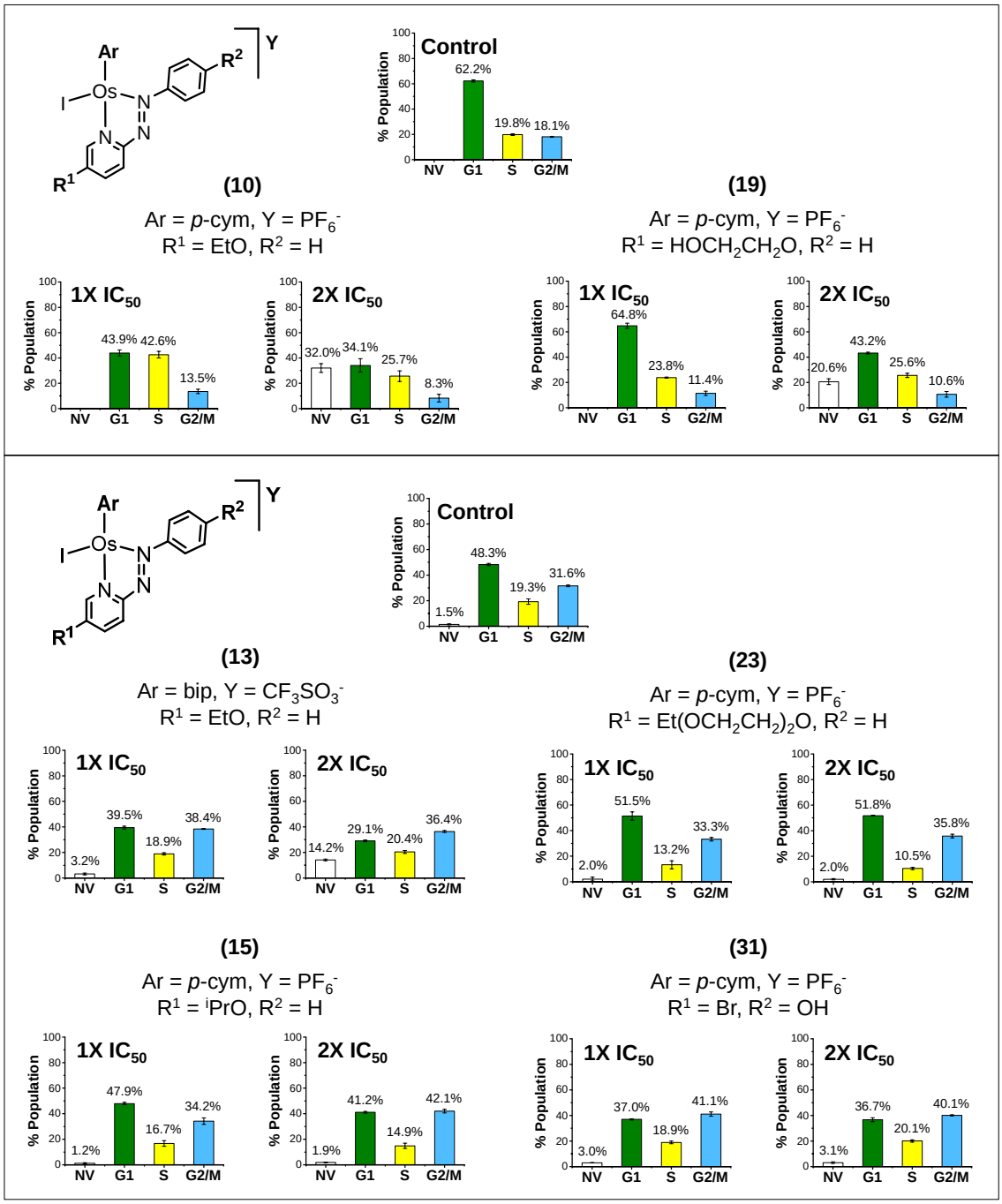

Figure 4.27. Cell cycle distributions of A2780 cells after 24 h incubation at 37 °C with complexes **10**, **13**, **15**, **19**, **23** and **31**, at 1x and 2x IC_{50}.

Figure 4.27 shows quantitatively the cell cycle distributions of A2780 cells after 24 h incubation with **10**, **13**, **15**, **19**, **23** and **31** at 1x and 2x IC_{50}. Complex **19**

caused a slight elevation in the G1-phase population at 1x IC_{50}, and doubling the concentration led to an increase in the proportion sub-diploid cells, which came primarily from the G1-phase. Complexes **13**, **15**, **23** and **31** all caused a small increase in the population of cells in the G2/M-phase at both 1x and 2x IC_{50}.

4.3.14. Apoptotic behaviour

Complexes **10**, **13**, **19** and **31** were tested for their ability to induce apoptosis in A2780 cells after 24 h incubation at 37 °C using flow cytometry, by Dr.Isolda Romero-Canelón (see Chapter 2, Section **2.3.7**). Apoptosis is a highly regulated process of programmed cell death which is triggered when cells become damaged or unhealthy. The early stages of apoptosis involve cell shrinkage and blebbing of the cell membrane. Later stages involve breakdown of the cellular components/DNA content and the formation of smaller apoptotic bodies, which are removed from the body by macrophages (see Figure 4.28). The histograms for the control experiment (no complex added), and complex **10** at three different concentrations (1x, 2x and 3x IC_{50}) are shown in Figure 4.28. Increasing the concentration of **10** led to an increase in the population of cells in Q2 (late stage apoptosis) and an even larger increase in the population of cells in Q1 (non-viable cells). Figure 4.29 shows quantitatively the induction of apoptosis caused after 24 h incubation with **10**, **13**, **19**, and **31**, at 1x and 2x IC_{50}. At 2x IC_{50}, complexes raise the proportion of cells in late-stage apoptosis in the order **31**>**10**>**19**>**13**, with populations of 27.2%, 22.5%, 5.7% and 2.8%,

respectively. However, the proportion of non-viable cells was raised to 54.3%, 40.9%, 17.6% and 5.8%, respectively.

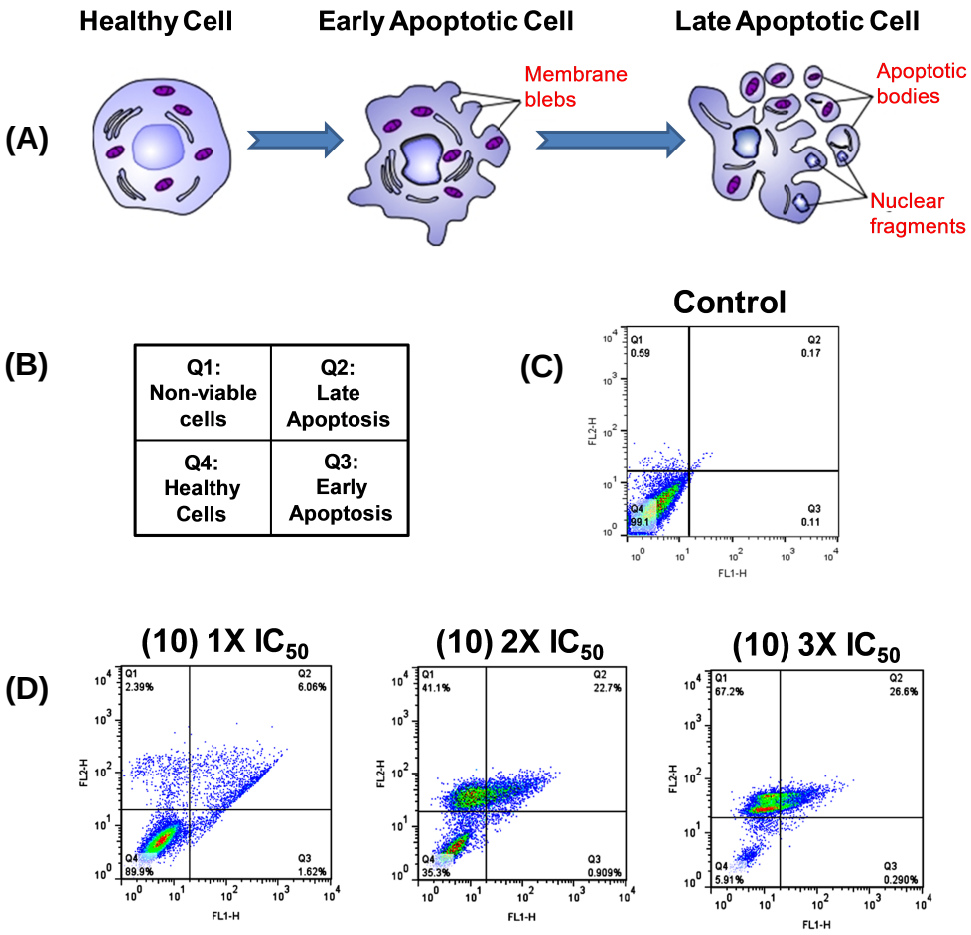

Figure 4.28. (A) Diagram representing the apoptosis process. (B) Diagram of the histogram showing four quadrants: Q1 = Non-viable cells, Q2 = cells in late-stage apoptosis, Q3 = cells in early-stage apoptosis, and Q4 = healthy cells. (C) Histogram of the control experiment where A2780 cells were incubated in the absence of any drug. (D) Histograms where A2780 cells were incubated with **10** at 1x, 2x and 3x the IC_{50}.

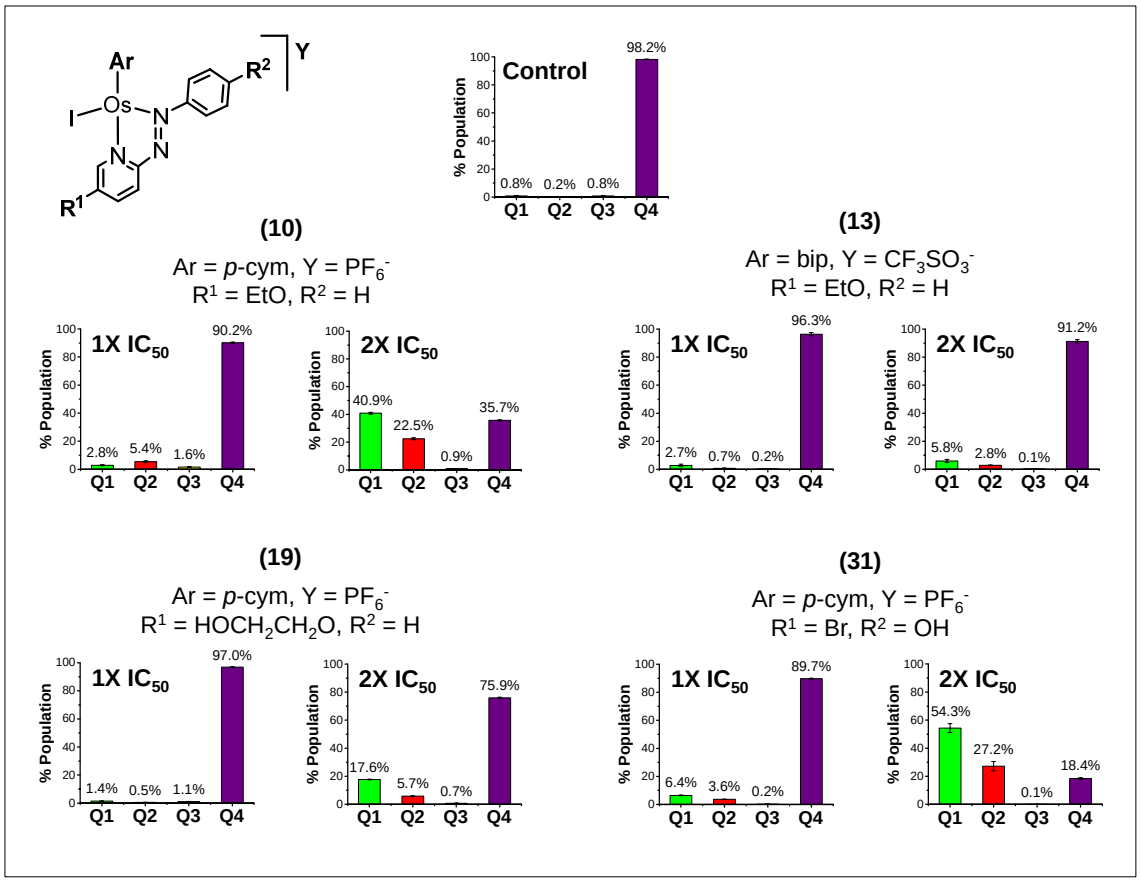

Figure 4.29. Proportions of healthy (Q4), early-apoptotic (Q3), late-apoptotic (Q2), and non-viable (Q4) A2780 cells after 24 h incubation at 37 °C with complexes **10**, **13**, **19**, and **31**, at 1x and 2x IC_{50}.

4.3.15. Induction of ROS

Complexes **7**, **10**, **13**, **15**, **23** and **31** were tested for their ability to elevate ROS levels in A2780 cells after 24 h incubation at 37 °C, by Dr. Isolda Romero-Canelón using flow cytometry (see Chapter 2, Section **2.3.6**). The protocol utilises a total ROS/Superoxide detection kit capable of distinguishing $O_2\cdot^-$ from other ROS.

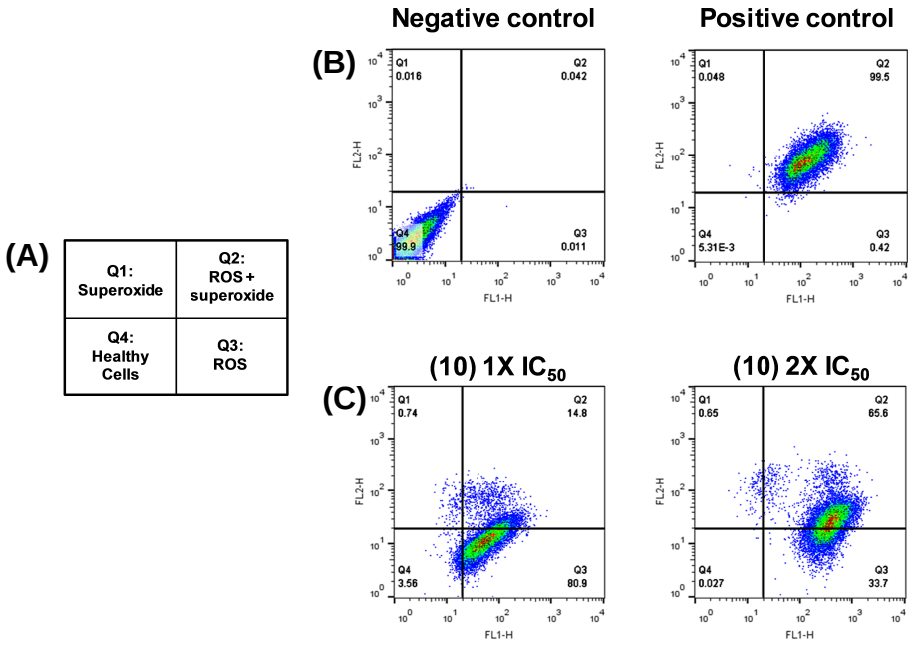

Figure 4.30. (A) Key to the histograms showing four quadrants: Q1 = cells expressing elevated $O_2\cdot^-$ levels, Q2 = cells expressing elevated ROS and $O_2\cdot^-$ levels, Q3 = cells expressing elevated ROS levels excluding $O_2\cdot^-$, and Q4 = healthy cells. (B) Histogram of the negative and positive control experiments where A2780 cells were untreated and treated with pyocyanin, respectively. (C) Histograms where A2780 cells were incubated with **10** at 1x and 2x the IC_{50}.

Figure 4.30 shows histograms for the positive (cells treated with pyocyanin) and negative (untreated cells) control experiments, and histograms for cells treated with complex **10** at 1x and 2x IC_{50}. The positive control shows that the vast proportion of cells expressed high levels of ROS and $O_2\cdot^-$ when treated with pyocyanin. The majority of cells treated with **10** at 1x IC_{50} expressed elevated ROS levels and when the concentration was doubled, the cells expressed higher levels of $O_2\cdot^-$. Figure 4.31 shows quantitatively the elevation of ROS after incubation with **7**, **10**, **13**, **15**, **23** and **31** at 1x and 2x IC_{50}. In every case, significantly elevated ROS and $O_2\cdot^-$ levels were observed after incubation.

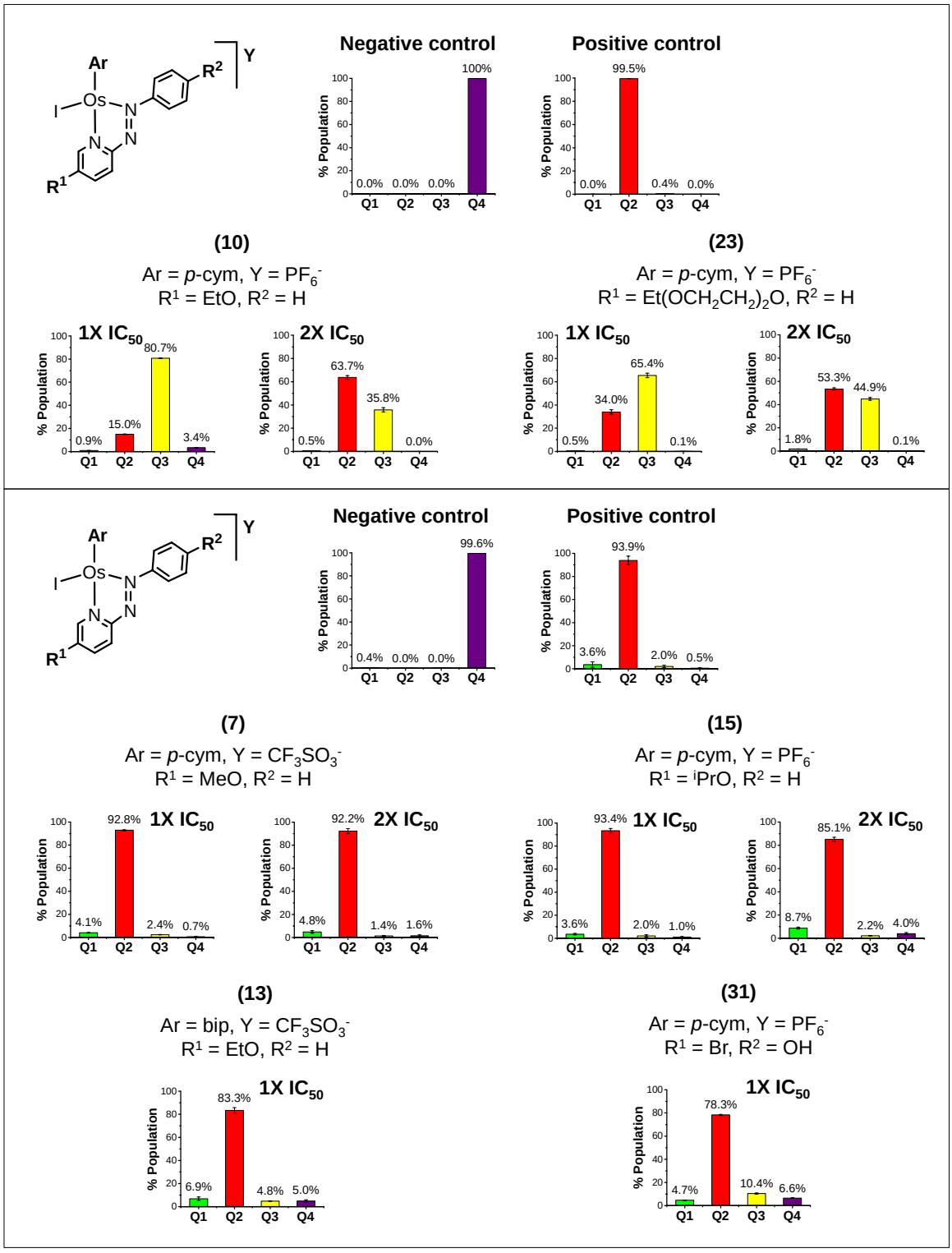

Figure 4.31. Proportions of A2780 cells that are healthy (Q4), with elevated ROS levels (Q3), with elevated ROS and $O_2\cdot^-$ levels (Q2), and with elevated $O_2\cdot^-$ levels (Q4) after 24 h incubation at 37 °C with complexes **10**, **13**, **19**, and **31**, at 1x and 2x IC_{50} concentrations.

4.4. Discussion

4.4.1. Anti-proliferative activity and selectivity factors

A total of 31 new Os(II) arene AZPY complexes were synthesised using the previously determined SARs as a guideline[13,15] (Chapter 1, Section **1.3.4.3**). Of which, 9 complexes exhibited potent sub micro-molar activity against A2780 cells, and 6 key complexes were selected for testing against other cancer cell lines (MCF-7, SUNE1, OE19) and a normal cell line (MRC-5). Complex **13**, [Os(η^6-bip)(5-EtO-AZPY)I]CF_3SO_3, exhibits the best activity profile with extremely potent activity against the OE19 cell line (96±4 nM) and the highest SF (IC_{50}-MRC-5/IC_{50}-A2780 = 12.0), which is comparable to that of *cis*-platin.[29] However, none of the complexes herein exhibit activity against A2780 cells greater than **FY026**, which also has a SF of 28.4.[13,29] It might be possible to improve on selectivity by synergistic treatment with *L*-BSO. This works by lowering levels of the cells primary antioxidant (GSH), hence inhibiting the normal cellular detoxification of ROS. Furthermore, a method for improving cancer cell selectivity is outlined in Chapter 7, Section **7.7**, where pharmacophoric groups are introduced which target specific proteins associated with cancerous cells.

According to the previously understood SARs,[15] complex **31**, [Os(η^6-*p*-cym)(5-Br-AZPY-OH)I]PF_6 was expected to have improved anti-cancer potency. However, it is not as potent as **FY026** and its selectivity is very poor (IC_{50}-MRC-5/IC_{50}-A2780 = 1.1). Gaining better insight into the activity profiles the complexes requires more extensive screening against a larger variety of cell

lines, including platinum resistant lines (particularly A2780cis) to determine if they overcome *cis*-platin resistance. They could also be tested further against a variety of normal cell lines to gain a better understanding of their selectivity. Despite its low SF, **31** is a highly novel complex with a colour dependence on pH. Under basic conditions the OH group is deprotonated giving rise to a deep blue colour, whereas acidic conditions gives rise to an orange colouration. The MLCT band (Os $5d^6 \rightarrow \pi^*$) of **31** shifts from 446 to 588 nm when the pH was raised from 1.96 to 12.76. Likewise, Dougan *et al* found a similar occurrence for chlorido Ru(II) arene AZPY-OH complexes.[30] Deprotonation of the hydroxyl substituent on the AZPY ligand (OH to O^-) decreases the π-acidity of the azo-bond, which in turn causes an increase in the energy of the Os(II) $5d^6$ orbitals. This results in a smaller energy gap for MLCT (Os $5d^6 \rightarrow \pi^*$, where π* is the anti-bonding orbital of the azo-bond in the AZPY ligand). The pK_a of the OH substituent was measured as 6.41 and under physiological conditions (pH 7.4) it was blue, therefore predominantly existing in a deprotonated zwitterionic state. It is believed that the negative charge is delocalised on the AZPY ligand, whereas its positive charge is centred around Os(II).

4.4.2. Trends in anti-cancer activity, solubility and lipophilicity

Figure 4.32 highlights the general trends in anti-cancer activity against A2780 cells, aqueous solubility in 100 mM NaCl, and capacity factor (*K*) for two classes of complex: (A) those with alkoxy substituents (**6**-**16** and **35**), and (B) those with glycolic substituents (**17**-**28**).

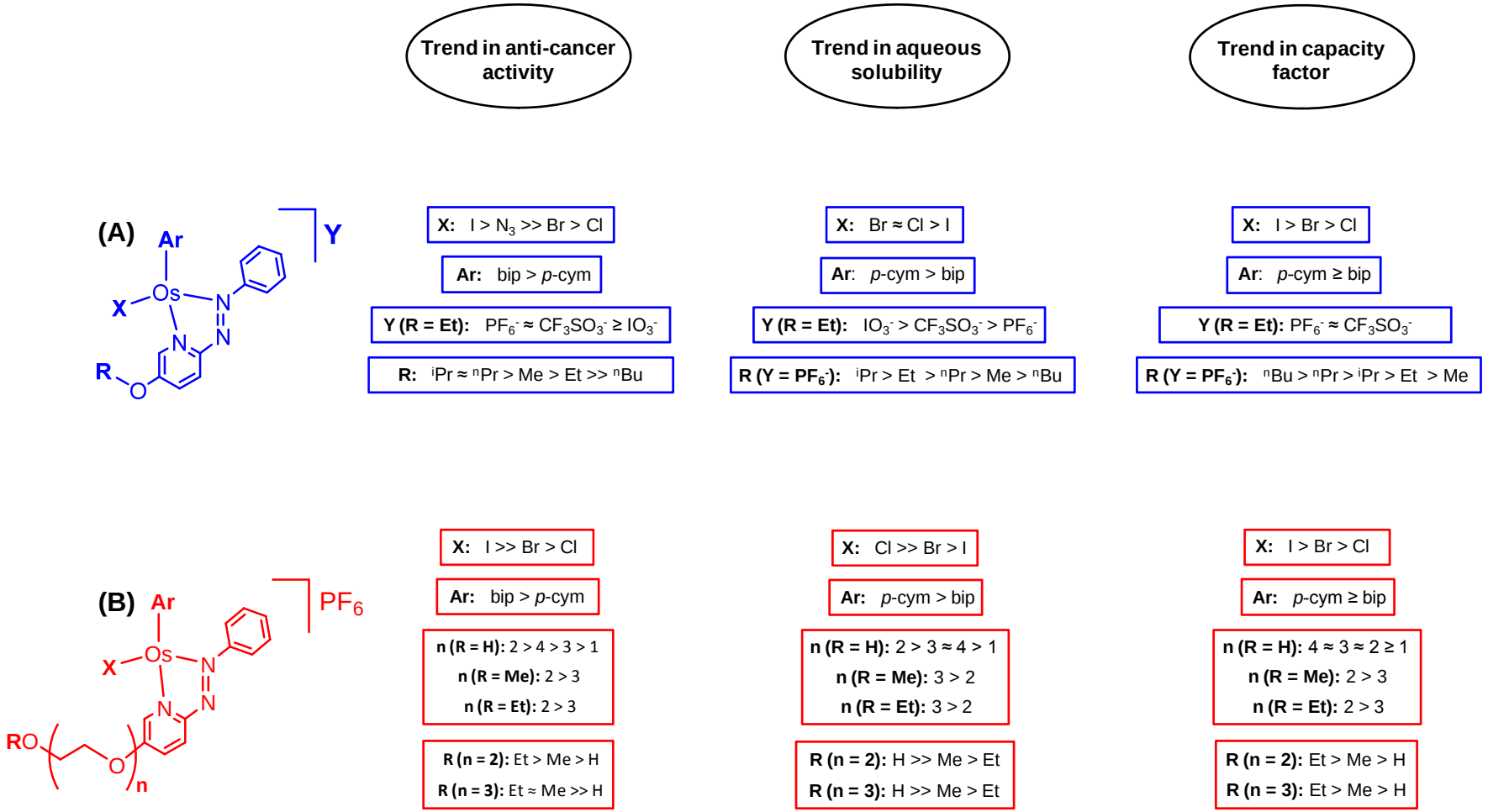

Figure 4.32. Trends in anti-cancer activity against A2780 cells, solubility in aqueous 100 mM NaCl solution, and capacity factor (relative lipophilicity) for: (A) complexes with alkoxy side-chain substituents (**6**-**16** and **35**), and (B) complexes with glycolic side-chain substituents (**17**-**28**).

The findings herein re-confirm that iodido Os(II) arene AZPY complexes are considerably more active than their chlorido and bromido analogues. In contrast to previous chlorido Os(II) arene AZPY complexes synthesised by Ying *et al* which were stable,[13] **8** (and bromido analogue **9**) both readily hydrolyse when incubated at 37 °C in phosphate buffer solution with 23 and 103 mM NaCl. The iodido analogue, **10**, was stable towards hydrolysis under the same conditions. The stability of iodido complexes may account for their improved activity as they are less likely deactivated by side reactions in extracellular conditions. Furthermore, iodido complexes are more lipophilic than their chlorido and bromido counter-parts, likely owing to a lesser polarised Os-I bond, which is more covalent in character than Os-Cl and Os-Br bonds. Likewise, chlorido and bromido complexes were considerably more water soluble, likely owing to a more polarised Os-X bond.

Analogous iodido complexes, **10**-**12**, share the same AZPY ligand (**L2**), but contain different counter anions (PF_6^-, $CF_3SO_3^-$ and IO_3^-, respectively). The trends show that varying the anion makes little difference to anti-cancer activity. This is expected because they are interchangeable with other anions in electrolytic solutions (e.g. cell culture medium containing 150 mM NaCl), and they exhibit no structural anti-cancer properties independently. Likewise, there is no difference in capacity factor between **10** and **11** because the anion is exchangeable with Cl^- in the mobile phase and the cationic fragments are identical. Varying the anion does however have a huge impact on water solubility without stifling activity, lipophilicity or cell uptake. Generally, complexes containing PF_6^- anions have poorer solubility but are easier to

crystallise during their synthesis. Changing the anion to IO_3^- or $CF_3SO_3^-$ increases aqueous solubility by lowering the crystal lattice energy in their solid states. This is the first time an extensive study into the aqueous solubility of complexes has been explored in the Sadler group. To the best of my knowledge, it is also the first time variation of the anion has been explored in any depth for cationic anti-cancer complexes.

Changing the arene from *p*-cym to bip in most cases results in a sharp increase in anti-cancer activity. It was previously speculated that complexes containing bip arene ligands were more lipophilic, hence exhibit improved cell uptake resulting in higher activity. However, the observed trends in *K* show that bip complexes are no more lipophilic than their *p*-cym analogues, and in some cases are slightly less lipophilic. Furthermore, the trend between **11** and **13** shows a decrease in cell uptake when *p*-cym is exchanged for bip. Perhaps the improvement in activity can be explained by factors other than lipophilicity, such as the potential for extended arenes to intercalate with DNA nucleobases.[15] Complexes containing bip are also significantly less soluble than their *p*-cym analogues. This may also be explained by increased crystal packing energies due to the greater likely hood of π-π and/or CH-π interactions between aromatic groups in the solid state.[16,31]

For complexes with alkoxy side-chain substituents (Figure 4.32, A), the differences in anti-cancer activity observed when the R-substituent is varied follows a complicated trend that is not understood at this point. The trend in *K*, however, follows a predictable trend where increasing the alkyl chain length of R increases the lipophilicity. Likewise, solubility follows a general trend where

increasing the alkyl chain length leads to decreases in solubility, which is likely dictated by hydrophobicity (Et>^{n}Pr>^{n}Bu). However, **6** (R= Me) and **15** (R= ^{i}Pr) were exceptions to the trend. Complex **15** was the most soluble, likely owing to the use of a branched alkyl group that destabilises crystal packing in the solid state. Disrupting planarity/symmetry *via* the introduction of bulky substituents is a known effective method for increasing the solubility of drug candidates.[16] Complex **6** has much poorer solubility than anticipated and might be due to high crystal lattice energy. The solubility of **6** was so poor that it was not possible to determine its activity against A2780 cells. However, changing the anion to $CF_3SO_3^-$ (**7**) created a 45-fold increase in solubility. The crystal packing energies of complexes could be further investigated by a comparison of their melting points.[16]

Complexes with glycolic side-chain substituents (Figure 4.32, B) have various chain lengths (n) and a variety of terminal of groups (R= H, Me or Et). When R= H, there was very little difference in *K* when the glycol chain length is varied. Solubility follows the trend n= 2>3>4>1 and anti-cancer activity follows the trend n= 2>4>3>1. These trends are not explainable at this point. Complex **21** (n = 2) has the best attributes for this series with the highest solubility and anti-cancer activity observed. When the terminal group, R, is replaced with a more lipophilic group (Me or Et), as expected *K* increases, and the solubility decreases dramatically due to increased hydrophobicity. The anti-cancer activity also increases, which is likely due to higher lipophilicity resulting in greater cell uptake. Interestingly, when R= Me or Et, increasing the glycol chain length from n= 2 to n= 3 led to a slight decrease in *K*, which is perhaps a result of increasing

the number of H-bond acceptor groups in the complex. This also led to a decrease in anti-cancer activity, which is also likely a consequence of lower lipophilicity.

4.4.3. Cell uptake and lipophilicity

Unfortunately, not all of the complexes in the series containing alkoxy/glycolic side-chains were tested for cell uptake in A2780 cells. However, the trends that are currently known are shown in Figure 4.33.

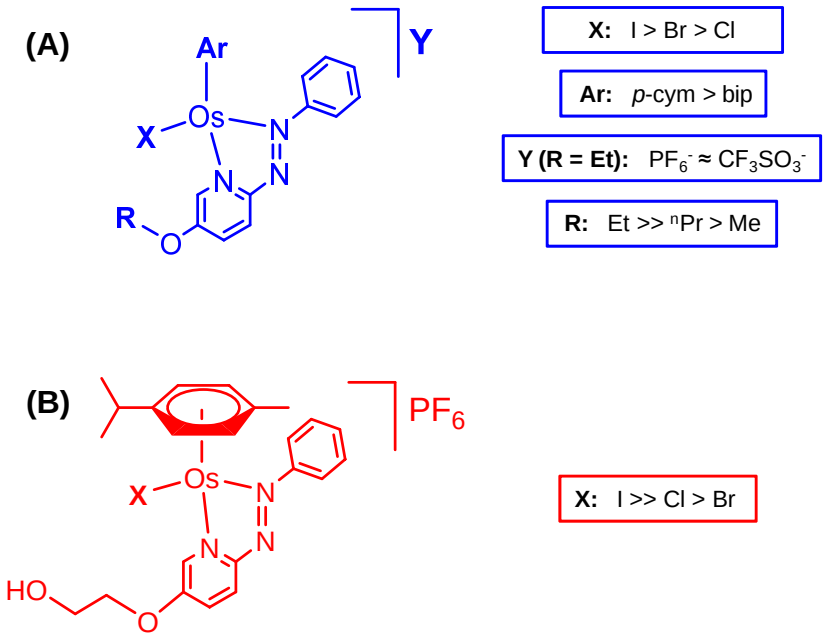

Figure 4.33. Trends in cellular accumulation in A2780 cells for: (A) complexes with alkoxy side-chain substituents, and (B) complexes with a monoethylene glycol side-chain substituent.

The trends show that iodido complexes have considerably better uptake than their chlorido and bromido counter-parts. This is likely related to the higher

lipophilicity of iodido complexes involving passive cell uptake. Interestingly, ruthenium complex, $[Ru(\eta^6\text{-}p\text{-cym})(IMPY\text{-}NMe_2)I]^+$ (where IMPY is a phenyliminopyridine ligand, analogous to AZPY), was found to accumulate into A2780 cells *via* passive transport, whereas its chlorido analogue entered cells primarily through active transport.[32] Changing the anion had no effect on cell uptake, which as explained previously in Section **4.4.1**, is due to the irrelevance of the counter anion once a complex is dissolved in cell culture media. Also previously explained in Section **4.4.1**, when the *p*-cym ligand of complex **11** changed with bip, cell uptake is reduced and could be the result of lower lipophilicity that was observed for bip complexes. For complexes with alkoxy side-chains (Figure 4.33, A), when the R-substituent is varied, cell uptake follows the order Et>>^{n}Pr>Me. It is not currently understood why the most lipophilic complex in this series (**14**, R= ^{n}Pr) is taken up into cells to a considerably lesser extent than analogous complex **10** (R= Et). Cell uptake was plotted against *K* for complexes **7**-**11**, **13**, **14** and **17**-**19** and a reasonably good correlation was found between the two properties (correlation coefficient = 0.78), thus indicating a general overall linear trend between lipophilicity and cell uptake (see Figure 4.34). However, **14** was treated as an outlier and does not fit the trend. A possible explanation for its low cell uptake could be a strong affinity towards binding to proteins in cell culture medium.

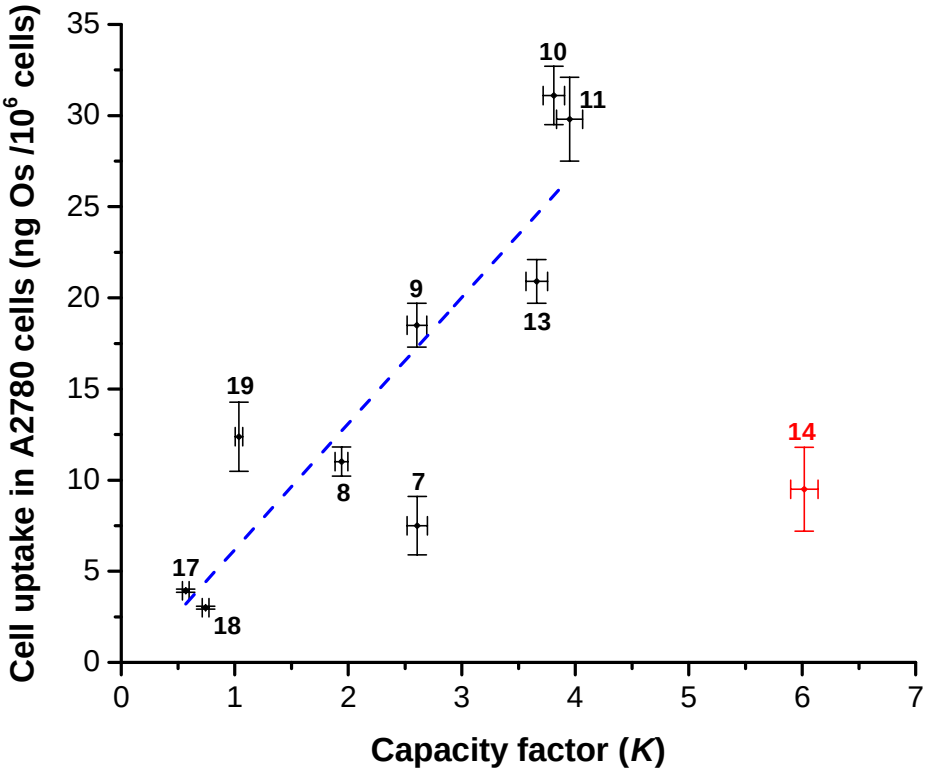

Figure 4.34. Plot of cell uptake vs. capacity factor (*K*) for complexes **7**-**11**, **13**, **14** and **17**-**19**.

Similarly, a previous study in the Sadler group utilised a non-isocratic reverse-phase HPLC method to determine the relative lipophilicities of chlorido Ir(III) Cp* complexes with 2-PhPy bidentate ligands.[33] Complexes contained either an electron withdrawing (F or NO_2) or electron donating (OH or Me) substituent at various different positions on the 2-PhPy ligand. A correlation analysis showed that an increase in complex lipophilicity results in an increase in cellular Ir-accumulation, which generally results in improved anti-cancer potency. It was found that the nature and positioning of the substituent dictates the overall lipophilicity of the complex, and lipophilicity is an important design feature for complexes that accumulate inside cancer cells in part by passive diffusion.

4.4.4. Log P_{HPLC}

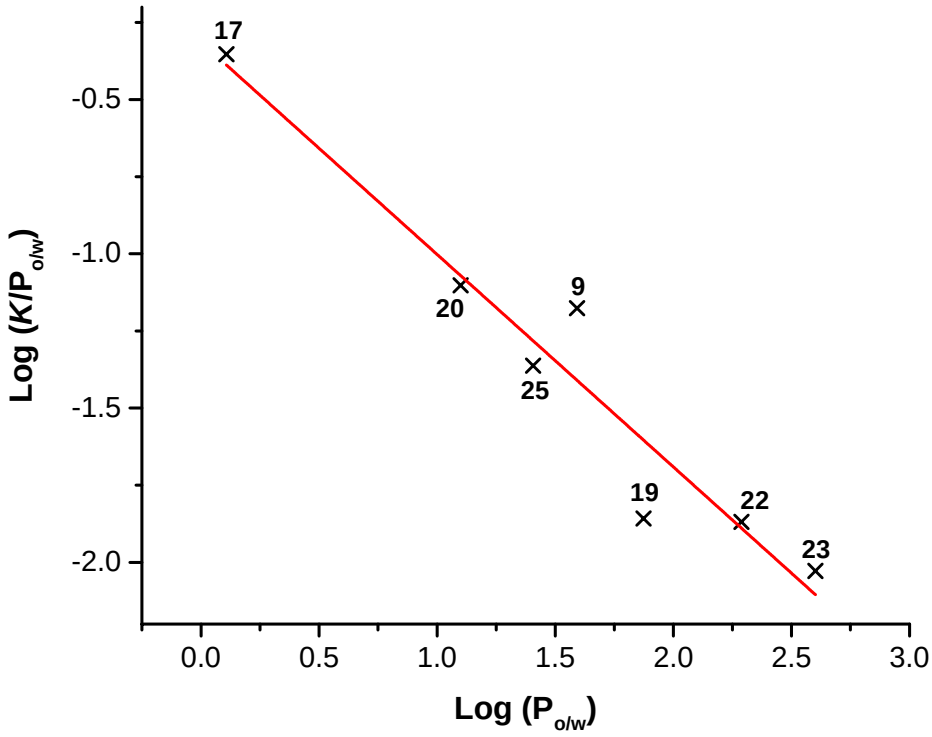

Figure 4.35. Plot of Log (K/$P_{o/w}$) vs. Log ($P_{o/w}$) for complexes **9**, **17**, **19**, **20**, **22**, **23** and **25**.

In Section **4.3.10**, the HPLC method used to determine the Log P_{HPLC} values for complexes proved to have low accuracy and large error margins were obtained. The calibration plot between Log $P_{o/w}$ and Log K does not have a strong enough correlation for these purposes. All of the determined Log P_{HPLC} values for the complexes fall well within the acceptable Ro5 range (-0.4 to 5.6).[19] Following an approach outlined by Sahu *et al*, Log $P_{o/w}$ was plotted on the x-axis as a reference indicator against the expression Log (K/$P_{o/w}$),[23] see Figure 4.35. This method determines if factors other than the lipophilicity contribute towards partitioning, e.g. chemical interactions with the solvents or hydrolysis. The graph

shows good correlation between Log ($K/P_{o/w}$) and Log $P_{o/w}$ (correlation coefficient = 0.935), indicating that the partitioning of complexes is mainly determined by their lipophilicity.

4.4.5. *Pseudo*-halide complexes

Metal based anti-cancer complexes containing thiocyanate monodentate ligands have been explored previously within other research groups. Human *et al* reported on dimeric Ag(I) thiocyanate complexes, $[Ag(\mu^2\text{-}SCN)(P\{Ar\}_3)_2]_2$ (where Ar = Ph, 4-MeC_6H_4, 4-FC_6H_4 or 4-ClC_6H_4), that are capable of inducing apoptosis in SNO-esophageal cancer cells.[34] Furthermore, Shi *et al* have reported a Cu(II) anti-cancer complex, Cu(Bipy)(*N*-$NCS)_2$, where interestingly, the IC_{50} against OVCAR-3 ovarian cancer cells depended strongly on the recovery time after drug exposure.[35] Thiocyanato complexes of Ru(II) and Os(II) arenes have been relatively under explored within the Sadler group apart from one example.[36] The complex $[Ru(\eta^6\text{-hmb})(en)Cl]^+$ was found to undergo aquation to $[Ru(\eta^6\text{-hmb})(en)H_2O]^{2+}$, which then reacted with KSCN to form the kinetically favoured product *S*-bound product, $[Ru(\eta^6\text{-hmb})(en)S\text{-}SCN]^+$. This undergoes slow conversion in solution to the thermodynamically favoured *N*-bound product, $[Ru(\eta^6\text{-hmb})(en)N\text{-}SCN]^+$, which exhibited moderate cytotoxicity towards A2780 cells (IC_{50} = 24 μM). Despite not being susceptible to hydrolysis, it was found to bind favourably to guanine bases in GMP.

In contrast, the chlorido complex complex **8**, $[Os(\eta^6\text{-}p\text{-cym})(5\text{-EtO-AZPY})Cl]^+$ was heated with 500 mol. equiv. of KSCN in MeOH/H_2O (1:1, v/v) under reflux

for 18 h and a mixture of *S*-bound (**34A**) and *N*-bound (**34B**) isomers were formed (88.5 and 14.0% respectively). Further heating did not change the ratios of products. After separating the isomers by HPLC, incubating them at 37 °C for 24 h under physiological conditions did not cause them to hydrolyse and no interconversion between isomers was observed. The *S*-bound complex is kinetically favoured, but it appears that both isomers are thermodynamically stable with tight binding of the monodentate ligand. Similarly to [Ru(η^6-hmb)(en)*N*-SCN]$^+$, **34B** was cytotoxic towards A2780 cells (IC_{50} = 25-50 μM), however the *S*-bound isomer was inactive. The inactivity of **34A** may be due to a strong Os-S bond, rendering it unable to become activated *via* hydrolysis in intracellular conditions.

The azido complex (**35**) on the other hand exhibited potent activity against A2780 cells with an IC_{50} of 1.2 μM. Previous studies on [Ru(η^6-hmb)(en)N_3]$^+$ showed that unlike its *N*-SCN analogue, it was capable of hydrolysis, albeit slower than the chlorido, bromido and iodido analogues.[37] It was also more active than [Ru(η^6-hmb)(en)*N*-SCN]$^+$ with an IC_{50} of 14 μM. Perhaps the improved activity of **35** over **34B** is down to the fact that the Os-N_3 bond is more susceptible to hydrolysis than the Os-NCS bond, allowing for easier intracellular activation. Chlorido and bromido analogues (**8** and **9**) on the other hand have monodentate ligands that are too labile and susceptible to deactivation before entering the cell, leading to reduced activities. The iodide monodentate ligand provides a happy medium where the complex is protected from deactivation in extracellular conditions, but the Os-I bond is still labile enough to allow for

cellular activation inside cells (see Chapter 5 for the intracellular activation of complex **10** and **FY026**).

4.4.6. Reduction potentials of 10

Complex **10**, [Os(η^6-*p*-cym)(5-EtO-AZPY)I]PF_6, has two reduction potentials corresponding to the transfer of two electrons into the π*-orbital centred on the azo-bond, at -0.26 and -0.81 V, respectively. The former of which falls within the biologically relevant range (+0.40 to -0.50 V).[29] The first reduction potential of **FY026**, [Os(η^6-*p*-cym)(AZPY-NMe_2)I]PF_6, and its Ru(II) analogue are -0.64 and -0.40 V respectively.[11,25] Due to the presence of a more easily reducible azo-bond, the Ru(II) analogue is capable of catabolising GSH to GSSG. In contrast, **FY026**, which has its first reduction potential outside of the biologically relevant range, does not catabolise GSH (see Chapter 1, Sections **1.3.3.2** and **1.3.4.3**). The notable low lying reduction potential of **10** might mean it is also capable of catalytic GSH oxidation, unlike **FY026**. This highlights how simple variations in substituents and their positioning on the AZPY ligand can have a profound effect on the electronic and chemical properties of the complex. Furthermore, complexes **7**, **10**, **13**, **15**, **23** and **31** were all found to significantly raise cellular ROS levels in A2780 cells in ROS assays. Chapter 6 explores the possible mechanistic routes in which intracellular ROS levels are raised in cancer cells.

4.4.7. Apoptosis and cell cycle analysis

Complexes **10**, **13**, **19** and **31** were tested for their ability to induce apoptosis in A2780 cells. The proportion of late apoptotic cells induced follows the order **31**>**10**>**19**>**13**, where **31** induced the largest proportion. Interestingly and in the same order, the complexes induced even higher populations of non-viable cells, suggesting that the main mechanism of cell death is non-apoptotic and could involve unregulated processes such as necrosis. During necrosis, the cell membrane's integrity is lost *via* membrane blebbing, followed by rupturing and the uncontrolled release of cellular contents into the extracellular environment.[38]

The cell cycle in mammalian cells consists of four distinct phases.[39] The S-phase is where DNA synthesis occurs and the chromosomes are duplicated. The M-phase is where the replicated chromosomes are separated into two separate nuclei and two daughter cells are produced. This step is called mitosis and requires the formation of mitotic spindles which pull the chromosomes apart. Finally, G1 and G2 are known as gap phases and occur before the S- and M-phases, respectively. During these stages the cells priorities are growth, synthesising cellular proteins and organelles, and for the G2-phase it also involves re-organising cellular contents in preparation for mitosis. Interestingly, the complexes tested in this chapter cause arrest at different stages in the cell cycle of A2780 cells despite having similar structures. Complex **10** caused moderate S-phase arrest, whereas **19** caused slight elevation in the proportion of cells in in the G1-phase. Complexes **13**, **15**, **23** and **31** all caused a small increase in the proportion of cells in the G2/M-phase. Cell cycle arrest is advantageous in reducing the proliferation of cancer cells. Due to their ability to increase cell populations in the G2/M-phase, complexes **13**, **15**, **23** and **31** may

be involved in the inhibition of tubulin polymerisation similarly to **FY069**, [Os(η^6-bip)(5-F-AZPY)I]PF_6. However, **FY069** causes a much greater degree of G2/M-phase arrest (see Chapter 1, Section **1.3.4.3**).[40] None the less it would provide an insightful further investigation.

4.5. Summary

A total of 31 new Os(II) arene AZPY complexes were developed utilising the SARs that are currently understood for this class of anti-cancer complex. The new library of complexes included many different variations: (1) *p*-cym or bip arene ligands, (2) a choice of Cl^-, Br^-, I^-, N_3^-, or SCN^- for the monodentate ligand, (3) PF_6^-, $CF_3SO_3^-$ or IO_3^- counter anions, (4) a variety of different electron donating alkoxy/glycolic substituents situated on the pyridyl ring of the AZPY ligand, (5) complexes with more than one substituent on its AZPY ligand (an electron donating OH group situated on the phenyl ring and an electron withdrawing Br or CF_3 group situated on the pyridyl ring).

Nine complexes exhibited anti-cancer activity against A2780 cells with sub micro-molar activity, and six were further tested against other cells lines and their SFs were determined. Complex **13** possesses the best activity profile, exhibiting extremely potent activity against OE19 oesophageal cancer cells and a SF comparable to that of *cis*-platin. None of the complexes herein are as active as the key Sadler group osmium complex, **FY026**, against A2780 cells, or as selective. However, it may be possible to improve cancer cell selectivity by synergistic treatment with *L*-BSO. Complex **31** exhibited potent anti-cancer

activity but very poor selectivity. However, it is a novel complex with colouration that is dependent on pH, and it exists as a zwitterion under physiological conditions.

The SARs were explored for anti-cancer activity, aqueous solubility, capacity factor, and cell uptake for the complexes containing alkoxy and glycolic side chains. This has provided a database of information on some of the key physical and biological properties of Os(II) arene AZPY complexes. The main aim was to explore methods of improving solubility without negatively impacting on activity. Two effective methods were found; changing the anion or changing alkoxy substituents with branched alkoxy groups. Both involve lowering crystal packing energy, and the former method was found to be the most effective. The counter anion plays no role in anti-cancer activity and are interchangeable with other anions in solution, so large increases in solubility were implemented without adversely effecting activity and lipophilicity. Iodido complexes were shown to be considerably more active than their chlorido and bromido analogues, owing to their enhanced stability under physiological conditions. They are also more lipophilic, which was attributed to better cellular accumulation. Bip complexes were mainly more active than their *p*-cym counter-parts, however were considerably less soluble and slightly less lipophilic resulting in reduced cellular accumulation. Moreover, the stability studies reveal the importance of the Os-X bond strength (where X = monodentate ligand) and how it plays a role in the activity. Complexes with a weak Os-X bond can be deactivated in extracellular conditions, whereas an Os-X bond that is overly strong will not undergo in-cell activation.

Os(II) complexes with *pseudo*-halide monodentate ligands were synthesised, which is the first time they have been explored within the Sadler group. Complex **8** was reacted with KSCN *via* exchange of the Cl^- ligand to form two structural isomers; *S*-bound *S*-SCN (**34A**) and *N*-bound *N*-SCN (**34B**), the former of which was the major product. The isomers were separated by preparative HPLC and were stable towards hydrolysis inter-conversion of the isomers. Following a similar synthesis with NaN_3, an azido analogue was also synthesised (**35**). Their activities against A2780 cells follow the order **35**(N_3)>**34B**(*N*-SCN)>**34A**(*S*-SCN). The inactivity of **34A**, and lower activity of **34B** in comparison to **35** could perhaps be explained by overly strong binding of the monodentate ligand to Os(II), which does not readily allow for cellular activation involving dissociation of the monodentate ligand.

Complex **10** was found to have reduction potentials corresponding to the transfer of two electrons into the π*-orbital of the azo-bond. The first of which, falling within the biologically relevant region, is of a low negative value, indicating an easily reducible azo-bond. The azo-bond is suspected to be capable of mediating redox reactions inside cells, leading to raised ROS levels. Consequently, **10** (and also **7**, **13**, **15**, **23** and **31**) were capable of elevating ROS levels inside A2780 cells in ROS assays. Many of the key complexes herein were also found to raise the proportion of cells in late stage apoptosis in apoptosis assays. However, apoptosis may not be the primary mechanism of cell death as even higher proportions of non-viable cells were observed. Furthermore, key complexes were capable of inducing cell cycle arrest in different phases of the cell cycle: **10** produced S-phase arrest, **19** slightly raised

the proportion of cells in the G1-phase, and complexes **13**, **15**, **23** and **31** each caused a small increase in the proportion of cells in the G2/M-phase. These effects could play a role in reducing the proliferation of cancer cells.

4.6. References

(1) Ueno, K.; Akiyoshi, S. *J. Am. Chem. Soc.* **1954**, *76*, 3670.

(2) Ogata, Y.; Takagi, Y. *J. Am. Chem. Soc.* **1958**, *80*, 3591.

(3) Brown, E. V.; Kipp, W. H. *J. Org. Chem.* **1971**, *36*, 170.

(4) Dalmagro, J.; Yunes, R. A.; Simionatto, E. L. *J. Phys. Org. Chem.* **1994**, *7*, 399.

(5) Wang, M.; Funabiki, K.; Matsui, M. *Dyes Pigments* **2003**, *57*, 77.

(6) Zhang, C.; Jiao, N. *Angew. Chem. Int. Ed.* **2010**, *49*, 6174.

(7) Garcia-Amorós, J.; Díaz-Lobo, M.; Nonell, S.; Velasco, D. *Angew. Chem. Int. Ed.* **2012**, *51*, 12820.

(8) Wegner, H. A. *Angew. Chem. Int. Ed.* **2012**, *51*, 4787.

(9) Krause, R. A.; Krause, K. *Inorg. Chem.* **1980**, *19*, 2600.

(10) Baumann, F.; Kaim, W.; Denninger, G.; Kümmerer, H. J.; Fiedler, J. *Organometallics* **2005**, *24*, 1966.

(11) Dougan, S. J.; Habtemariam, A.; McHale, S. E.; Parsons, S.; Sadler, P. J. *Proc. Natl. Acad. Sci. U.S.A.* **2008**, *105*, 11628.

(12) Pizarro, A.; Habtemariam, A.; Sadler, P. *Top Organomet. Chem.* **2010**, 32, 21.

(13) Fu, Y.; Habtemariam, A.; Pizarro, A. M.; van Rijt, S. H.; Healey, D. J.; Cooper, P. A.; Shnyder, S. D.; Clarkson, G. J.; Sadler, P. J. *J. Med. Chem.* **2010**, *53*, 8192.

(14) Romero-Canelón, I.; Mos, M.; Sadler, P. J. *J. Med. Chem.* **2015**, *58*, 7874.

(15) Fu, Y.; Habtemariam, A.; Basri, A. M. B. H.; Braddick, D.; Clarkson, G. J.; Sadler, P. J. *Dalton Trans.* **2011**, *40*, 10553.

(16) Ishikawa, M.; Hashimoto, Y. *J. Med. Chem.* **2011**, *54*, 1539.

(17) Lipinski, C. A.; Lombardo, F.; Dominy, B. W.; Feeney, P. J. *Adv. Drug Deliver. Rev.* **2001**, *46*, 3.

(18) Herbert, V.; Streiff, R. R.; Sullivan, L. W. *Medicine* **1964**, *43*, 679.

(19) Ghose, A. K.; Viswanadhan, V. N.; Wendoloski, J. J. *J. Comb. Chem.* **1999**, *1*, 55.

(20) Spingler, B.; Schnidrig, S.; Todorova, T.; Wild, F. *Cryst. Eng. Comm.* **2012**, *14*, 751.

(21) Henczi, M.; Nagy, J.; Weaver, D. F. *J. Liq. Chromatogr.* **1994**, *17*, 2605.

(22) Fujisawa, S.; Masuhara, E. *J. Biomed. Mater. Res.* **1981**, *15*, 787.

(23) Sahu, S. K.; Pandit, G. G. *J. Liq. Chromatogr. R. T.* **2003**, *26*, 135.

(24) Clayden, J.; Greeves, N.; Warren, S.; Wothers, P. *Organic Chemistry*; First Ed.; Oxford University Press: Oxford, 2001.

(25) Shnyder, S. D.; Fu, Y.; Habtemariam, A.; van Rijt, S. H.; Cooper, P. A.; Loadman, P. M.; Sadler, P. J. *Med. Chem. Commun.* **2011**, *2*, 666.

(26) Alsenz, J.; Kansy, M. *Adv. Drug Deliver. Rev.* **2007**, *59*, 546.

(27) http://www.americanpharmaceuticalreview.com/Featured-Articles/160452-Thermodynamic-vs-Kinetic-Solubility-Knowing-Which-is-Which/

(28) van Rijt, S. H.; Romero-Canelon, I.; Fu, Y.; Shnyder, S. D.; Sadler, P. J. *Metallomics* **2014**, *6*, 1014.

(29) Romero-Canelon, I.; Salassa, L.; Sadler, P. J. *J. Med. Chem.* **2013**, *56*, 1291.

(30) Dougan, S. J.; Melchart, M.; Habtemariam, A.; Parsons, S.; Sadler, P. J. *Inorg. Chem.* **2006**, *45*, 10882.

(31) Janiak, C. *J. Chem. Soc., Dalton Trans.* **2000**, *21*, 3885.

(32) Romero-Canelon, I.; Pizarro, A. M.; Habtemariam, A.; Sadler, P. J. *Metallomics* **2012**, *4*, 1271.

(33) Millett, A. J.; Habtemariam, A.; Romero-Canelón, I.; Clarkson, G. J.; Sadler, P. J. *Organometallics* **2015**, *34*, 2683.

(34) Human, Z.; Munyaneza, A.; Omondi, B.; Sanabria, N. M.; Meijboom, R.; Cronjé, M. J. *BioMetals* **2015**, *28*, 219.

(35) Shi, Y.; Toms, B. B.; Dixit, N.; Kumari, N.; Mishra, L.; Goodisman, J.; Dabrowiak, J. C. *Chem. Res. Toxicol.* **2010**, *23*, 1417.

(36) Wang, F.; Habtemariam, A.; van der Geer, E. P.; Deeth, R. J.; Gould, R.; Parsons, S.; Sadler, P. J. *J. Biol. Inorg. Chem.* **2009**, *14*, 1065.

(37) Wang, F.; Habtemariam, A.; van der Geer, E. P. L.; Fernández, R.; Melchart, M.; Deeth, R. J.; Aird, R.; Guichard, S.; Fabbiani, F. P. A.; Lozano-Casal, P.; Oswald, I. D. H.; Jodrell, D. I.; Parsons, S.; Sadler, P. J. *Proc. Natl. Acad. Sci. U.S.A.* **2005**, *102*, 18269.

(38) Proskuryakov, S. Y. a.; Konoplyannikov, A. G.; Gabai, V. L. *Exp. Cell Res.* **2003**, *283*, 1.

(39) Romero-Canelon, I. Ph.D Thesis, University of Warwick, 2012.

(40) Fu, Y. Ph.D Thesis, University of Warwick, 2011.

Chapter 5

Radio-tracing the Cellular Activation of Osmium(II) Arene Phenylazopyridine Complexes using Iodine-131

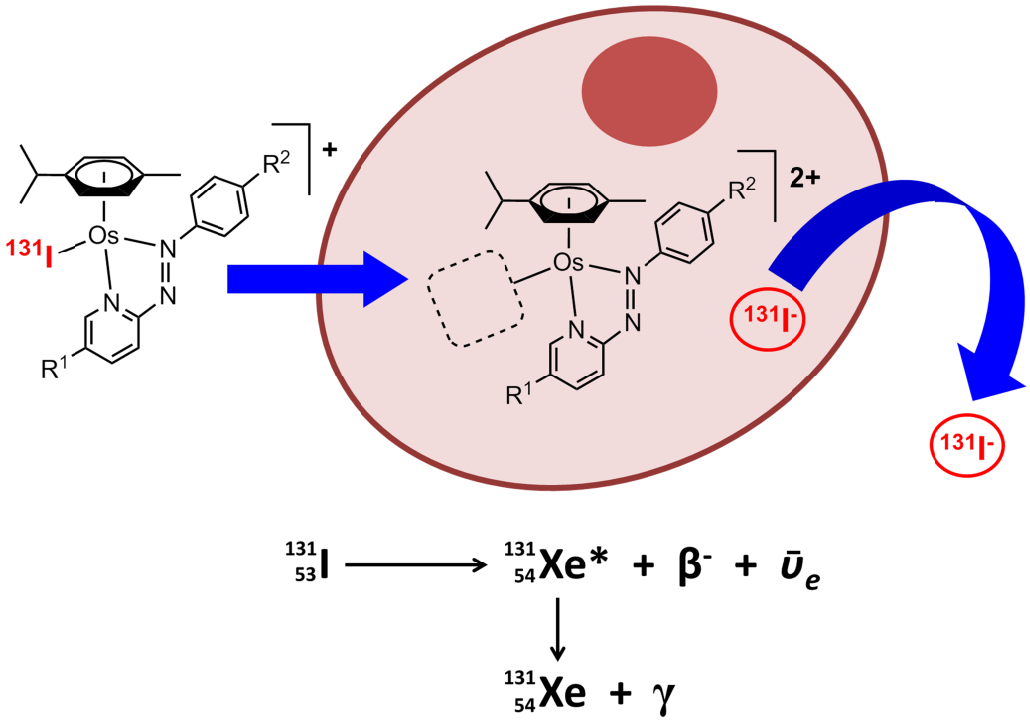

$$^{131}_{53}I \longrightarrow {}^{131}_{54}Xe^{*} + \beta^{-} + \bar{\upsilon}_{e}$$

$$\downarrow$$

$$^{131}_{54}Xe + \gamma$$

5.1. Introduction

Iodine-131 has long been known as a major fission product from uranium and plutonium, comprising nearly 3% of the total fission products.[1] Interestingly, because of its relatively short half-life of 8.02 days and decay mechanism involving the production of β^-- and γ-emissions, iodine-131 has been developed for both clinical treatments and *in vivo* radio-imaging. Quite notably, the unique property of thyroid follicular cells to trap and concentrate iodide *via* Na^+/I^- symporters (NIS) for the synthesis of thyroid hormones (triiodothyronine and throxyine),[1,2] allows the effective diagnosis and treatment of thyroid cancers[3-5] and hyperthyroidism[6] using radio-iodine. Utilising its ability as a β^--emitter (tissue penetration of 0.6 – 2 mm), iodine-131 has been successfully used in the clinic since 1948 for the treatment of thyroid cancer,[7] significantly improving the prognosis of the patients and making thyroid cancer one of the most manageable cancers. Due to its capacity to also produce secondary γ-emissions, there are also numerous applications of iodine-131 labelled compounds as imaging agents *in vivo* using Single Photon Emission Computed Tomography (SPECT).[8-11]

Os(II) arene AZPY complexes bearing monodentate iodide ligands, such as key complexes **10** (see Chapter 4, Section **4.3.7**) and **FY026**,[12] exhibit potent anti-cancer activity amongst multiple cell lines. Both structurally similar complexes incorporate an electron donating group on their AZPY ligand, situated on either the pyridyl or phenyl ring at positions *para* to the azo-bond (Figure 5.1). Iodido complexes of this nature are more lipophilic than their chlorido counterparts and are accumulated more effectively into cancer cells.[13] Owing to the stability of the

Os-I bond, they are also resistant to hydrolysis in aqueous solutions and it has been speculated they may undergo intracellular redox reactions mediated through their azo-ligands.[12-14]

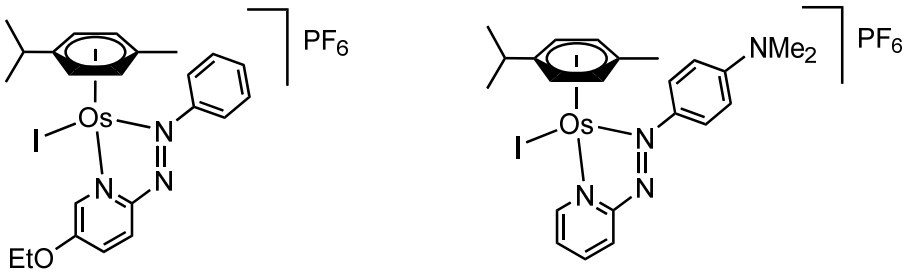

10 **FY026**

Figure 5.1. Two Os(II) arene AZPY complexes bearing iodide ligands that were used in these studies.

According to Breast Cancer UK, 1 in 8 women will be diagnosed with breast cancer at some point in their lives in the UK, and the rate of breast cancer in England has increased by 90% since records began in 1971.[15] There is always a demand for new anti-cancer drugs to enter the clinic. Complexes **10** and **FY026** exhibit anti-cancer activity towards MCF-7 human breast cancer cells with IC_{50} values of 1.2 and 0.20 μM respectively.[12] Exploiting the known stability of these complexes, the aim of this study is to label **10** and **FY026** with iodine-131 at the monodentate ligand position for the purpose of *in vitro* and *in vivo* tracing in MCF-7 human breast cancer cells. Within this chapter, the cellular activation of these complexes is investigated and a cellular activation pathway is proposed.

5.2. Experimental

All research involving use of the radioactive iodine-131 isotope was carried out at King's College London at the Division of Imaging Sciences and Biomedical Engineering in St Thomas's hospital. Research was carried out under the supervision of Prof. Phil Blower and with assistance from Dr. Levente Meszaros and Dr. Maggie Cooper. Further work involving MCF-7 cells was carried out at The University of Warwick in the School of Life Sciences, with assistance from Dr. Isolda Romero-Canelón.

5.2.1. Materials

5.2.1.1. Materials used at King's College London

Iodine-131 was purchased from Perkin-Elmer as an aqueous sodium iodide-131 solution (74 MBq; 185 GBq/mg) in 0.1M NaOH (pH 12-14). Human blood serum (male, O-positive) was obtained from myself at the St. Thomas's hospital blood centre facility. Blood was drawn into 2x 5 mL BD vacutainer tubes with BD Hemogard closures. The tubes contained a clot activator and a gel for serum separation. The blood clotted after ~30 min and the serum was separated by centrifuge (3600 rpm, 10 min). Approximately 5 mL of serum was obtained and stored in a refrigerator for no more than 4 days. DMEM cell culture medium, penicillin/streptomycin mixture, foetal bovine serum, L-glutamine, phosphate buffered saline solution (PBS), trypsin and PI were all purchased from Sigma-Aldrich. The DMEM cell culture medium was fully prepared as described in

Chapter 2, Section **2.1.1.2**. MCF-7 cells were purchased from the European Collection of Cell Cultures and used between 15 – 25 passages.

5.2.1.2. Materials used at The University of Warwick

Materials were obtained as described in Chapter 2, Section **2.1.1**. **FY025** and **FY026** were synthesised following previously described methods,[12] and complexes **8** and **10** were synthesised as shown in Chapter 4, Section **4.2.2.2**.

5.2.2. Radio-labelling of complexes

Stock solutions of the precursor osmium chlorido complexes (**8** and **FY025**) were made in MeOH (5 mg/mL). An aliquot of a stock solution (50 µL) was transferred into a 2 mL plastic sealable tube and added with NaI-$131_{(aq)}$ (30-70 MBq). Additional water was added to make a water:MeOH (1:1) solvent matrix, then the solution was heated for 18 h at 60 °C and with 300 rpm stirring. The reaction progress was monitored by Radio-TLC (see Chapter 2, Section **2.4.3.1**). The radio-labelled complexes ([^{131}I]**10** and [^{131}I]**FY026**) were purified by preparative radio-HPLC (see Chapter 2, Section **2.4.3.2**). The purified radio-tracers were in HPLC solvents containing 0.1% TFA, and so were diluted with approximately three parts PBS solution to bring the pH to around 6-7, then immediately stored at -80 °C to minimise degradation.

5.2.3. Methods

All of the methods and instruments used at KCL have been described in detail in Chapter 2, Section **2.4.** Some additional methods were carried out at the University of Warwick in the School of Life Sciences and at the Department of Chemistry, and are described below.

5.2.3.1. Manual cell counting

Manual cell counting was required for the cell calibration method. From a single-celled stock solution of MCF-7 cells, 10 μL was injected into both side A and B of a plastic disposable invitrogen^{TM} hemocytometer, ensuring that no air bubbles are trapped (Figure 5.2).

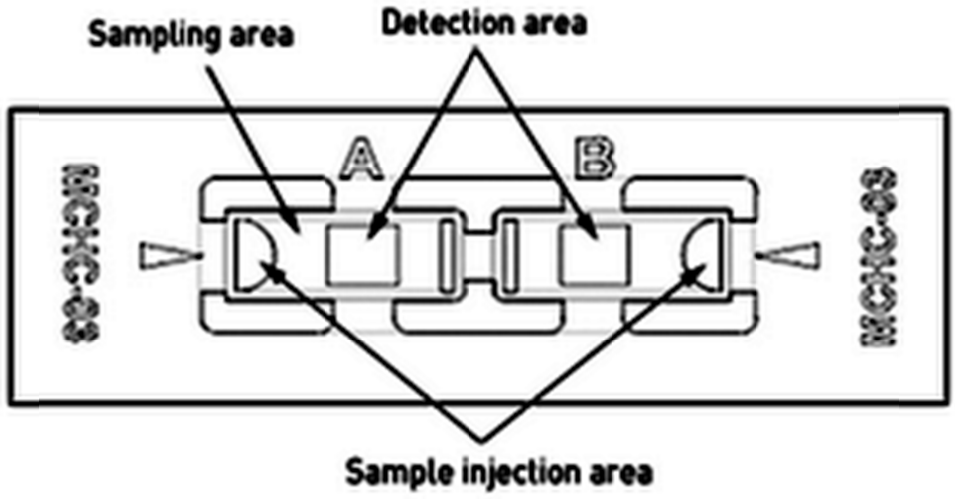

Figure 5.2. Diagram of a hemocytometer showing detection areas A and B.

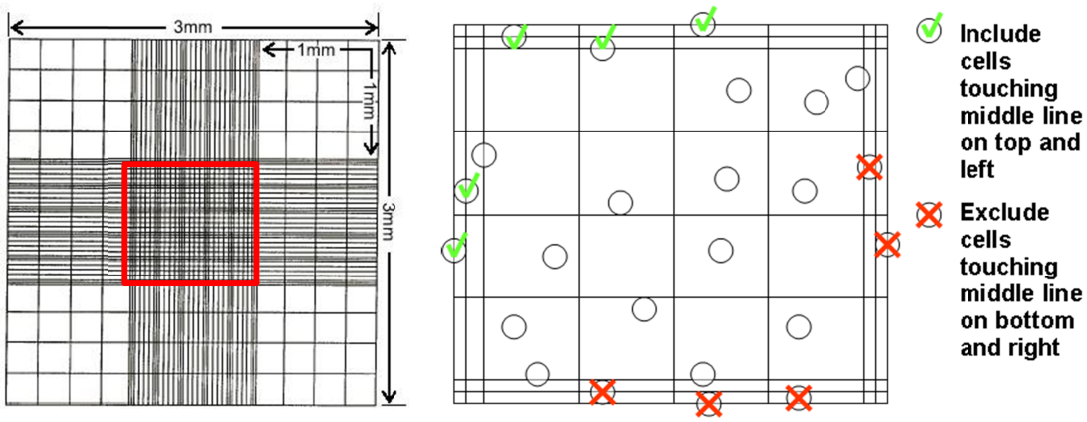

Figure 5.3. The cross-hatched areas of the hemocytometer under magnification.

The central cross-hatch of the two detection areas were examined under a microscope at 10x magnification, and the numbers of cells within the cross-hatch were counted (Figure 5.3). The border around the cross-hatch consists of three lines. For the top and left hand side, any cells touching the central border line were counted. For the bottom and right-hand side, any cells touching the central border line were not counted. For cell counts greater than 350, the sample was diluted first. The average number of cells was calculated from the cell counts of sides A and B, then multiplied by 10^4 to give the number of cells/mL.

5.2.3.2. Cell calibration method

MCF-7 Cell samples from the cellular accumulation studies of iodine-131 carried out at KCL were digested in sodium hydroxide, forming cell lysates. These were transported to the University of Warwick after 8 half-lives had

passed. In order to accurately determine cellular accumulation, the number of cells per 1 mL was determined by producing a calibration curve.

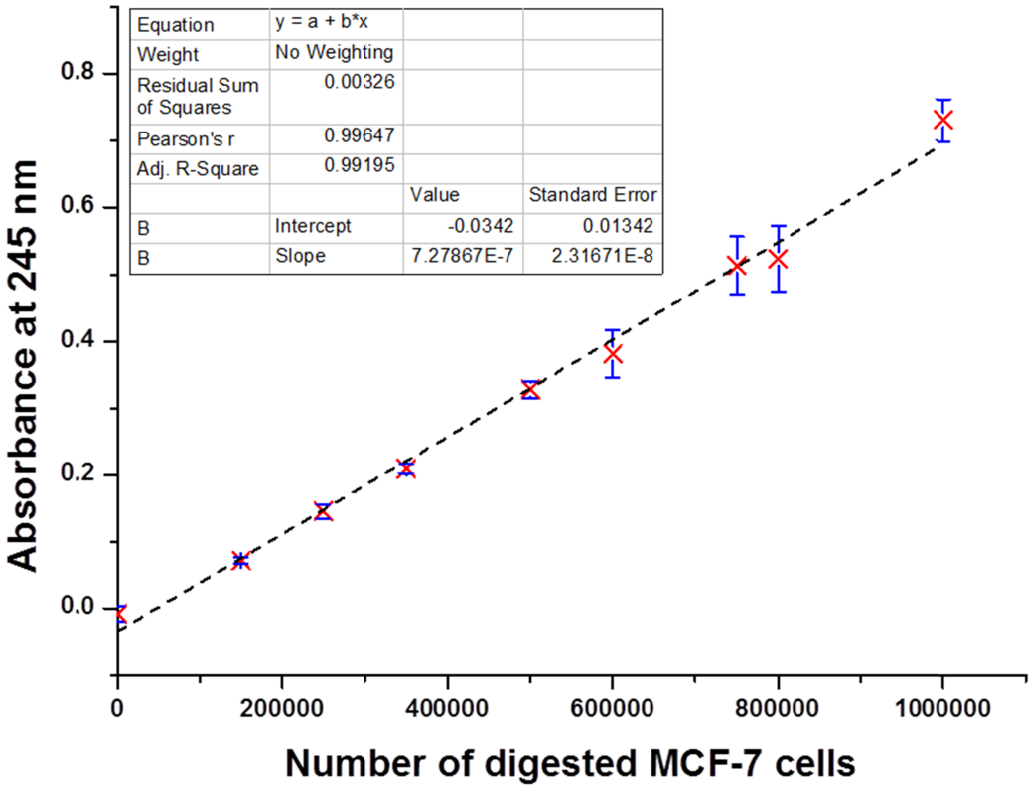

Figure 5.4. Calibration curve for UV absorbance at 245 nm against number of digested MCF-7 cells

From a 10-15 mL single-celled stock solution of MCF-7 cells in PBS:AccuMax (1:1, v/v) containing 4-5 x 10^6/mL cells, the following single-celled solutions (1 mL) were produced in triplicates: 0, 0.15, 0.25, 0.35, 0.5, 0.6, 0.75, 0.80 and 1.00 (x 10^6/mL cells). After centrifuging (5 min, 1000 rpm, 22 °C) and removing the supernatants, the cell pellets were digested in 1 M NaOH (1 mL) and incubated for 30 min at 37 °C, forming cell lysates. PBS (2 mL) was added to

the lysates so that they were in the same solvent matrix as the KCL samples. This method was repeated once more to produce duplicates of triplicates. The samples were analysed on a UV-Vis absorption instrument at 25 °C, scanning between 200-400 nm. A calibration curve was generated by plotting absorbance at 245 nm against number of digested MCF-7 cells (Figure 5.4).

The UV-Vis absorption of the KCL samples were analysed in the same manner in triplicates, recording the maximum absorbance at 245 nm. Dilutions with 1M NaOH:PBS (1:2, v/v) were necessary so that samples fell within the calibration range. Using the calibration curve, the average number of MCF-7 cells and standard deviation were calculated for each sample.

5.3. Results

5.3.1. Synthesis of iodine-131 labelled complexes

The labelling of radio-tracer complexes with iodide-131 occurs *via* a halide exchange process, involving the chlorido analogues of **10** and **FY026** (**8** and **FY025**, respectively, see Scheme 5.1). The chloride ligand is displaced by iodide which forms a stronger osmium-halide bond. Since sodium iodide-131 (NaI-131) is measured in radioactive units (Becquerel's, Bq, where 1 MBq of iodine-131 is equivalent to 5.4 ng), the chlorido complex was added in large excess, ensuring good conversion and minimising radioactive waste. Typically, **8** or **FY025** (0.25 mg) was mixed with NaI-131 (30-70 MBq, 0.0006-0.0015 mol. equiv.).

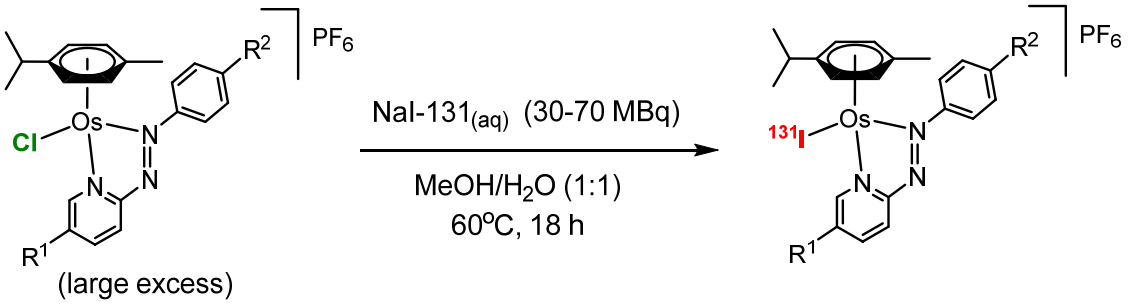

Complex	R^1	R^2
FY025	H	NMe_2
8	EtO	H

Complex	R^1	R^2
[^{131}I]**FY026**	H	NMe_2
[^{131}I]**10**	EtO	H

Scheme 5.1. Synthesis of radio-tracer complexes, [^{131}I]**FY026** and [^{131}I]**10**, from their chlorido analogues, **FY025** and **8**, respectively.

Reactions were followed by radio-TLC chromatograms using silica TLC plates. Cationic organometallic Os(II) complexes have a strong affinity for silica and reside close to the baseline. However, NaI-131 strongly solubilises in the eluent and travels with the solvent front. A distinct separation between the radio-tracer complex (R_f = 0.03-0.04) and NaI-131 (R_f = 0.95 - 0.96) was observed. Figure 5.5 shows the radio-TLC chromatograms for (A); aqueous NaI-131, and the radio-synthesis of (B); [^{131}I]**10** and (C); [^{131}I]**FY026** after two hours reaction. The halide exchange process occurs more slowly for the radio-labelling of **FY026** and so an 18 h reaction period was employed.

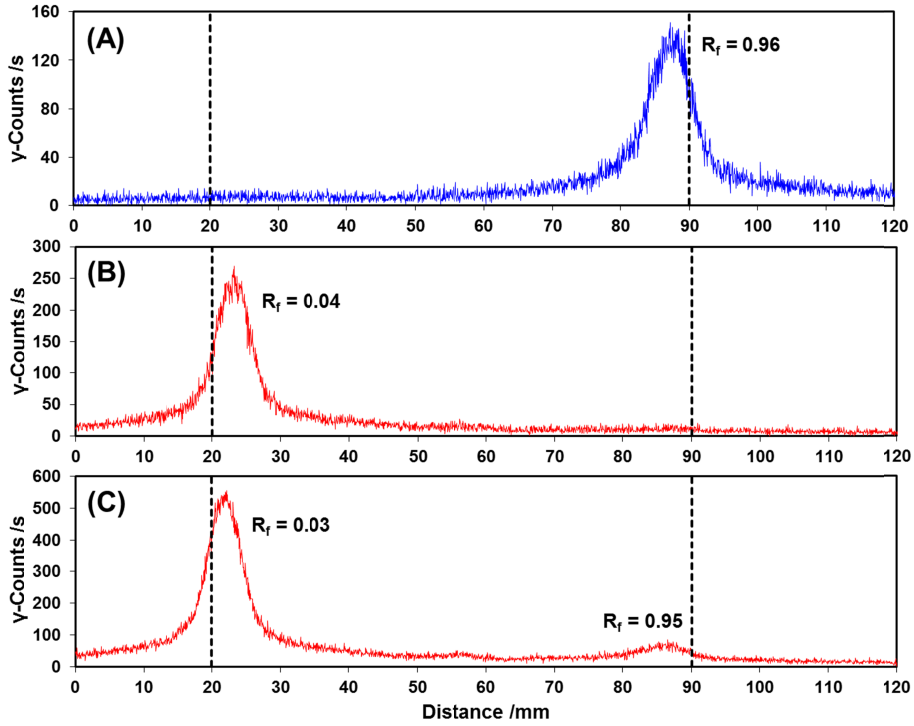

Figure 5.5. Radio-TLC analysis of; (A) aqueous NaI-131, (B) the radio-synthesis of [^{131}I]**10** after 2 h, (C) the radio-synthesis of [^{131}I]**FY026** after 2 h. The change in R_f value from a high to low values signifies the transformation from free iodide-131 to complex bound I-131.

The reactions were analysed after completion by Radio-HPLC. Chromatograms for UV-Vis absorption (254 nm) and γ-detection were generated simultaneously (Figure 5.6). Residual chlorido complexes were observable in the UV-Vis absorption chromatogram with retention times of 20.70 and 19.12 min for **8** and **FY025**, respectively. Also observable were hydrophilic peaks that were identified as hydroxido-adducts (products of hydrolysis). These had retention times of 11.62 and 11.50 min for **10-OH** and **FY026-OH**, respectively. Major lipophilic peaks were observed in the radio-chromatograms, which correspond to I-131 labelled species (23.85 and 22.40 min for [^{131}I]**10** and [^{131}I]**FY026**,

respectively). To confirm that the signals correspond to iodine-131 labelled complexes, the reactions were also carried out with 0.5 mol. equiv. of naturally abundant NaI added. This yielded peaks in the UV-Vis chromatograms that overlap the radio-signals, with retention times of 23.43 and 22.03 min for **10** and **FY026**, respectively. The slight off-set in retention times by about 0.4 min occurs because γ-detection takes place after the UV detection.

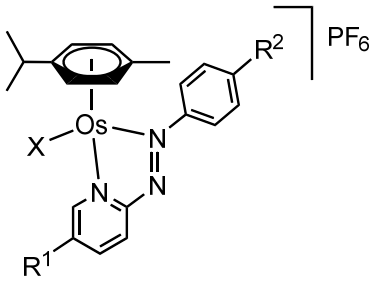

Species	X	R^1	R^2	RT
[^{131}I]**10**	^{131}I	OEt	H	23.85
10	I	OEt	H	23.43
8	Cl	OEt	H	20.70
10-OH	OH	OEt	H	11.62
[^{131}I]**FY026**	^{131}I	H	NMe_2	22.40
FY026	I	H	NMe_2	22.03
FY025	Cl	H	NMe_2	19.12
FY026-OH	OH	H	NMe_2	11.50

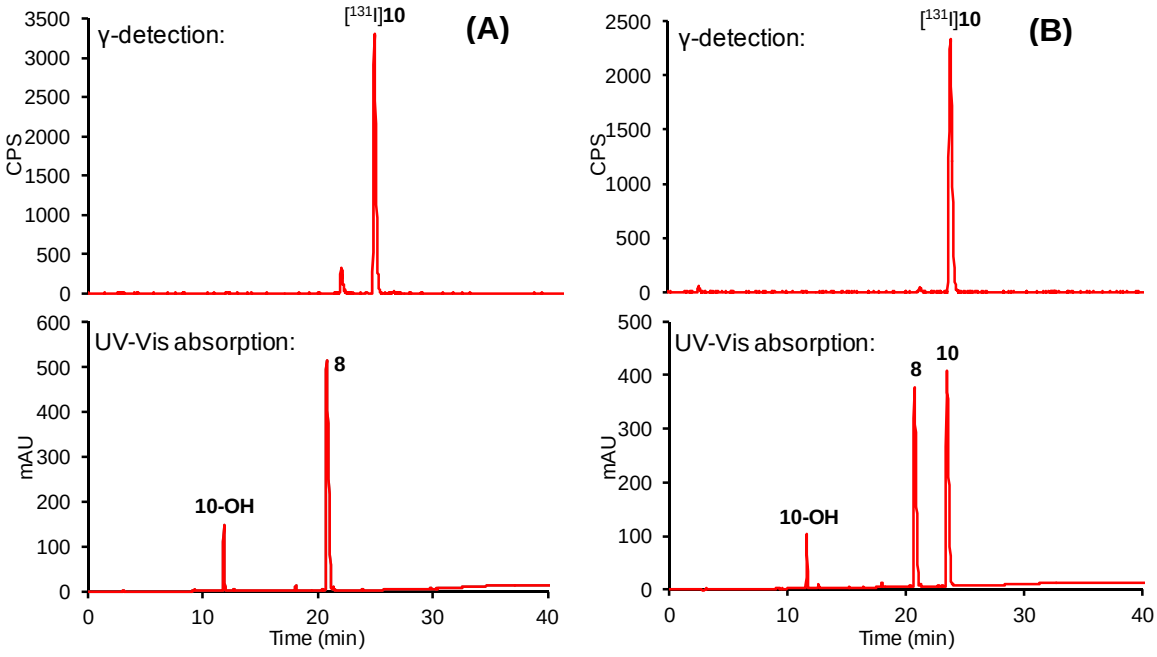

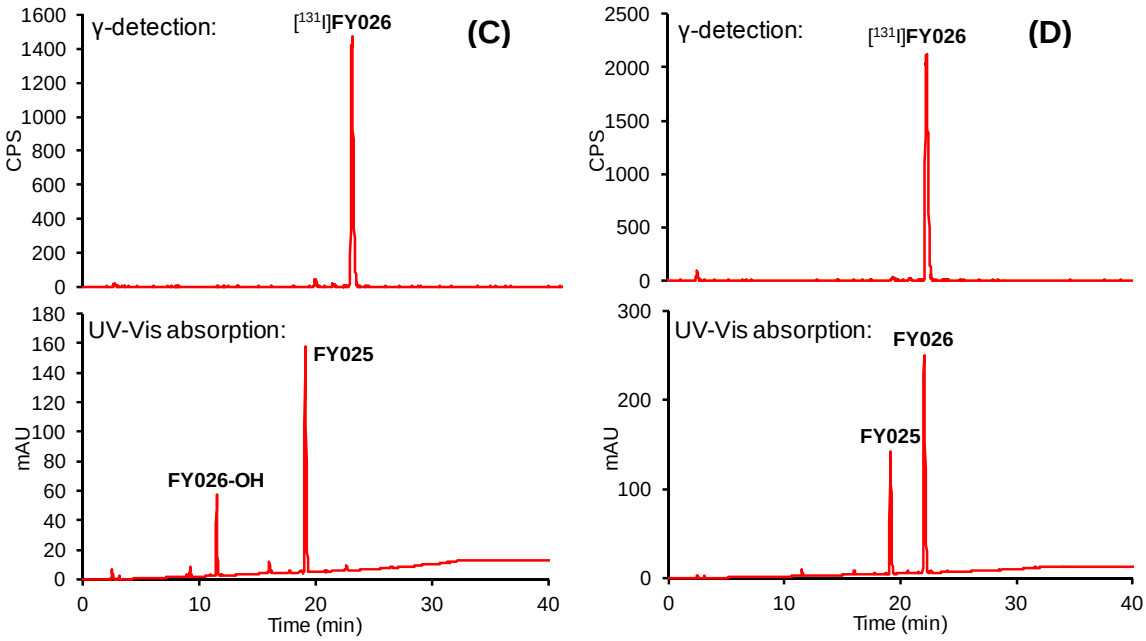

Figure 5.6. Radio-HPLC chromatograms of reaction mixtures from the synthesis of radio-tracer complexes, showing all the major species present. (A); Synthesis of [^{131}I]**10**. (B) Synthesis of [^{131}I]**10** in the presence of 0.5 mol. equiv. NaI. (C); Synthesis of [^{131}I]**FY026.** (D); Synthesis of [^{131}I]**FY026** in the presence of 0.5 mol. equiv. NaI.

The radio-tracer complexes were purified *via* preparative HPLC to remove residual chlorido complexes and any other impurities. In order to dilute the amount of acetonitrile and TFA in the purified samples, they were combined with approximately 3 parts PBS (v/v). PBS solution also acts as a pH buffer, raising the pH from ~1 to 6-7. After 3 days storage at 0-3 °C, decomposition of both radio-tracers was observed *via* radio-HPLC. Purified radio-tracers were stored at -80^{o}C conditions to minimise degradation.

5.3.2. Stability of radio-tracers in extracellular conditions

The stabilities of [^{131}I]**10** and [^{131}I]**FY026** were tested in human blood serum in non-carrier added and carrier added conditions (carrier added conditions are where the non-radiolabelled complex is also added with the radio-tracer at a concentration comparable to the IC_{50} value; in this case 0.25 μM). Samples were incubated at 37 °C and the amount of free iodide-131 generated in solution was observed by radio-HPLC, indicating the amount of iodide-131 monodentate ligand dissociated from the complex. [^{131}I]**FY026** exhibits good stability in serum over a 24 h period, showing 9% free iodide-131 generated after 1h and 11% generated after 24 h. In contrast, [^{131}I]**10** exhibits lesser stability in serum, with 13% and 25% free iodide-131 generated after 1 h and 24 h, respectively. In both cases, the addition of the carrier makes little or no difference (Figure 5.7).

Furthermore, it was possible to estimate the amount of iodine-131 accumulated by serum proteins after 24 h by separating the proteins from the supernatants and using a gamma-counter to measure the activity of the fractions. For [^{131}I]**10**, 5.2% and 5.3% accumulation was found for the non-carrier and carrier added experiments, respectively. For [^{131}I]**FY026**, it was 5.0% and 5.5%, respectively.

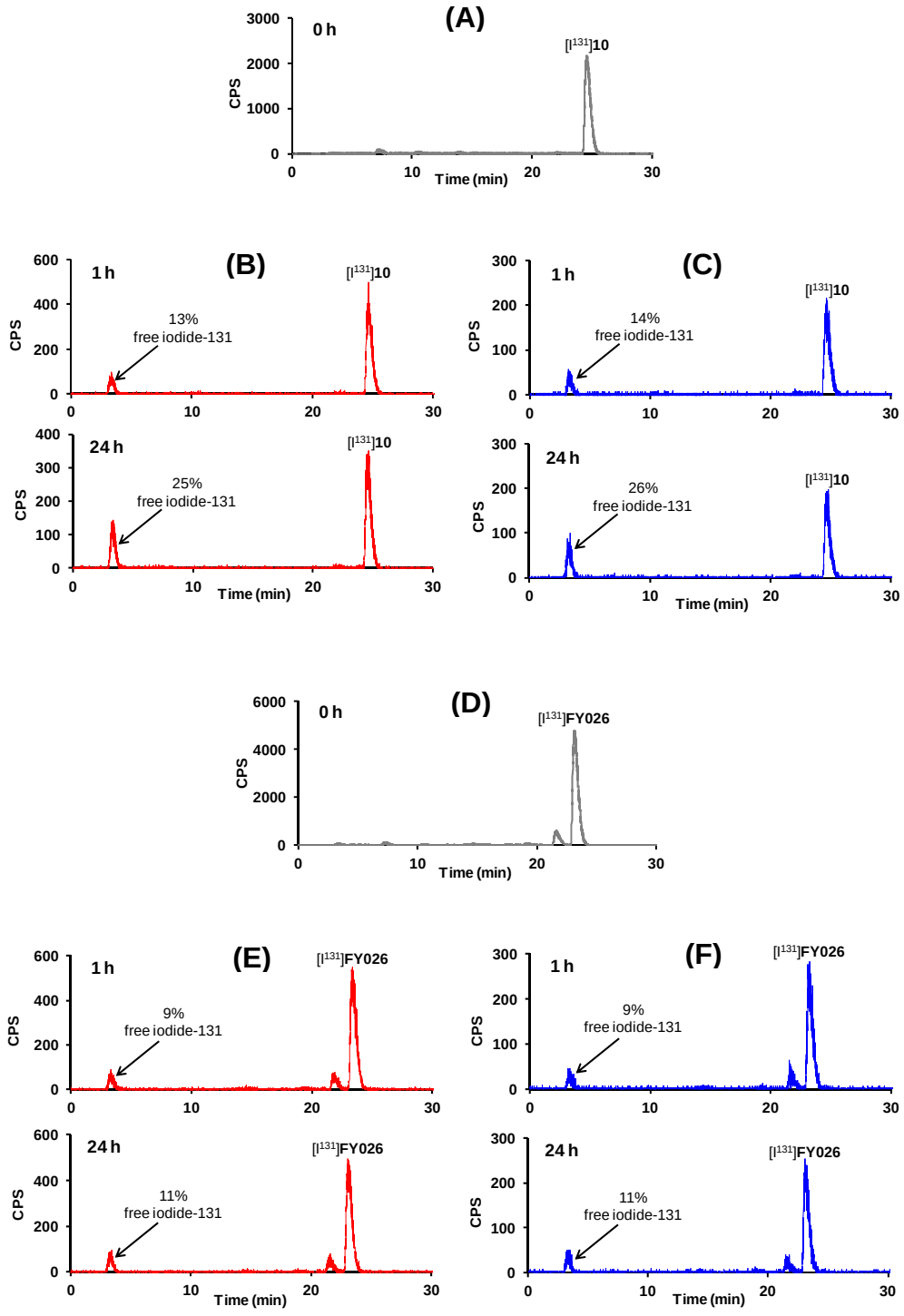

Figure 5.7. Radio-chromatograms for the stabilities of [^{131}I]**10** and [^{131}I]**FY026** in human blood serum after incubation at 37 °C. (A) [^{131}I]**10** before incubation in serum. (B) [^{131}I]**10** after incubating in serum for 1 and 24 h. (C) [^{131}I]**10** after incubating in serum for 1 and 24 h with 0.25 μM carrier. (D) [^{131}I]**FY026** before incubating in serum. (E) [^{131}I]**FY026** after incubating in serum for 1 and 24 h. (F) [^{131}I]**FY026** after incubating in serum for 1 and 24 h with 0.25 μM carrier.

5.3.3. *In vitro* stability assay

The stabilities of [^{131}I]**10** and [^{131}I]**FY026** were studied in cell culture medium in the presence and absence of MCF-7 cells, and in non-carrier and carrier added conditions (for carrier added conditions, non-radioactive complexes were added at IC_{50}/3 concentration; 0.40 and 0.06 μM for **10** and **FY026**, respectively). Samples were incubated for 2, 4, 8 and 24 h at 37 °C and the amount of free iodide-131 generated in the supernatants is observable by radio-HPLC. For both [^{131}I]**10** and [^{131}I]**FY026**, after 24 h incubation with MCF-7 cells, very little residual radio-tracer complex remains in the supernatants (*c.a.* 3.3 and 1.0%, respectively) and a very large amount of free iodide-131 was present (*c.a.* 96.7 and 99.0%, respectively, see Figure 5.8).

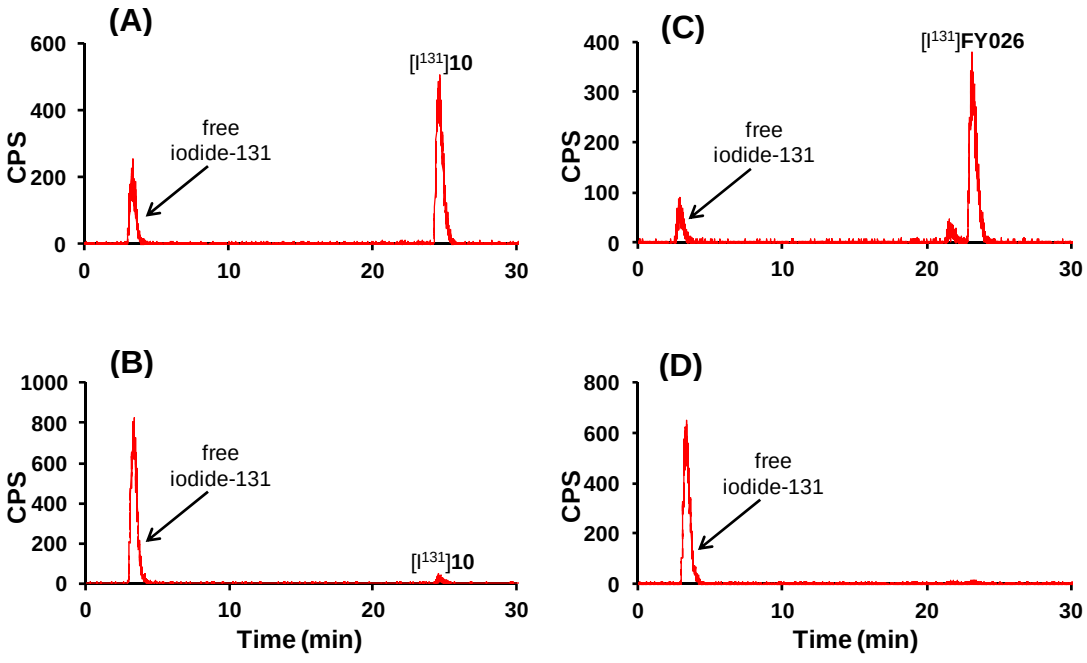

Figure 5.8. Radio-chromatograms of radio-tracer complexes (non-carrier added) incubated in cell culture medium for 24 h at 37°C. (A) [^{131}I]**10** with no cell present. (B) [^{131}I]**10** with MCF-7 cells present. (C) [^{131}I]**FY026** with no cell present. (D) [^{131}I]**FY026** with MCF-7 cells present.

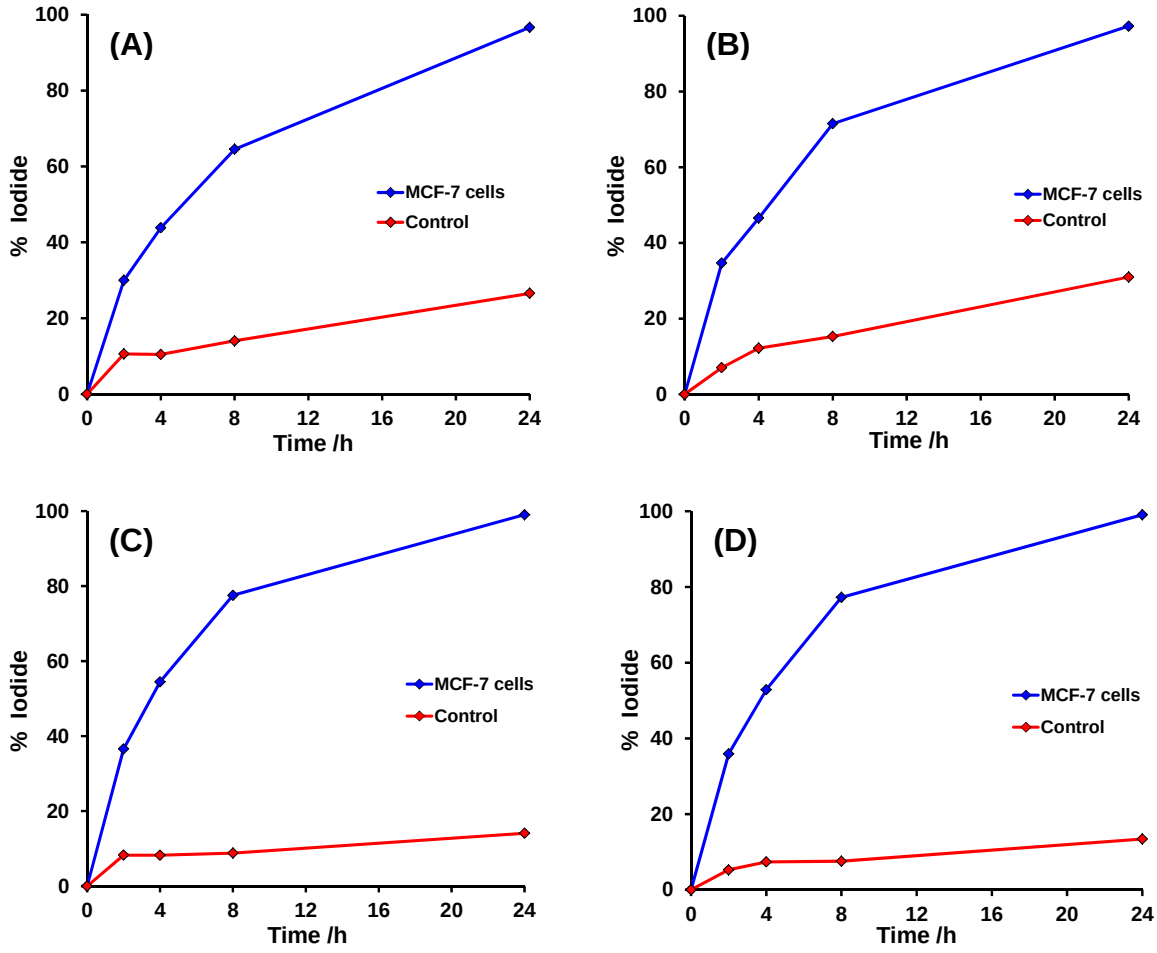

Figure 5.9. Graphs showing the extent of free iodide-131 generation in the supernatants at different time points: blue graphs show its generation in the presence of MCF-7 cells, and red graphs in the absence of MCF-7 cells. (A) [^{131}I]**10** with no carrier added. (B) [^{131}I]**10** with carrier added at IC_{50}/3. (C) [^{131}I]**FY026** with no carrier added. (D) [^{131}I]**FY026** with carrier added at IC_{50}/3.

The generation of free iodide-131 in the supernatants was measured at different time points of incubation. Figure 5.9 shows that [^{131}I]**FY026** is more stable than [^{131}I]**10** in the control experiments (where no MCF-7 are cells present) as less free iodide-131 is released. However, in the presence of MCF-7 cells

[^{131}I]**FY026** generates free iodide-131 in the supernatants at a faster rate than [^{131}I]**10**, as the shape of the curve in the graph changes more dramatically. Adding the carrier complex makes little difference to the extent or rate of free iodide-131 generation.

5.3.4. Cellular accumulation of iodine-131

The cellular accumulation of iodine-131 in MCF-7 cells was determined at different time points when cells were exposed to [^{131}I]**10** and [^{131}I]**FY026** (15-17 KBq). The % cell uptake in each sample was determined by γ-detection of the supernatant and cellular fractions using a gamma counter instrument (LKB Wallac 1282 Compugamma universal). The number of MCF-7 cells in the samples were determined *via* the cell calibration method (Section **5.2.3.2**), and the % cellular accumulation of I-131 /10^6 MCF-7 cells were calculated and plotted vs. time (min). Both radio-tracer complexes show an initial small spike in iodine-131 uptake at 5 min: 0.75 and 1.78% /10^6 MCF-7 cells, for [^{131}I]**10** and [^{131}I]**FY026**, respectively. From this point onwards, the amount of accumulated iodine-131 declines gradually (Figure 5.10).

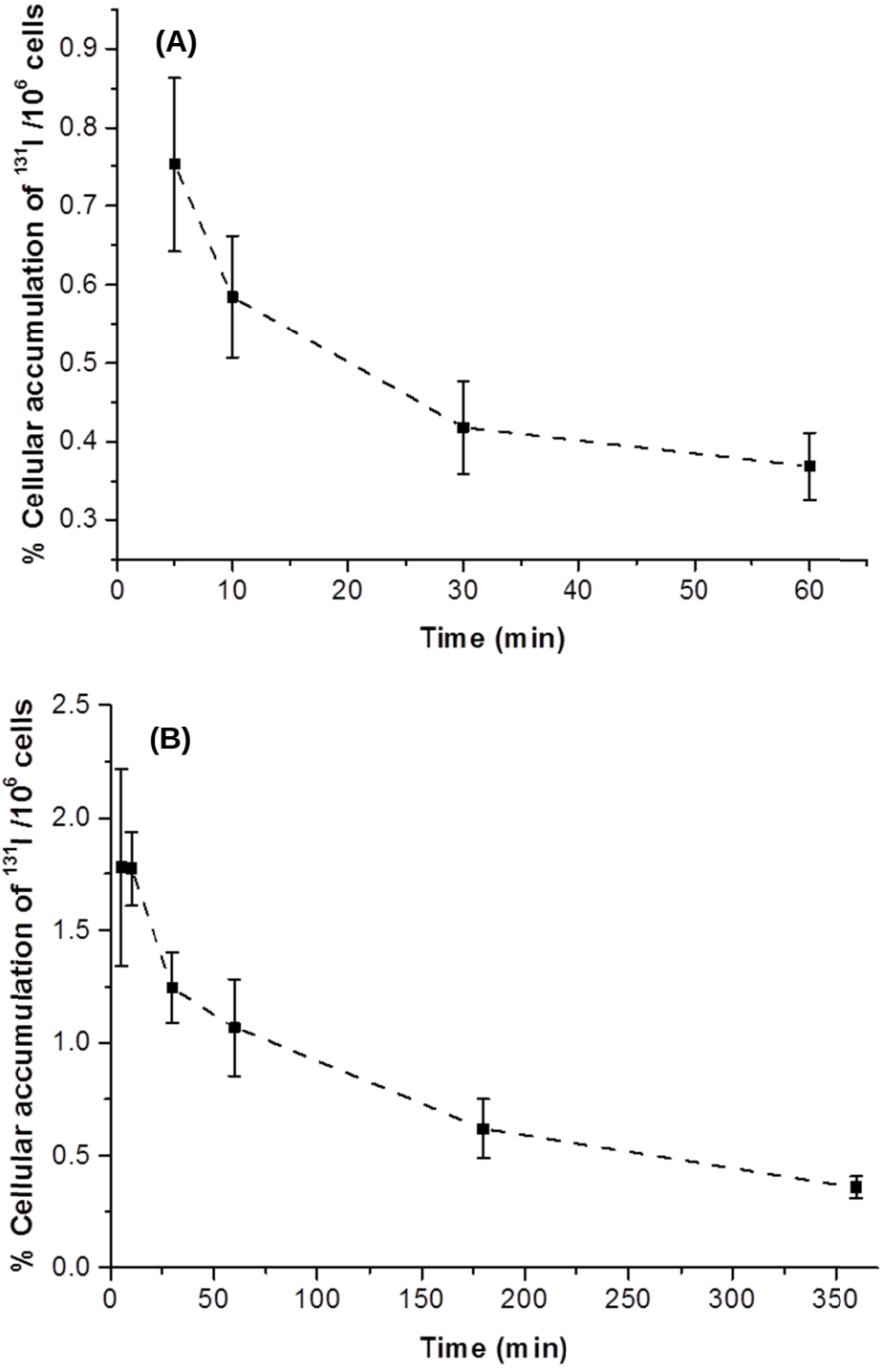

Figure 5.10. Cellular accumulation of iodine-131 in MCF-7 cells at different time points. (A) [^{131}I]**10**, and (B) [^{131}I]**FY026**.

5.4. Discussion

5.4.1. Extracellular stability of radio-tracers

For the [^{131}I]**FY026** radio-tracer stock solutions, a new species was observed with a retention time of 21.58 min in the radio-chromatogram when samples were stored at 0-3°C (Figure 5.11). Unfortunately, it was not possible to identify this species due to the amount being insufficient for MS detection. However, this impurity was vastly reduced by buffering the samples with PBS and storing at -80 °C.

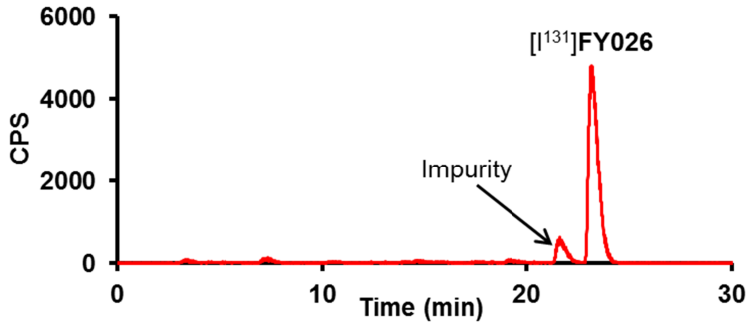

Figure 5.11. Radio-chromatogram showing a re-occurring impurity in [^{131}I]**FY026** stock solutions.

Both radio-tracer complexes show good stability in extracellular conditions over a 24 h time period with only 11% and 25% free iodide-131 being released from the complex after 24 h incubation in human blood serum at 37 °C, for [^{131}I]**10** and [^{131}I]**FY026**, respectively. When the iodide ligand is released it is likely to be replaced by a water molecule, forming the hydroxido-adducts identified during the radio-synthesis. (The reactivity of the hydroxido-adduct **10-OH** will be

discussed in greater detail in Chapter 6). Alternatively, it may be possible for Os(II) to form S-bonded adducts with sulphur-containing protein/peptide side chains. Ru(II) arene complexes have been previously shown to undergo similar behaviour with glutathione.[16,17] It is also apparent that the stability of [^{131}I]**FY026** is greater than that of [^{131}I]**10** as its iodide-131 ligand is released less readily. It appears that the substituents on the AZPY ligand and their positions on the *N,N*-chelating ligand may affect the electronic distribution in the complex in a way that dictates Os-I bond strength.[12]

It was also shown that for both radio-tracers there was a 5-6% uptake of iodine-131 into the serum proteins. However, it was not possible to deduce whether the accumulated I-131 was in the form of free iodide-131, or complex-bound iodine-131. It may be possible for both lipophilic complexes to accumulate into the hydrophobic pockets of serum proteins whilst remaining intact. It has been reported that lipophilic platinum drugs can accumulate in human albumin, which can be utilised as a potential mechanism for drug delivery.[18]

5.4.2. Intracellular activation of radio-tracers and iodide efflux

It was originally theorised that iodido Os(II) arene AZPY complexes remained intact upon entering cells and undergo redox reactions mediated through the azo-bond.[13] To our surprise, these new data suggest that the Os-I bond is more labile in intracellular conditions than originally anticipated. In the presence of MCF-7 cells both radio-tracer complexes rapidly release their iodide-131 monodentate ligand, which was observable in the supernatants. This was not

found to nearly the same extent in the control experiments where no cells were present. Despite its stronger stability in extracellular conditions, [^{131}I]**FY026** is shown to release its iodide-131 ligand at a slightly quicker rate than [^{131}I]**10** in the presence of MCF-7 cells. The cellular accumulation of iodine-131 by MCF-7 cells was explored when cells were exposed to radio-tracers at incubation times of; 5, 10, 30, 60, 120, 360 min. An initial spike in uptake was observed at 5 min, however the accumulation of I-131 was always very low and declined over time.

I hypothesise that the radio-tracers are taken up by cell,s which then undergo intracellular release of the iodide-131 monodentate ligand. Iodide-131 is then most likely pumped out of cells *via* chloride transport channels (Figure 5.12). Iodide efflux *via* the Cystic Fibrosis Transmembrane Regulator (CFTR) chloride channels has previously been demonstrated in NIH-3T3 fibroblast cells using an iodine-selective electrode.[19] Such processes might activate these complexes inside cancer cells. Previous studies utilising ICP-MS to determine osmium concentration show that complex **10** (Chapter 4, Section **4.3.8**) accumulates substantially into A2780 ovarian cancer cells after 24 h incubation (31±2 ng /10^6 cells was determined). **FY026** also shows fast accumulation in A549 cells with significant uptake after just 30 min of incubation time.[13] It is therefore likely that the rate of cell uptake of the radio-tracers is initially fast, explaining the initial spike in I-131 observed after 5 min. The rate of uptake is in competition with a rapid rate of efflux of iodide-131, explaining the decline in cellular I-131 observed after 5 min. We also cannot entirely rule out the possibility that an activation process involving the dissociation of the iodide at the cellular surface, occurs in parallel.

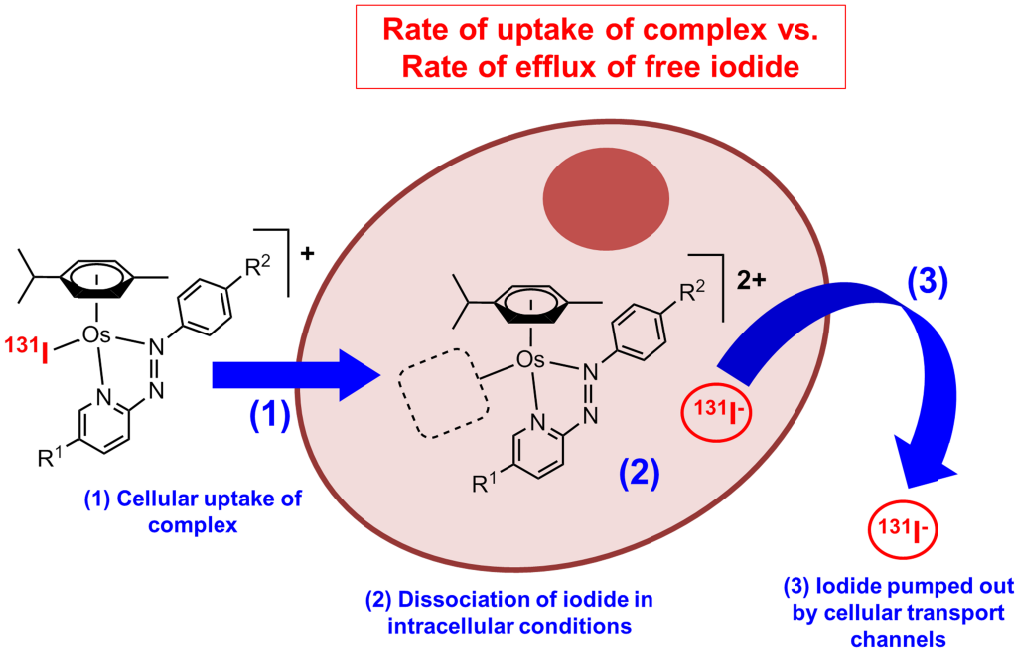

Figure 5.12. Diagram showing the proposed cellular pathway and intracellular activation mechanism of iodido Os(II) arene AZPY complexes.

For [^{131}I]**FY026** it was noted that after 6 h incubation, the cellular accumulation of I-131 starts to level off and not decline to zero. This may account for intact radio-tracer becoming trapped inside the cell membrane. It has been previously shown in cellular distribution studies that **FY026** accumulates mainly into the cell membrane and particulate fraction of cancer cells,[13] likely owing to its lipophilic nature. After dissociation of the iodide ligand, it is speculated that either the reactive hydroxido-adduct can form or direct binding and interactions with biological targets may occur (see Chapter 6).

Interestingly, breast carcinoma biopsy tissues have been known to uptake more radio-iodide than their normal breast cancer tissue counterparts.[1,20] Iodide uptake in breast cancer tissues can be attributed to an increased expression of

sodium iodide symporters (NIS), which allow the coupled transport of one iodide anion with two sodium cations inside cells.[21-23] Despite NIS expression being identified in breast cancers, only a low percentage of tumours capable of radio-iodide uptake at detectable levels were confirmed in a later study,[24] leading to the hypothesis that NIS may be incorrectly localized within the cells of some breast tumours and hence incapable of taking up iodide.[1,21] MCF-7 cells have previously been shown to accumulate radio-iodide. However, this was achieved only when cells were treated with all-*trans* retinoic acid (atRA) to stimulate NIS expression.[25] A study by C. Spitzweg *et al* reports on a synergistic effect; by pre-treating MCF-7 cells with a combination of atRA and the synthetic glucocorticoid, dexamethasone (Dex), a 16-fold stimulation of NIS protein expression was observed, followed by a 3- to 4-fold increase in radio-iodide uptake in comparison to cells pre-treated with atRA alone.[26] However, they report that no radio-iodide accumulation was observed above background radiation levels in untreated cells or cells treated only with Dex. This is consistent with our findings and concludes that MCF-7 cells do not readily uptake radio-iodide. Furthermore, they study the iodide efflux of MCF-7 cells and find that cells pre-treated with atRA rapidly efflux iodide, releasing 80% of the accumulated radio-iodide into the supernatants after 2 min.

5.5. Summary

In order to study the cellular distribution of two key complexes, **FY026** and **10**, within MCF-7 breast cancer cells, complexes were labelled with iodine-131 and

purified using typical radio-labelling procedures. As anticipated, both radio-labelled complexes exhibit good stability in extracellular conditions over a 24 h incubation period, owing to the high Os-I bond strength inherent in iodido Os(II) arene AZPY complexes, as previously observed for this class of compounds.[12,14,27] Unexpectedly, when exposed to MCF-7 cells, iodide-131 readily dissociates from both radio-tracers as observed by radio-HPLC of the supernatant. From this point forward the study was re-focussed to investigate cellular activation, as distribution and imaging studies with labile radiolabels would not be possible.

Cellular accumulation studies of the radio-tracers in MCF-7 cells were performed by analysing I-131 uptake *via* gamma ray detection. A very low uptake of iodine-131 was observed for both radio-tracer complexes, peaking at the initial measurement at 5 min, after which cellular iodine-131 levels decline. Meanwhile, it has been shown previously that both complexes can accumulate in other cancer cell lines when osmium uptake is measured by ICP-MS. These observed trends can be explained by our hypothesis: complexes are rapidly taken up into cells, where an activation process takes place involving dissociation of the iodide ligand. The rate of uptake of the complex is in competition with a rapid rate of iodide efflux, likely involving cellular transport channels. Further studies would need to be performed to support this hypothesis. A cellular accumulation assay involving the simultaneous detection of osmium and iodine by ICP-MS may provide a good comparative means of measurement.

Furthermore, it was shown for [^{131}I]**FY026** that the cellular accumulation of iodine-131 levels off after 6h and a residual portion remains inside the cells. A study by C. Spitzweg *et al* concludes that MCF-7 cells do not readily uptake iodide and no radio-iodide was observable above background radiation levels.[26] This suggests that the observed residual iodine-131 is most likely to be in the form of intact radio-tracer complex trapped inside the cell membrane.

5.6. References

(1) Poole, V. L.; McCabe, C. J. *J. Endocrinol.* **2015**, *227*, R1.

(2) Dohán, O.; Carrasco, N. *Mol. Cell. Endocrinol.* **2003**, *213*, 59.

(3) Beierwaltes, W. H. *Semin. Nucl. Med.* **1978**, *8*, 79.

(4) Shimura, H.; Haraguchi, K.; Miyazaki, A.; Endo, T.; Onaya, T. *Endocrinology* **1997**, *138*, 4493.

(5) Park, H.-M. *J. Nucl. Med.* **2002**, *43*, 77.

(6) Ross, D. S. *N. Engl. J. Med.* **2011**, *364*, 542.

(7) Robbins, R. J.; Schlumberger, M. J. *J. Nucl. Med.* **2005**, *46*, 28S.

(8) Eskandari, N.; Yavari, K.; Outokesh, M.; Sadjadi, S.; Ahmadi, S. J. *J. Labelled Compd. Radiopharm.* **2013**, *56*, 12.

(9) Shi, X.; Zhu, J.; Zhao, L.; Cheng, Y.; Xiong, Z.; Tang, Y.; Shen, M.; Zhao, J. *Nanoscale* **2015**, *7*, 18169.

(10) Chang, C. C.; Chang, C. H.; Shen, C. C.; Chen, C. L.; Liu, R.-S.; Lin, M. H.; Wang, H. E. *Biorg. Med. Chem.* **2015**, *23*, 2261.

(11) Li, C. C.; Chi, J. L.; Ma, Y.; Li, J. H.; Xia, C. Q.; Li, L.; Chen, Z.; Chen, X. L. *Radia. Oncol.* **2014**, *9*, 144.

(12) Fu, Y.; Habtemariam, A.; Pizarro, A. M.; van Rijt, S. H.; Healey, D. J.; Cooper, P. A.; Shnyder, S. D.; Clarkson, G. J.; Sadler, P. J. *J. Med. Chem.* **2010**, *53*, 8192.

(13) van Rijt, S. H.; Romero-Canelon, I.; Fu, Y.; Shnyder, S. D.; Sadler, P. J. *Metallomics* **2014**, *6*, 1014.

(14) Fu, Y.; Habtemariam, A.; Basri, A. M. B. H.; Braddick, D.; Clarkson, G. J.; Sadler, P. J. *Dalton Trans.* **2011**, *40*, 10553.

(15) www.breastcanceruk.org.uk

(16) Wang, F.; Xu, J.; Habtemariam, A.; Bella, J.; Sadler, P. J. *J. Am. Chem. Soc.* **2005**, *127*, 17734.

(17) Soldevila-Barreda, J. J. Ph.D Thesis, University of Warwick, 2014.

(18) Zheng, Y. R.; Suntharalingam, K.; Johnstone, T. C.; Yoo, H.; Lin, W.; Brooks, J. G.; Lippard, S. J. *J. Am. Chem. Soc.* **2014**, *136*, 8790.

(19) Long, K.; Walsh, K. *Methods Cell Sci.* **1997**, *19*, 207.

(20) Eskin, B. A.; Parker, J. A.; Bassett, J. G.; George, D. L. *Obstet. Gynecol.* **1974**, *44*, 398.

(21) Welcsh, P. L.; Mankoff, D. A. *Nature* **2000**, *406*, 688.

(22) Spitzweg, C.; Harrington, K. J.; Pinke, L. A.; Vile, R. G.; Morris, J. C. *The J. Clin. Endocrinol. Metab.* **2001**, *86*, 3327.

(23) Upadhyay, G.; Singh, R.; Agarwal, G.; Mishra, S.; Pal, L.; Pradhan, P.; Das, B.; Godbole, M. *Breast Cancer Res. Treat.* **2003**, *77*, 157.

(24) Wapnir, I. L.; Goris, M.; Yudd, A.; Dohan, O.; Adelman, D.; Nowels, K.; Carrasco, N. *Clin. Cancer Res.* **2004**, *10*, 4294.

(25) Kogai, T.; Schultz, J. J.; Johnson, L. S.; Huang, M.; Brent, G. A. *Proc. Natl. Acad. Sci. U.S.A.* **2000**, *97*, 8519.

(26) Unterholzner, S.; Willhauck, M. J.; Cengic, N.; Schütz, M.; Göke, B.; Morris, J. C.; Spitzweg, C. *J. Clin. Endocrinol. Metab.* **2006**, *91*, 69.

(27) Fu, Y. Ph.D Thesis, University of Warwick, 2011.

Chapter 6

Elucidating the Mechanisms of Action of Osmium(II) Arene Phenylazopyridine Complexes

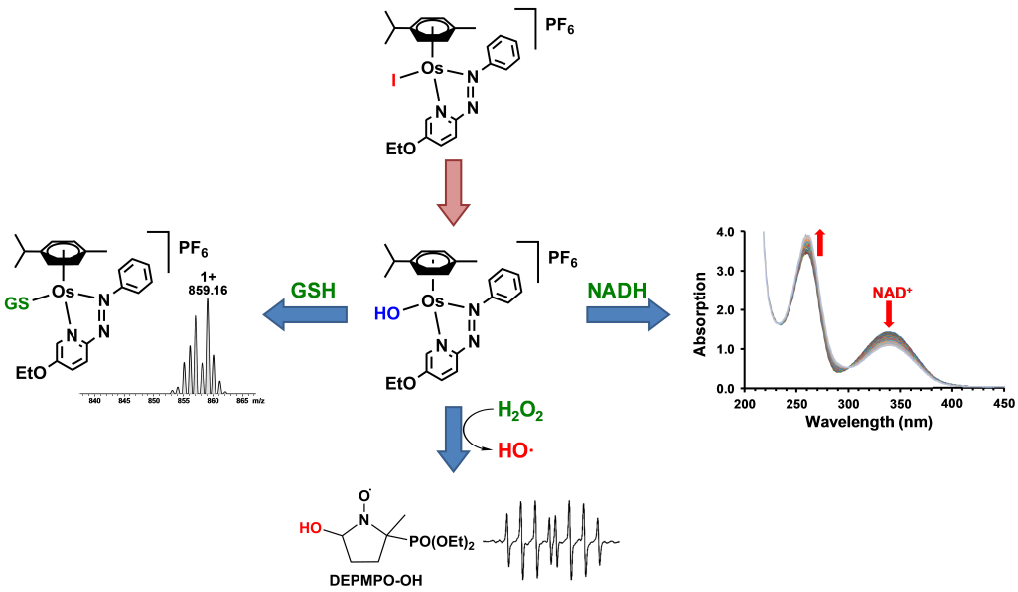

6.1. Introduction

In Chapter 4, Os(II) arene complexes bearing AZPY ligands were shown to be effective at elevating ROS levels within A2780 cancer cells, as well as causing apoptotic and non-apoptotic cell death and cell cycle arrest in different phases of the cell cycle. Chapter 5 showed that the seemingly stable iodido complexes undergo an unexpected cellular activation pathway, whereby the iodido monodentate ligand dissociates *in vitro* and is rapidly expelled from MCF-7 cancer cells. Herein, we explore the potential mechanisms of action that lead to elevated intracellular ROS levels and also address the mechanism of cellular activation involving iodide ligand loss and the subsequent formation of the hydroxido-adduct. The reactivity of Os(II) arene AZPY complexes is explored with several biological targets present in cancer cells, including H_2O_2, GSH and NADH.

Scheme 6.1 briefly summarises some of the cellular redox processes of mammalian cells.[1] NADPH oxidases (Nox) are responsible for the generation of $O_2{\cdot}^-$ radicals and are situated on the cell membrane.[2] These radical species have relatively low reactivity in physiological conditions and the damage they cause is based on reactions with other radicals and metal ions.[3] Superoxide dismutases (SOD) which are present in the mitochondria and cytosol, catalyse the dismutation of $O_2{\cdot}^-$ to O_2 and the weakly oxidising H_2O_2.[3] Catalase is located inside peroxisome organelles and very effectively convert H_2O_2 to H_2O and O_2 at one of the fastest turnover rates known for any enzyme.[3] Glutathione (GSH) is a tripeptide produced intracellularly in the body from its constituent amino acids: glutamic acid, cysteine and glycine. It is a crucial cellular antioxidant and

detoxifier present in mammalian cells at concentrations of 1-10 mM, mediating redox processes *via* its thiol side-chain.[4] It is capable of directly scavenging HO· and O_2·$^-$ radicals generating glutathione disulfide (GSSG) in the process, and also serves as a substrate for GSH peroxidases (GPx) for the reduction of H_2O_2 to H_2O.[3] Due to the highly efficient NADPH-dependent reduction of GSSG by GSH reductase (GR), low cellular levels of GSSG are maintained at around 5-50 μM.[4]

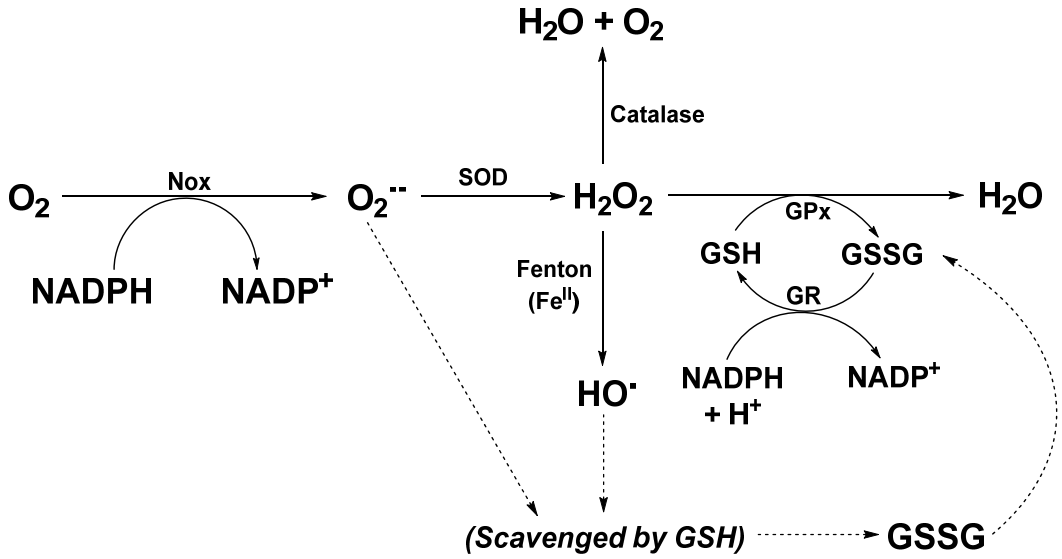

Scheme 6.1. Cellular redox and oxidative stress pathways occurring within the cytosol and mitochondria of mammalian cells. Nox = NADPH oxidase, SOD = superoxide dismutase, GPx = glutathione peroxidases, and GR = glutathione reductase.

Whilst playing a vital role in the detoxification of ROS in cells, GSH is often present at elevated concentrations amongst some cancer cell lines, increasing their resistance to certain chemotherapeutic agents.[5,6] Quite notably, platinum-drug resistant cell lines such as A2780cis (human ovarian cancer cells) generate higher levels of GSH in order to detoxify platinum drugs.[7] There are

numerous examples of platinum,[8,9] and even some ruthenium[10,11] anti-cancer complexes that are capable of binding and forming adducts with GSH. Moreover, ruthenium complexes of the form $[Ru(\eta^6\text{-arene})(AZPY\text{-}R)I]PF_6$ (where R = OH or NMe_2 and arene = *p*-cym or bip), were found to catalytically oxidise GSH to GSSG.[10] The process is believed to involve ligand centred reduction of the azo-bond by GSH where the reduction potentials of the azo-bond were found to fall within the biologically accessible range (-0.50 to +0.40 V).[12] Such catalytic drugs could be capable of vastly depleting cancerous cells of their GSH source, causing ROS levels to rise above a threshold where apoptosis is triggered. Interestingly, the analogous osmium complexes with AZPY or IMPY ligands are not capable of catalytic GSH oxidation because their reduction potentials fall outside the biologically accessible range.[13,14]

In mammalian cells, the intracellular physiological concentrations of H_2O_2 can vary from as low as ~0.001 µM and reach maximum concentrations of 0.5-0.7 µM.[15] These sub-micromolar quantities are a necessity for the normal functioning of cellular signalling pathways.[16] Elevated levels of H_2O_2 have been reported in extracellular conditions. Suspensions of mammalian cells in cell culture medium have been shown to generate extracellular levels of 0.02 - 2 µM,[15] and levels of 0.25-5 µM are found in blood plasma.[17] Numerous studies show that H_2O_2 plays a vital role in cancer development and cancer cells are well known for producing H_2O_2 in large quantities.[18-20] Szatrowski *et al* studied the H_2O_2 production of 10 tumour cell lines and found 7 of which exhibited fast rates of H_2O_2 production ranging from 0.2-0.5 nmol/10^4 cells h^{-1}.[21] NADPH oxidases are over-expressed in certain cancer cell lines and have been

attributed to increased ROS and H_2O_2 production. When Nox1 was expressed in NIH3T3 fibroblast cells, they developed malignant characteristics and showed a 10-fold increase in H_2O_2 levels. However, when catalase was expressed in the transformed Nox1 expressing cells, H_2O_2 concentrations decreased and the cells reverted back to normal appearance and growth rates (Arnold *et al*).[2]

In comparison to the weakly oxidising H_2O_2 species, HO· is the most reactive ROS, reacting immediately with almost every molecule found in living cells.[3] Briefly mentioned in Chapter 1, Section **1.2.3**, is a novel approach to treating cancerous cells, whereby their over-production of H_2O_2 can be exploited.[18] Ferrocenium salts,[22,23] and water soluble ferrocene derivatives[19] (Figure 6.1) are understood to cleave DNA *via* the production of HO· radicals from H_2O_2.

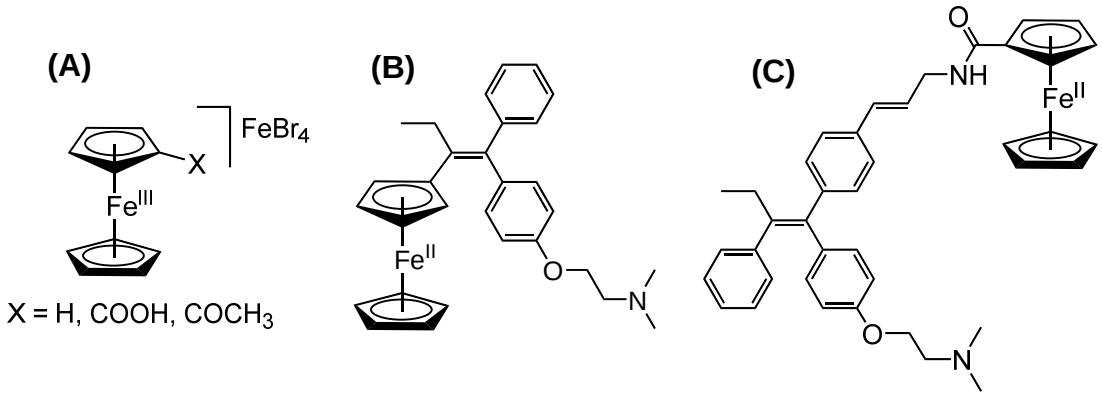

Figure 6.1. Molecular structures of (A) ferrocenium salts,[22] and ferrocene derivatives; (B) ferrocifen, and (C) ferrocene-tamoxifen complex.[19]

This is the first class of compounds found to utilise the selective accumulation of H_2O_2 in cancer cells as a pro-drug. Although the mechanism of HO· formation is not well understood, it has been proposed that the Fenton reaction is likely,

which involves the Fe(II) metal centre undergoing redox reactions with H_2O_2 (Scheme 6.2).[24]

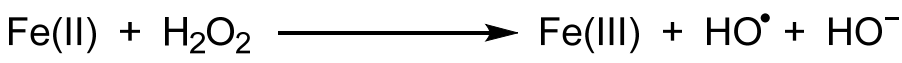

Scheme 6.2. The Fenton reaction where Fe(II) is oxidised to Fe(III) by H_2O_2, generating the highly reactive HO· radical species. In intracellular conditions, $O_2{\cdot}^-$, ascorbate and GSH are capable of reducing Fe(III) back to Fe(II).[3]

Nicotinamide adenine dinucleotide (NADH) is a naturally occurring coenzyme found in all living cells that plays an important role in cellular metabolism.[25] In normal cells, adenosine triphosphate (ATP) is produced *via* oxidative phosphorylation in the mitochondrial inner membrane where NADH is oxidised to NAD^+, accompanied by the reduction of O_2 to H_2O by electron transfer processes.[26] ATP is an important chemical energy source for a variety of cellular processes including DNA repair and cell division. Cancerous cells rely primarily on high rates of glycolysis (involving conversion of NAD^+ to NADH) in the cytosol to produce ATP, rather than mitochondrial respiration. Dependence on glycolysis is due to the mitochondrial defects associated with cancer cells and their adaptation to the hypoxic tumour microenvironment (the Warburg effect).[27] The balance of NADH/NAD^+ plays an integral role in providing energy for cancer cells, which have greater energy demands than normal cells. Furthermore, NADH behaves as a cellular antioxidant and NADH/NAD^+ forms a part of a cellular redox balance system (Figure 6.2).[25]

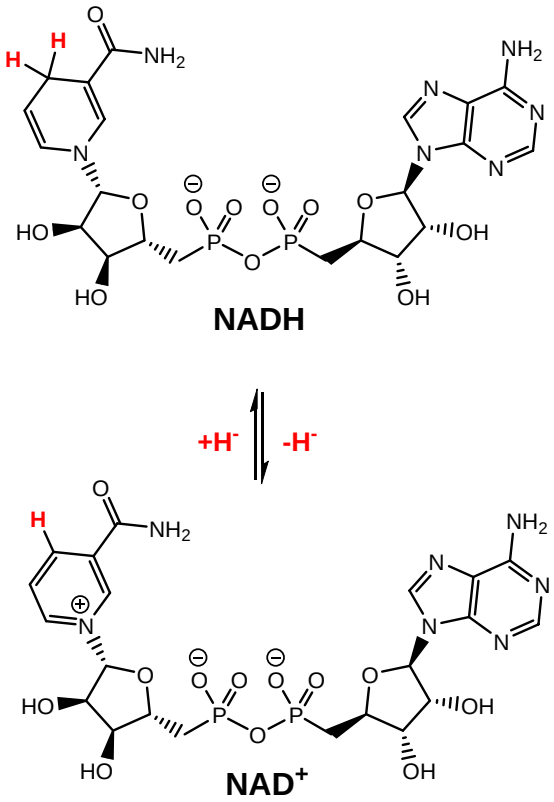

Figure 6.2. The conversion of NADH to NAD^+ *via* hydride transfer.

Targeting the NADH/NAD^+ redox system using catalytic drugs is an attractive prospect as it could allow low doses of drugs to be administered and introduce a novel mechanism of activity for overcoming resistance to platinum anti-cancer drugs.[28] Previous studies in the Sadler group have shown Ru(II) and Ir(III) catalysts that are capable of reducing NAD^+ to NADH by working synergistically with formate, which is added in non-toxic amounts to provide a source of hydride.[28-30] Such complexes are capable of inducing reductive stress on cancer cells. In contrast, there also exists Ir(III) and Os(II) catalysts from the Sadler group capable of oxidising NADH, hence inducing oxidative stress.[14,31,32] The common theme in both cases are complexes that form a M-H bond *in situ* and transfer hydride from one species to another.

6.2. Experimental

6.2.1. Materials

$[Os(\eta^6\text{-}p\text{-cym})Cl_2]_2$ was prepared as described in Chapter 2, Section **2.1.2**, and 5-EtO-AZPY as shown in Chapter 4, Section **4.2.2.1**. **FY026** was synthesised following literature procedures.[33] Silver nitrate, hydrogen peroxide 30 wt.%, perchloric acid 70 wt.%, reduced and oxidised forms of glutathione, 9-ethylguanine, N-acetyl-*L*-cysteine and β-nicotinamide adenine dinucleotide (reduced dipotassium salt) were all purchased from Sigma Aldrich. Sodium hydroxide was purchased from Fisher Scientific. Quantofix® peroxide 25 (0.5-25 mg/L) H_2O_2 semi-quantitative strips were purchased from Sigma Aldrich and used for H_2O_2 concentration determinations. EPR tubes were purchased from Wilmad Labglass, and the spin trap 5-(diethoxyphosphoryl)-5-methyl-1-pyrroline-N-oxide (DEPMPO) was obtained from Enzo Life Sciences. Lysozyme, ≥40,000 U/mg (from chicken egg white) was purchased from Sigma Aldrich. Deionised water was prepared as described in Chapter 2, Section **2.1.1.1**. Deuterated solvents used for NMR spectroscopy were purchased from Cambridge Isotope Laboratories Inc. and Sigma Aldrich and phosphate buffer solution was prepared as described in Chapter 2, Section **2.1.1.1**.

6.2.2. Synthesis of 10-OH

$[Os(\eta^6\text{-}p\text{-cym})(5\text{-EtO-AZPY})OH]PF_6$ (10-OH). To a stirring solution of $[Os(\eta^6\text{-}p\text{-cym})Cl_2]_2$ (100.0 mg, 126.5 μmol) in MeOH (3 mL), $AgNO_3$ (58.867 g/L, 1459 μL) in water was added. The mixture turned yellow and a white precipitate

formed, which was removed *via* filtration. A solution of 5-EtO-AZPY (60.4 mg, 265.6 µmol) in MeOH (5 mL) was added drop-wise to the yellow solution and it turned brown. The mixture was stirred for 18 h at ambient temperature, then NH_4PF_6 (206.2 mg, 1.27 mmol) was added. The product was extracted with DCM (10 mL) and washed with water (2 x 10 mL). DCM was removed under reduced pressure and the product was re-dissolved in a minimum amount of MeOH (~2 mL), and placed in a freezer overnight. A brown precipitate formed, which was collected *via* vacuum filtration then washed with ice-cold EtOH (2 x 1 mL) and Et_2O (2 x 5 mL), and dried overnight in a vacuum desiccator. Yield: 160.6 mg, (89%). ^{1}H NMR (D_2O): δ 9.04 (d, 1H, J = 2.2 Hz), 8.76 (d, 1H, J = 9.1 Hz), 7.98-7.95 (m, 3H), 7.76-7.73 (m, 3H), 6.51-6.50 (m, 1H), 6.16-6.15 (m, 1H), 6.01-5.98 (m, 2H), 4.48-4.44 (m, 2H), 2.34 (s, 3H), 2.17 (sept., 1H, J = 6.9 Hz), 1.54 (t, 3H, J = 7.0 Hz), 0.80 (d, 3H, J = 6.9 Hz), 0.68 (d, 3H, J = 6.9 Hz). ESI-MS calculated for $C_{23}H_{28}N_3O_2Os^+$: m/z 570.2. Found: 570.2. CHN analysis: Found: C, 35.54%; H, 3.64%; N, 5.86%. Calculated for $C_{23}H_{28}F_6N_3O_2OsP$ + CH_2Cl_2: C, 36.10%; H, 3.79%; N, 5.26%.

6.2.3. Measuring the pK_a of 10-OH[34]

A 2 mM solution of **10-OH** was prepared in D_2O and 4 mM dioxane was added as an internal ^{1}H NMR standard (at 3.75 ppm). The solution was aliquoted into 8 samples of 600 µL and the pH* values of the samples were adjusted sequentially by the addition of 1-10 µL of either KOD or $DClO_4$ (0.01, 0.1, 1, 2, 3, 4, 6, 8 or 10 M) in D_2O. The pH* of the samples were measured over a range

of 1.50 – 13.5 using a portable pH meter as described in Chapter 2, Section **2.2.7.2** (without correction for the effect of deuterium on the glass electrode). Changes in the chemical shifts of the peaks of complex **10-OD** were followed by ^{1}H NMR. The pH* values were corrected using the equation; pH = 0.936(pH*) + 0.412,[35] and the data were fitted to the Henderson-Hasselbalch equation using Origin 8.5.

6.2.4. Measuring the stability of 10-OH in aqueous media

6.2.4.1. ^{1}H NMR spectroscopy

A sample of **10-OH** (1 mM) was prepared in D_2O with phosphate buffer (100 mM, pH* 7.4). The ^{1}H NMR spectrum was recorded on a 600 MHz instrument before incubation (512 scans), and after 24 h incubation (1024 scans) at 37 °C.

6.2.4.2. HPLC

Two samples of **10-OH** (1 mM) were prepared in phosphate buffer (100 mM, pH 7.4). One sample was incubated at 37 °C for 24 h, while the other was prepared without incubation to be analysed immediately. The samples were diluted by 10x in water, then analysed *via* HPLC (see Chapter 2, Section **2.2.9** for the instrumental parameters used). The wavelength of detection observed was 254 nm (referenced to 510 nm). Integrals of the peaks were used to estimate how much compound was lost through precipitation.

6.2.5. Reactions of complexes with H_2O_2

6.2.5.1. UV-Vis spectroscopy

Solutions of **8**, **10-OH** and **11** (75 μM) were prepared in phosphate buffer solution (75 mM, pH 7.4) either with or without 7.5% EtOH, and with H_2O_2 (50 or 100 mol. equiv.). UV-Vis experiments were conducted at 37 °C in scanning kinetics mode and a spectrum was scanned at different time intervals. Quantofix® peroxide test sticks were used to quantify the concentrations of H_2O_2 remaining in solution. Control experiments were also conducted with no H_2O_2 added.

6.2.5.2. ^{1}H NMR spectroscopy

A solution of **10-OH** (3 mM) was prepared in D_2O with phosphate buffer (300 mM, pH* 7.4) and H_2O_2 (10 mol. equiv.). Using a kinetic ^{1}H NMR experiment, a spectrum was collected every 10 min at 5 °C for 2 h on a 600 MHz instrument.

6.2.5.3. Detection of free radicals by EPR spectroscopy

Solutions of complexes (1 mM) were prepared in phosphate buffer (75 mM, pH 7.4) with diethoxyphosphoryl-5-methyl-1-pyrroline *N*-oxide (DEPMPO, 6 mM) and H_2O_2 (10 mM). For complexes **8** and **11**, DMF (50%) was used to solubilise the complexes to 1 mM. The EPR spectra were recorded immediately after sample preparation (see Chapter 2, Section **2.2.12** for the instrumental

parameters used). Three control studies were also conducted: H_2O_2 control (complex absent), **10-OH** control (H_2O_2 absent), Complex **10-OH** + H_2O_2 in the presence of one drop of EtOH (HO· quench).

6.2.5.4. Lysozyme cleavage assay[36]

Lysozyme (75 μM) was incubated with different concentrations of H_2O_2 (0, 0.1, 1 and 10 mM) in the presence of either **10-OH**, **8** or **11** (10 μM) in phosphate buffer (60 mM, pH 7.4) for 2 h at 37 ºC, and analysed by gel electrophoresis (4-12% polyacrilamide mini stacking gel; 90 min at 100 V in MES buffer). The protein was stained using coomasie blue and quantified using the ImageJ and Origin software.

6.2.6. Binding experiments of complexes with 9-EtG, NAC, GSH and GSSG

6.2.6.1. ^{1}H NMR spectroscopy

Solutions of **10-OH** (1 mM) with either 9-ethylguanine (9-EtG), N-acetyl-L-cysteine (NAC), reduced glutathione (GSH), or oxidised glutathione (GSSG) (1 mol. equiv.) were prepared in D_2O with phosphate buffer (100 mM, pH* 7.4). The ^{1}H NMR spectrum was recorded before (512 scans) and after (1024 scans) incubation at 37 °C for 24 h, using either a 500 or 600 MHz instrument. Control experiments were also conducted where NAC and GSH were incubated in the absence of **10-OH** to determine the extent of oxidation under aerobic conditions.

6.2.6.2. HPLC/LC-MS

Samples of **10-OH** (1 mM) were prepared in phosphate buffer (100 mM, pH 7.4) with either NAC, GSH, or GSSG (1 mol. equiv.), or no substrate (control). Samples were incubated at 37 °C for 0 and 24 h, then stored in a freezer. The samples required 10x dilution in water before HPLC analysis was carried out (see Chapter 2, Section **2.2.9** for the instrumental parameters used). The samples that received 24 h incubation were later analysed *via* LC-MS to identify the species in solution (see Chapter 2, Section **2.2.10** for the instrumental parameters used).

Likewise, complexes **11** and **FY026** (75 µM) were prepared in phosphate buffer (75 mM, pH 7.4) with either 1 or 100 mol. equiv. of NAC, GSH or GSSG, or no substrate. Samples were incubated for 0, 3, 6, 12 and 24 h, and did not require dilution prior to HPLC or LC-MS analysis. The HPLC wavelengths of detection used were 254 nm (referenced to 510 nm) for **10-OH** and **11** and 610 nm (referenced to 360 nm) for **FY026**.

6.2.7. Reactions of complexes with NADH

6.2.7.1. UV-Vis spectroscopy

Complexes **10-OH**, **11** and **31** (4 µM) were prepared in phosphate buffer solution (1 mM, pH 7.4) with NADH (200 µM, 50 mol. equiv.). The samples were incubated at 37 °C and spectra were collected every hour for 24 h. A control study was also conducted to monitor NADH oxidation in the absence of any

complex. For the kinetic study, the Cary software was used in kinetics mode and the same sample concentrations were used as above. The absorption at 339 nm was monitored over a 24 h period at 37 °C, with measurements determined every 5 min.

6.2.7.2. HPLC

Complexes **10-OH**, **11** and **31** (50 μM) were prepared in phosphate buffer (5 mM, pH 7.4) with NADH (200 μM, 4 mol. equiv.). Samples were incubated at 37 °C for time periods of 0, 3, 6, 12 and 24 h, then stored in a freezer before analysing *via* HPLC. See Chapter 2, Section **2.2.9** for the instrumental parameters used. Control studies were conducted where **11** and **31** were incubated in the absence of NADH. The HPLC wavelength of detection used was 254 nm (referenced to 360 nm) for all complexes.

6.2.7.3. ^{1}H NMR spectroscopy

Solutions of complex **10-OH** (2 mM) were prepared in D_2O with phosphate buffer (200 mM, pH* 7.4) and NADH (3 mol. equiv.). The solutions were incubated at 37 °C for different time periods (0, 4 and 23 h), then the ^{1}H NMR spectrum was recorded on a 600 MHz field instrument with 512 scans.

6.3. Results

In this chapter the synthesis of complex **10-OH** is described. Complex **10-OH** is analogous to **10** and contains a monodentate hydroxide ligand instead of an iodide ligand. Its reactivity with different biological targets was explored and compared with complex **11**. Complex **11** is analogous to **10** with a $CF_3SO_3^-$ counter anion in place of PF_6^-, and was used in these studies instead of **10** because of its increased solubility in water. As shown in Chapter 4, Section **4.3.7**, the change of anion has no effect on anti-cancer activity, only water solubility. This chapter also explores the reactivity of complexes **8** (analogous to 10 with a chloride monodentate ligand), **31**, and **FY026** with biological targets for comparison. Figure 6.3 lists the molecular structures of all the complexes explored within this chapter.

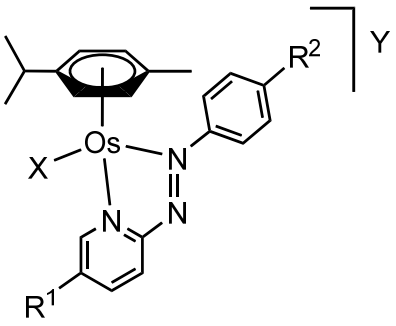

Complex	X	Y	R^1	R^2
8	Cl	PF_6	OEt	H
10-OH	OH	PF_6	OEt	H
10	I	PF_6	OEt	H
11	I	CF_3SO_3	OEt	H
31	I	PF_6	Br	OH
FY026	I	PF_6	H	NMe_2

Figure 6.3. Structures of the complexes studied in this chapter, where X is a monodentate ligand, Y is a negatively charged counter ion, and R^1 & R^2 are substituents on the bidentate AZPY ligand.

6.3.1. The pK_a of 10-OH

The pK_a* of the monodentate ligand of **10-OD** was determined using ^{1}H NMR, by observing the change in chemical shift of an aromatic *p*-cym proton as the pH* in D_2O solution was varied (pH* corresponds to the pH reading of a D_2O solution using a H_2O calibrated pH-meter). The pH* values were corrected to pH values[35] and the data were fitted to the Henderson-Hasselbalch equation. The pK_a of **10-OH** was calculated as 4.55±0.01 (pK_a* of **10-OD** = 4.43±0.01). The error was obtained as a computer fitting error using Origin 8.5, see Figure 6.4. Under physiological and basic conditions, **10-OH** exists as the hydroxido-adduct with an overall +1 charge, and under acidic conditions the hydroxide ligand is protonated yielding the aqua species with an overall +2 charge (Scheme 6.3).

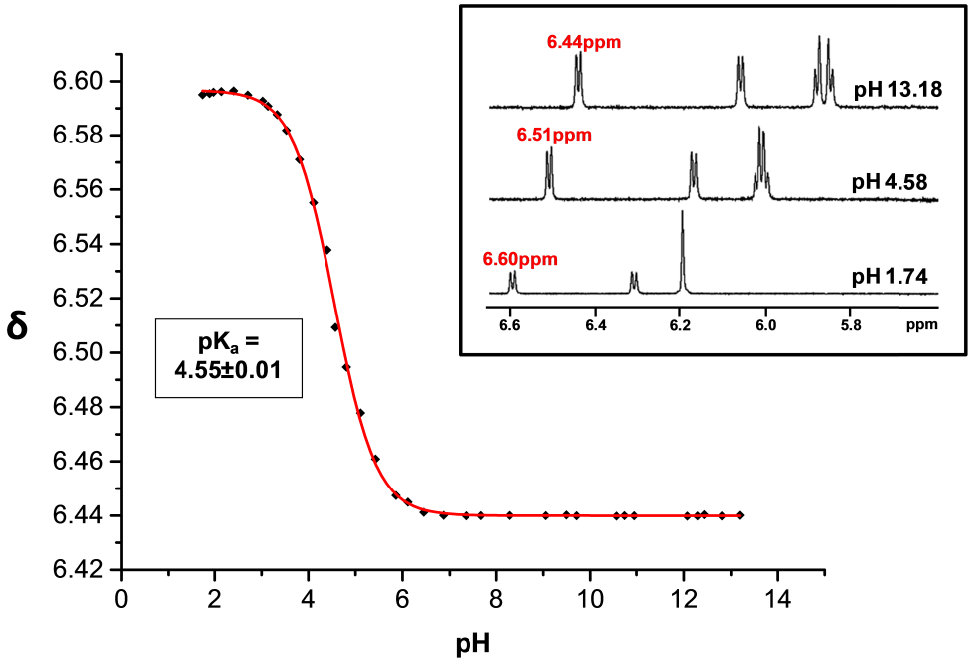

Figure 6.4. Variation of the chemical shift of an aromatic *p*-cym proton of **10-OH** with pH. The red line represents a computer fit to the values following the Henderson-Hasselbalch equation.

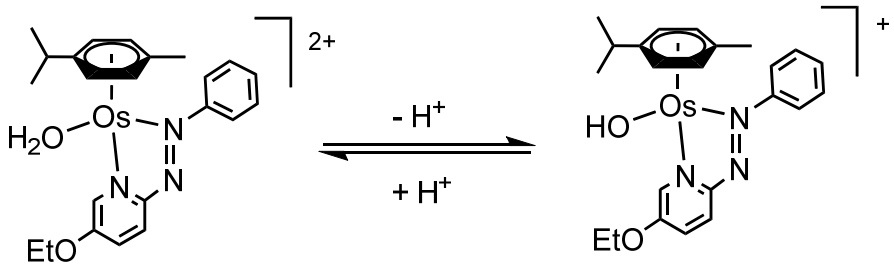

Scheme 6.3. Protonation and deprotonation of **10-OH** under acid and basic conditions, respectively.

6.3.2. Aqueous stability of 10-OH

6.3.2.1. ^{1}H NMR spectroscopy

The ^{1}H NMR spectrum of **10-OH** in D_2O (pH* 7.4) was recorded before and after 24 h incubation at 37 °C (see Figure 6.5). Complex **10-OH** is not entirely stable in aqueous media, giving rise to more than one unknown species. The peaks labelled in blue are protons belonging to **10-OH**. After incubation these peaks diminish in intensity and a new set of peaks are present labelled in red, most likely corresponding to free *p*-cym. Also present are several broad peaks denoted by ‡. The presence of a black insoluble precipitate was also noted after incubation.

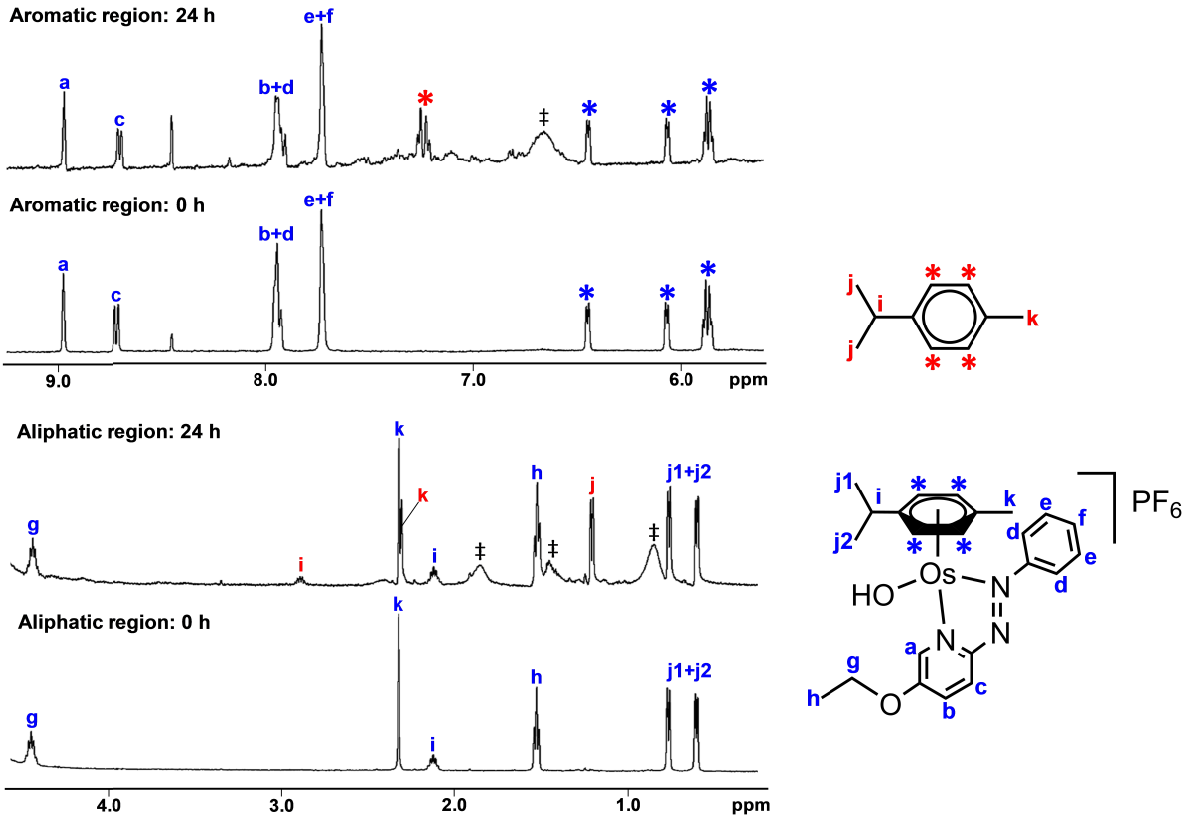

Figure 6.5. ^{1}H NMR spectra of **10-OH** (2mM) in D_2O (pH* 7.4) before and after 24 h incubation at 37 °C. Spectra were collected on a 600 MHz instrument.

6.3.2.2. HPLC

HPLC analysis was carried out for **10-OH** (1 mM) at pH 7.4 before and after 24 h incubation at 37 °C, shown in Figure 6.6. The samples were filtered before analysis and the presence of a black precipitate was noted again after the sample had been incubated. Due to presence of TFA in the HPLC mobile phase, **10-OH** will predominantly exist as the aqua species inside the column. Complex **10-OH** has a retention time of 12.68 min. Before incubation, a minor impurity is observable in the chromatogram with a retention time of 12.05 min. This is most likely due to reaction of **10-OH/OH$_2$** with MeCN in the mobile

phase. By assessing the integrals of the peaks, there was an estimated 62% loss of **10-OH** through degradation after the sample was incubated (the black precipitate accounts for approximately 58% and other peaks in the chromatogram account for approximately 4%).

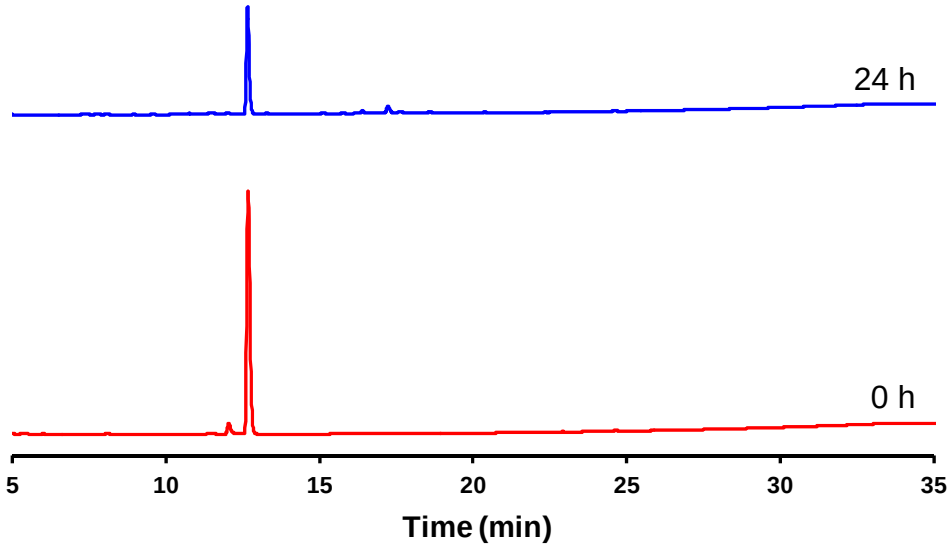

Figure 6.6. HPLC chromatograms of **10-OH** before and after 24 h incubation at 37 °C and pH 7.4 (254 nm wavelength of detection).

6.3.3. Reactivity of complexes with H_2O_2

6.3.3.1. UV-Vis spectroscopy

The reactivity of **8**, **10-OH** and **11** with H_2O_2 was explored using UV-Vis spectroscopy. Complexes (75 µM) were incubated at 37 °C and pH 7.4 with H_2O_2 (50 mol. equiv.). Figure 6.7 shows UV-Vis spectra of **8**, **10-OH** or **11** in the presence of H_2O_2 recorded every 2 min. A decline in the intensity of the complexes absorption bands is observed in each case. After the intensity of the

absorption bands is lost the bands continue to flatten out towards the baseline with respect to time, thus indicating decomposition of the complexes. After 30 min incubation, bubbles were observed in the cuvettes together with complete loss of colour of the solution. The rates of decomposition follow the trend **10-OH**>**8**>**11**.

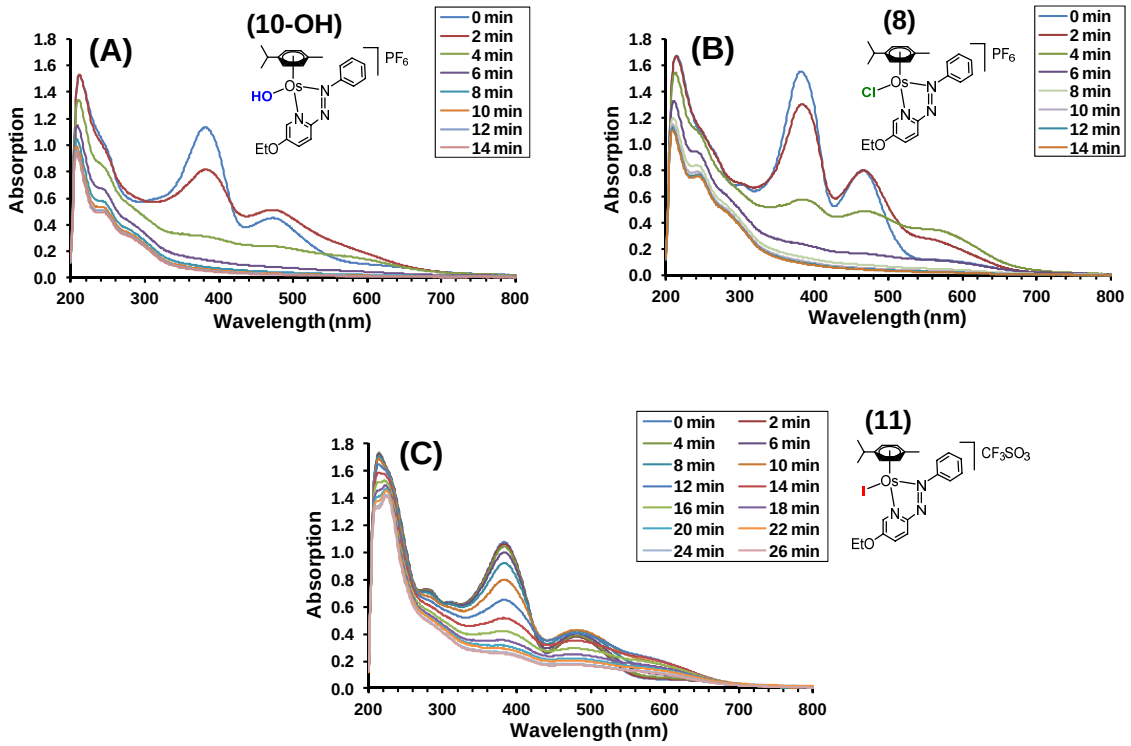

Figure 6.7. UV-Vis spectra showing the decomposition of; (A) **10-OH**, (B) **8**, and (C) **11**, in the presence of 50 mol. equiv. of H_2O_2 at pH 7.4 and 37 °C.

Further experiments were conducted with complexes in the presence of 100 mol. equiv. H_2O_2 in phosphate buffer solution using Quantifix® H_2O_2 semi-quantitative testing sticks to measure the presence of H_2O_2, as well as measuring the UV-Vis spectra. Figure 6.8 shows the spectra recorded for **10-**

OH, **8** and **11** after every 30 min for 2 h at 37 °C. Control studies included samples of the complexes incubated in the absence of H_2O_2. Table 6.1 shows the levels of H_2O_2 remaining after each 30 min intervals, including a control study of H_2O_2 with no added complex. All three complexes are stable over a 2 h period in the control studies. However, in the presence of H_2O_2 all three complexes show significant levels of decomposition within the first 30 min of exposure. Furthermore, H_2O_2 levels are depleted to 0 ppm within the initial 30 min of exposure time with all three complexes. In the control study where H_2O_2 is incubated without complexes, the level of H_2O_2 remains greater than 25 ppm throughout the entire 2 h period.

Table 6.1. Measurements of H_2O_2 levels for the reactions of **10-OH**, **8** and **11** with 100 mol. equiv. of H_2O_2 at pH 7.4 with 37 °C incubation. Measurements made using H_2O_2 semi-quantitative testing sticks.

	10-OH	**8**	**11**	**Control**
0 min	>25 ppm	>25 ppm	>25 ppm	>25 ppm
30 min	~0 ppm	~0 ppm	~0 ppm	>25 ppm
60 min	~0 ppm	~0 ppm	~0 ppm	>25 ppm
90 min	~0 ppm	~0 ppm	~0 ppm	>25 ppm
120 min	~0 ppm	~0 ppm	~0 ppm	>25 ppm

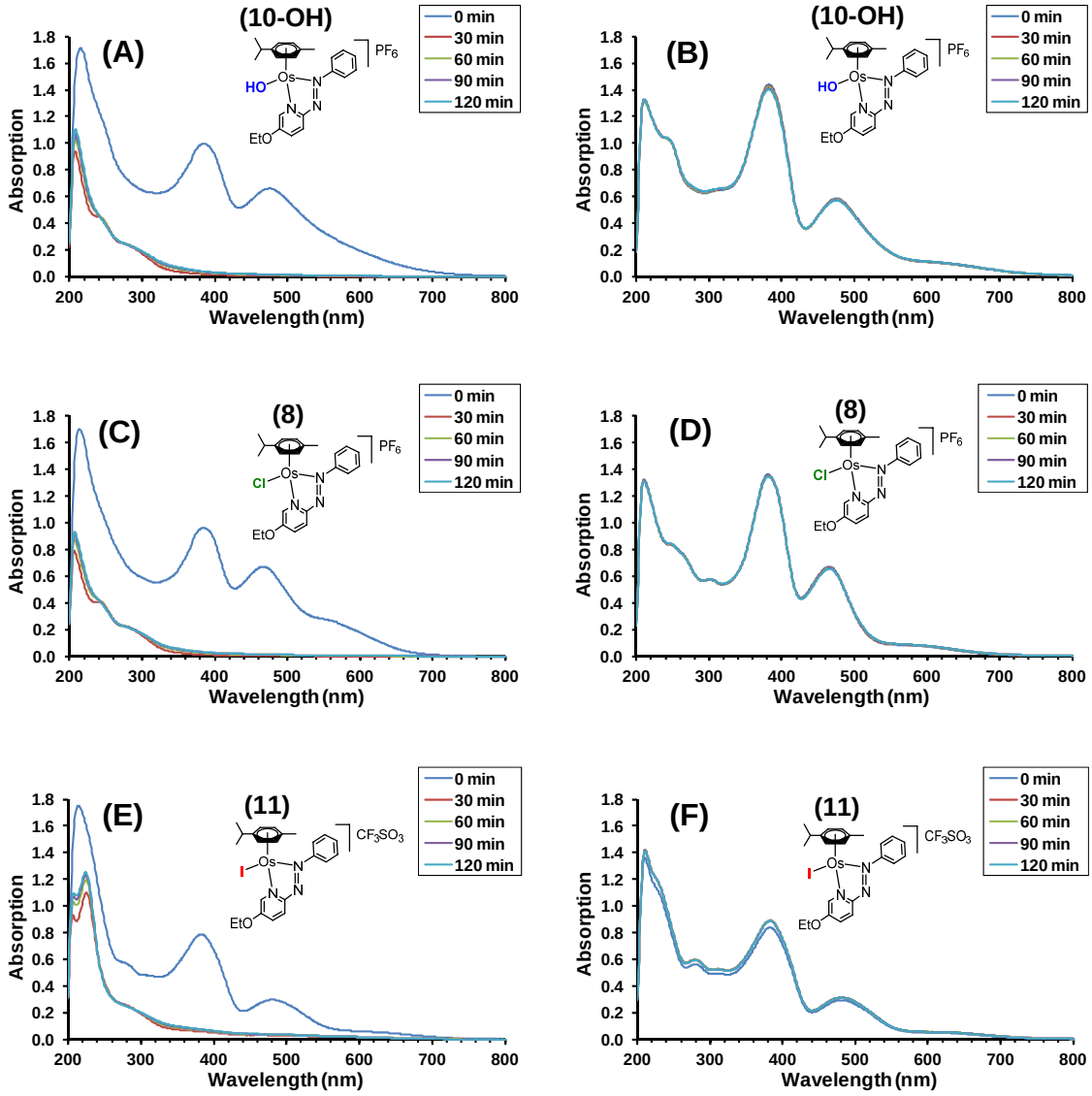

Figure 6.8. UV-Vis spectra of the reactions of complexes (75 µM) in the presence of 100 mol. equiv. of H_2O_2 at pH 7.4; (A) **10-OH**, (C) **8**, and (E) **11**, and control studies in the absence of H_2O_2; (B) **10-OH**, (D) **8**, and (F) **11**. Spectra were recorded every 30 min for 2 h with 37 °C incubation.

The same experiment was repeated as above but in the presence of 7.5% EtOH, which is known for its ability to quench HO· radicals.[37] Figure 6.9 shows

the variation in the UV-Vis spectra and Table 6.2 shows how H_2O_2 levels vary over the 2 h incubation period.

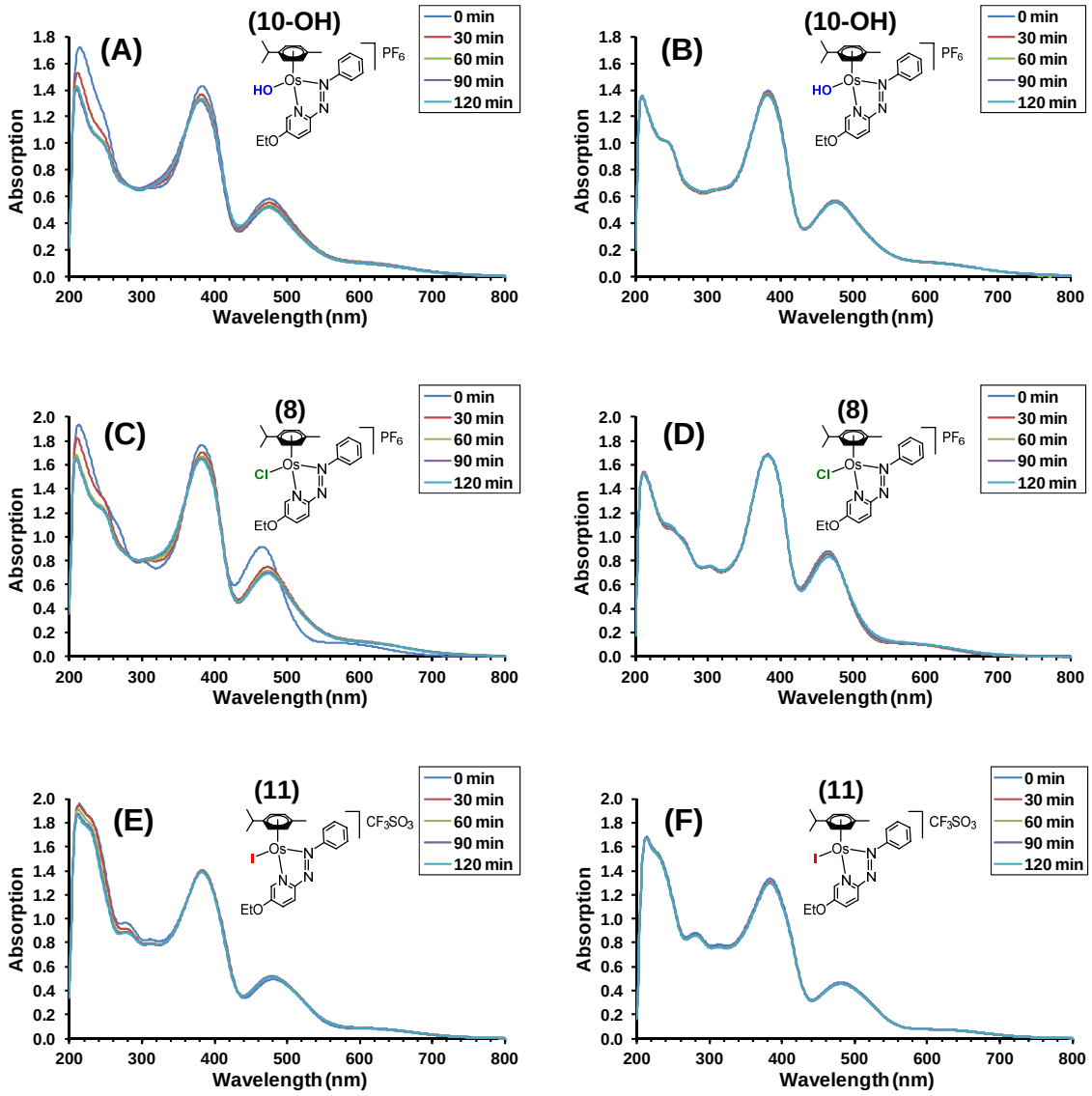

Figure 6.9. UV-vis spectra showing the reactions of complexes (75 μM) in the presence of 100 mol. equiv. of H_2O_2 and 7.5% ethanol at pH 7.4; (A) **10-OH**, (C) **8**, and (E) **11**, and control studies in the absence of H_2O_2; (B) **10-OH**, (D) **8**, and (F) **11**. Spectra were recorded every 30 min for 2 h after incubation at 37 °C.

Table 6.2. Measurements of H_2O_2 levels for the reactions of **10-OH**, **8** and **11** with 100 mol. equiv. of H_2O_2 in phosphate buffer solution (7.5% ethanol) at 37 °C. Measurements made using H_2O_2 semi-quantitative testing sticks.

	10-OH	**8**	**11**	**Control**
0 min	>25 ppm	>25 ppm	>25 ppm	>25 ppm
30 min	>25 ppm	>25 ppm	>25 ppm	>25 ppm
60 min	~25 ppm	~25 ppm	>25 ppm	>25 ppm
90 min	~2 ppm	~5 ppm	>25 ppm	>25 ppm
120 min	~0 ppm	~0 ppm	~25 ppm	>25 ppm

All three complexes are stable in the control experiments and no drastic changes in the UV-Vis spectra were observed in the presence of H_2O_2 when EtOH was added. Moreover, the complexes produce a much slower decline in H_2O_2 levels in the presence of EtOH than in its absence. The extent of degradation of H_2O_2 produced by the complexes follows the trend **10-OH**>**8**>**11**.

6.3.3.2. ^{1}H NMR spectroscopy

A kinetic ^{1}H NMR study was carried out for the reaction between **10-OH** and H_2O_2 (10 mol. equiv.) in phosphate buffered D_2O at 5 °C. The spectra in Figure 6.10 show that the peaks of **10-OH** broaden and disappear within 90 min. A dark brown precipitate was observed in the NMR tube after the experiment. The line broadening may be a result of increasingly poorer shimming of the sample over time. The disappearance of **10-OH** peaks suggest that it decomposes,

however, no other peaks corresponding to its break-down products were observed in the spectra.

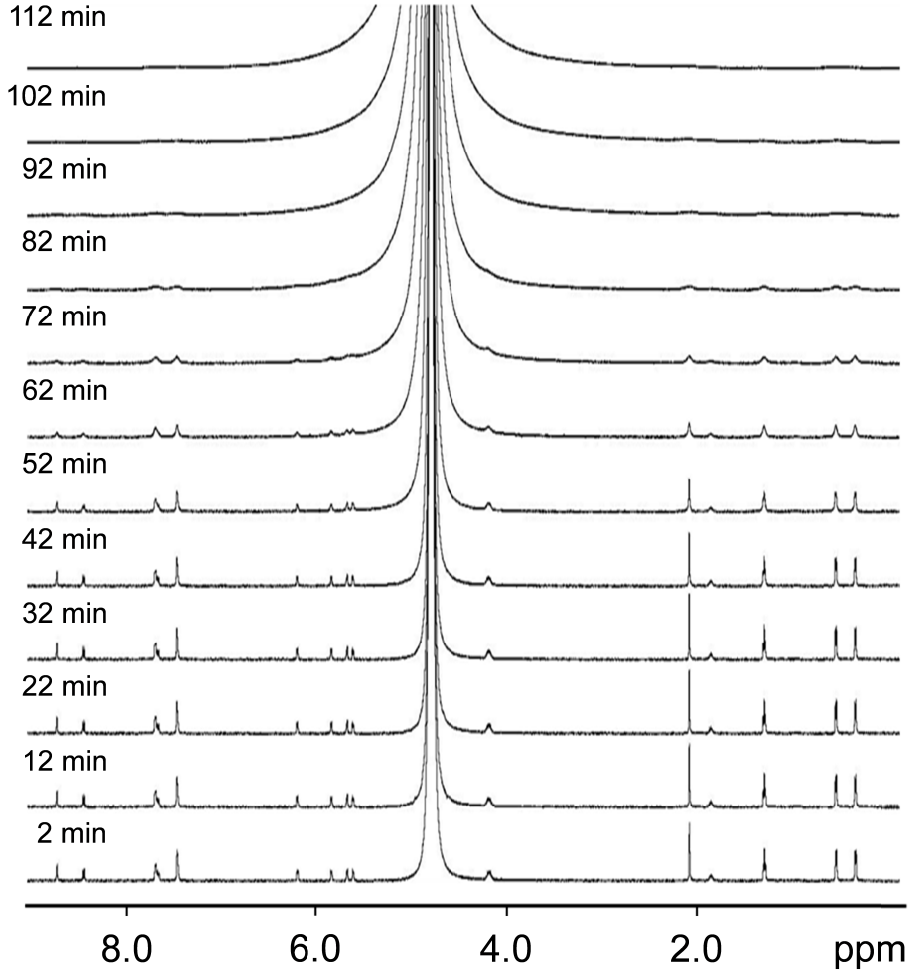

Figure 6.10. ^{1}H NMR spectra for the reaction between **10-OH** and 10 mol. equiv. of H_2O_2 in D_2O (pH* 7.4) at 5 °C. Spectra obtained every 10 min on a 600 MHz instrument.

6.3.3.3. Mass spectrometry

Complexes **8** and **11** were incubated with H_2O_2 (10 mol. equiv.) for 20 min at 37 °C then analysed by mass spectrometry. For complex **8**, the spectrum shows a peak corresponding to unreacted complex (**8**-PF_6), $C_{23}H_{27}ClN_3OOs$: m/z

588.0, and a peak corresponding to the hydroxido-adduct (**10-OH**-PF_6), $C_{23}H_{28}N_3O_2Os$: m/z 570.1, where the chloride ligand is replaced by hydroxide. Also an unidentified peak was observed with a m/z value of 604.0 (+16 units greater than **8**-PF_6). Similarly, the spectrum for **11** showed the following peaks; $C_{23}H_{27}IN_3OOs$: m/z 680.0 (**11**-CF_3SO_3), $C_{23}H_{28}N_3O_2Os$: m/z 570.1 (**11-OH**-CF_3SO_3), and an unidentified peak with a m/z value of 696.0 (+16 units greater than **11**-CF_3SO_3).

6.3.3.4. Detection of generated free radicals by EPR spectroscopy

The ability of **8**, **10-OH** and **11** to generate free radicals from H_2O_2 was explored using Electron Paramagnetic Resonance (EPR) Spectroscopy, utilising 5-diethoxyphosphoryl-5-methyl-1-pyrroline *N*-oxide (DEPMPO) as a spin trap. As shown in Scheme 6.4, DEPMPO is capable of trapping HO· radicals yielding an 8-peak spectrum (DEPMPO-OH),[38] O_2^{-}· radicals yielding a 12-peak spectrum (DEPMPO-OOH),[38-41] and H· radicals yielding a 16-peak spectrum (DEPMPO-H).[42] A sample of **10-OH** (1 mM) was prepared with H_2O_2 (10 mol. equiv.) and DEPMPO (6 mol. equiv.) at pH 7.4 and the EPR spectrum was recorded (Figure 6.11). The observed spectrum was an 8-peak signal corresponding to DEPMPO-OH (trapped HO· radicals).

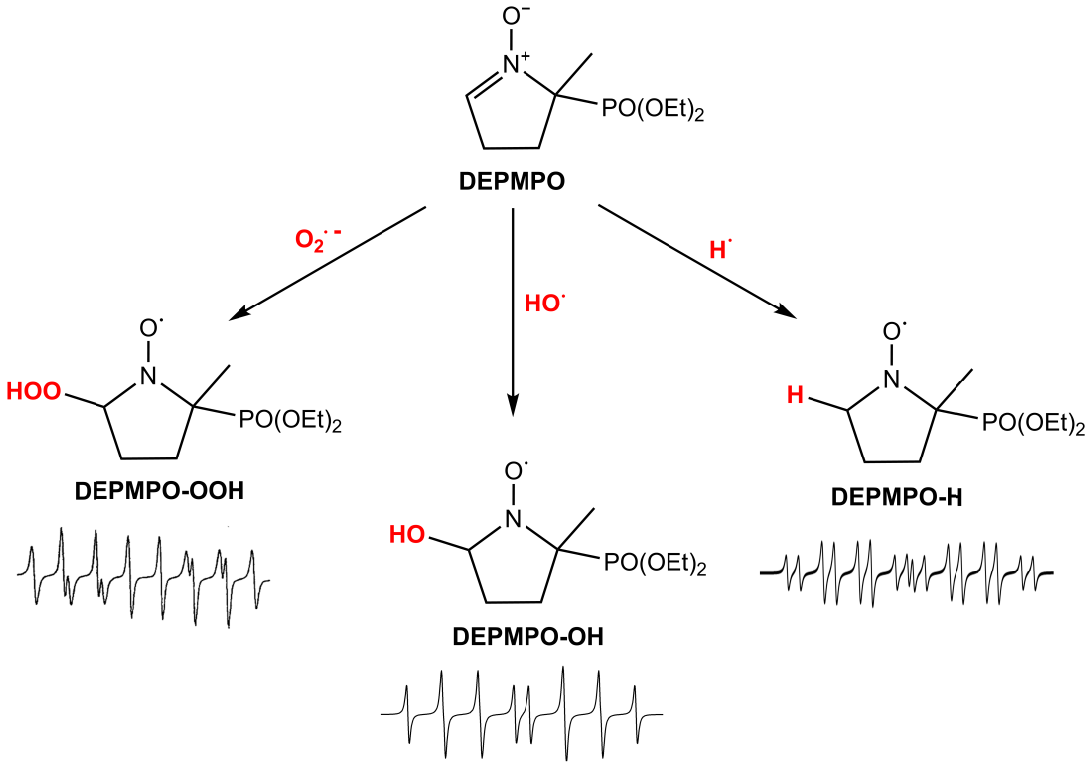

Scheme 6.4. The structure of DEPMPO and the structures of DEPMPO-OOH (formed after trapping $O_2^{\cdot -}$ radicals), DEPMPO-OH (formed after trapping HO· radicals), and DEPMPO-H (formed after trapping H· radicals). Computer simulated EPR spectra show the appearance of the 12-peak, 8-peak and 16-peak signals for DEPMPO-OOH, DEPMPO-OH and DEPMPO-H, respectively.

A large accumulation of bubbles in the EPR tube was also observed (Figure 6.12). When the experiment was repeated with the addition of two drops of EtOH the signal was significantly reduced as EtOH scavenges HO· radicals, preventing formation of DEPMPO-OH.[36] Two control studies were also carried out; one in the absence of H_2O_2, and the other in the absence of **10-OH**. Both showed no EPR signal, hence proving that the generation of HO· radicals only occur when **10-OH** and H_2O_2 are combined.

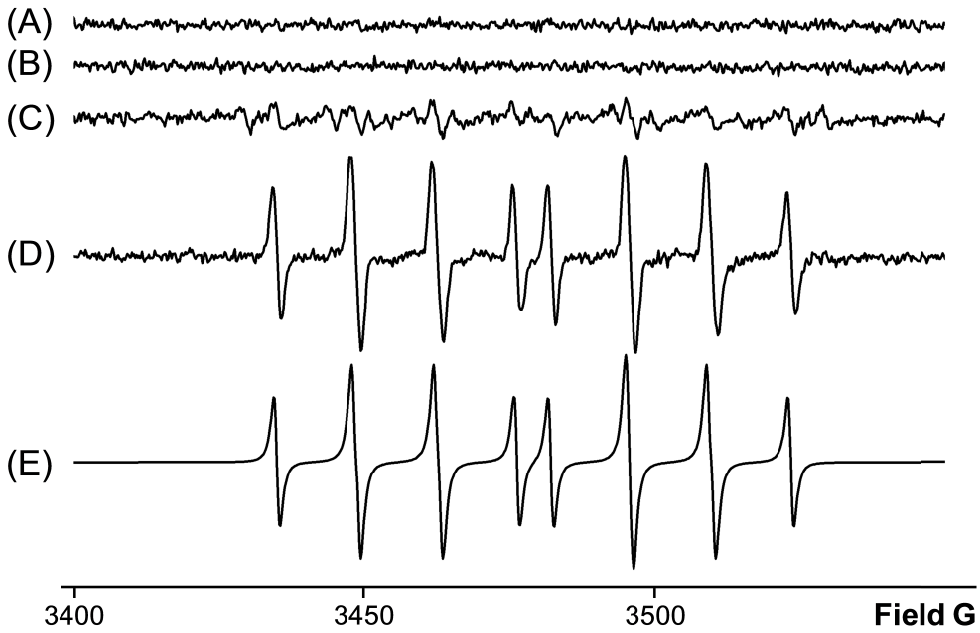

Figure 6.11. EPR spectra of samples containing 1 mM **10-OH**, 6 mM DEPMPO and 10 mM H_2O_2 at pH 7.4. (A) H_2O_2 + DEPMPO; (B) **10-OH** + DEPMPO; (C) **10-OH** + H_2O_2 + DEPMPO + EtOH; (D) **10-OH** + H_2O_2 + DEPMPO; (E) Simulated spectrum for DEPMPO-OH. Spectra were recorded within 30 min of sample preparation.

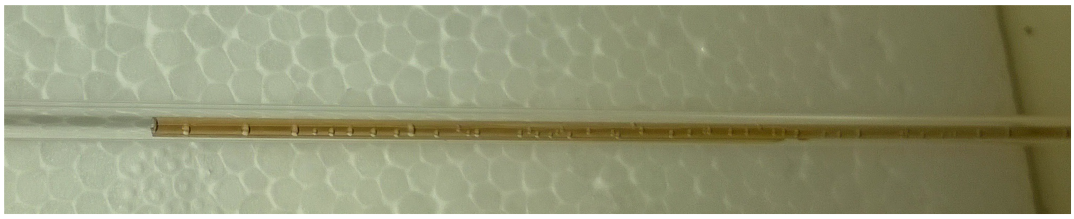

Figure 6.12. Bubbles produced in the reaction between **10-OH** and H_2O_2.

The ability to generate HO· from H_2O_2 radicals was compared for complexes **8**, **10-OH** and **11**. Complexes **8** and **11** have much poorer solubility in water than **10-OH** so the complexes were prepared in phosphate buffer solution with 50% DMF and the same quantities of DEPMPO and H_2O_2 as used previously. The

EPR spectra in Figure 6.13 shows that the 8-peak spectrum produced by **10-OH** is reproducible in 50% DMF. Complexes **8** and **11**, however, produce HO· radicals less effectively than **10-OH** as shown by the significantly weaker signal for the 8-peak spectrum of DEPMPO-OH. Another secondary species also appears to be present in the spectra. A simulated spectrum of DEPMPO-H (produced by trapping H· radicals) was generated and shares some resemblance to the secondary signals produced by **8** and **11**.

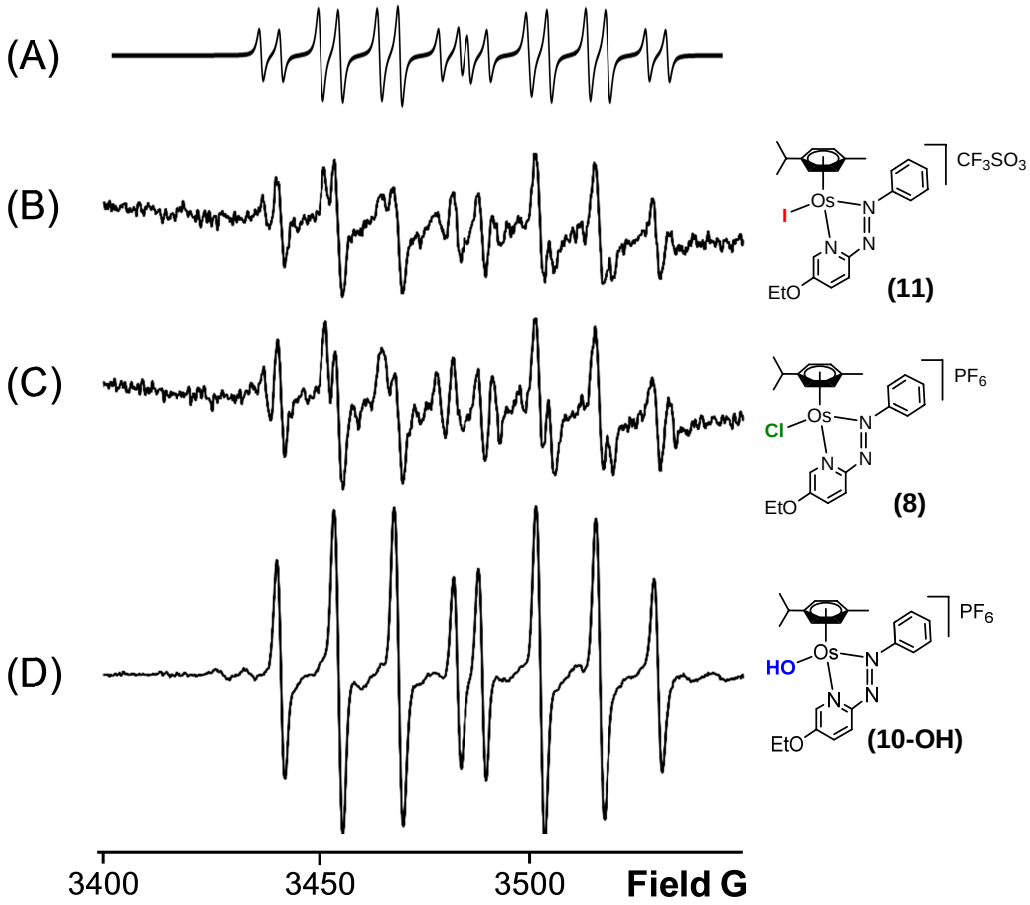

Figure 6.13. EPR spectra for samples containing 1 mM complex, 6 mM DEPMPO and 10 mM H_2O_2 in 75 mM Phospate buffer solution with 50% DMF. (A) Simulated spectrum for DEPMPO-H. (B) **11** + H_2O_2 + DEPMPO; (C) **8** + H_2O_2 + DEPMPO; (D) **10-OH** + H_2O_2 + DEPMPO. Spectra were recorded within 30 min of sample preparation.

6.3.3.5. Lysozyme cleavage assay

Complexes **8**, **10-OH** and **11** were tested for their ability to cleave lysozyme *via* the production of HO· radicals generated from H_2O_2. Lysozyme (75 µM) was incubated with the complexes (10 µM) and H_2O_2 (10 mM) at 37 °C and pH 7.4 for 2 h. SDS-PAGE electrophoresis was used to analyse hydrolysis of the protein. The gel shown in Figure 6.14 shows smearing after the incubation of lysozyme with H_2O_2 and complexes, indicating that they all cause break-down of the lysozyme protein. ImageJ software was used to measure the intensity of coomasie blue stain and quantify the ratios of lysozyme protein left intact after incubation. Complexes **8** and **10-OH** degraded significantly more lysozyme (19±5% and 22±9% of unreacted protein remained, respectively), in comparison to **11** (66±8% unreacted protein).

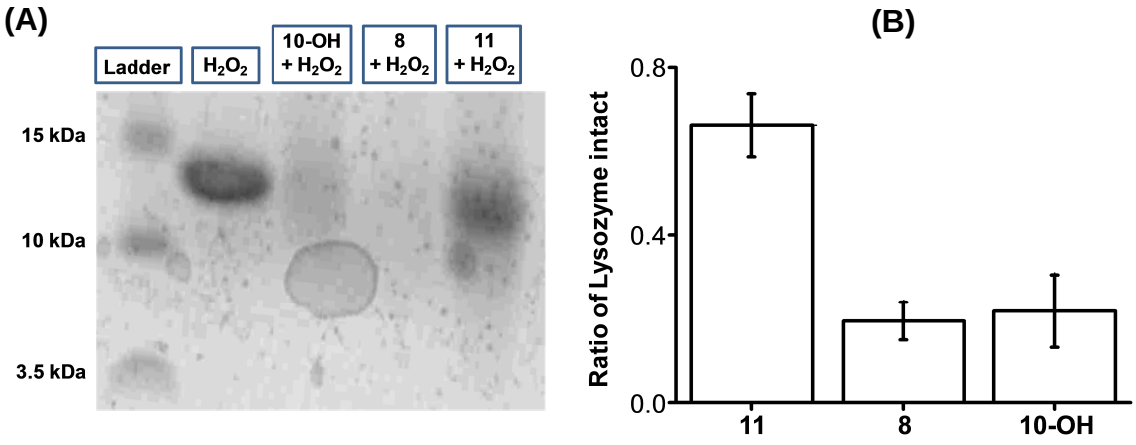

Figure 6.14. (A) Gel electrophoresis plate of the degradation of lysozyme when incubated with; H_2O_2, **10-OH** + H_2O_2, **8** + H_2O_2, and **11** + H_2O_2, at 37 °C and pH 7.4. (B) Ratios of lysozyme left intact after incubation with H_2O_2 in combination with **10-OH**, **8** or **11**, determined by the measured intensities of coomaise blue stain.

Furthermore, lysozyme degradation was studied with **8**, **10-OH** and **11** in varying concentrations of H_2O_2. As expected, no lysozyme degradation was observed in the absence of H_2O_2. Moderate lysozyme degradation was observed when in the presence of 0.1 and 1 mM H_2O_2 (20-40%), but only when the concentration of H_2O_2 was raised to 10 mM was significant lysozyme degradation observed (>70%), and with the following order of complex reactivity; **10-OH**~**8**>**11** (Figure 6.15).

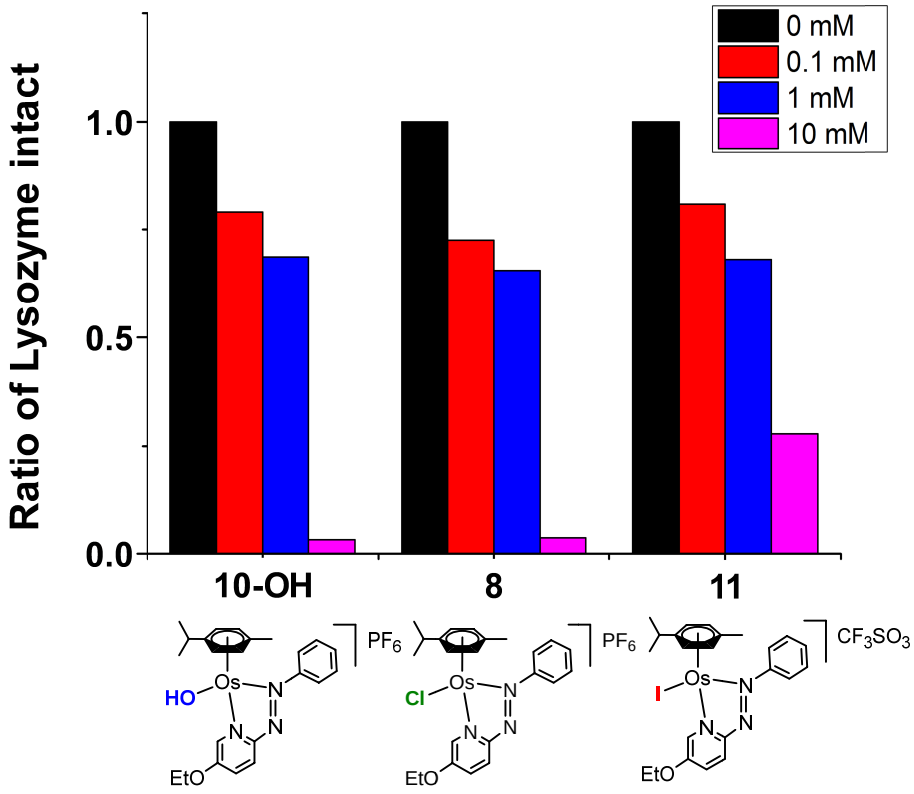

Figure 6.15. Ratios of lysozyme left intact after 2 h incubation at 37 ºC with **10-OH**, **8** or **11** at different concentrations of H_2O_2 (0, 0.1, 1, and 10 mM), determined by the measured intensities of Coomassie blue stain.

6.3.4. Binding of complexes to biological targets

In this section, the binding capabilities of **10-OH**, **11** and **FY026** were studied with 9-ethylguanine (9-EtG), N-acetyl-*L*-cysteine (NAC), and glutathione in its reduced (GSH) and oxidised (GSSG) forms. NAC is structurally similar to *L*-cysteine with an acetyl group protecting its reactive primary amine moiety. It provides a biomolecule model to explore the complexes ability to bind to thiol containing cysteine residues which are found extensively in cellular proteins. The binding was studied *via* HPLC and LC-MS. Since **10-OH** can be made into solutions of concentration >1 mM its binding was also studied by ^{1}H NMR.

6.3.4.1. ^{1}H NMR Spectroscopy

The ability of **10-OH** (1 mM) to bind to 9-EtG, GSH, GSSG and NAC (1 mol. equiv.) was studied in phosphate buffered D_2O at 37 °C. A ^{1}H NMR spectrum was recorded before and after 24 h incubation with the different biomolecule models. When **10-OH** was incubated with 9-EtG no binding was observed in the spectrum (Figure 6.16). The only peaks observed after incubation were the original peaks belonging to **10-OH** and 9-EtG, and peaks belonging to *p*-cym which are a product of **10-OH** degradation (as shown in Section **6.3.2**). After incubation with NAC, various species were observed in the ^{1}H NMR spectrum (Figure 6.16). The vast majority of **10-OH** binds with NAC to form a thiolato adduct (**10-NAC**, as shown in Section **6.3.4.2**), where binding occurs between Os(II) and the sulfur atom of the NAC thiol side chain, replacing the monodentate hydroxide ligand. Interestingly, since both NAC and **10-OH** have

chiral centres, **10-NAC** has two diastereomers and therefore two sets of peaks were observed in some instances. No free NAC was observed after 24 h incubation, however un-reacted **10-OH**, *p*-cym peaks corresponding to complex degradation, and oxidised NAC were observed. NAC has a tendency to oxidise in aerobic conditions forming a S-S bridged disulfide species (Scheme 6.5.), which gave rise to a set of peaks (marked in yellow in Figure 6.16).[43] In a control study, NAC was incubated in the absence of **10-OH** for 24 h and over 50% conversion to oxidised NAC was observed.

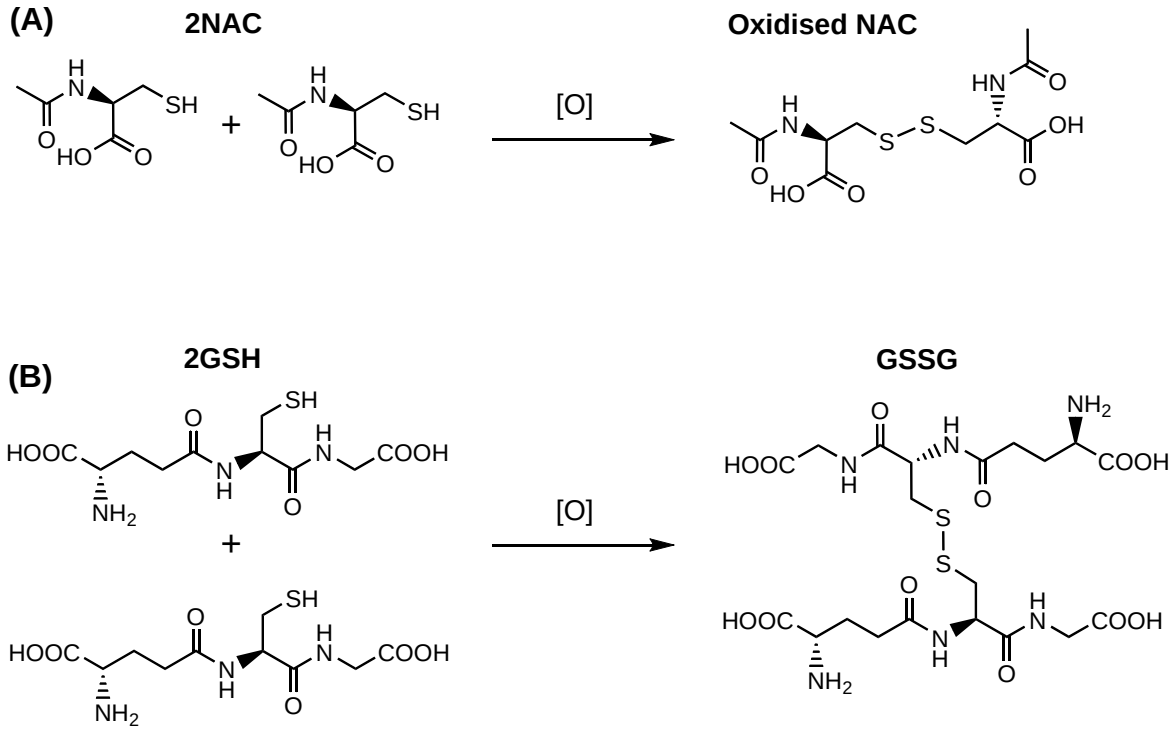

Scheme 6.5. Oxidation of (A) NAC, and (B) GSH in aerobic conditions involving the formation of S-S bridged dimeric disulfide species.

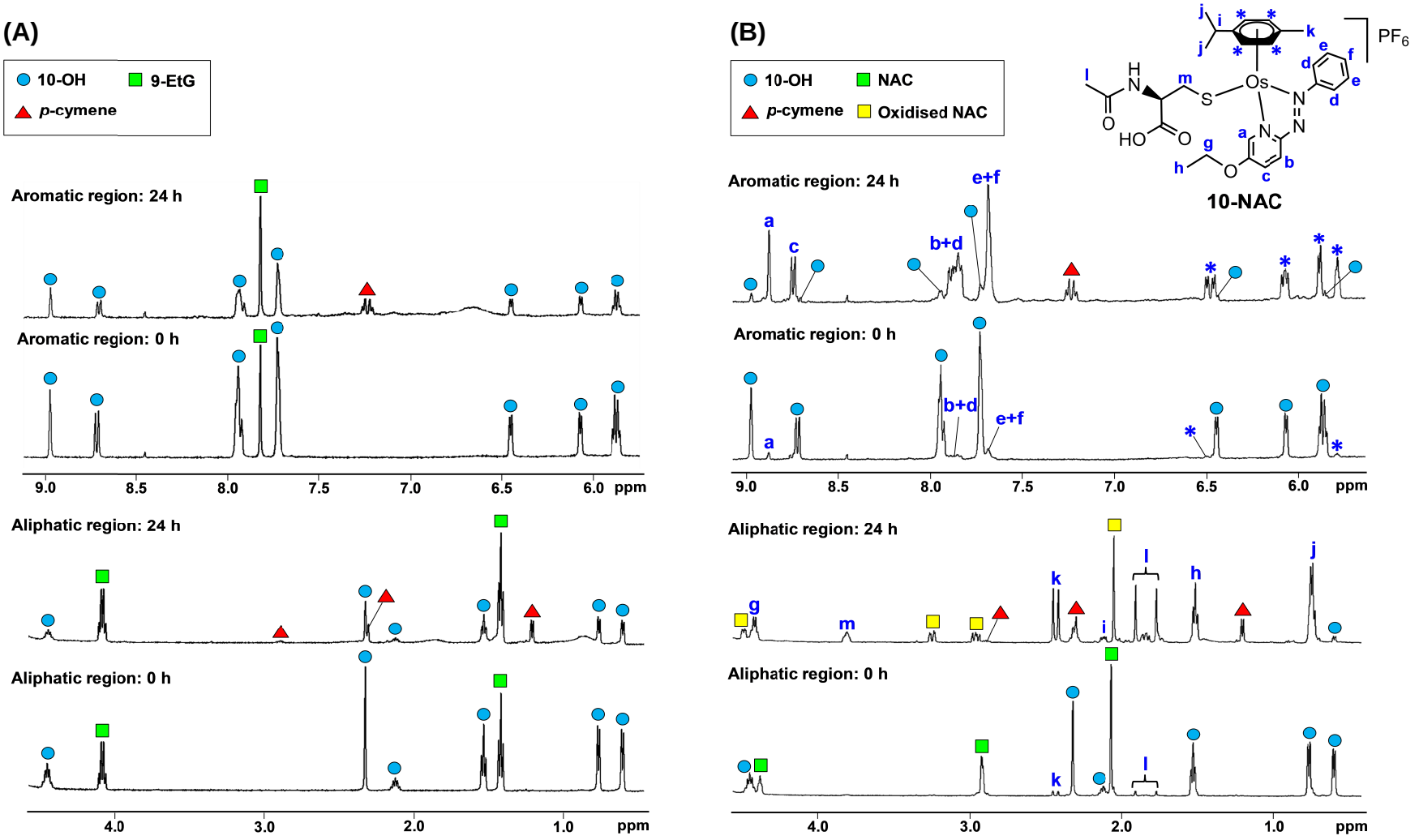

Figure 6.16. ^{1}H NMR spectra of **10-OH** (1mM) before and after 24 h incubation at 37 °C with; (A) 1 mM of 9-EtG, and (B) 1 mM of NAC. Samples were prepared in D_2O (pH* 7.4). Spectra were collected on a 500 or 600 MHz instrument.

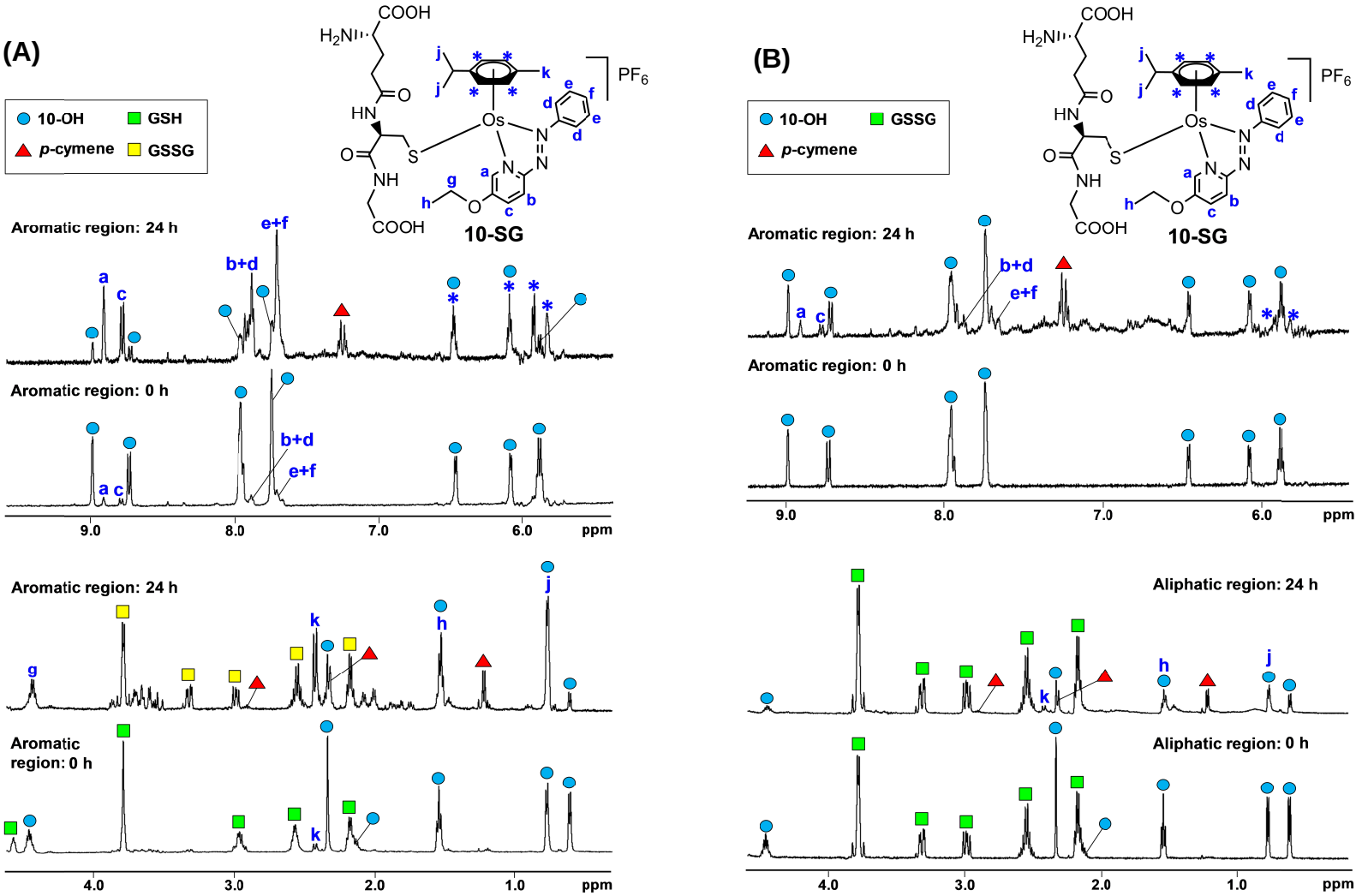

Figure 6.17. ^{1}H NMR spectra of **10-OH** (1mM) before and after 24 h incubation at 37 °C with; (A) 1 mM of GSH, and (B) 1 mM of GSSG. Samples were prepared in D_2O (pH* 7.4). Spectra were collected on a 500 or 600 MHz instrument.

Similarly, the incubation of **10-OH** with GSH resulted in the formation of a thiolato-adduct (**10-SG**) as shown in Section **6.3.4.2**, also having two diastereomers due to the chiral centre in GSH (Figure 6.17). Likewise, GSH also oxidises in aerobic conditions to form a bridged disulfide species (GSSG, Scheme 6.5), which was observable in the ^{1}H NMR spectrum. A control study where GSH was incubated by itself showed 100% conversion to GSSG after 24 h. Also observable are peaks belonging to un-reacted **10-OH** and *p*-cym peaks. Interestingly, upon incubation with GSSG, **10-OH** was also able to form the **10-SG** adduct (Figure 6.17), but to a much lesser extent. Due to the presence of multiple species and precipitation occurring in the NMR tubes, it proved difficult to identify all of the peaks (particularly for the reaction between **10-OH** and GSH). To overcome this problem the reactions were monitored by HPLC.

6.3.4.2. HPLC/LC-MS

The binding of complex **10-OH** with NAC, GSH and GSSG was also explored using HPLC. Complex **10-OH** (1 mM) was incubated with NAC, GSH or GSSG (1 mol. equiv.) at 37 ºC and pH 7.4 for 24 h, and samples were analysed before and after incubation (Figure 6.18). Furthermore, samples were analysed by LC-MS to identify the species in the chromatograms and the mass spectroscopy peaks are shown in Figure 6.21, observed as positively charged complexes without their counter ions (PF_6^- or $CF_3SO_3^-$). Remarkably, when **10-OH** was incubated with NAC and GSH, not only were thiolato-adducts **10-NAC** and **10-SG** observed but also sulfenato-adducts, **10-NAC(O)** and **10-SOG**, likely

occurring due to oxidation of sulfur in aerobic conditions. Moreover, incubating **10-OH** with GSSG was shown again to produce the **10-SG** adduct in small quantities.

For comparison, the binding capabilities of **11** and **FY026** were also analysed to determine whether the presence of a stable Os-I bond could block the binding to biological targets. Because of their poor solubility in aqueous media samples were prepared with 75 μM of complex. When **11** and **FY026** were incubated with 1 mol. equiv. of either NAC, GSH or GSSG no substrate binding was observed (Figure 6.19). Interestingly however, formation of the hydroxido species (**11-OH** and **FY026-OH**) was observed. As the HPLC method was carried out with 0.1% TFA ion-pairing agent in the mobile phase, both **10-OH** and **11-OH** lose their PF_6^- and $CF_3SO_3^-$ counter-ions in exchange for $CF_3CO_2^-$. Hence, **10-OH** and **11-OH** are observed as the same species in HPLC and exhibit identical retention times. The extent of complex hydrolysis caused by each biological target follows the order GSH>NAC>GSSG, where GSH produced the greatest conversion to the hydroxido-adduct. Furthermore, **FY026** was less prone to hydrolysis than **11**. In a control study where **11** and **FY026** were incubated in the absence of a substrate in phosphate buffer solution, complexes remained stable over 24 h with <1% hydroxide-adducts generated.

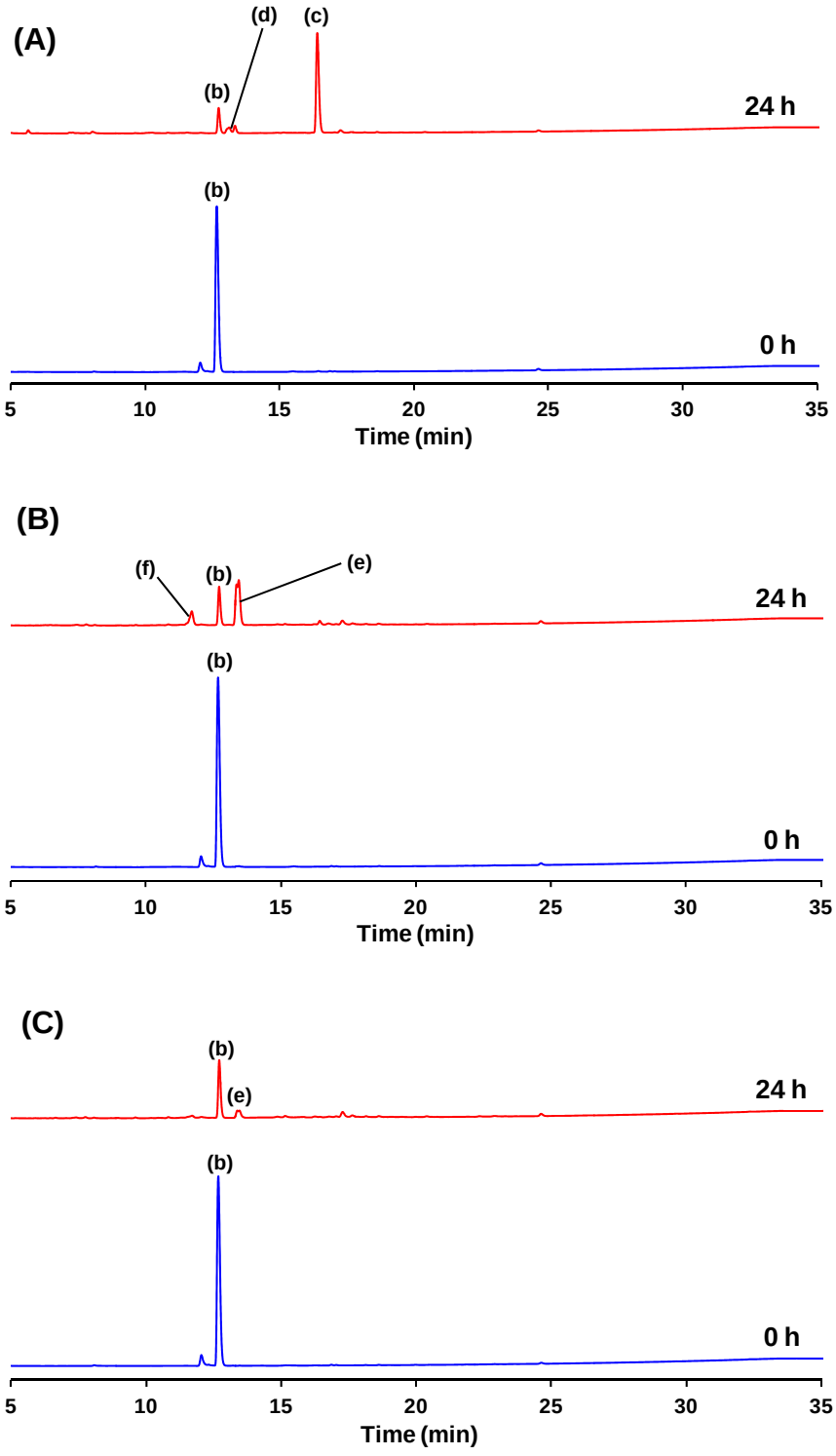

Figure 6.18. HPLC chromatograms (254 nm wavelength of detection) of **10-OH** (1 mM) before and after 24 h incubation at 37 °C with; (A) 1 mM NAC, (B) 1mM GSH, and (C) 1 mM GSSG. Species b to f are shown in Figure 6.21 with their mass spectrometry peaks. Assignments: (b) **10-OH**, (c) **10-NAC**, (d) **10-NAC(O)**, (e) **10-SG**, (f) **10-SOG**.

When **11** and **FY026** were incubated with 100 mol. equiv. of NAC or GSH (7.5 mM), the formation of thiolato-adducts **11-SG**, **11-NAC**, **FY026-SG** and **FY026-NAC** was observed (Figure 6.20). Complex **11** was the most reactive, completely binding to NAC and GSH (accompanied by the disappearance of **11**) after 3 h incubation. Complex **FY026** binds more slowly and was entirely consumed after 12 h and 6 h of incubation for NAC and GSH, respectively. Moreover, both **11** and **FY026** were also capable of forming sulfenato-adducts, **11-SOG**, **11-NAC(O)**, **FY026-SOG** and **FY026-NAC(O)**, with small peaks observable in HPLC chromatograms. Unlike **10-OH**, complexes **11** and **FY026** were not capable of forming adducts thiolato-adducts upon incubation with GSSG. Increasing the amount of GSSG from 1 to 100 mol. equiv. produced a greater extent of hydrolysis, but no thiolato-adduct was observed. All samples incubated for 24 h were further analysed by LC-MS and all mass-spectrometry peaks of the species are also shown in Figure 6.21. Table 6.3 summarises all of the species identified by HPLC and LC-MS.

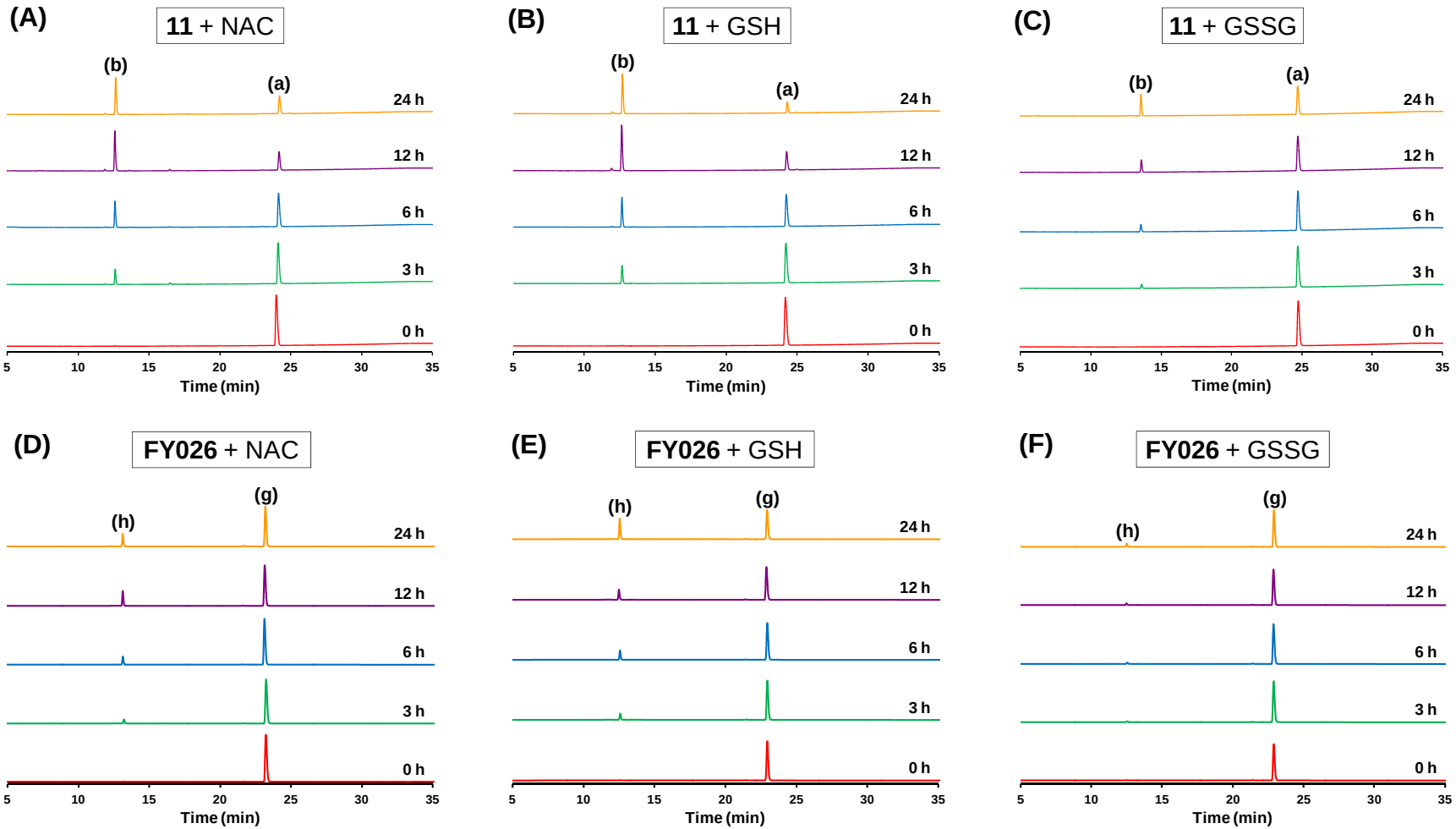

Figure 6.19. HPLC chromatograms of **11** and **FY026** (75 µM) after incubation with 1 mol. equiv. NAC, GSH or GSSG for 0, 3, 6, 12 and 24 h at 37 °C and pH 7.4. (A) **11** with NAC. (B) **11** with GSH. (C) **11** with GSSG. (D) **FY026** with NAC. (E) **FY026** with GSH. (F) **FY026** with GSSG. The wavelengths of detection used for **11** and **FY026** were 254 and 610 nm respectively. Assignments of (a), (b), (g) and (h) are shown in Figure 6.21 and Table 6.3.

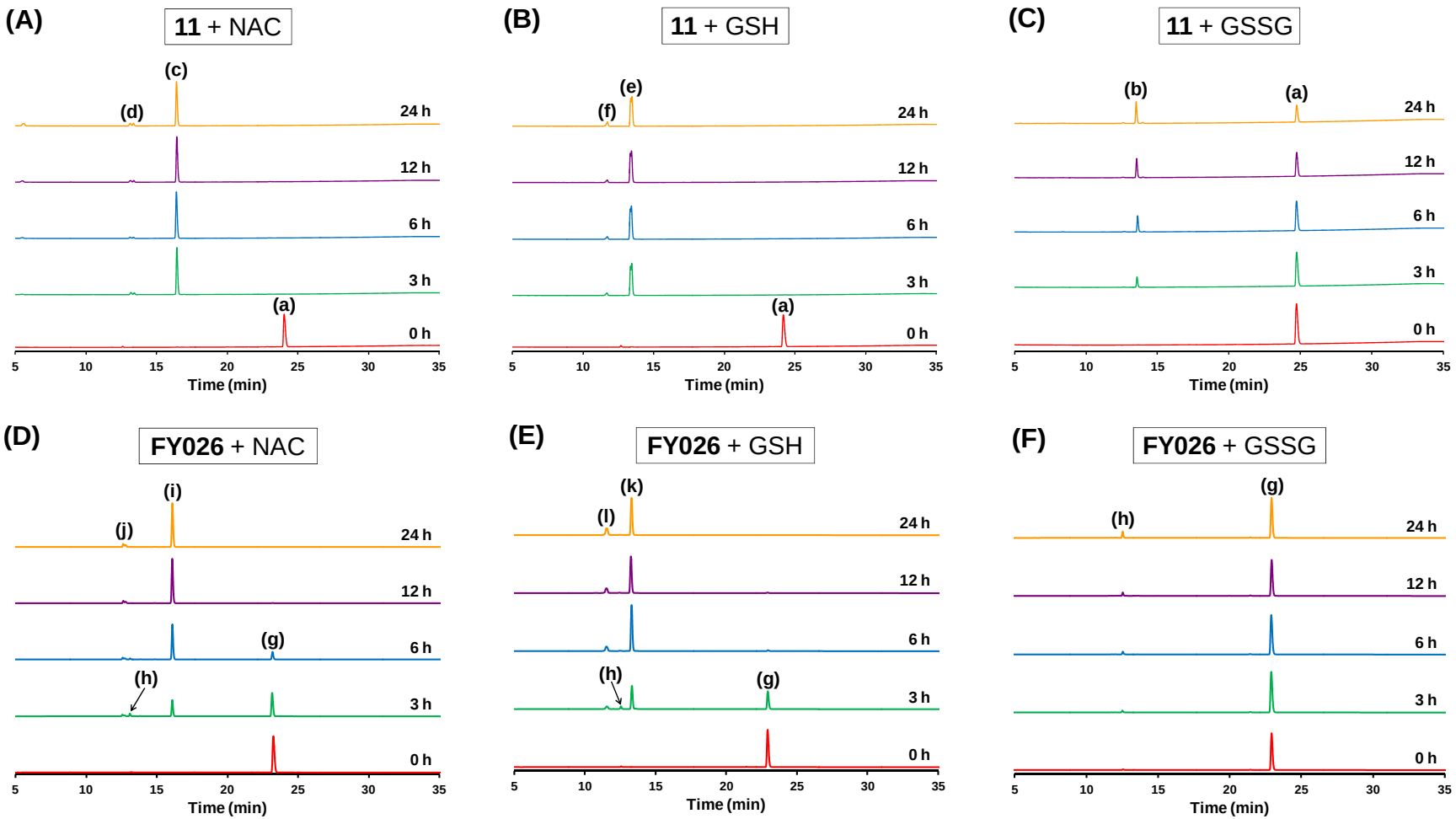

Figure 6.20. HPLC chromatograms of **11** and **FY026** (75 μM) after incubation with 100 mol. equiv. NAC, GSH or GSSG for 0, 3, 6, 12 and 24 h at 37 °C and pH 7.4. (A) **11** with NAC. (B) **11** with GSH. (C) **11** with GSSG. (D) **FY026** with NAC. (E) **FY026** with GSH. (F) **FY026** with GSSG. The wavelengths of detection used for **11** and **FY026** were 254 and 610 nm respectively. Assignments of (a)-(l) are shown in Figure 6.21 and Table 6.3.

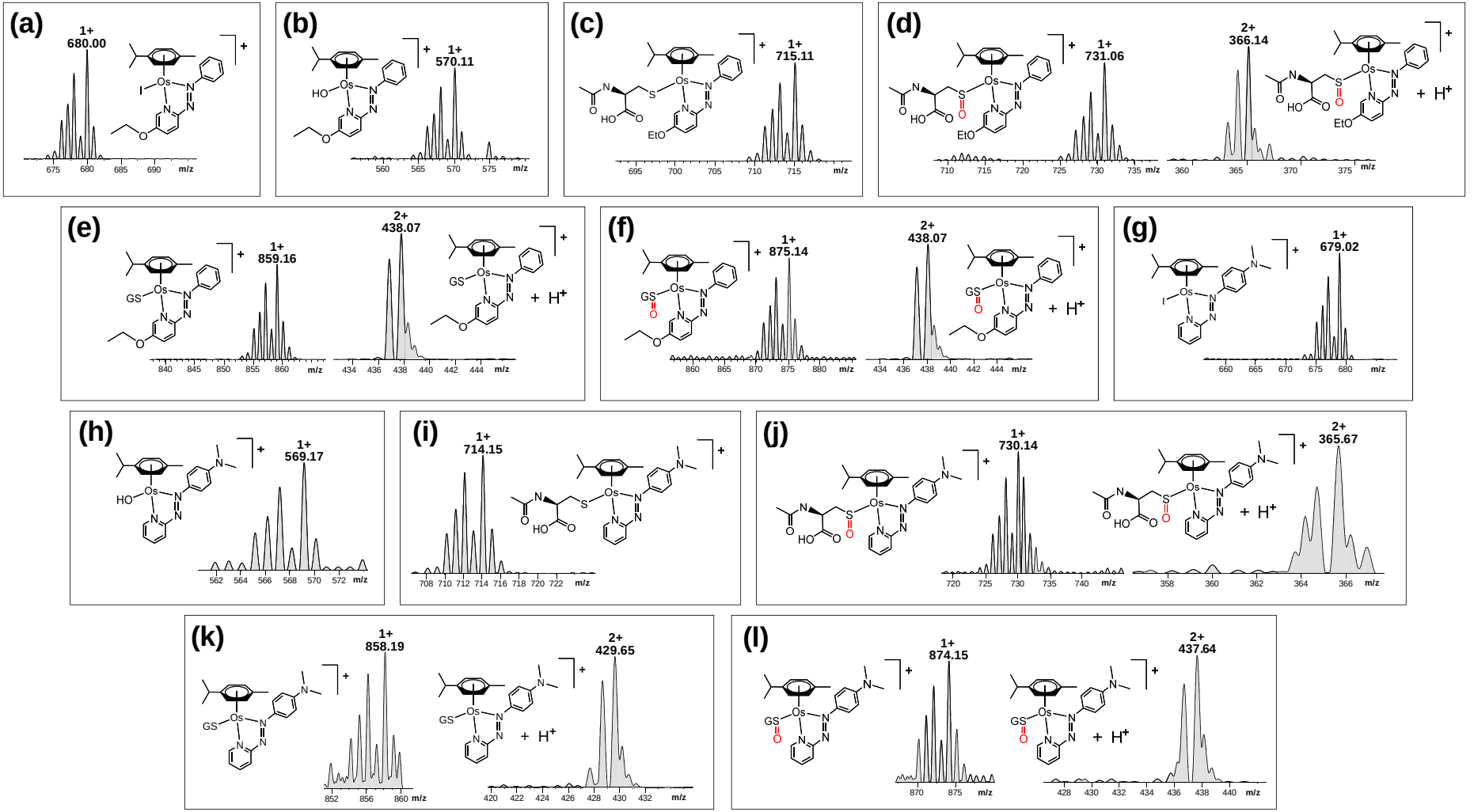

Figure 6.21. LC-MS data showing all the species found in the HPLC studies for **10-OH**, **11** and **FY026** when incubated with NAC, GSH and GSSG. All mass spectrometry peaks were observed as positively-charged ions without their counter ions (PF_6^- or $CF_3SO_3^-$).

Table 6.3. All of the species identified by HPLC/LC-MS and their molecular formulas, calculated and observed m/z values, and HPLC retention times

Assignment	Species	Molecular formula	Calculated m/z	Observed m/z	HPLC retention (min)
(a)	**11**(-CF_3SO_3)	$C_{23}H_{27}IN_3OOs^+$	680.08	680.00	24.05
(b)	**10-OH**(-PF_6) or **11-OH**(-CF_3SO_3)	$C_{23}H_{28}N_3O_2Os^+$	570.18	570.11	12.61
(c)	**10-NAC**(-PF_6) or **11-NAC**(-CF_3SO_3)	$C_{28}H_{35}N_4O_4OsS^+$	715.20	715.11	16.39
(d)	**10-NAC(O)**(-PF_6) or **11-NAC(O)**(-CF_3SO_3)	$C_{28}H_{35}N_4O_5OsS^+$	731.19	731.06	13.25
	10-NAC(O)(-PF_6+H^+) or **11-NAC(O)**(-CF_3SO_3+H^+)	$C_{28}H_{36}N_4O_5OsS^{2+}$	366.10	366.14	
(e)	**10-SG**(-PF_6) or **11-SG** (-CF_3SO_3)	$C_{33}H_{43}N_6O_7OsS^+$	859.25	859.16	13.38
	10-SG(-PF_6+H^+) or **11-SG** (-CF_3SO_3+H^+)	$C_{33}H_{44}N_6O_7OsS^{2+}$	430.13	438.07	
(f)	**10-SOG**(-PF_6) or **11-SOG**(-CF_3SO_3)	$C_{33}H_{43}N_6O_8OsS^+$	875.25	875.14	11.68
	10-SOG(-PF_6+H^+) or **11-SOG**(-CF_3SO_3+H^+)	$C_{33}H_{44}N_6O_8OsS^{2+}$	438.13	438.07	
(g)	**FY026** (-PF_6)	$C_{23}H_{28}IN_4Os^+$	679.10	679.02	23.02
(h)	**FY026-OH** (-PF_6)	$C_{23}H_{29}N_4OOs^+$	569.20	569.17	12.53
(i)	**FY026-NAC** (-PF_6)	$C_{28}H_{36}N_5O_3OsS^+$	714.22	714.15	16.09
(j)	**FY026-NAC(O)** (-PF_6)	$C_{28}H_{36}N_5O_4OsS^+$	730.21	730.14	12.68
	FY026-NAC(O) (-PF_6+H^+)	$C_{28}H_{37}N_5O_4OsS^{2+}$	365.61	365.67	
(k)	**FY026-SG** (-PF_6)	$C_{33}H_{44}N_7O_6OsS^+$	858.27	858.19	13.29
	FY026-SG (-PF_6+H^+)	$C_{33}H_{45}N_7O_6OsS^{2+}$	429.64	429.65	
(l)	**FY026-SOG** (-PF_6)	$C_{33}H_{44}N_7O_7OsS^+$	874.26	874.15	11.54
	FY026-SOG (-PF_6+H^+)	$C_{33}H_{45}N_7O_7OsS^{2+}$	437.64	437.64	

6.3.5. Oxidation of NADH

6.3.5.1. UV-Vis spectroscopy

Complexes **10-OH**, **11**, and **31** (4 μM) were incubated at 37 °C and pH 7.4 with NADH (50 mol. equiv.), and the UV-Vis spectrum was recorded every 1 h for 24 h. NADH has two major absorption bands at 260 and 339 nm. As NADH is oxidised to NAD^+, the intensity at 339 nm declines and the intensity at 260 nm increases.[31]

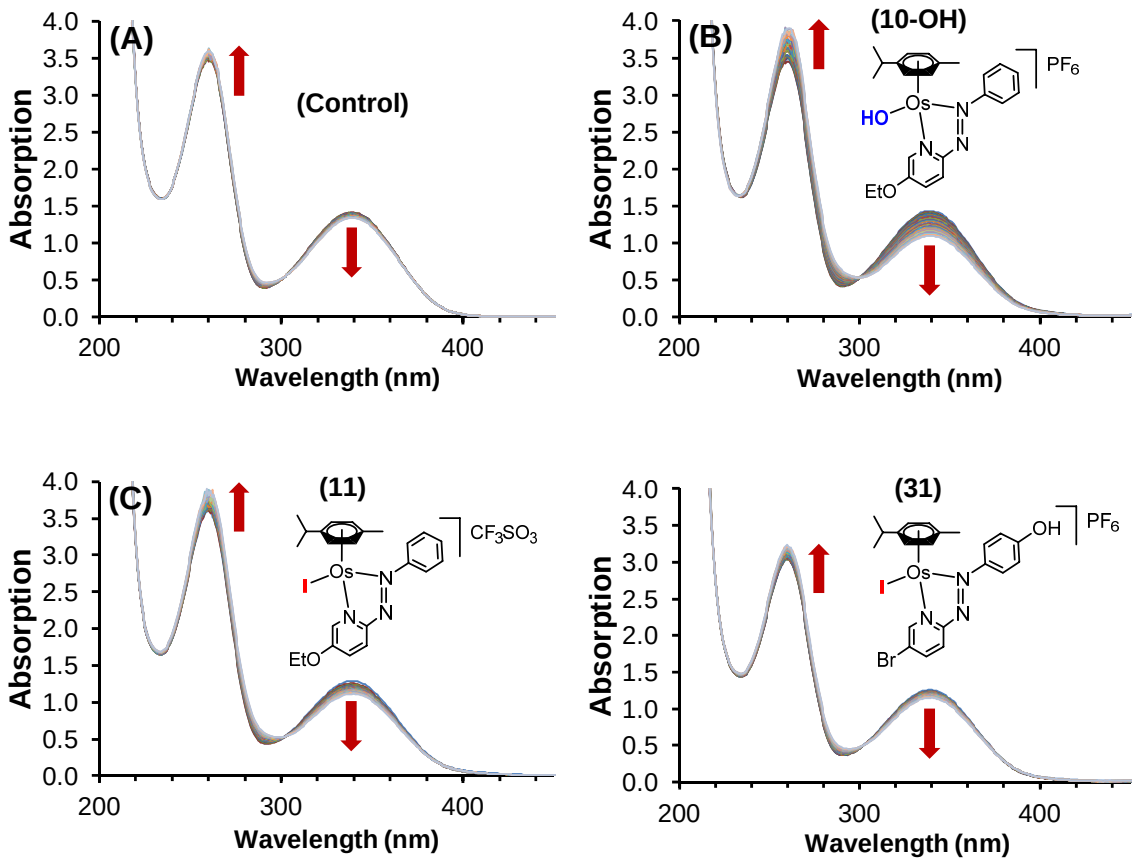

Figure 6.22. UV-Vis spectra of 200 μM NADH incubated at 37 °C and pH 7.4 for 24 h. (A) control experiment with no complex added. (B) with 4 μM **10-OH**. (C) with 4 μM **11**. (D) with 4 μM **31**.

In a control experiment where no complex was added, only a small degree of NADH oxidation was observed (noted by the decline in intensity at 339 nm). In comparison to the control, **10-OH** caused the greatest extent of NADH oxidation, followed by **11**. Complex **31** on the other hand caused little more NADH oxidation than that observed in the control study (Figure 6.22). Using the same sample concentrations, a kinetic UV-Vis experiment was conducted where the intensity of the absorption band at 339 nm was monitored over a 24 h period every 5 min at 37 °C. The 'absorbance/(absorbance at t = 0)' min was plotted versus time to display the extent of decline in NADH over a 24 h period (see Figure 6.23).

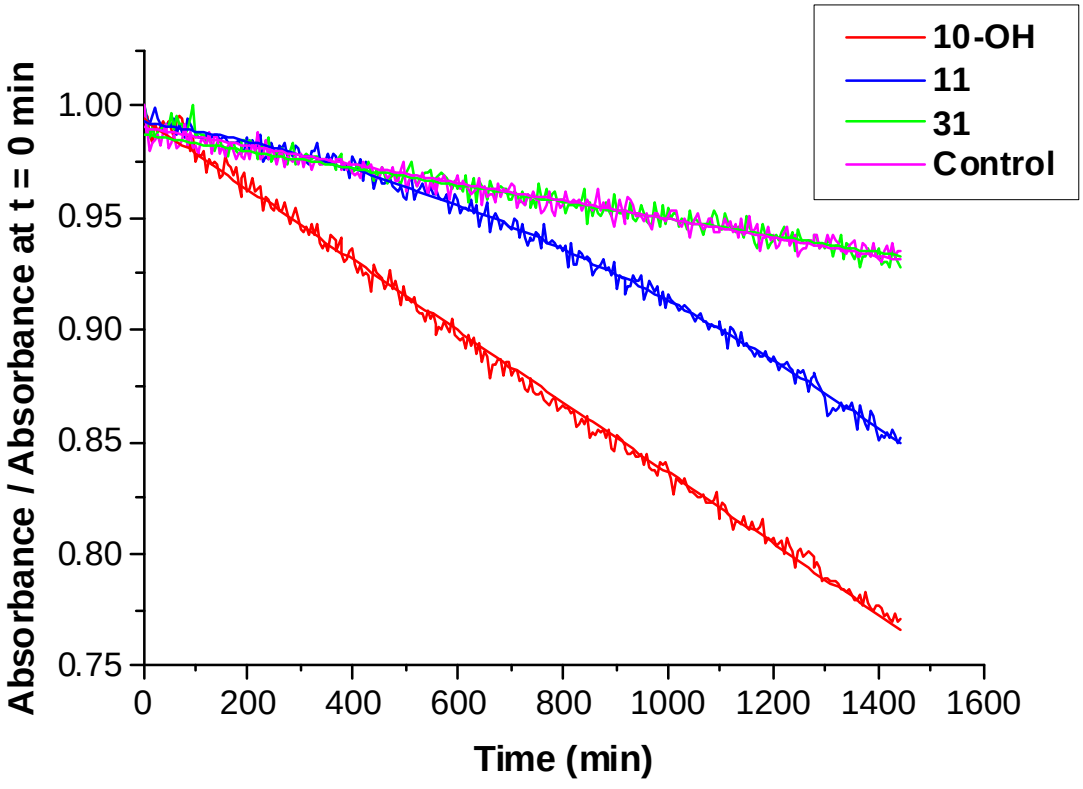

Figure 6.23. Reaction profiles for the oxidation of NADH to NAD^+ caused by complexes **10-OH**, **11**, **31** and no complex (control). Showing the normalised absorbance at 339 nm vs. time (min).

Complex **10-OH** produces the fastest rate of NADH oxidation followed by **11**, then **31** which produces little or no more NADH oxidation than the auto-oxidation of NADH observed in the control experiment. Since the complexes also absorb light at 339 nm it was not possible to accurately determine [NADH] at varying time points from absorption at 339 nm. The reaction profile between NADH and **11** follows a different non-linear path, where the rate of conversion of NADH to NAD^+ is initially slow and gradually increases with the progression of time until it is comparable to that of **10-OH** with NADH.

6.3.5.2. HPLC

Complexes **10-OH**, **11** and **31** (50 μM) were incubated at 37 °C with NADH (4 mol. equiv.) with phosphate buffer (5 mM, pH 7.4) for 0, 3, 6, 12 and 24 h, and the HPLC chromatograms were recorded. NADH and NAD^+ both have very low retention times of below 5 min and it was therefore not possible to distinguish between them. However, HPLC proves useful for determining the stabilities of the complexes in the presence of NADH (Figure 6.24).

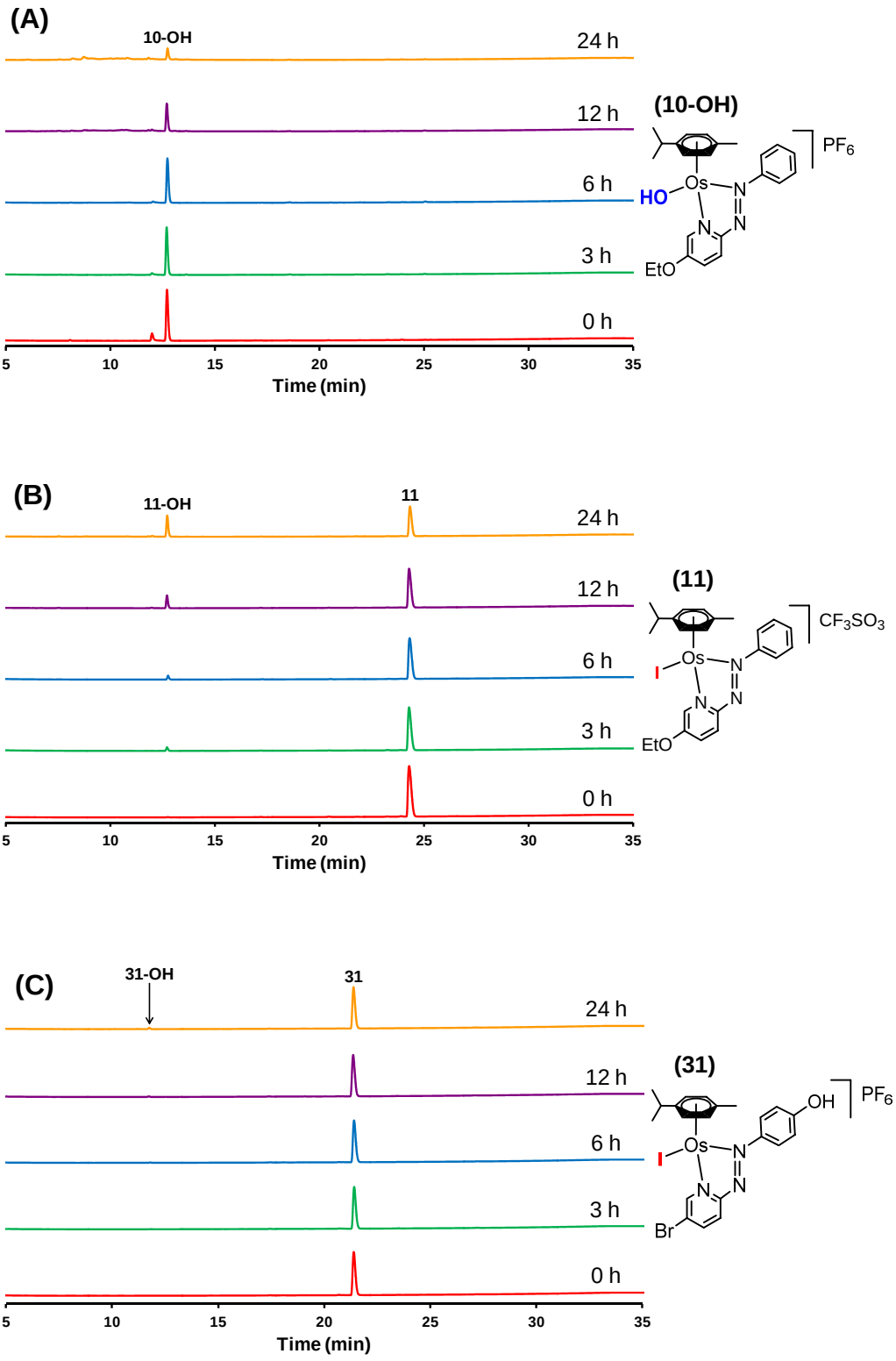

Figure 6.24. Chromatograms for complexes (50 μM) after incubation with 4 mol. equiv. NADH at 37 °C and pH 7.4, after 0, 3, 6, 12 and 24 h. (A) **10-OH**, (B) **11** and (C) **31**.

Complex **10-OH** remains reasonably stable over the initial 6 h incubation period, but major degradation was observed after 12 h. This is consistent with the stability testing of **10-OH** shown in Section **6.3.2**. Complex **11** hydrolyses in the presence of NADH to form the hydroxido-adduct, showing 30% **11-OH** after 24 h incubation. In contrast, complex **31** remains almost entirely stable upon incubation with NADH, forming only 2% hydroxido-adduct (**31-OH**) after 24 h incubation. In the control experiments where **11** and **31** were incubated in the absence of NADH, 1% and 0% of the hydroxido-adducts (**11-OH** and **31-OH**) were observed, respectively, in the chromatograms after 24 h.

6.3.5.3. ^{1}H NMR Spectroscopy

Complex **10-OH** (2 mM) was prepared in phosphate buffered D_2O (pH* 7.4) with NADH (3 mol. equiv.). A ^{1}H NMR spectrum was obtained after 0, 4 and 23 h incubation at 37 °C. Figure 6.25 shows the aromatic region of the spectra between 5.8 - 9.6 ppm and part of the aliphatic region between 2.6 - 2.8 ppm. The peaks corresponding to NADH, NAD^+ and **10-OH** were characterised. With no sample incubation the presence of NAD^+ peaks was already observable, as a small amount of NADH oxidation occurred between preparing the sample and acquiring the ^{1}H NMR spectrum at ambient temperatures. After 23 h incubation, all of the NADH peaks completely disappeared and NADH was completely oxidised to NAD^+. Peaks corresponding to **10-OH** also show a decline after 24 h, owing to the characteristic degradation of **10-OH** shown previously. Aliphatic NADH proton peaks, d1 and d2 correspond to the site where dehydrogenation

occurs. These peaks characteristically disappear as NADH is oxidised to NAD^+ and are replaced by a single aromatic doublet at 8.81 ppm, proton d.

Furthermore, **10-OH** (75 μM) was incubated at 37 °C with NADH (100 mol. equiv.) in phosphate buffer and the solution was tested for the presence of H_2O_2 using Quantifix® H_2O_2 semi-quantitative test sticks. Low levels of H_2O_2 (~0.5 ppm) were observed in solution after 30 and 60 min, after which the levels of H_2O_2 were undetectable (see Table 6.4).

Table 6.4. Measurements of H_2O_2 levels during the reaction between **10-OH** and 100 mol. equiv. NADH in phosphate buffer solution at 37 °C. Measurements made using H_2O_2 semi-quantitative testing sticks.

Time (min)	H_2O_2 levels (ppm)
0 min	0.0
30 min	~0.5
60 min	~0.5
120 min	~0.0
180 min	~0.0

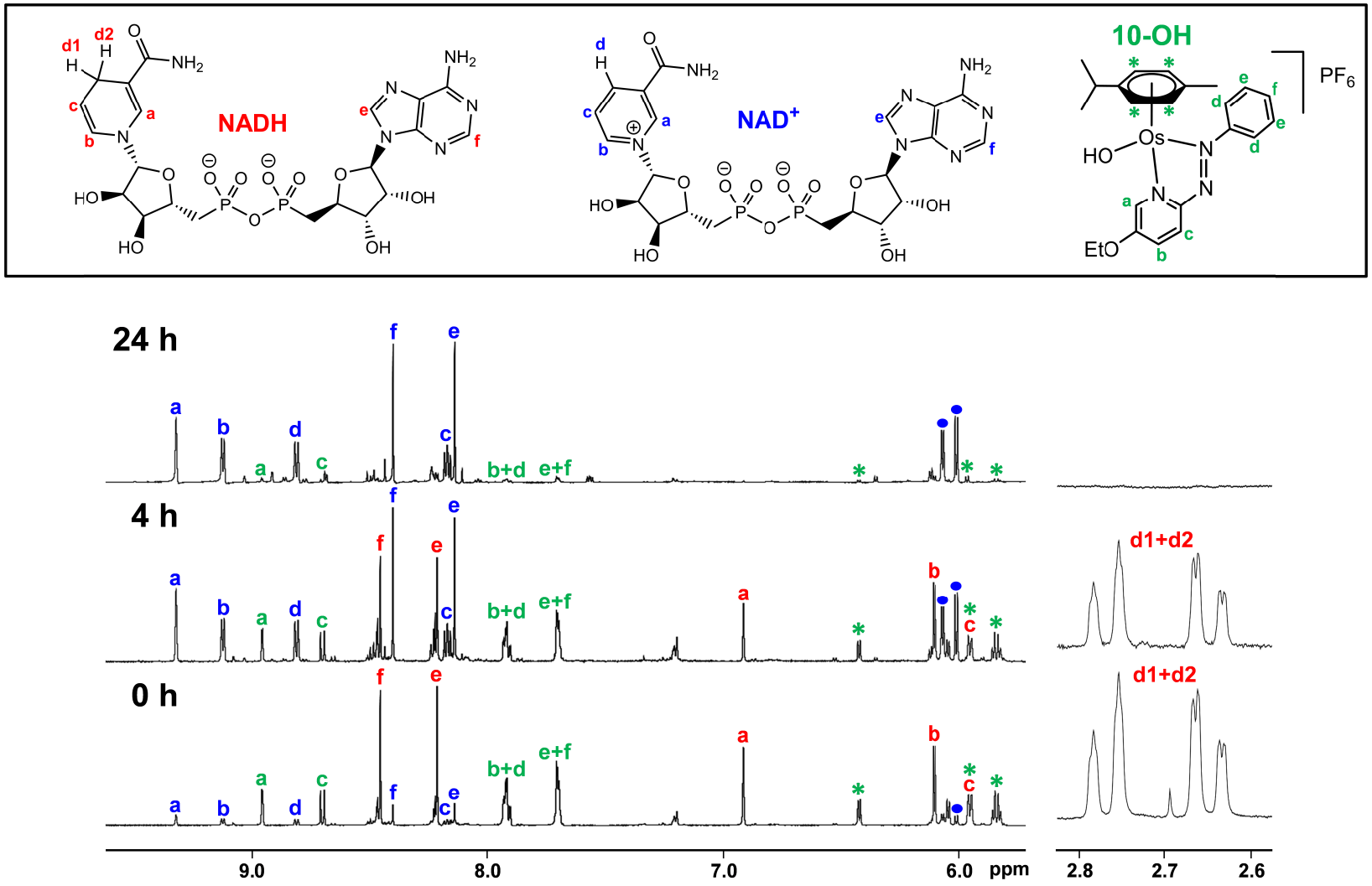

Figure 6.25. ^{1}H NMR spectra recorded during the reaction between 2mM **10-OH** and 3 mol. equiv. NADH. The experiment was performed in phosphate buffered D_2O (pH* 7.4) and spectra were recorded after incubations of 0, 4 and 23 h at 37 °C. Spectra were collected on a 600 MHz instrument.

6.4. Discussion

6.4.1. The pK_a and stability of 10-OH

The pK_a measurement of the coordinated water molecule in an aqua-complex is an important measure of drug activity. It determines whether the active aqua-adduct species (Os-OH_2) will predominate, or the more stable hydroxido species (Os-OH) at any given pH.[44] Since iodido Os(II) arene AZPY pro-drugs (**10** and **11**) do not readily hydrolyse in aqueous media, complex **10-OH** was synthesised for study. The low pK_a value of **10-OH** is consistent with the low values observed for Ru(II) arene AZPY complexes,[45] showing that under physiological conditions (pH 7.4) the hydroxido species predominates. Strong π-acceptor ligands such as AZPYs draw electron density away from the metal centre rendering it more electropositive, which in turn makes the H_2O ligand more acidic (lower pK_a).[44] In contrast, anionic ligands such as acetylacetone and picolinate place more electron density around the metal centre, hence producing the opposite effect (Figure 6.26).[46-48] Moreover, Os(II) arene complexes have a greater tendency for lower pK_a values in their aqua-adducts than their Ru(II) analogues.[44] Interestingly, when compared to the diverse range of aqua-species of Os(II) and Ru(II) arene anti-cancer complexes from the Sadler group, **10-OH** is the most acidic species to be determined to date. Its acidity is even greater than that of $[Os(\eta^6\text{-}p\text{-cym})(IMPY\text{-}NMe_2)H_2O]^{2+}$ (containing an IMPY bidentate ligand,[14] which is analogous to the AZPY ligand in **FY026**), and the Ru(II) AZPY complex, $[Ru(\eta^6\text{-}p\text{-cym})(AZPY\text{-}NMe_2)H_2O]^{2+}$.[45]

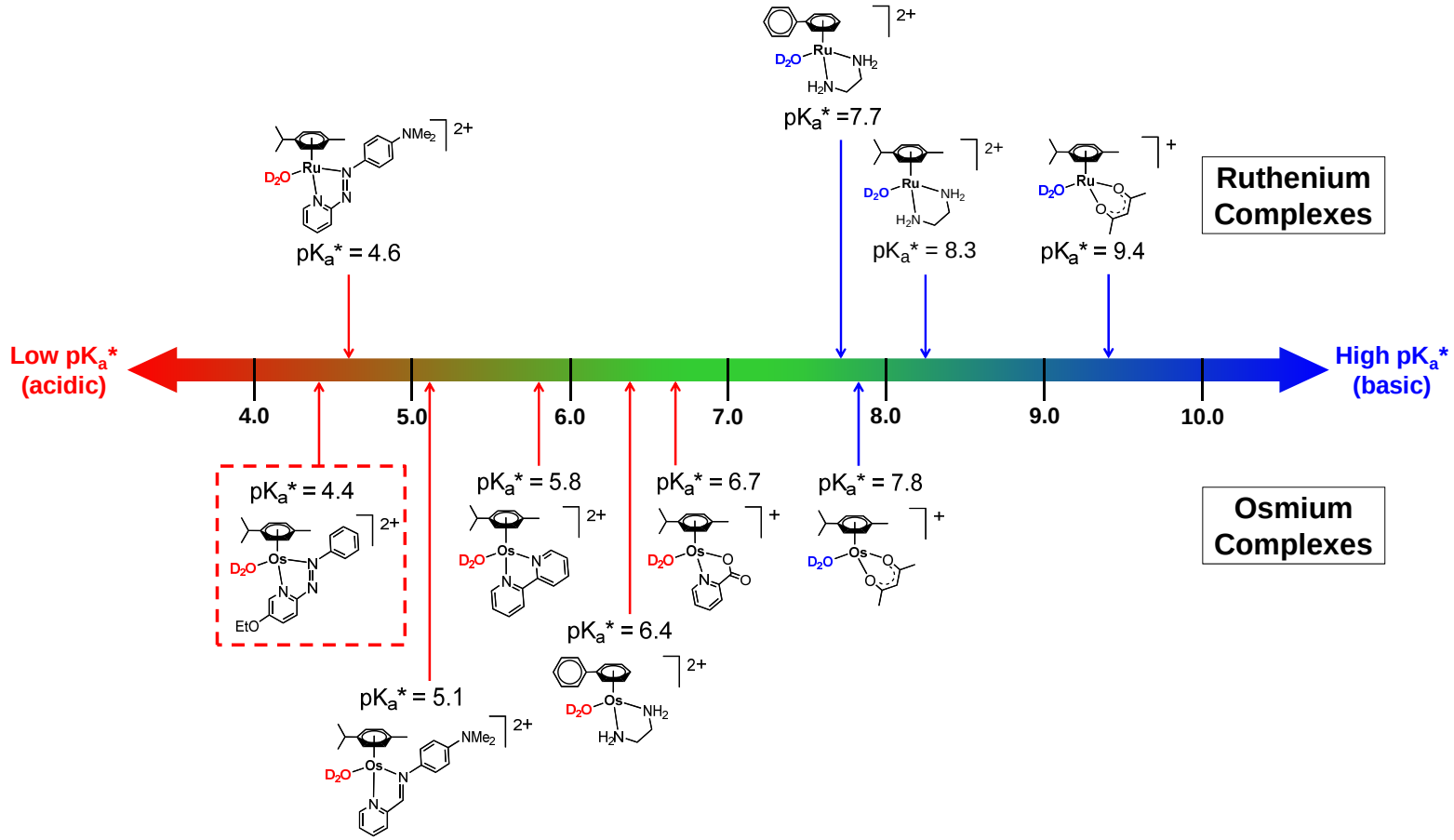

Figure 6.26. A comparison of the pK_a* values for M-OD_2 found in various aqua-species of Sadler group complexes. The pK_a* values shown were determined by ^{1}H NMR in D_2O where pH* was not corrected for the effect of deuterium on the glass electrode. The complexes shown are Os(II) and Ru(II) η^6-arene complexes with different bidentate ligands capable of tuning electron density around the metal centre, hence dictating the acidity of the monodentate D_2O ligand. Complex **10-OH** is the most acidic aqua-species.[14,45-51]

Complex **10-OH** was shown to be unstable upon incubation in phosphate buffer solution (pH 7.4), with only 38% remaining intact after 24 h and approximately 58% lost as an unknown black precipitate. In the ^{1}H NMR experiment unknown peaks corresponding to **10-OH** degradation products were also observed. Large broad unidentified peaks were observable at 6.65, 1.85, 1.45 and 0.86 ppm. It may be possible for higher oxidation states of osmium species to form (e.g. Os(III)), which would yield broad peaks due to the shorter relaxation times associated with paramagnetic species. Also present was a new set of *p*-cym peaks with two aromatic doublets at 7.26 and 7.22 ppm, which are speculated to belong free *p*-cym. However, *p*-cym is insoluble in D_2O and therefore not likely to show peaks in the spectrum. Peacock *et al* previously reported the formation of a hydroxido-bridged dimeric species, $[(\eta^6\text{-}p\text{-cym})Os(\mu\text{-}OD)_3Os(\eta^6\text{-}p\text{-cym})]^+$, after preparing Os(II) *p*-cym maltolato complexes in D_2O (pH* 7.3).[52] However, the aromatic *p*-cym doublets are reported to be at 6.04 and 5.82 ppm and are therefore not consistent with these findings.

6.4.2. Generation of HO· radicals from H_2O_2

Complexes **8**, **10-OH** and **11** fully decompose 50-100 mol. equiv. H_2O_2 within 30 min of incubation at 37 °C. The depletion of H_2O_2 is accompanied by degradation of the complexes as observed by UV-Vis spectroscopy, and the generation of gases. In Chapter 4, Section **4.3.15**, it was shown that Os(II) arene AZPY complexes are capable of raising ROS levels, including $O_2^{\cdot -}$ radicals, within A2780 cancer cells. However, EPR spin trapping experiments

prove that **8**, **10-OH** and **11** generate HO· and not $O_2^{\cdot -}$ radicals in the presence of H_2O_2.

Since relatively high concentrations of H_2O_2 (3-10 mM) were used in these experiments in comparison to physiological concentrations, it was suspected that HO· radicals were being produced in large amounts and contributing to the degradation of the complexes. When UV-Vis spectroscopy experiments were repeated in the presence of 7.5% (v/v) EtOH (a known HO· quencher),[37] decomposition of the complexes was mainly prevented over a 2 h period, suggesting that HO· is responsible for their degradation. However, the rates of decomposition of H_2O_2 were also significantly reduced when EtOH was introduced. These observations suggest that the complexes are decomposed by HO·, generating new species *in situ* which in turn causes further rapid H_2O_2 degradation. Currently the mechanism(s) of HO· production are not yet understood, but are likely to involve the oxidation of Os(II) to higher oxidation states. Further experimentation involving X-ray Absorption Near Edge Spectroscopy (XANES) could be used as a means to determine which oxidation states of osmium are present in solution.[53] Furthermore, it was speculated that when **8** and **11** react with H_2O_2, H· radicals could also be produced alongside HO·, but the EPR signal of DEPMPO-H was weak and its presence is not entirely certain. DEPMPO has been previously reported to trap both H· and HO· radicals simultaneously in plant plasma membranes.[42] Gas chromatography could be utilised to determine if hydrogen is being produced upon H_2O_2 degradation with these complexes.[30] Until more is understood about the mechanism of action and whether a catalytic cycle takes place, it cannot be

said with any certainty whether the process of HO· production resembles that of Fenton chemistry.[24]

The rate of decomposition of the complexes with H_2O_2 occurs in the order **10-OH**>**8**>**11**, as does the speediness of H_2O_2 degradation. Moreover, the activity towards HO· radical production occurs in the order **10-OH**>**8**~**11**, and the extent of lysozyme degradation (*via* HO· production) follows the order **10-OH**~**8**>**11**. Lysozyme degradation might occur indiscriminately with no site specific pre-binding of an active species occurring before protein cleavage, as indicated by the smearing on the electrophoresis gels. The extent of protein cleavage increases with higher concentrations of H_2O_2, showing that the high H_2O_2 level microenvironment of a tumour is more likely to sustain damage caused by HO· generation than the lower H_2O_2 level environments of normal cells. However, substantial lysozyme damage (>70%) was only observed in 10 mM H_2O_2, which is significantly higher than the typical H_2O_2 levels found within tumour microenvironments.[2,15,21]

Finally, it was shown that pro-drugs **8** and **11** are not as reactive with H_2O_2 as their hydroxido analogue **10-OH**. Furthermore, MS data shows the presence of **10-OH** when **8** and **11** were incubated with H_2O_2, suggesting that the initial barrier in the formation of HO· radicals could involve loss of the halido monodentate ligand. The chlorido complex (**8**) was found to degrade lysozyme to a much greater extent than the iodido complex (**11**) in 10 mM H_2O_2. Likely because the chloride ligand is considerably more labile than iodide, hence enabling faster conversion to the activated complex **10-OH**. However, it is not yet fully understood.

6.4.3. Binding to cellular targets

Complex **10-OH** was found not to bind to the guanine derivative, 9-EtG. This observation might be partly explained by the very low pK_a* (4.4) of $[Os(\eta^6\text{-}p\text{-cym})(5\text{-EtO-AZPY})H_2O]^{2+}$, which exists predominantly as a hydroxido-adduct under physiological conditions. Hydroxido-adducts are generally less reactive than aqua-adducts, in this case showing no interaction with neutral N-lone pair donor ligands, such as DNA nucleobases.[44] In contrast, $[Os(\eta^6\text{-}p\text{-cym})(5\text{-IMPY-}NMe_2)H_2O]^{2+}$ and $[Ru(\eta^6\text{-}p\text{-cym})(AZPY\text{-}NMe_2)H_2O]^{+}$, also exhibiting low pK_a* values for their monodentate water ligands (5.2 and 4.6 respectively) are both capable of limited binding to 9-EtG under physiological conditions.[14,45] However, quicker and more extensive binding to 9-EtG is generally observed for Os(II) and Ru(II) arene aqua-complexes with anionic or strong σ-donor bidentate ligands, which exhibit higher pK_a* values for their monodentate water ligands.[46,47]

Unlike neutral guanine bases that bind through N-lone pairs and form complexes in a +2 charged state, the nucleophilic thiolate side chains of GSH and NAC were found to bind readily with **10-OH** to form +1 charged complexes (Scheme 6.6). Sulfur containing amino acid side chains are known for their ability to bind to platinum group metals like ruthenium, due to the good interaction between a soft acid (Ru^+) and soft bases (RS^-).[10,11] However, this is the first report of Os(II) arene AZPY complexes binding to GSH. Complex **10-OH** was also capable of forming a **10-SG** adduct when incubated with GSSG. Such a process would require reduction of the stable S-S bond. The mechanism of this process is unknown, but could potentially involve the transfer of an

electron from Os(II) to GSSG (see Scheme 6.7). New broadened peaks were present in the ^{1}H NMR spectrum when **10-OH** was reacted with GSSG, which are not present when it was reacted with GSH. This could indicate the presence of Os(III) paramagnetic species. However, no peak broadening was observed for the peaks corresponding to **10-OH** or **10-SG**.

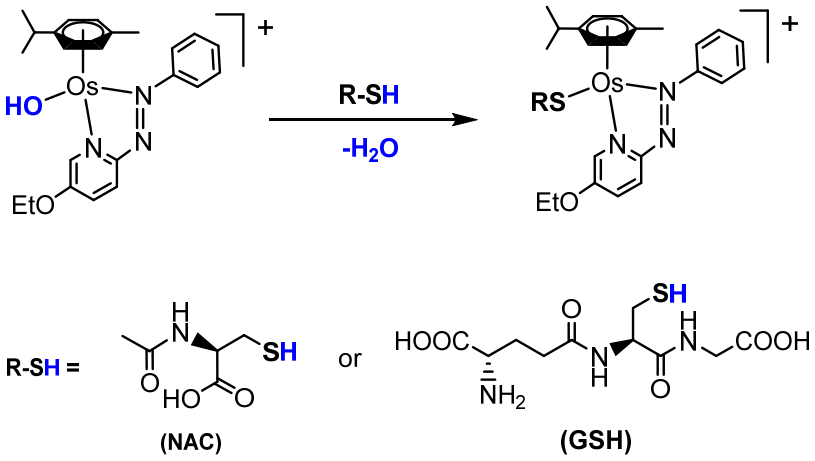

Scheme 6.6. The nucleophilic substitution reaction between **10-OH** and GSH or NAC.

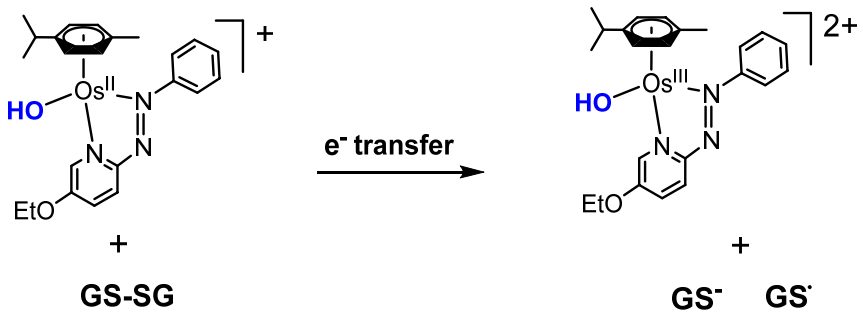

Scheme 6.7. Possible mechanism for the reduction of GSSG with **10-OH**, involving one electron transfer from the Os(II) metal centre to form Os(III).

When **11** and **FY026** were incubated with 1 mol. equiv. of GSH or NAC (75 µM), no binding to the thiol side chains were observed, however formation of the

hydroxido/aqua-adducts occurred (see Scheme 6.8). Furthermore, **FY026** was less prone to hydrolysis than **11**, showing a similarity to the results shown in Chapter 5, Section **5.3.2**. In comparison, in control studies where **11** and **FY026** were incubated in the absence of GSH and NAC no more than 1% hydrolysis occurred. This suggests that such reactions with peptides/proteins containing thiol side chain groups may be responsible for the activation of iodido pro-drugs inside cells, to generate the less inert hydroxido-adducts. Further investigations are required to uncover the mechanism of activation.

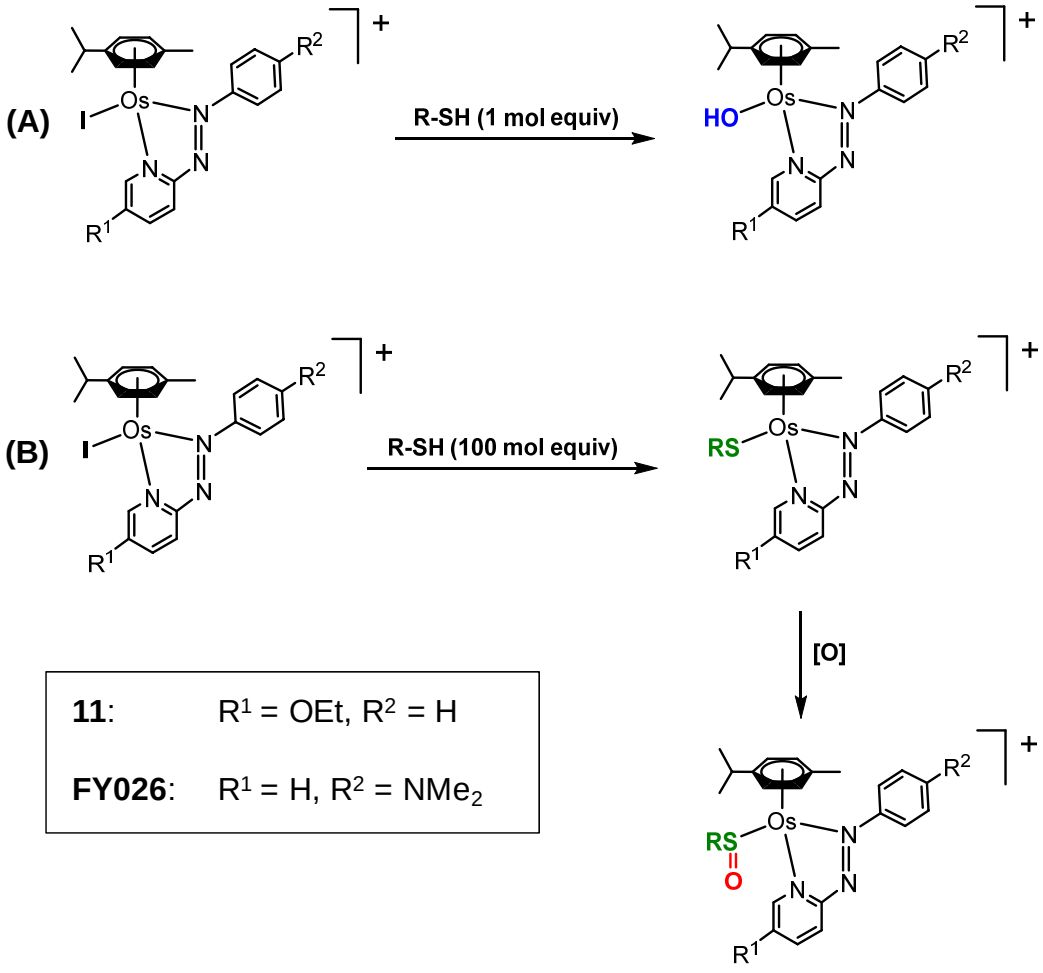

Scheme 6.8. Reaction between **11** or **FY026** (75 μM) and R-SH (GSH or NAC). (A) 1 mol. equiv. of R-SH. (B) 100 mol. equiv. R-SH. Oxidation by O_2 is denoted by [O].

However, when **11** and **FY026** were incubated with 100 mol. equiv. of GSH or NAC, no hydroxido-adducts were observed in the chromatograms, except when **FY026** was reacted with GSH or NAC a very small peak occurred after 3h which later disappeared. After less than 24 h, **11** and **FY026** completely reacted with GSH or NAC to form a thiolato-adduct (major product) and a sulfenato-adduct (minor product). The latter of which is likely a consequence of O_2 oxidation as samples were not purged with N_2 prior to incubation. Likewise, a sulfenato-species was previously observed in the Sadler group when [Ru(η^6-bip)(en)Cl]PF_6 was incubated with GSH in aerobic conditions. Its formation was largely suppressed when incubation occurred under anaerobic conditions.[11]

The iodido-species might undergo direct binding to GSH or NAC *via* the thiol side chain, accompanied by the loss of the iodide monodentate ligand (Scheme 6.8). Similarly, a ruthenium complex, [Ru(η^6-bip)(AZPY-NMe_2)I]PF_6, was also found to directly bind with GSH, involving complete substitution of the iodide ligand with GS^- to produce a thiolato-adduct.[10] Given that intracellular levels of GSH are high (1-10 mM)[4] it is probable that thiolato-adducts (**11-SG** and **FY026-SG**) would form predominantly *in vitro*. However, such species are not necessarily 'dead end' products with no further involvement in anti-cancer activity. The sulfenato-species previously observed when [Ru(η^6-bip)(en)Cl]PF_6 was incubated with GSH in aerobic conditions was capable of binding to DNA nucleobases.[11] Moreover, an Ir(III) cyclopentadienyl complex, Ir(η^5-Cp^{xbip})(2-PhPy)Cl, was found to form a stable thiolato-adduct with GSH.[54] However, in the presence of H_2O_2 it was able to form sulfenato- and even sulfinato-adducts that are believed to play a further role in anticancer activity and could interact

with other cellular targets. Further studies mimicking these conditions are required to determine whether such reactions are reproducible for **11** and **FY026**.

6.4.4. Catalytic oxidation of NADH to NAD^+

Complexes **10-OH**, **11** and **31** were capable of oxidising NADH to NAD^+ with capabilities following the order **10-OH**>**11**>**31**. Furthermore, the control study shows a small degree of NADH oxidation occurring in the absence of a complex, likely a consequence of O_2 exposure. Interestingly, iodido pro-drugs (**11** and **31**) were less capable of oxidising NADH than the hydroxido complex (**10-OH**), which is proposed to be the species occurring after cellular activation of **10** (or **11**). Moreover, the HPLC studies showed that **11** undergoes 30% hydrolysis after a 24 h incubation period in the presence of 4 mol. equiv. of NADH. However, in the absence of NADH only 1% hydrolysis of **11** was observed, thus indicating that NADH is capable of activating iodido pro-drugs. These results reveal the importance of the presence of hydroxido species in the oxidation of NADH to NAD^+. Complex **11** starts initially with a slow rate of NADH oxidation. However, as **11-OH** is produced *in-situ* through hydrolysis of the Os-I bond, the reaction rate gradually increases until it resembles the rate of NADH oxidation found for **10-OH**. Complex **31** on the other hand remains almost entirely stable throughout the 24 h period, showing only 1% hydrolysis, and oxidises NADH at a rate only marginally quicker than that of the control study.

The mechanism of NADH oxidation may be catalytic and similar to the mechanism of action proposed for Os(II) arene IMPY complexes (analogous to AZPY complexes), where a Os-H species is formed.[14] However, the presence of the hydride species was not confirmed herein and more studies are required to prove that the reaction occurs catalytically. A hydride species has previously been observed by ^{1}H NMR in H_2O for Os(II) arene IMPY complexes,[14] and also for Ir(III) Cp* complexes.[31,32] Some Ir(III) Cp* complexes were found to produce H_2 in GC experiments when incubated with NADH, confirming that the hydride species is converted back to the aqua-species *via* the release of gaseous H_2.[30] In contrast, Os(II) arene IMPY complexes did not produce H_2 and a mechanism involving hydride transfer to O_2, resulting in the formation of H_2O_2 was proposed. When **10-OH** was incubated with NADH, low levels of H_2O_2 were detected using H_2O_2 semi-quantitative test sticks, hence providing partial evidence that **10-OH** could behave similarly to Os(II) arene IMPY complexes.

6.5. Summary

Following on from the findings in Chapter 5, hydroxido-species of the form $[Os(\eta^6\text{-arene})(R_1\text{-AZPY-}R_2)OH]^+$ were proposed to be the active species formed *via* cellular activation of their iodido pro-drug counterparts. A hydroxido complex was synthesised (**10-OH**) and the pK_a of its monodentate aqua ligand was determined as 4.55(±0.01). The very low observed pK_a is a signature of Os(II) arene complexes featuring bidentate ligands with strong π-acceptor/weak σ-donor capabilities, and suggests that under physiological conditions it exists

predominantly as the hydroxido-species as opposed to the more reactive aqua-species. Unlike its iodido analogue which is stable upon incubation, **10-OH** was shown to undergo 62% degradation. However, it is more reactive towards biological targets: H_2O_2, NAC, GSH, GSSG and NADH.

Complexes **8**, **10-OH** and **11** were all found to generate HO· radicals in the presence of H_2O_2, which were observed in EPR experiments employing DEPMPO as a spin trap. The mechanism of HO· generation is not understood, but it was found that generated HO· radicals caused degradation of the complexes and higher oxidation states of osmium are likely generated, which in turn caused rapid decomposition of H_2O_2. It was shown that the HO· radicals generated from H_2O_2 by these complexes can be utilised to break down the protein lysozyme. Hence, it is proposed that raised H_2O_2 levels present in cancerous cells could be utilised, which upon incubation with the complexes would generate HO· radicals capable of damaging/destroying the cells, whilst leaving normal cells with considerably lower levels of H_2O_2 relatively unscathed. In the presence of H_2O_2, complex **10-OH** was found to decompose more quickly and generate HO· radicals more efficiently, causing more damage to lysozyme in comparison to its halido analogues. Thus adding weight to the notion that the hydroxido-adduct is the activate species inside cells.

Complexes **10-OH** and **11** were found to oxidise NADH to NAD^+. The reaction profile for **11** followed a particular path, whereby the initial reaction rate is slow and did not speed up until ~12 h of incubation. HPLC analysis revealed that **11** undergoes slow hydrolysis in the presence of NADH to form **11-OH**, showing that the presence of the hydroxido-adduct is necessary for NADH oxidation.

Interestingly, incubation with NADH also provides an activation route for iodido pro-drugs to form their corresponding hydroxido-adducts. The rate of NADH oxidation caused by **31** was only slightly greater than that found in the control study where NADH was incubated by itself. HPLC analysis showed that **31** does not readily hydrolyse with NADH, which could account for its poor activity. The mechanism of NADH oxidation is unknown, but is suspected to follow a catalytic cycle similarly to the catalytic cycle proposed for Os(II) arene IMPY complexes by Ying Fu.[14] However, further studies are required to confirm the reaction is occurring catalytically and confirm the presence of a hydride species (Os-H bond) by ^{1}H NMR.

Complex **10-OH** does not to bind to 9-EtG. This was explained by its acidic nature and its tendency to form the +1 charged hydroxido-adduct over the +2 charged aqua-species under physiological conditions. Complex **10-OH** was however capable of binding to NAC and GSH *via* their thiol groups to form +1 charged thiolato-adducts (major product) and sulfenato-adducts (minor product). The latter was likely formed by O_2 oxidation of the thiolato-adduct under aerobic conditions. Interestingly, **10-OH** was also capable of forming small amounts of the thiolato-adduct when incubated with GSSG. Such a process requires the reduction of GSSG, which is speculated to occur *via* electron transfer from Os(II).

When iodido pro-drugs, **11** and **FY026**, where incubated with 1 mol. equiv. of NAC or GSH (75 μM), formation of the hydroxido-species occurred. Interactions with such species at low concentrations could provide activation routes for iodido complexes inside cells. However, When **11** and **FY026** were incubated

with 100 mol. equiv. of NAC or GSH (7.5 mM), formation of the thiolato-adducts were observed with sulfenato-adducts present as a minor product. Since GSH levels are present in milli-molar concentrations in intracellular conditions, the most likely scenario would involve **11** and **FY026** binding to GSH *in vitro* forming thiolato- and sulfenato-adducts. However, such species are not necessarily 'dead end' products and could play a role in other biological activities.[11,54]

6.6. References

(1) Pelicano, H.; Carney, D.; Huang, P. *Drug Resist. Update* **2004**, *7*, 97.

(2) Arnold, R. S.; Shi, J.; Murad, E.; Whalen, A. M.; Sun, C. Q.; Polavarapu, R.; Parthasarathy, S.; Petros, J. A.; Lambeth, J. D. *Proc. Natl. Acad. Sci. U.S.A.* **2001**, *98*, 5550.

(3) Jungwirth, U.; Kowol, C. R.; Keppler, B. K.; Hartinger, C. G.; Berger, W. *Antioxid. Redox Sign.* **2011** *15*, 1085.

(4) Balendiran, G. K.; Dabur, R.; Fraser, D. *Cell Biochem. Funct.* **2004**, *22*, 343.

(5) Barranco, S. C.; Perry, R. R.; Durm, M. E.; Quraishi, M.; Werner, A. L.; Gregorcyk, S. G.; Kolm, P. *Dis. Colon Rectum* **2000**, *43*, 1133.

(6) Backos, D. S.; Franklin, C. C.; Reigan, P. *Biochem. Pharmacol.* **2012**, *83*, 1005.

(7) Jansen, B. A. J.; Brouwer, J.; Reedijk, J. *J. Inorg. Biochem.* **2002**, *89*, 197.

(8) Kasherman, Y.; Sturup, S.; Gibson, D. *J. Med. Chem.* **2009**, *52*, 4319.

(9) Fakih, S.; Munk, Vivienne P.; Shipman, Michelle A.; Murdoch, Piedad del S.; Parkinson, John A.; Sadler, Peter J. *Eur. J. Inorg. Chem.* **2003**, *2003*, 1206.

(10) Dougan, S. J.; Habtemariam, A.; McHale, S. E.; Parsons, S.; Sadler, P. J. *Proc. Natl. Acad. Sci. U.S.A.* **2008**, *105*, 11628.

(11) Wang, F.; Xu, J.; Habtemariam, A.; Bella, J.; Sadler, P. J. *J. Am. Chem. Soc.* **2005**, *127*, 17734.

(12) Romero-Canelon, I.; Salassa, L.; Sadler, P. J. *J. Med. Chem.* **2013**, *56*, 1291.

(13) Fu, Y.; Habtemariam, A.; Pizarro, A. M.; van Rijt, S. H.; Healey, D. J.; Cooper, P. A.; Shnyder, S. D.; Clarkson, G. J.; Sadler, P. J. *J. Med. Chem.* **2010**, *53*, 8192.

(14) Fu, Y.; Romero, M. J.; Habtemariam, A.; Snowden, M. E.; Song, L.; Clarkson, G. J.; Qamar, B.; Pizarro, A. M.; Unwin, P. R.; Sadler, P. J. *Chem. Sci.* **2012**, *3*, 2485.

(15) Stone, J. R.; Yang, S. *Antioxid. Redox Sign.* **2006**, *8*, 243.

(16) Gough, D. R.; Cotter, T. G. *Cell Death Dis.* **2011**, *2*, 213.

(17) Burdon, R. H. *Free Radical Biol. Med.* **1995**, *18*, 775.

(18) López-Lázaro, M. *Cancer Lett.* **2007***, 252*, 1.

(19) Wlassoff, W. A.; Albright, C. D.; Sivashinski, M. S.; Ivanova, A.; Appelbaum, J. G.; Salganik, R. I. *J. Pharm. Pharmacol.* **2007**, *59*, 1549.

(20) Lisanti, M. P.; Martinez-Outschoorn, U. E.; Lin, Z.; Pavlides, S.; Whitaker-Menezes, D.; Pestell, R. G.; Howell, A.; Sotgia, F. *Cell Cycle* **2011**, *10*, 2440.

(21) Szatrowski, T. P.; Nathan, C. F. *Cancer Res.* **1991**, *51*, 794.

(22) Tamura, H.; Miwa, M. *Chem. Lett.* **1997**, *26*, 1177.

(23) Osella, D.; Ferrali, M.; Zanello, P.; Laschi, F.; Fontani, M.; Nervi, C.; Cavigiolio, G. *Inorg. Chim. Acta* **2000**, *306*, 42.

(24) Barbusiński, K. *Ecol. Chem. Eng. S* **2009**, *16*, 347.

(25) Ying, W. *Antioxid. Redox Sign.* **2007**, *10*, 179.

(26) Dobson, C. M. *Foundations of Chemical Biology*; Oxford University Press: New York, 2001.

(27) Chen, Z.; Lu, W.; Garcia-Prieto, C.; Huang, P. *J. Bioenerg. Biomembr.* **2007**, *39*, 267.

(28) Soldevila-Barreda, J. J.; Romero-Canelón, I.; Habtemariam, A.; Sadler, P. J. *Nat. Commun.* **2015**, *6*, 6582.

(29) Yan, Y. K.; Melchart, M.; Habtemariam, A.; Peacock, A. F. A.; Sadler, P. J. *J. Biol. Inorg. Chem.* **2006**, *11*, 483.

(30) Liu, Z., Ph.D Thesis, University of Warwick, 2011.

(31) Millett, A. J.; Habtemariam, A.; Romero-Canelón, I.; Clarkson, G. J.; Sadler, P. J. *Organometallics* **2015**, *34*, 2683.

(32) Liu, Z.; Romero-Canelón, I.; Qamar, B.; Hearn, J. M.; Habtemariam, A.; Barry, N. P. E.; Pizarro, A. M.; Clarkson, G. J.; Sadler, P. J. *Angew. Chem. Int. Ed.* **2014**, *53*, 3941.

(33) Fu, Y. Ph.D Thesis, University of Warwick, 2011.

(34) Bezençon, J.; Wittwer, M. B.; Cutting, B.; Smieško, M.; Wagner, B.; Kansy, M.; Ernst, B. *J. Pharm. Biomed. Anal.* **2014**, *93*, 147.

(35) Krężel, A.; Bal, W. *J. Inorg. Biochem.* **2004**, *98*, 161.

(36) Lechevalier, V.; Musikaphun, N.; Gillard, A.; Pasco, M.; Guerin-Dubiard, C.; Husson, F.; Nau, F. *Food Funct.* **2015**, *6*, 1578.

(37) Anbar, M.; Meyerstein, D.; Neta, P. *J. Biol. Chem. B* **1966**, 742.

(38) Karoui, H.; Hogg, N.; Fréjaville, C.; Tordo, P.; Kalyanaraman, B. *J. Biol. Chem.* **1996**, *271*, 6000.

(39) Frejaville, C.; Karoui, H.; Tuccio, B.; le Moigne, F.; Culcasi, M.; Pietri, S.; Lauricella, R.; Tordo, P. *J. Chem. Soc., Chem. Commun.* **1994**, *15*, 1793.

(40) MojoviĆ, M.; VuletiĆ, M.; BaČIĆ, G. G. *Ann. N.Y. Acad. Sci.* **2005**, *1048*, 471.

(41) Hardy, M.; Rockenbauer, A.; Vásquez-Vivar, J.; Felix, C.; Lopez, M.; Srinivasan, S.; Avadhani, N.; Tordo, P.; Kalyanaraman, B. *Chem. Res. Toxicol.* **2007**, *20*, 1053.

(42) Mojović, M.; Spasojević, I.; Bačić, G. *J. Chem. Inf. Model.* **2005**, *45*, 1716.

(43) Abedinzadeh, Z.; Arroub, J.; Gardès-Albert, M. *Can. J. Chem.* **1994**, *72*, 2102.

(44) Pizarro, A.; Habtemariam, A.; Sadler, P. J. *Top Organomet. Chem.* **2010**, 32, 21.

(45) Dougan, S. J.; Melchart, M.; Habtemariam, A.; Parsons, S.; Sadler, P. J. *Inorg. Chem.* **2006**, *45*, 10882.

(46) Fernández, R.; Melchart, M.; Habtemariam, A.; Parsons, S.; Sadler, P. J. *Chem. Euro. J.* **2004**, *10*, 5173.

(47) Peacock, A. F. A.; Habtemariam, A.; Fernández, R.; Walland, V.; Fabbiani, F. P. A.; Parsons, S.; Aird, R. E.; Jodrell, D. I.; Sadler, P. J. *J. Am. Chem. Soc.* **2006**, *128*, 1739.

(48) Peacock, A. F. A.; Parsons, S.; Sadler, P. J. *J. Am. Chem. Soc.* **2007**, *129*, 3348.

(49) Peacock, A. F. A.; Habtemariam, A.; Moggach, S. A.; Prescimone, A.; Parsons, S.; Sadler, P. J. *Inorg. Chem.* **2007**, *46*, 4049.

(50) Wang, F.; Chen, H.; Parsons, S.; Oswald, I. D. H.; Davidson, J. E.; Sadler, P. J. *Chem. Euro. J.* **2003**, *9*, 5810.

(51) Chen, H.; Parkinson, J. A.; Morris, R. E.; Sadler, P. J. *J. Am. Chem. Soc.* **2003**, *125*, 173.

(52) Peacock, A. F. A.; Melchart, M.; Deeth, R. J.; Habtemariam, A.; Parsons, S.; Sadler, P. J. *Chem. Euro. J.* **2007**, *13*, 2601.

(53) Conradson, S. D.; Al Mahamid, I.; Clark, D. L.; Hess, N. J.; Hudson, E. A.; Neu, M. P.; Palmer, P. D.; Runde, W. H.; Drew Tait, C. *Polyhedron* **1998**, *17*, 599.

(54) Liu, Z.; Sadler, P. J. *Inorg. Chem. Front.* **2014**, *1*, 668.

Chapter 7

Future work

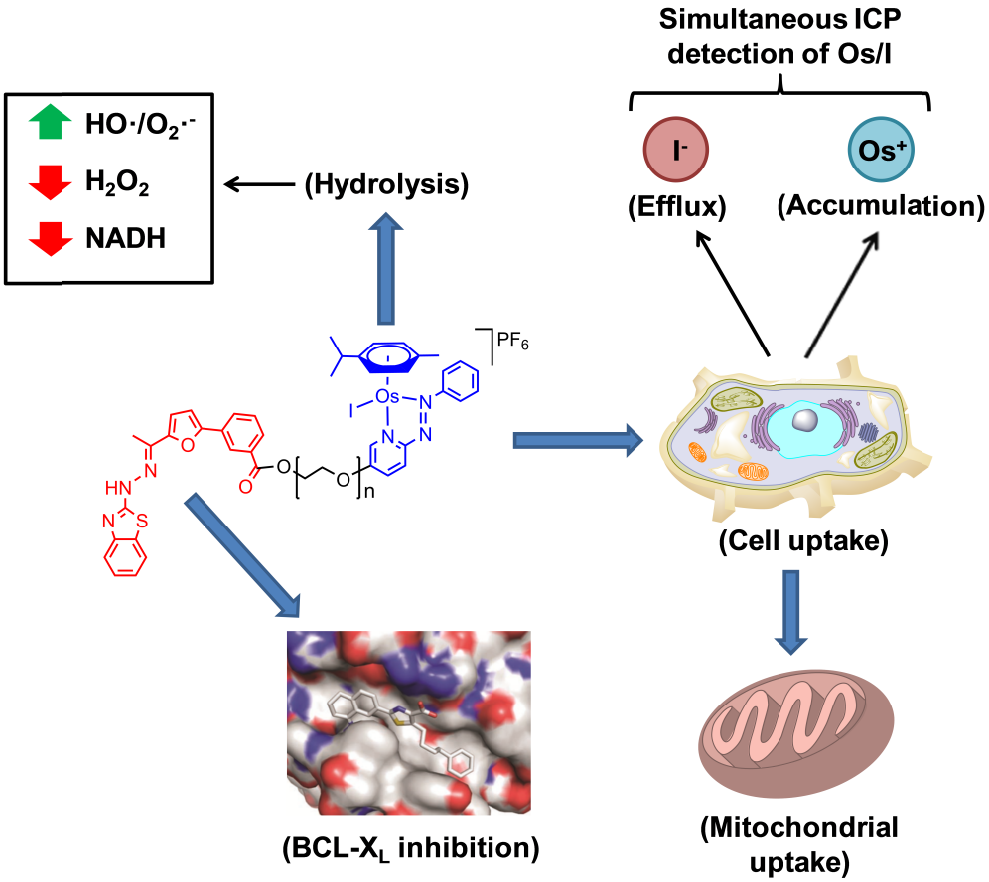

7.1. Introduction

This chapter explores potential areas of future work in the research of Os(II) arene complexes containing bidentate azo-ligands. It is mainly based on the results of previous chapters and preliminary data that were not included. Herein I discuss further studies required to develop our understanding of the mechanisms of action of the complexes shown in previous chapters. I also discuss new areas of research to explore, including the synthesis of novel pharmacophoric species.

7.2. Solubilisation of Os(II) arene AZBTZ complexes

In Chapter 3, Os(II) *p*-cym complexes containing novel bidentate phenylazobenzothiazole (AZBTZ) ligands were shown to exhibit unique chemical and structural properties. Unfortunately these species (particularly neutral *N,C*-coordinated species) have extremely poor solubility in aqueous media (<10 μM determined by ICP-MS for saturated solutions in water with 5% DMSO), likely owing to the highly conjugated aromatic AZBTZ ligands. As such, it was not possible to progress to biological evaluations. Further complexes were synthesised with various electron withdrawing or water solubilising substituents on the AZBTZ ligand in an attempt to improve water solubility (see Figure 7.1), however, it proved relatively ineffective. Further attempts included incorporating complexes into water soluble cyclic sugars (α- and β-cyclodextrin), but it provided only very limited increases in solubility due to the size and shape specific cavities of the cyclodextrins.[1,2]

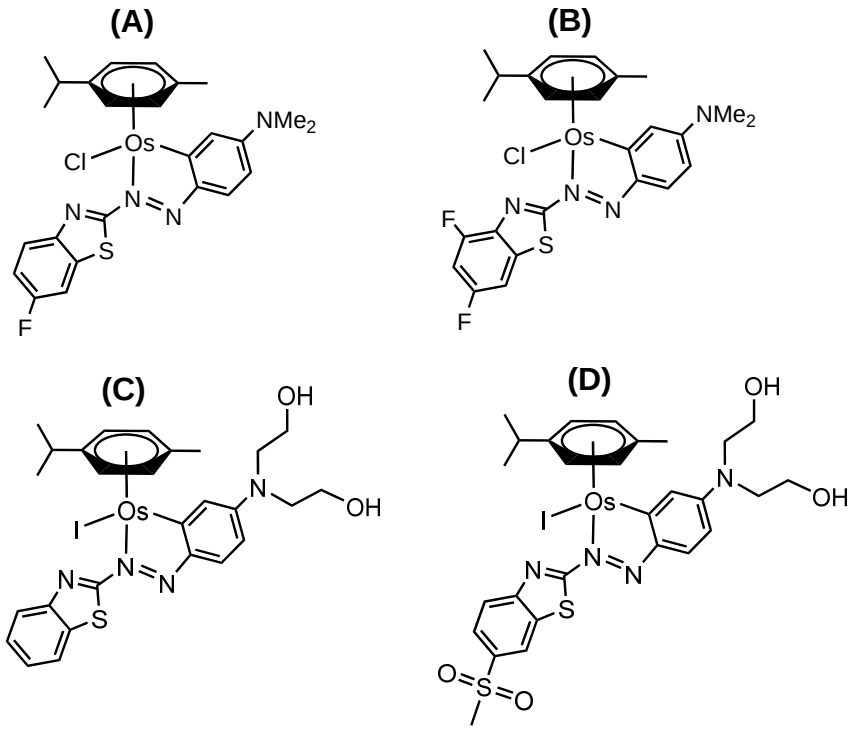

Figure 7.1. Structures of other novel complexes that were synthesised with electron withdrawing groups; (A) Os(η^6-*p*-cym)(*N,C*-6-F-AZBTZ-NMe_2)Cl, and (B) Os(η^6-*p*-cym)(*N,C*-6,8-F,F-AZBTZ-NMe_2)Cl, and complexes synthesised with water solubilising groups, (C) Os(η^6-*p*-cym)(*N,C*-AZBTZ-N{CH_2CH_2OH}$_2$)I, and (D) Os(η^6-*p*-cym)(*N,C*-6-$MeSO_2$-AZBTZ-N{CH_2CH_2OH}$_2$)I.

A feasible method for improving the water solubility of lipophilic metal complexes is to encapsulate them into a water soluble polymer. This has previously been achieved for strongly hydrophobic ruthenium arene dithiolato-carborane complexes designed for boron neutron capture therapy.[3] These insoluble complexes were encapsulated into Pluronic® triblock copolymer P123 to form water soluble micellar structures with potent anti-cancer activity and enhanced selectivity towards cancerous cells over normal cells. Copolymer P123 exhibits central lipophilic side-chains and terminal hydrophilic groups.

After self-assembly, the complex sits inside the hydrophobic core of the micelle whilst the hydrophilic groups surround the surface of the micelle structure (Figure 7.2). Such methods could also be utilised to encapsulate lipophilic Os(II) arene AZBTZ complexes for the purpose of solubilising them in aqueous media and selectively transporting them inside cancer cells.

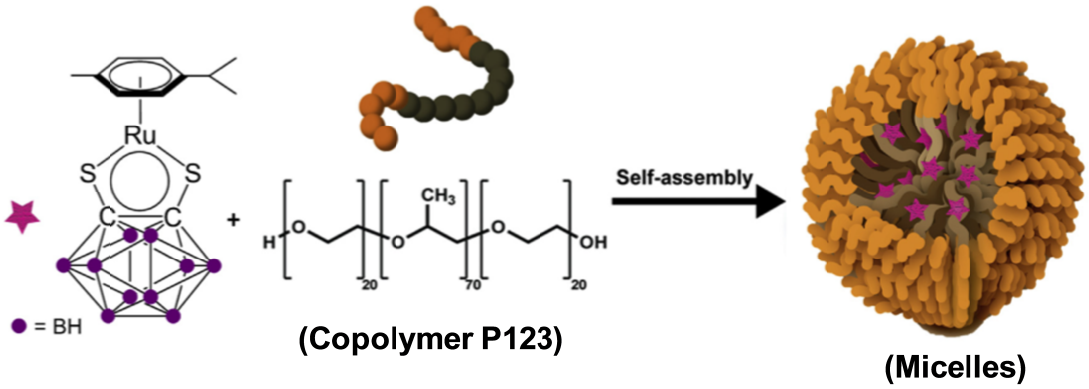

Figure 7.2. The encapsulation of lipophilic Ru(II) *p*-cym dithiolato-carborane complexes in Pluronic® triblock copolymer P123 to form water soluble micelles. Graphics are taken directly from reference.[3]

7.3. Simultaneous detection of Os and I by ICP-MS for cellular accumulation studies

In Chapter 4, complex **10** was found to accumulate in A2780 cancer cells with 31(±2) ng Os /10^6 cells observed after 24 h incubation. The method of detection used was ICP-MS, which determined the levels of ^{189}Os isotope. In Chapter 5, complex **10** was shown to release its iodide monodentate ligand in MCF-7 cells and very low levels of accumulated iodide were observed using radio-tracing methods. To provide a good comparative means of simultaneous detection of

accumulated iodide and osmium levels inside cancer cells after incubation with complexes, the development of an ICP-MS methodology for the dual detection of osmium and iodine may be possible. Cell samples are typically digested in concentrated HNO_3 because its combined strong acid and oxidising properties enable the effective break down of all cellular components into a homogeneous sample.[4] Osmium has a tendency to be oxidised and generate the volatile OsO_4 species in the presence of HNO_3, which can lead to false high readings for osmium.[5] However, this can be prevented by the addition of ascorbic acid and thiourea.[6] The digestion of samples containing iodide is even more problematic. Under low pH environments iodide can be easily oxidised to volatile I_2 by O_2 exposure in the samples (Scheme 7.1), leading to erroneous measurements.[7] Furthermore, other volatile iodine species can form in acidic conditions such as HI.[8]

$$4I^- + O_2 + 4H^+ \longrightarrow 2H_2O + 2I_2$$

Scheme 7.1. The oxidation of iodide to molecular iodine by exposure to oxygen in acidic conditions.[7]

Preventing the formation of volatile iodine species can be achieved using digestion processes under basic conditions,[9] which has been proven successful in several reports.[7,9-11] The digestion of cells under various basic conditions was tested and it was found that MCF-7 cells are readily digested in 1M KOH. However, the ICP-MS instrument does not tolerate levels of KOH greater than around 10 mM, and subsequent sample dilutions are likely to leave the levels of

Os/I below the detection limits of the instrument. Cellular digestion conditions of 100 mM KOH at 80 °C for 18 h were tested and were found to be not extreme enough to homogenise samples. Further cell digestion media tested included 32% NH_3 solution, and the combination of 100 mM KOH or 32% NH_3 with 30% H_2O_2. None of these methods were capable of homogenising cell samples after heating at 80 °C for 18 h, and H_2O_2 caused excessive foaming of the samples and pressure build up inside the wheaton vials, making them difficult to manipulate. Microwave-assisted digestion could prove to be an effective method for digesting cell samples in basic media as it allows heating to take place at temperatures greater than the boiling point of water. The reports referenced also demonstrate the use of microwave digestion in basic media and subsequent analysis of iodine content. However, little is known about the effect of basic conditions in the ICP analysis of osmium. One report suggests that ICP analysis of osmium in basic conditions leads to a decrease in ICP sensitivity.[12]

7.4. Sub-cellular distribution of complexes and mitochondrial uptake

The cellular distribution of a complex can be determined using cell fractionation kits to break down cells into their cytosolic, membrane, nuclear, and cytoskeletal fractions. HNO_3 digestion followed by ICP-MS analysis of the samples is then used to determine accumulated metal content.[13] The cellular distributions of my Chapter 4 complexes were not determined. However, previous Os(II) arene AZPY complexes synthesised by Ying *et al* were reported to be largely accumulated into the membrane fraction,[13,14] which consists of the

cellular membrane and its proteins, and cellular organelles and their membranes (including mitochondria).

A membrane potential of -180 mV is maintained across the lipid bilayer of mitochondria, larger in magnitude than that of any other organelle, providing an opportunity for selective chemical targeting.[15] Mitochondria are understood to be the cellular target of **FY026** and other analogous lipophilic positively charged complexes. As previously reported, **FY026** is capable of altering the potential of the mitochondrial membrane in both A2780 and A549 cancer cell lines, observed using a JC-10 mitochondrial membrane potential assay kit and flow cytometry.[16,17] The mitochondrial stain produces a red intensity when inside mitochondria. Upon changes in the mitochondrial membrane potential, the dye is released into the cytosol and converted into its monomeric green form and detected *via* flow cytometry. These changes indicate the induction of mitochondrial dysfunction brought about by the complex. Lipophilic cationic species are well known for their targeting of the mitochondrial membrane, exploiting its negative potential gradient as an electrostatic driving force.[15] The complexes of Chapter 4 are all cationic and mainly lipophilic as shown by their Log $P_{o/w}$ values and HPLC capacity factor measurements. Studies into the mitochondrial uptake of **FY026** and Chapter 4 complexes could provide further insight and help establish the importance of targeting mitochondria inside cancer cells. Similar to cell fractionation kits, mitochondria isolation assay kits are also commercially available and are used to isolate mitochondria from other cellular organelles and components, which with ICP-MS analysis can be used to determine the accumulation of osmium.

7.5. Further studies into mechanisms of cellular ROS elevation

Chapter 6 provided insight into the potential mechanisms of ROS elevation within cancer cells caused by complexes **8**, **10**, **10-OH**, **11**, **31** and **FY026**. The three main cellular targets explored were H_2O_2, GSH and NADH. Further studies are required to gain a fuller understanding of the roles that these species play in the mechanism of cell death.

7.5.1. Hydrogen peroxide (H_2O_2)

In Chapter 6, complexes **8**, **10-OH** and **11** were all capable of catabolising 100 mol. equiv. of H_2O_2, producing HO· radicals in the process which are capable of destroying cellular proteins. The mechanism of HO· generation is currently unknown but is expected to involve the formation of higher oxidation states of osmium and may resemble Fenton chemistry.[18] To better understand these processes the oxidation states of the osmium species formed during reaction with H_2O_2 need to be determined. X-ray Absorption Near Edge Spectroscopy (XANES) can be utilised to analyse the oxidation states of a metal centre in a given solid or solution.[19] Furthermore, gases were released when complexes **8**, **10-OH** and **11** reacted with H_2O_2, as shown by the bubbles observed in the EPR tubes (Chapter 6, Section **6.3.3.4**). Identifying released gases could also provide key insight into the mechanism of H_2O_2 degradation/HO· generation. This could be achieved using GC analysis.[20]

Quantofix® peroxide test strips that were used for testing H_2O_2 levels in Chapter 6, Section **6.3.3.1**, unfortunately only give semi-quantitative measurements.

Quantifying the amount of H_2O_2 depleted by complexes could be achieved using UV-Vis spectroscopy. H_2O_2 absorbs light at ~240 nm, which in phosphate buffer solution lies too close to the solvent cut-off point for reliable measurements. However, ammonium heptamolybdate tetrahydrate can be used as a H_2O_2 indicator. It interacts with H_2O_2 to yield a species with strong absorption at 405 nm.[21] Os(II) arene AZPY complexes also absorb light at 405 nm, but complex concentrations can be lowered to minimise interference. Furthermore, to better understand the impact of complexes on H_2O_2 levels *in vitro*, cellular H_2O_2 assay kits that are available commercially could be utilised to determine the effectiveness of complexes in a real cancer cell environment with physiological H_2O_2 concentrations and low levels of complex resembling sub IC_{50} concentrations. Assays for the determination of cellular H_2O_2 content utilise highly fluorescent probes, specific to the detection of H_2O_2 where it is possible to observe very small changes in fluorescence.[22]

7.5.2. Glutathione (GSH)

The binding studies of complexes **11** and **FY026** with 100 mol. equiv. of GSH were conducted in aerobic conditions and formed both thiolato- and sulfenato-adducts. Previous studies showed that a ruthenium complex, [Ru(η^6-bip)(en)I]PF_6, was also able to form a sulfenato-adduct with GSH in the presence of air, which was inhibited in an Ar atmosphere.[23] Further studies of complexes **11** and **FY026** in anaerobic conditions (achieved by bubbling samples with Ar or N_2) are required to prove that the oxidation of thiolato- to

sulfenato-adducts is caused by O_2 exposure. Conducting experiments in reduced levels of O_2 also resembles more closely the hypoxic environment of cancer cells, which in theory could inhibit the formation of sulfenato-adducts as with $[Ru(\eta^6\text{-bip})(en)I]PF_6$. However, there are other species present in cancer cells (such as H_2O_2) that may be capable of oxidising thiolato species. As discussed in Chapter 6, Section **6.4.3**, an Ir(III) Cp^{xbip} complex was capable of forming a thiolato-adduct with GSH, which formed sulfenato and sulfinato species upon reaction with H_2O_2.[24] Mimicking these reactions for **11-SG** and **FY026-SG** with small amounts of H_2O_2 could provide further insights into the role of these species in anti-cancer activity.

Furthermore, no study was conducted to determine whether complex **10** is capable of catalytically oxidising GSH to GSSG. In Chapter 4, Section **4.3.12**, it was shown that the first reduction potential of **10** is -0.26 V (lying well within the biologically relevant range). It demonstrates that **10** is even more easily reducible than $[Ru(\eta^6\text{-p-cym})(AZPY\text{-}NMe_2)I]^+$ (first reduction potential = -0.40 V), which is a known catalyst for GSH oxidation. Based on the hypothesis outlined by Dougan *et al*,[25] that M(II) arene AZPY complexes (where M = Ru or Os) with low and accessible reduction potentials can mediate redox reactions *via* their azo-bonds, **10** may be capable of such processes that are inaccessible for analogous complexes like **FY026** (first reduction potential = -0.64 V).[26]

7.5.3. Nicotinamide adenine dinucleotide (NADH)

It is suspected that the mechanism for the reaction between **10-OH** and NADH involves the transfer of hydride from NADH to Os(II), similarly to Os(II) arene IMPY complexes.[27] Further experiments are required to confirm the presence of the Os-H bond formed *in-situ*. Formation of the hydride species was previously confirmed *via* ^{1}H NMR for [Os(η^6-*p*-cym)(IMPY-NMe_2)I]$^+$, yielding a resonance at -4.2 ppm when it was incubated with 4 mol. equiv. NADH.[27] The presence of H_2O_2 was observed during the reaction between **10-OH** and NADH. This provides limited evidence that under aerobic conditions, O_2 may react with a Os-H species to regenerate the catalyst and release H_2O_2 in a similar manner to [Os(η^6-*p*-cym)(IMPY-NMe_2)I]$^+$. Further experiments are required to determine whether the reaction occurs catalytically (as it does with [Os(η^6-*p*-cym)(IMPY-NMe_2)I]$^+$), and to determine whether the oxidation of NADH still proceeds under the hypoxic conditions of cancerous cells, by performing reaction under anaerobic conditions. Osmium-bound hydride may be released *via* alternative pathways such as the generation of H_2, which was observed by GC for some Ir(III) Cp complexes.[20]

7.6. Chiral resolution of complexes

Ever since the Thalidamide disaster in 1957 when the (S)-enantiomer of the morning sickness drug caused children to be born with phocomelia, all chiral drugs are now subject to compulsory isolation and purification of enantiomers to identify their toxicities. 3-Legged piano stool osmium(II) arene complexes containing a monodentate halide ligand and a bidentate AZPY ligand all have

chiral metal centres, owing to the in-equivalent N-binding groups in AZPY ligands. They crystallise as racemates (an equimolar mixture of two enantiomers), which is clearly observable in the X-ray crystal structure of complex **10** reported in Chapter 4, Section **4.3.3** (see Figure 7.3).

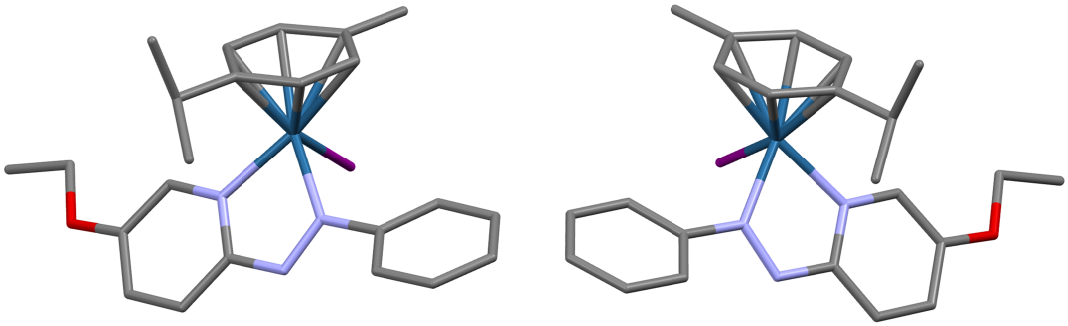

Figure 7.3. Two enantiomers observed in the X-ray crystal structure of **10** ([Os(η^6-*p*-cym)(5-EtO-AZPY)I]PF_6). Ellipsoids are shown at the 50% probability level and all hydrogens, counter ions and solvent molecules have been omitted for clarity.

Δ-Trisphat is a chiral anion and an efficient NMR chiral shift reagent for chiral cationic compounds.[28,29] On addition to complex **10**, it forms diastereomeric ion pairs that have different chemical shifts. Hence, the resolution of enantiomers can be observed by ^{1}H NMR (see Figure 7.4). The spectrum revealed the splitting of several peaks, particularly those corresponding to protons in close proximity to the chiral centre.

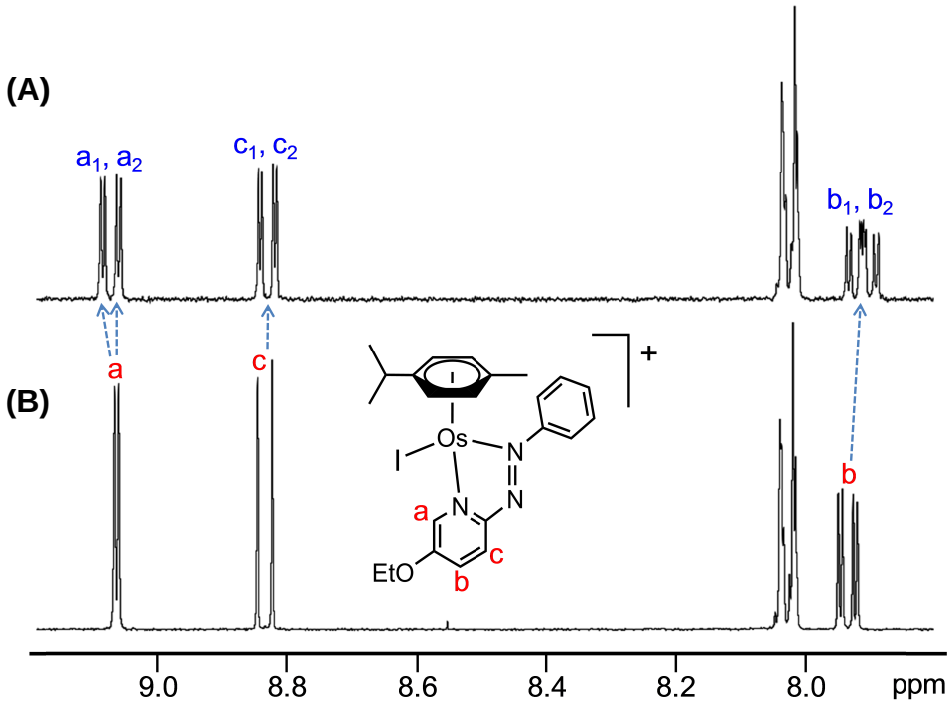

Figure 7.4. Part of the aromatic region of the ^{1}H NMR spectrum of complex **10** in methanol-d_4. (A) After the addition of Δ-Trisphat. (B) Before the addition of Δ-Trisphat. After addition shows the splitting of several aromatic peaks that correspond to protons residing close to the Os chiral centre.

An attempt was made to chirally resolve complex **10** by HPLC using a CHIRALPAK ID chiral HPLC column with a mobile phase of EtOH (0.3% TFA, 0.5% TEA) at a flow rate of 2.2 mL/min. The chromatogram shows two peaks with retention times of 3.70 and 3.83 min, however, the latter peak is approximately double the size of the former suggesting that the enantiomers were not fully resolved (Figure 7.5). Optimisation of HPLC conditions are required to obtain complete resolution of the two enantiomers. Further work is also required to isolate the two enantiomers and test them for racemisation under physiological conditions. Stable enantiomers should be studied

individually for anti-proliferative activity. Most isomers of chiral drugs in the clinic exhibit marked differences in biological activity.[30] However, Os(II) arene AZPY complexes are not designed for targeted therapy and so differences in activities between enantiomers are not considered likely. Nonetheless, chiral separation and analysis of racemic drugs are vital prerequisites within the pharmaceutical industry and a key safety measure for moving into clinical trials.

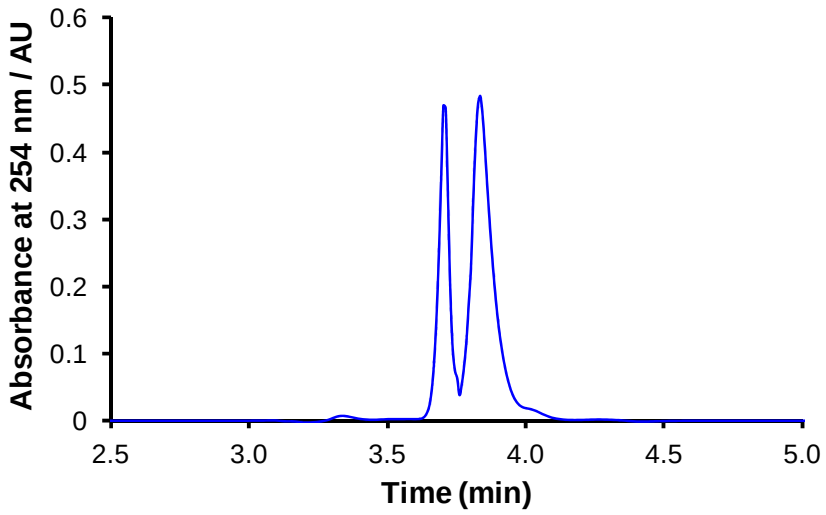

Figure 7.5. Chromatogram of the partial resolution of the enantiomers of **10**, using a CHIRALPAK ID chiral HPLC column, a mobile phase of EtOH (0.3% TFA, 0.5% TEA), and flow rate of 2.2 mL/min.

7.7. Complexes incorporating BCL-X_L inhibitors

The pro-survival BCL-2 family of proteins are responsible for regulating cell death by suppressing the induction of apoptosis. However, in cancer cells certain BCL-2 proteins such as BCL-X_L are over-expressed, rendering malignant tumour cells resistant to anti-cancer agents.[31] One proposed idea is

to incorporate a known BCL-X_L inhibitor pharmacophore onto an Os(II) arene AZPY complex, hence producing a dual functional metal complex capable of targeting a biologically active site. BCL-X_L is known to reside inside mitochondria of cancer cells, which provides a strong advantage since Os(II) arene AZPY complexes are believed to target mitochondria.[16]

In Chapter 1, Section **1.2.2**, a lipophilic BCL-X_L inhibitor (WEHI-539) was described with the capability of docking into a hydrophobic groove on the active site. It may be possible to attach pharmacophores like WEHI-539 onto an AZPY ligand utilising the glycol side chains reported in Chapter 4, Section **4.3.1.1** (Figure 7.6). The length of the glycol linkage can be tailored so as to allow the metal centre to sit on the surface of the protein and exert its multiple mechanisms of elevating cellular ROS levels, whilst the WEHI-539 moiety fulfils its role of inhibiting BCL-X_L. Such modifications have the potential to improve cancer cell selectivity of Os(II) arene AZPY complexes, an issue highlighted in Chapter 4, Section **4.4.1** which requires addressing. At the same time it would fulfil an industry demand for targeted chemotherapies, whilst still retaining the desirable properties associated with organometallic drugs such as multiple mechanisms of activity. A synthetic scheme is proposed for the attachment of BCL-X_L inhibiting molecules to Os(II) arene AZPY complexes in Scheme 7.2.

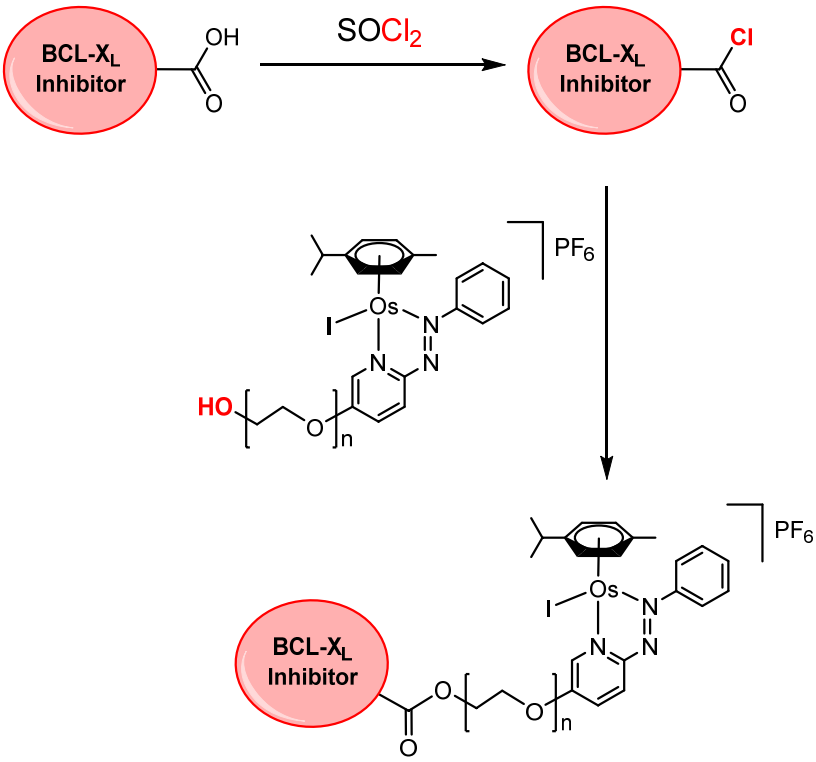

Scheme 7.2. Proposed synthesis scheme for the attachment of BCL-X$_L$ inhibitors to Os(II) arene AZPY complexes with glycol substituents.

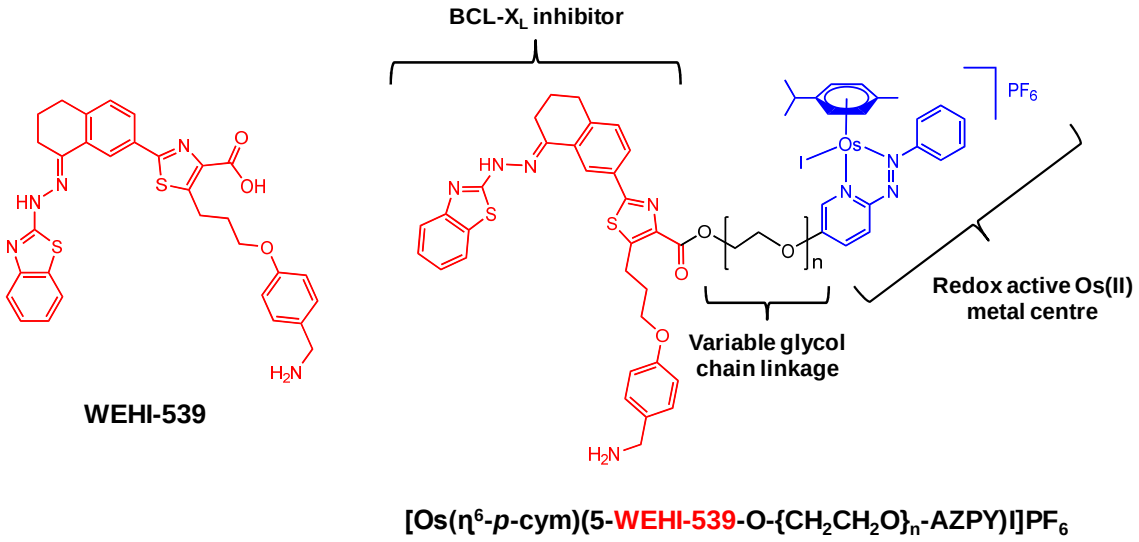

Figure 7.6. The structure of BCL-X$_L$ inhibitor, WEHI-539, and proposed Os(II) arene AZPY complex with a WEHI-539 pharmacophore attached to the AZPY ligand *via* a glycol chain linkage.

7.8. References

(1) Zhang, Q. F.; Nie, H. C.; Shangguang, X. C.; Yin, Z. P.; Zheng, G. D.; Chen, J. G. *J. Agric. Food. Chem.* **2013**, *61*, 151.

(2) Morrison, P. W. J.; Connon, C. J.; Khutoryanskiy, V. V. *Mol. Pharmaceut.* **2013**, *10*, 756.

(3) Romero-Canelón, I.; Phoenix, B.; Pitto-Barry, A.; Tran, J.; Soldevila-Barreda, J. J.; Kirby, N.; Green, S.; Sadler, P. J.; Barry, N. P. E. *J. Organomet. Chem.* **2015**, *796*, 17.

(4) Romero-Canelón, I.; Salassa, L.; Sadler, P. J. *J. Med. Chem.* **2013**, *56*, 1291.

(5) Filak, L. K.; Göschl, S.; Heffeter, P.; Ghannadzadeh Samper, K.; Egger, A. E.; Jakupec, M. A.; Keppler, B. K.; Berger, W.; Arion, V. B. *Organometallics* **2013**, *32*, 903.

(6) Venzago, C.; Popp, M.; Kovac, J.; Kunkel, A. *J. Anal. At. Spectrom.* **2013**, *28*, 1125.

(7) Reid, H. J.; Bashammakh, A. A.; Goodall, P. S.; Landon, M. R.; O'Connor, C.; Sharp, B. L. *Talanta* **2008**, *75*, 189.

(8) Patriarca, M.; A. Kratchowil, N.; J. Sadler, P. *J. Anal. At. Spectrom.* **1999**, *14*, 633.

(9) Nóbrega, J. A.; Santos, M. C.; de Sousa, R. A.; Cadore, S.; Barnes, R. M.; Tatro, M. *Spectrochim. Acta B* **2006**, *61*, 465.

(10) Fernandez Sanchez, L.; Szpunar, J. *J. Anal. At. Spectrom.* **1999**, *14*, 1697.

(11) Vanhoe, H.; Van Allemeersch, F.; Versieck, J.; Dams, R. *Analyst* **1993**, *118*, 1015.

(12) Chiweshe, T. T.; Purcell, W.; Venter, J. A. *Bull. Chem. Soc. Jpn.* **2015**, *88*, 1054.

(13) Romero-Canelon, I.; Salassa, L.; Sadler, P. J. *J. Med. Chem.* **2013**, *56*, 1291.

(14) Fu, Y.; Habtemariam, A.; Basri, A. M. B. H.; Braddick, D.; Clarkson, G. J.; Sadler, P. J. *Dalton Trans.* **2011**, *40*, 10553.

(15) Hoye, A. T.; Davoren, J. E.; Wipf, P.; Fink, M. P.; Kagan, V. E. *Acc. Chem. Res.* **2008**, *41*, 87.

(16) Romero-Canelón, I.; Mos, M.; Sadler, P. J. *J. Med. Chem.* **2015**, *58*, 7874.

(17) van Rijt, S. H.; Romero-Canelon, I.; Fu, Y.; Shnyder, S. D.; Sadler, P. J. *Metallomics* **2014**, *6*, 1014.

(18) Barbusiński, K. *Ecol. Chem. Eng. S* **2009**, *16*, 347.

(19) Conradson, S. D.; Al Mahamid, I.; Clark, D. L.; Hess, N. J.; Hudson, E. A.; Neu, M. P.; Palmer, P. D.; Runde, W. H.; Drew Tait, C. *Polyhedron* **1998**, *17*, 599.

(20) Liu, Z., Ph.D Thesis, University of Warwick, 2011.

(21) Vitro, N. G. N. M. *Open Enz. Inhib. J.* **2008**, *1*, 34.

(22) Werner, E. *Sci. Signal.* **2003**, *2003*, pl3.

(23) Wang, F.; Xu, J.; Habtemariam, A.; Bella, J.; Sadler, P. J. *J. Am. Chem. Soc.* **2005**, *127*, 17734.

(24) Liu, Z.; Sadler, P. J. *Inorg. Chem. Front.* **2014**, *1*, 668.

(25) Dougan, S. J.; Habtemariam, A.; McHale, S. E.; Parsons, S.; Sadler, P. J. *Proc. Natl. Acad. Sci. U.S.A.* **2008**, *105*, 11628.

(26) Fu, Y. Ph.D Thesis, University of Warwick, 2011.

(27) Fu, Y.; Romero, M. J.; Habtemariam, A.; Snowden, M. E.; Song, L.; Clarkson, G. J.; Qamar, B.; Pizarro, A. M.; Unwin, P. R.; Sadler, P. J. *Chem. Sci.* **2012**, *3*, 2485.

(28) Lacour, J.; Ginglinger, C.; Favarger, F.; Torche-Haldimann, S. *Chem. Commun.* **1997**, 2285.

(29) Monchaud, D.; Lacour, J.; Coudret, C.; Fraysse, S. *J. Organomet. Chem.* **2001**, *624*, 388.

(30) Nguyen, L. A.; He, H.; Pham-Huy, C. *Int. J. Biomed. Sci.* **2006**, *2*, 85.

(31) Lessene, G.; Czabotar, P. E.; Sleebs, B. E.; Zobel, K.; Lowes, K. N.; Adams, J. M.; Baell, J. B.; Colman, P. M.; Deshayes, K.; Fairbrother, W. J.; Flygare, J. A.; Gibbons, P.; Kersten, W. J. A.; Kulasegaram, S.; Moss, R. M.; Parisot, J. P.; Smith, B. J.; Street, I. P.; Yang, H.; Huang, D. C. S.; Watson, K. G. *Nat. Chem. Biol.* **2013**, *9*, 390.

8. Appendices

8.1. Chapter 3 complexes

1a

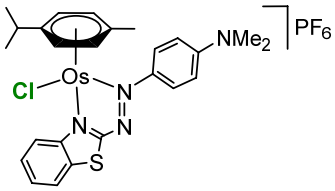

2a

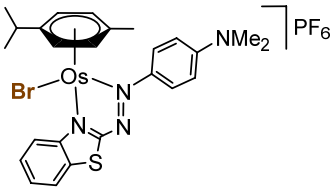

3a

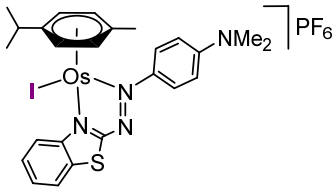

1b

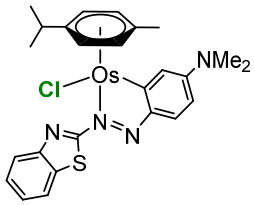

2b

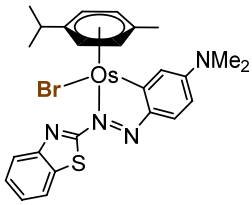

3b

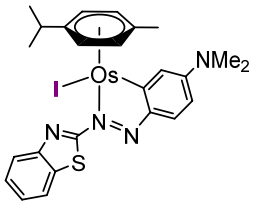

4

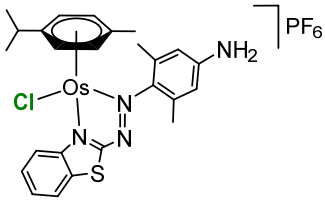

5

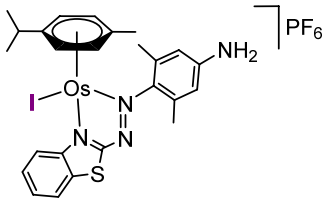

8.2. Chapter 4 complexes

6

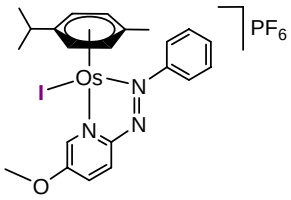

7

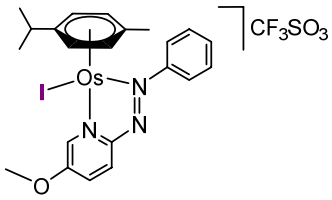

8

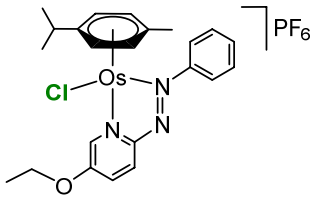

9

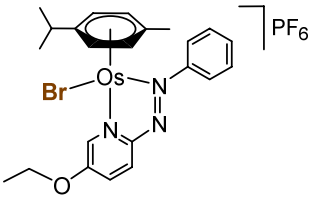

10

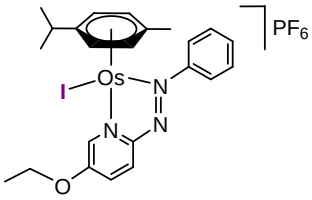

11

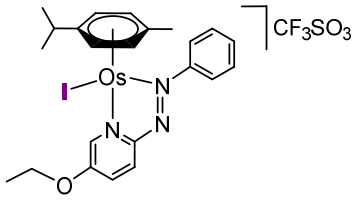

12

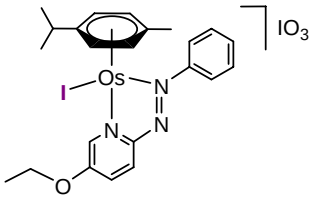

13

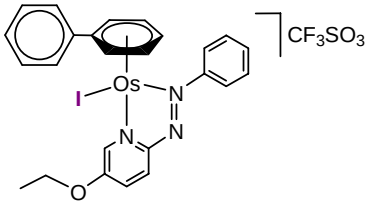

13A

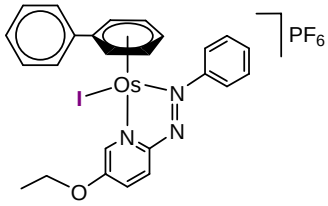

14

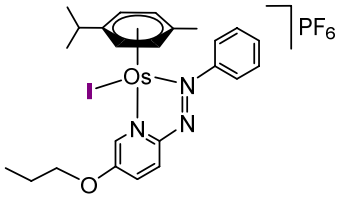

15

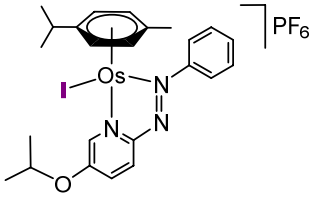

16

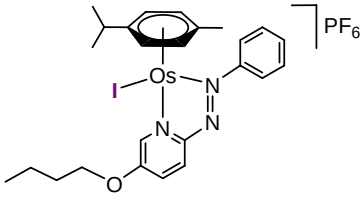

17

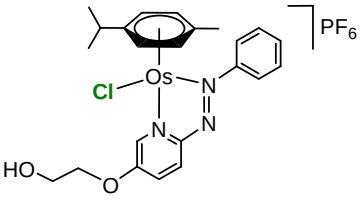

18

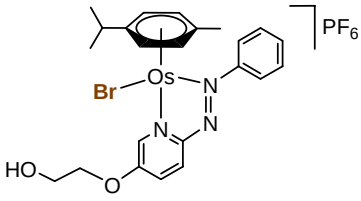

19

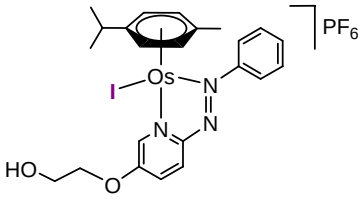

20

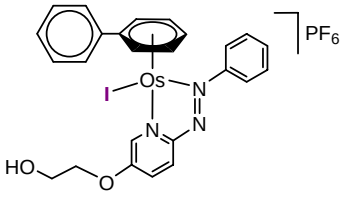

21

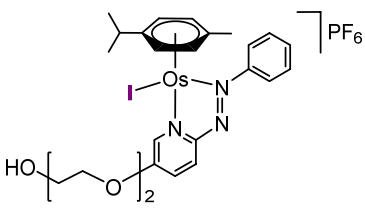

22

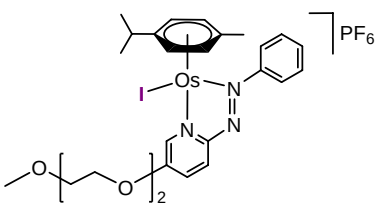

23

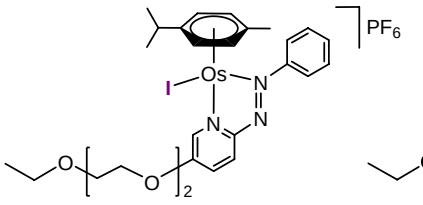

24

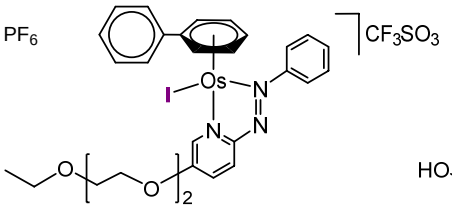

25

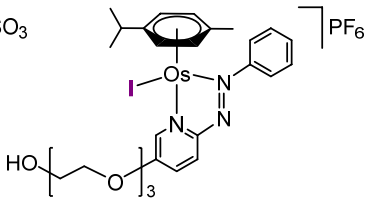

26

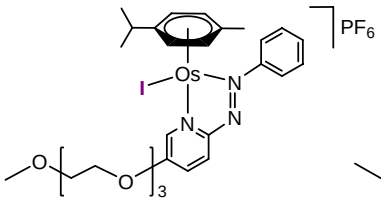

27

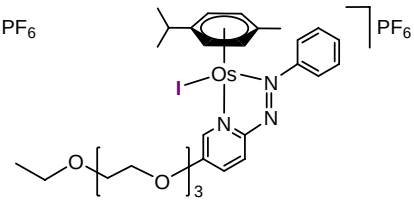

28

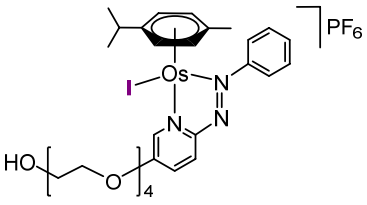

29

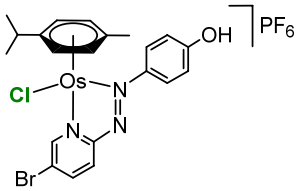

30

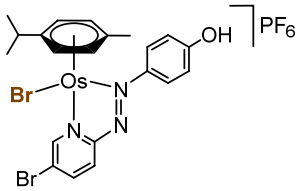

31

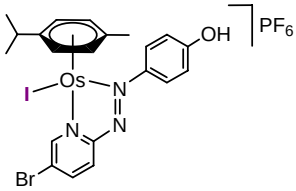

32

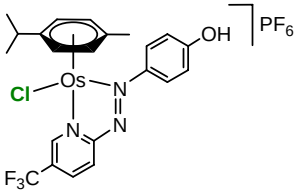

33

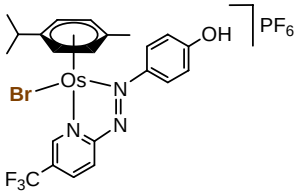

34A

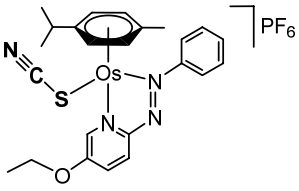

34B

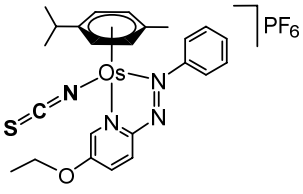

35

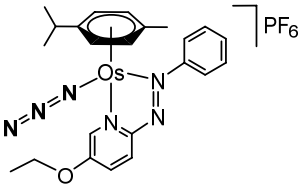

8.3. Chapter 5 complexes

FY026

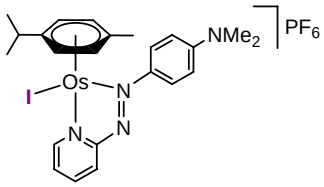

[^{131}I]FY026

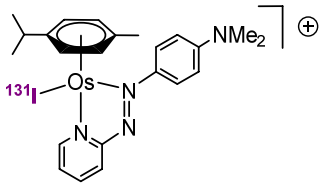

[^{131}I]10

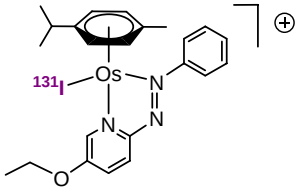

8.4. Chapter 6 complexes

10-OH